Università degli Studi di Palermo

AREA QUALITÀ, PROGRAMMAZIONE E SUPPORTO STRATEGICO
SETTORE STRATEGIA PER LA RICERCA
U. O. DOTTORATI

Corso di Dottorato di Ricerca in
"Energia e Tecnologie dell'Informazione - curriculum Fisica Tecnica e Ingegneria Nucleare"
Dipartimento di Ingegneria
Settore Scientifico Disciplinare ING-IND/19

THERMOFLUID-DYNAMICS OF DEMO DIVERTOR CASSETTE

IL DOTTORE
ANDREA QUARTARARO

IL COORDINATORE
CH.MO PROF. MAURIZIO CELLURA

IL TUTOR
CH.MO PROF. PIETRO ALESSANDRO DI MAIO

CICLO XXXV
ANNO CONSEGUIMENTO TITOLO 2023

To my father.

To Eleonora.

Contents

List of Figures

List of Tables

Acronyms

ADRANOS Advanced Divertor paRametric Analysis for coolaNt Operating Scenarios

BB Breeding Blanket

BC Boundary Condition

CB Cassette Body

CAD Computer Aided Design

CHF Critical Heat Flux

CFD Computational Fluid Dynamic

CS Central Solenoid

dpa Displacement per Atom

DBTT Ductile-to-Brittle Transition Temperature

DEMO DEMOnstration fusion power reactor

D-T Deuterium-Tritium

EFDA European Fusion Development Agreement

EM ElectroMagnetic

ENEA *Agenzia nazionale per le nuove tecnologie, l'energia e lo sviluppo economico sostenibile*

EU European

FEM Finite Element Method

FoM Figure of Merit

FTTT Fracture Toughness Transition Temperature

GCI Grid Convergence Index

GEKO Generalized $k - \omega$

GR Growth Rate

FPP Fusion Power Plant

FPY Full Power Year

FVM Finite Volume Method

FW First Wall

ITER International Thermonuclear Experimental Reactor

IVST Isotropic Virtual Swirl Tape

IVT Inner Vertical Target

LS Least-Square

OVST Orthotropic Virtual Swirl Tape

OVT Outer Vertical Target

MOGA Multi-Objective Genetic Algorithm

NS Neutron Shield

PCD Pre-Conceptual Design

PF Poloidal Field

PFC Plasma Facing Component

PFU Plasma Facing Unit

PHTS Primary Heat Transfer System

RAFM Reduced-Activation Ferritic/Martensitic

RANS Reynolds Averaged Navier Stokes

RC Rear Channel

RH Remote Handling

RNG Re-Normalisation Group

RP Reflector Plate

SOL Scrape-Off Layer

SL Shielding Liner

SST Shear Stress Transport

ST Swirl Tape

TB Target Body

tokamak TOroidal'naya KAmera s MAgnaitnymi Katushkami

TF Toroidal Field

VST Virtual Swirl Tape

VT Vertical Target

VV Vacuum Vessel

WP-DIV Work Package Divertor

Nomenclature

α	Constant of the Richardson extrapolation
α_t	Turbulent thermal diffusivity
χ	Braching factor
Δp	Pressure drop
δ	Swirl tape thickness
Δ_{CHF}	CHF margin non-uniformity coefficient
Δ_v	Velocity non-uniformity coefficient
$\dot{m}$	Mass flow rate
ϵ	Surface roughness
ϵ_ϕ	Relative span
γ	Swirl tape dimensionless twist ratio
λ	Thermal conductivity
μ	Dynamic viscosity
μ_b	Bulk dynamic viscosity
μ_t	Turbulent dynamic viscosity
μ_w	Wall dynamic viscosity
ω	Specific rate of dissipation of turbulence
$\overline{v}$	Average axial velocity
ρ	Density
ρ_v	Water vapor saturation density
ρ_{ref}	Reference density for pressure drop fitting

σ Standard deviation

σ_t Turbulent Prandtl number

τ Divertor lifetime

θ Preferred flow angle

$\underline{n}_1$,$\underline{n}_2$,$\underline{n}_3$ Main directions in OVST modelling

$\underline{S}$ Momentum source term of the Navier-Stokes equation

$\underline{u}$ Velocity vector

A Area

a Pressure drop fitting parameter

A_r Dimensionless area ratio

B OVST fitting coefficient

b Pressure drop fitting exponent

C OVST fitting coefficient

C_f Swirl tape correction factor of Tong-75 correlation

c_p Fluid heat capacity under isobaric conditions

CV Coefficient of Variation

D OVST fitting coefficient

d_0 Internal diameter

d_h Hydraulic diameter

d_r Dimensionless diameter ratio

d_{ref} Reference diameter

e Specific internal energy

e_r Relative error

F_s GCI safety factor

H Swirl tape pitch

h_i Average linear size for the Richardson extrapolation

i	Fluid specific enthalpy
Ja	Jacob number
k	Turbulent kinetic energy
K_c	Sudden contraction loss coefficient
K_e	Sudden expansion loss coefficient
$K_{loss,1}$	OVST porous medium loss coefficient
$K_{loss,2-3}$	OVST porous medium loss coefficient
K_{loss}	Porous medium loss coefficient
L	Length
l	Distance between two pressure monitoring surfaces
L_{fluid}	Distance travelled by the fluid
l_{ST}	ST length
n	Number of PFU channels
Nu	Nusselt number
P	Pumping power
p	Pressure
p_{crit}	Critical pressure
Pr	Prandtl number
q	Heat flux
q_{bi}	Boiling incipience heat flux
$q_{q_{fdnb}}$	Fully developed nucleate boiling heat flux
q_{sp}	Single-phase heat flux
$q_{w,max}$	Maximum wall heat flux
r	Specific enthalpy of vaporization
R_{crit}	Threshold radius
Re	Reynolds number

s	Curvilinear coordinate
T	Temperature
$T_{ave,ch}$	Line-average surface temperature
T_{bulk}	Coolant bulk temperature
T_{sat}	Saturation temperature
u_0	Equivalent empty-pipe velocity
u_θ	Tangential velocity
u_z	Axial velocity
W	Total deposited power

Disclaimer

This work has been carried out within the framework of the EUROfusion consortium and has received funding from the Euratom research and training programme 2014-2018 and 2019-2020 under grant agreement No 633053.

The views and opinions expressed herein do not necessarily reflect those of the European Commission.

Abstract

The divertor is a critical in-vessel component of nuclear fusion reactors, being responsible for the fulfilment of certain fundamental functions for the machine: it must be able to handle the power deposited by charged particle and neutron irradiation, ensure the presence of channels through which the fusion ashes can be removed from the Vacuum Vessel (VV), provide plasma-compatible surfaces, and shield the VV and magnets from nuclear loads.

The heat load that can be tolerated by the divertor under normal and off-normal operating conditions is a pivotal parameter when dimensioning a fusion power plant since exceptionally high heat fluxes can be observed in some regions of the divertor, in the order of some tens of MW/m^2. It is therefore clear that the proper functioning of this component in steady-state or long pulse conditions is inextricably linked to the correct design of its cooling circuit, which is required to prevent structural and functional materials to operate outside their operative limits, avoid unduly high pressure drops, and operate at the highest possible temperature to ensure the maximum achievable thermodynamic cycle efficiency while complying with all the applicable constraints.

In particular, for the case of the European DEMO power plant, during the Pre-Conceptual Design (PCD) phase which ended in 2020, attention was focused on the study of a "Double-Circuit" divertor concept, in which two independent cooling circuits served by two different Primary Heat Transfer Systems (PHTS) were used to cool the divertor Plasma-Facing Components (PFC) and the Cassette Body (CB).

The possibility to adopt a single cooling circuit to serve both PFCs and CB, suggested during the divertor final design Review Meeting of the PCD phase, led to the definition of a new divertor concept, namely the "Single-Circuit Cooling Option". This novel divertor was originally conceived to allow for a simpler balance of plant design, as it would require a single PHTS, and to ease remote maintenance, as only one inlet and one outlet pipe should be cut and reweld for each divertor cassette during replacement operations.

The research activities carried out during the Ph.D. aimed to identify the strengths and possible shortcomings of this divertor design solution. To this purpose, attention was at first focussed on the development, validation and application of a dedicated numerical tool able to perform quick parametric analyses of the

divertor cooling circuit, allowing for a first screening of coolant operating conditions and cooling circuit layouts that do not comply with most of the applicable thermal and thermal-hydraulic requirements and constraints. Therefore, with the final aim to perform a detailed thermofluid-dynamic assessment with the tools of Computational Fluid Dynamics (CFD), a simulation technique based on an equivalent porous medium concept was developed. With this technique it is possible to reduce the computational costs required to simulate the coolant flow inside swirl tape-equipped cooling channels, being the most computationally demanding components of the entire divertor cooling circuit, without compromising the quality of the results. Finally, the complete 3D-CFD thermofluid-dynamic simulation of the entire single-circuit cooling option divertor cassette was performed, confirming the outcomes of parametric analyses and highlighting the occurrence of additional criticalities in terms of cooling performance and thermal hot spots. In this dissertation are reported the methodologies developed and their validation, together with the models, assumptions, and outcomes of this research campaign.

Introduction

In recent years, the European Union has promoted research and technological development for the exploitation of nuclear fusion to produce electricity in order to meet the ever-increasing demand for energy, while at the same time ensuring a reduction in greenhouse gas emissions and permitting a decrease in dependence on conventional fossil fuels.

In 2012, the European Fusion Development Agreement (EFDA) published the first Fusion Roadmap [1]. This is the pivotal document in fusion research, as it defines the priorities and the key challenges to be addressed for the realisation of industrial Fusion Power Plants (FPPs), and sets timelines for achieving the specified goals. The roadmap was afterwards updated in 2018 [2] after EFDA was succeeded by EUROfusion, a consortium of fusion research institutes with partners from the European Union, Switzerland, Ukraine and the United Kingdom, which acts as an "umbrella" organisation for Europe's fusion research laboratories. The three main steps outlined in the roadmap are as follows:

1. the technical demonstration of large-scale fusion power by means of the International Thermonuclear Experimental Reactor (ITER) machine;

2. the delivery to the grid of electricity via a DEMOnstration fusion power reactor (DEMO), in parallel with the exploration of alternative machine concepts, such as stellarators;

3. the large-scale industrial production and exploitation of FPP.

Funded under Horizon 2020, the EUROfusion consortium carried out the Pre-Conceptual Design (PCD) of the European (EU) DEMO machine, paving the way for the ongoing conceptual design phase, which is being carried out under the 2021-2027 Framework Programme for Research and Technological Development (FP9) Horizon Europe.

Among the milestones defined by this new roadmap, the realisation of DEMO is of great importance. It is expected to be operational by the end of this century, delivering several hundred MW of electricity to the grid while operating with a closed fuel cycle and replicating many of the characteristics required for future commercial FPPs, thus demonstrating their feasibility.

There are several challenges to be overcome to achieve a sound DEMO design, and one of the most critical is the technological development of the divertor cassette, the in-vessel component responsible for power handling and particle exhaust. In fact, one of the essential aspects of the design of a power-producing FPP is the amount of power that can be reliably controlled within it. This is highly dependent, among other things, on the heat load that the divertor can tolerate under normal and off-normal operation [3], and the correct functioning of the divertor in steady-state or long-pulse conditions is inextricably linked to the correct design of its cooling circuit.

The research activity carried out during the *XXXV* cycle of the Ph.D. course in *Energia e Tecnologie dell'Informazione - Curriculum Fisica Tecnica e Ingegneria Nucleare*, held at the University of Palermo, is framed within DEMO conceptual design activities and was supported by the EUROfusion consortium, of which the University of Palermo is an affiliated entity through the *Agenzia nazionale per le nuove tecnologie, l'energia e lo sviluppo economico sostenibile* (ENEA). In particular, the research activity focused on the thermofluid-dynamic study of the *Single-Circuit Cooling Option* divertor, developed in 2020 and 2021 and proposed as an alternative solution to the *Double-Circuit Cooling Option*, whose design was carried out during the PCD phase. This solution was investigated with the aim of simplifying the layout of the divertor Primary Heat Transfer Systems (PHTSs) and easing maintenance operations. A general description of these two divertor concepts, together with the details of their cooling circuits and the main constraints and requirements which guided their design, can be found in chapter 1 of this dissertation.

During the Ph.D. years, the research activity developed along two parallel paths. The first, detailed in chapter 2, involved the development of a calculation tool, implemented in the MATLAB environment, to determine the thermofluid-dynamic operating map of this new divertor cassette solution. This novel numerical tool, named Advanced Divertor paRametric Analysis for coolaNt Operating Scenarios (ADRANOS), performs quick assessments of the mass flow rate, coolant temperature, and coolant pressure distribution among the different sub-components constituting the cassette, by adopting a lumped-parameters approach. Moreover, a 2D-Finite Element Method (FEM) module is embedded in ADRANOS and allows the evaluation of detailed temperature distribution inside the Plasma Facing Unit (PFU) structures, so to check the compliance with materials temperature limits.

The tool was validated against experimental results and exploited to carry out a broad parametric analysis campaign to determine the limits and acceptable operating ranges of different DEMO divertor cooling circuit layouts, both single and double circuit cooling options. The outcomes of these analyses highlighted some criticalities for the adoption of the single-circuit solution, being not possible to

guarantee sufficiently high temperatures for the cassette structures without violating the Critical Heat Flux (CHF) margin constraint, which results in a reduction of the divertor cassette lifetime, excepting for a rather complex cooling circuit layout foreseeing the target connected in parallel and a suitable bypass of the entire Cassette Body (CB) which would entail additional potential issues to be further investigated. Moreover, the same tool was employed to check suitable operating conditions for the divertor Plasma Facing Component (PFC) cooling circuit considering the two targets connected both in series and parallel, questioning the current constraints on maximum coolant velocity and CHF margin and exploring the effects of higher peak plasma heat fluxes.

The second research line focussed instead on the assessment of the complete thermofluid-dynamic behaviour of the divertor cassette employing detailed 3D-Computational Fluid Dynamic (CFD) calculations. Given the great complexity of the component, it was deemed necessary to preliminarily define some modelling techniques to reduce the computational cost required to perform the analyses. In particular, as will be detailed in chapter 3, the attention was focused on the Swirl Tape (ST)-equipped PFU cooling channels, difficult to integrate into the complete cassette model, as they would require an excessive computational cost and an unduly high pre-processing effort. Several analysis campaigns were carried out to assess the flow field inside these components, highlighting the occurrence of peculiar fluid-dynamic phenomena that significantly affect pressure drop and heat transfer, and to validate the numerical results against relevant correlations. Then, the Virtual Swirl Tape (VST) approach, a novel modelling technique based on the adoption of porous media, was developed and tested to assess its pressure drop and heat transfer coefficient predictive capabilities.

The VST approach was then employed to allow the complete 3D-CFD simulation of the single-circuit cooling option divertor cassette, as described in chapter 4. First of all, an extensive mesh independence assessment of the divertor cassette main components was performed, selecting the optimal mesh size to be adopted, thus providing reliable results in terms of pressure, temperature, and mass flow rate distribution. Then, the calculations confirmed the criticalities already observed with the parametric analyses in chapter 2, confirming the predictive capabilities of ADRANOS, and highlighted additional issues that must be addressed in the future design revisions of the divertor cassette, i.e. the occurrence of severe thermal hot spots in the target supports and in the Shielding Liner (SL).

The research activity described in this dissertation was carried out during my Ph.D. course from the end of 2019 to the second half of 2022, both at University of Palermo and Max-Planck-Institut für Plasmaphysik, Garching bei München (Germany), where I spent a month as a visiting researcher.

Chapter 1

Fusion Reactor Divertors

1.1 Introduction

The TOroidal'naya KAmera s MAgnaitnymi Katushkami (tokamak) machines are the most advanced and best-investigated fusion device concepts available today [4]. These machines rely on the usage of very intense magnetic fields to confine the plasma particles, i.e. ions and electrons, within a toroidal plasma chamber, allowing outstandingly high plasma temperatures while protecting the integrity of the reactor structures. The first generation of FPP will exploit Deuterium-Tritium (D-T) reaction [5]:

$$ {}^{2}_{1}D + {}^{3}_{1}T \rightarrow {}^{4}_{2}He(3.54MeV) + {}^{1}_{0}n(14.05MeV), \tag{1.1} $$

where deuterium and tritium nuclei fuse, producing a Helium-4 nucleus, also referred to as α particle, and a neutron. While neutrons are not affected by the magnetic confinement and are free to escape from the plasma carrying most of the energy generated by D-T reactions, α particles are purposely conveyed along narrow paths, resulting in high particle fluxes, and consequently in high heat fluxes, in the intersection between these trajectories and the reactor inner walls.

In this framework, the divertor is a key in-vessel component of FPP, since it must be able to handle the above-mentioned power and particle fluxes, together with neutron irradiation, while ensuring the presence of channels through which the fusion ashes can be removed from the Vacuum Vessel (VV), providing plasma-compatible surfaces, and shielding the VV and magnets from nuclear loads [6]. Besides, neutron irradiation produces defects and damages in the structural materials leading to embrittlement, while pulsed operation causes fatigue owing to thermal stress variation, challenging the divertor lifetime. Its importance is emphasised in the Fusion Roadmap, which defines reliable power exhausting as one of the main challenges in the realization of a FPP [2]. Moreover, the heat load that can be

tolerated by the divertor under normal and off-normal operating conditions is a pivotal parameter when dimensioning an FPP [3].

From these considerations, it is therefore clear that the proper functioning of this component in steady-state or long-pulse conditions is inextricably linked to the correct design of its cooling circuit, which is required to prevent structural and functional materials to operate outside their operative temperature limits, avoid unduly high pressure drops, and operate at the highest possible temperature to ensure the maximum achievable thermodynamic cycle efficiency while complying with all the applicable constraints.

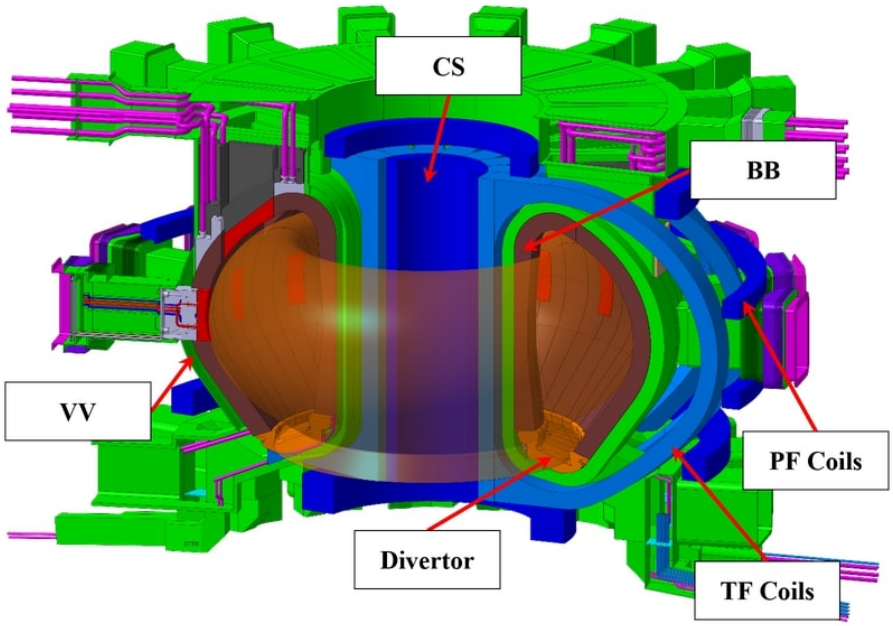

Figure 1.1: EU DEMO tokamak and position of the main components [7].

Figure 1.1 shows the DEMO tokamak, with an indication of the position of the main components: the VV, the Breeding Blanket (BB), the superconducting coils, i.e., the Toroidal Field (TF) and Poloidal Field (PF) coils and the Central Solenoid (CS), and the divertor. This latter component directly faces the plasma, and it is placed in the lower part of the VV. Moreover, it should be mentioned, as it will be discussed later, that the main tokamak components located below the divertor are the VV, the TF coils and the lowest PF coil, referred to as PF6.

1.2 Divertor functions and design requirements

As anticipated, the main divertor function is the heat and particle exhaust: in fact, for a stable fusion operation, the helium concentration accumulated in the plasma must remain below a threshold concentration value. The ash control is obtained with the diverted magnetic configuration, in which a mixture of ashes and

fuel particles drifts outwards, crosses the separatrix at the core plasma edge and enters the Scrape-Off Layer (SOL). These particles are then guided along the SOL towards the divertor targets, where they are neutralized and pumped out together with the plasma impurities.

Impinging upon the divertor targets, the particles transfer their kinetic energy to the divertor, thus macroscopically resulting in intense heat fluxes, which sums up with the radiative heat fluxes coming from the core plasma and the SOL and the neutrals, originated by charge exchange reactions in the pedestal region [8]. These energy channels transport most of the fusion power carried by α particles, together with the auxiliary heating provided to the plasma for control, heating and current drive, and this thermal power must be continuously exhausted at the targets by means of active cooling to enable steady-state or long-pulse operations.

As the characteristic power decay length of the SOL is small, the thermal power density is concentrated on a narrow band of the targets, around the so-called *strike point*, leading to localized high heat flux values.

To reduce the amplitude of this peak, two solutions are generally employed: the targets are inclined at a shallow angle (few degrees) relative to the grazing magnetic field lines, so as to increase the projected area [9], and power is preventively radiated from the SOL using seeded inert gases, forming a detached plasma condition [10].

These strategies make it possible to significantly reduce the expected heat fluxes at the divertor targets to values that are manageable with the available technologies, but normal and off-normal plasma transients can lead to very high heat loads that must be handled by the divertor, in the order of several tens of MW/m^2.

Apart from removing the heat deposited by the plasma onto the divertor surfaces, as well as coping with the neutronic heating, the divertor must fulfil the following functions:

- to ensure the presence of gas streaming channels towards the pumping ports for exhausting ashes, as well as limit the eroded impurities entering the main plasma, with the aim of controlling plasma composition [11];
- to shield the VV, the TF coils and the PF6 superconducting magnets against nuclear loads, so as to reduce thermal loads and neutron damage on these components that are not expected to be replaced during the plant lifetime;
- to provide plasma-facing surfaces physically compatible with the plasma, in terms of sputtering and tritium retention.

Additionally, in an FPP devoted to delivering electricity to the grid, and therefore for DEMO, the divertor must be compliant with fundamental engineering constraints and design drivers [12], so it has to minimize nuclear waste from replaced components, minimize the manufacturing costs and maximize the recycling potential, and reduce the maintenance downtime.

1.3 DEMO divertor general design description

The architecture of the EU DEMO divertor, according to the current design, is the following: it is a modular structure subdivided into 16 toroidal sectors, each one hosting a set of 3 divertor cassettes, namely one central and two side cassettes (differentiated only in the position and routing of the coolant pipes), for a total of 48 components distributed symmetrically along the toroidal direction, whose angular range is equal to 7.5°, toroidally spaced with a gap of 20 mm [6]. Figure 1.2 shows three different views of the entire EU DEMO divertor, indicating with the dashed lines the boundaries of the different sectors.

The division into sectors is imposed by the presence of 16 TF coils, the space between which houses the lower ports. Through these ports, the divertor coolant feeding pipes and the outlet pipes are routed and connected to the PHTSs of the plant, the divertor cassettes are replaced by employing a robot arm manipulator, and/or pumping path to the main plasma chamber is provided. A sketch of a lower port devoted exclusively to pumping is depicted in figure 1.3.

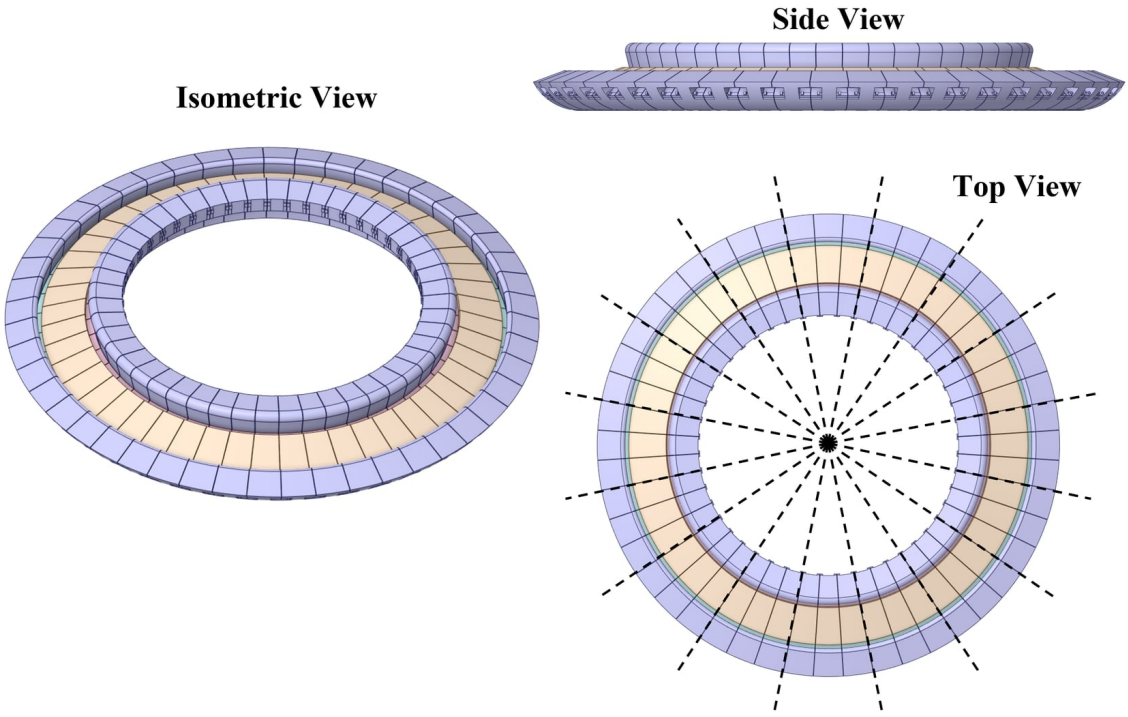

Figure 1.2: Entire EU DEMO divertor assembly.

The characteristics of the single divertor cassette, together with the details of their cooling circuit, have been studied and optimized within the EUROfusion project, and a final design has not been established yet. In this dissertation, reference will be made to two cassette designs, namely the 2019 and 2021 configurations, thoroughly described in the following sections.

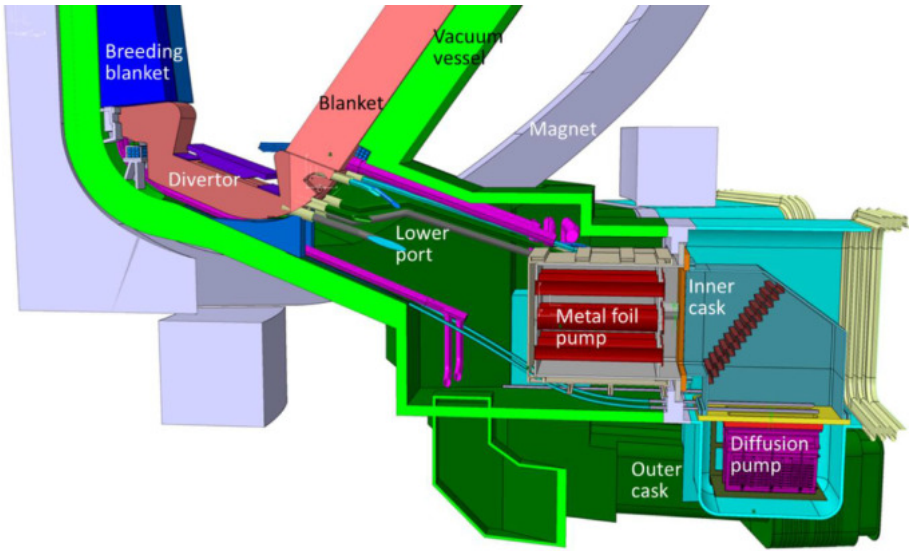

Figure 1.3: Lower port region and the rear casks of the EU DEMO design [13].

1.4 EU DEMO divertor 2019

The DEMO divertor cassette, according to its 2019 design [14], is composed of a CB equipped with a SL and two Reflector Plates (RPs), and supporting two PFCs, namely Inner Vertical Target (IVT) and Outer Vertical Target (OVT). This cassette configuration, with an indication of the position of the supported components, is depicted in figure 1.4, while a detailed description of all the divertor main components is given in the following subsections.

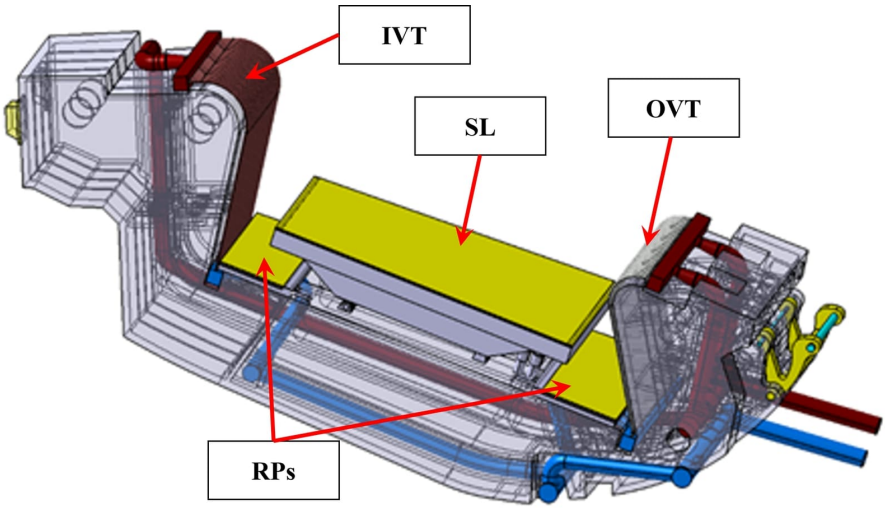

Figure 1.4: EU DEMO divertor cassette (2019 design).

1.4.1 Cassette Body

The CB is a Eurofer97 (a Reduced-Activation Ferritic/Martensitic (RAFM) steel) welded box-like structure made of a 30 mm external shells and internal ribs of 20

mm, acting as stiffeners to provide adequate structural robustness while serving as partition walls with holes for guiding coolant streaming [6]. A square-shaped pumping duct penetrates the central region of the CB, referred to as the *vacuum pumping hole*, required to provide a gas channel towards the pumping lower ports.

The CB is designed to achieve the following main functions [15]:

- to support the major sub-components, allowing for the removal of the CB itself and all the sub-components through the lower port;
- to ensure the correct positioning and alignment of the Vertical Targets (VTs);
- to provide structural stability under ElectroMagnetic (EM) impact loads and primary/secondary loads by means of suitable cassette-to-VV fixation systems;
- to exhaust volumetric thermal power by means of an appropriate cooling water system;
- to shield the VV from direct exposure to neutron radiation;
- to guide the gas flow to enhance pumping efficiency.

The EU DEMO divertor CB (2019 design) is depicted in figure 1.5, together with its cross-section, clearly showing the internal ribs and the connection holes required to route the coolant.

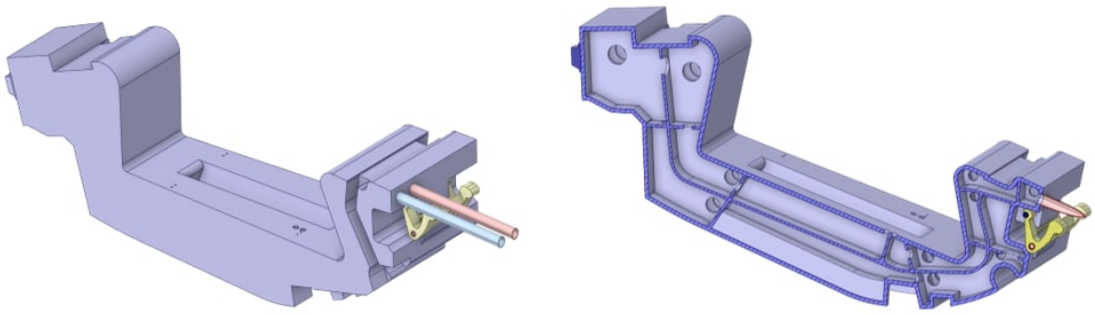

(a) (b)

Figure 1.5: EU DEMO divertor CB (a) with the details of its internal structure (b), 2019 design.

The CB-to-VV fixation system acts as an interface between the divertor system and VV. It is required to withstand all the loads resulting from EM events (i.e. disruptions or discharge of the magnet system) and to ensure electrical connection between the divertor and the VV.

On the inboard side, two *noses*, placed symmetrically with respect to the poloidal-radial cassette midplane, have been selected for the fixation system, designed to reduce the gap with the blanket during final installation movements and to be engaged in the VV to react radial moments. The noses will be in radial contact with the VV in their installed configuration, thus precisely controlling the position of the targets, being locked to a socket pair mounted on the inboard wall of

the VV. Once engaged, the locking gives rise to full constraints against toroidal and poloidal displacement, maintaining the required gap between the blanket edge and the CB. The details of the inboard cassette fixation support are shown in figure 1.6.

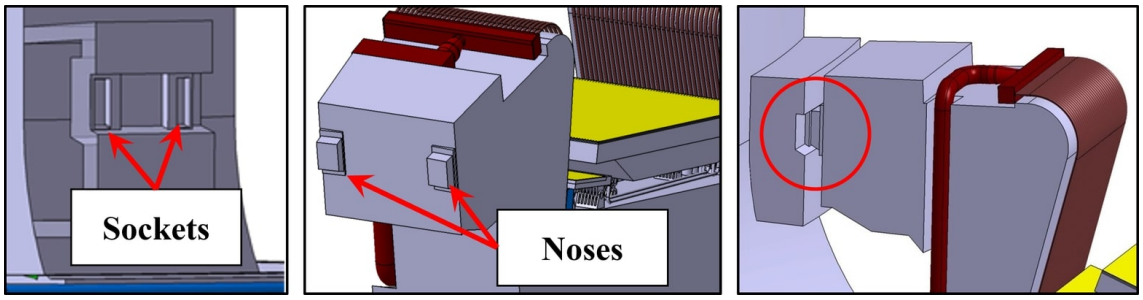

Figure 1.6: Details of the inboard cassette fixation support.

The outboard fixation system relies on the adoption of a special component, referred to as *wishbone*, which is depicted in figure 1.7 in its locked position. In addition to fixing function, the wishbone is designed to provide the flexibility required to accommodate differential thermal expansion of the VV and CB during both plasma and eventually baking operating conditions [6], allowing radial expansion and transferring vertical and toroidal loads at the same time, while ensuring electrical continuity and maintaining its properties under irradiation. The material selected for the wishbone is the Ti-6Al-4V alloy and, since the divertor cassettes will be replaced through Remote Handling (RH) systems, it must be compatible with the RH manipulators and tools.

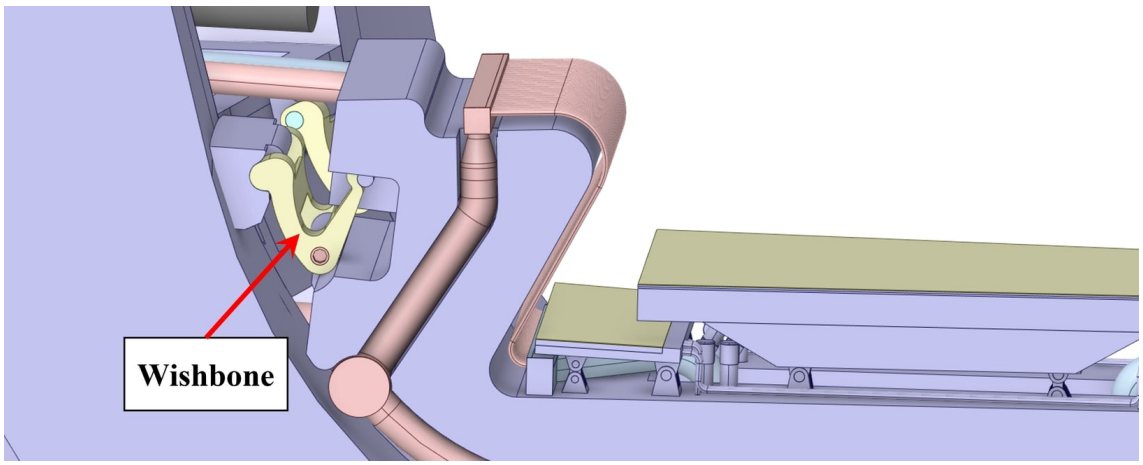

Figure 1.7: Details of the onboard cassette fixation support in the locked position (wishbone).

1.4.2 Vertical Targets

The VTs are deemed to be the most important and technologically critical component of the entire divertor, since they must withstand the outstanding peak

heat fluxes at the strike point, and are provided with a dedicated cooling circuit, that will be thoroughly detailed in section 1.5.1.

The VTs are composed of ITER-like PFUs [16], designed with monoblocks made of tungsten cooled by pressurized water flowing through CuCrZr pipes running through the centre bore of the blocks. The PFUs are grouped in toroidally-arranged PFU assemblies, 31 and 43 respectively for IVT and OVT. A sketch of the two VTs with the detail of a single PFU assembly is visible in figure 1.8.

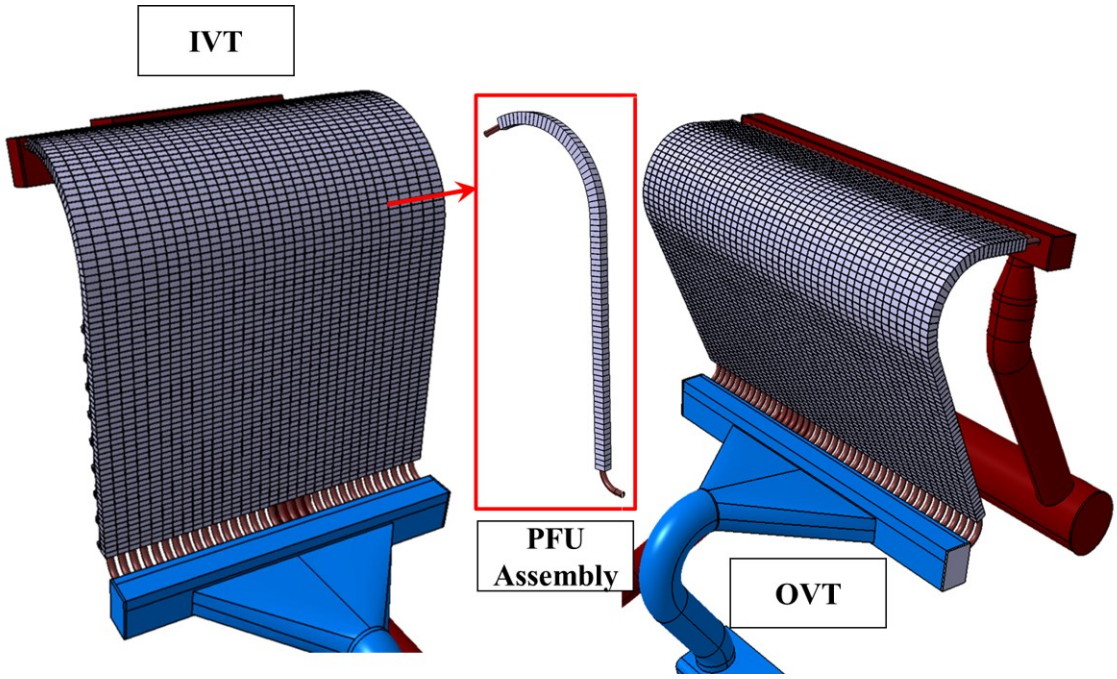

Figure 1.8: Details of the VTs and of a single PFU assembly [6].

Each cooling channel is equipped with a thin copper ST turbulence promoter, whose width is 0.8 mm, to enhance heat transfer performance, which extends along the entire straight part of the channel, for a length of approximately 575 mm for the IVT and 493 mm for the OVT. Moreover, the PFUs cooling channels are joined to the tungsten blocks with a thin (1 mm) copper interlayer to accommodate their differential thermal expansions. Each individual monoblock is a parallelepiped structure with a width of 23 mm, height of 28 mm and depth of 12 mm. Its geometrical features are depicted in figure 1.9a, while the details of part of one PFU with its connection to the CB are depicted in the figure 1.9b.

The design of the monoblock is the same as the one adopted in ITER, except for the section width, reduced from 28 to 23 mm, in order to improve the structural integrity to crack propagation [17]. Moreover, the front side armour thickness of 8 mm was chosen to maximize the erosion lifetime, paying the price of higher tungsten temperatures.

The gap clearance between tungsten monoblocks are 0.5 mm in both toroidal and poloidal direction, and it is kept constant over the entire target, including the

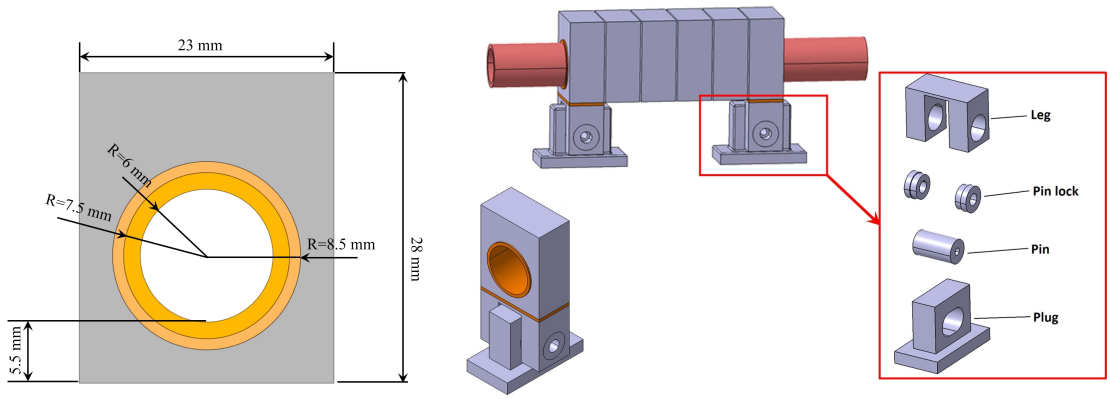

(a) (b)

Figure 1.9: Geometrical details of the DEMO PFU monoblock, (a), and details of a region of the PFU assembly and its supports, (b).

curved baffle region, where the axial section of the monoblocks is tapered so as to maintain a constant gap clearance along the curvature.

The PFU supports, inherited from ITER design, consist of four Eurofer97 components, providing their connection to the CB: support plug, support leg, fixing pin, and pin lock, whose details are depicted in figure 1.9b. In the bottom zone of the support plug, there is a rectangular base that is inserted and welded in a dedicated hollow inside the CB surface. The plug hosts an obround hole enabling the sliding of the inserted fixing pin to provide the anchoring element between the support plug and the support leg, which is brazed directly to the tungsten monoblock, allowing for axial thermal expansion of the cooling pipe to reduce pipe stress.

Additionally, to ensure electric insulation of the target from the CB, the contact surfaces of all constituents within the attachment unit shall be coated with a thin ceramic film [18].

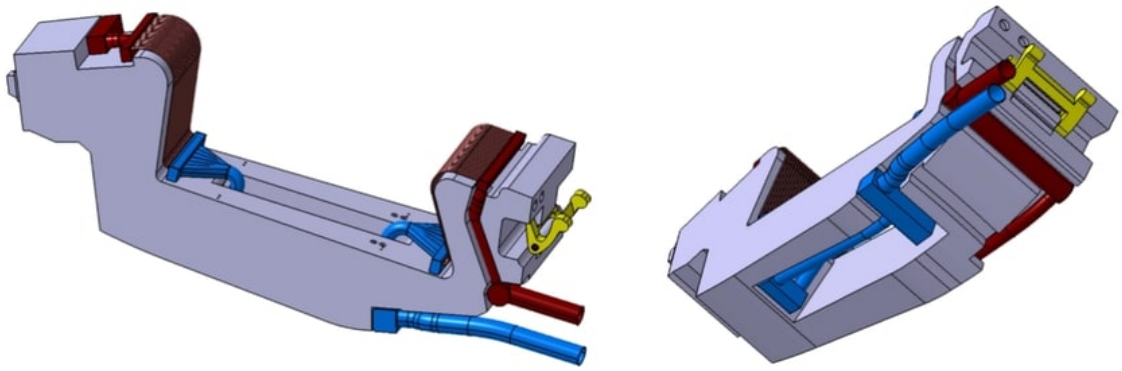

Figure 1.10: Integration of PFCs cooling circuit on CB.

As anticipated, the PFUs are supplied with cooling water from a dedicated cooling circuit. This routes the water through a system of pipes and manifolds that

wrap around the CB, feeding, through the vacuum pumping hole, two distributors internally equipped with specially shaped baffles to improve the uniformity of water distribution in the various PFUs cooling channels. The integration between the cooling circuit of the VTs, which is usually reported as the cooling circuit of the PFCs, and the CB is shown in figure figure 1.10, while the detail of the distributor of the IVT is shown in figure 1.11. The pipes and distributors/manifolds composing the PFC cooling circuit will be made of AISI 316 [19].

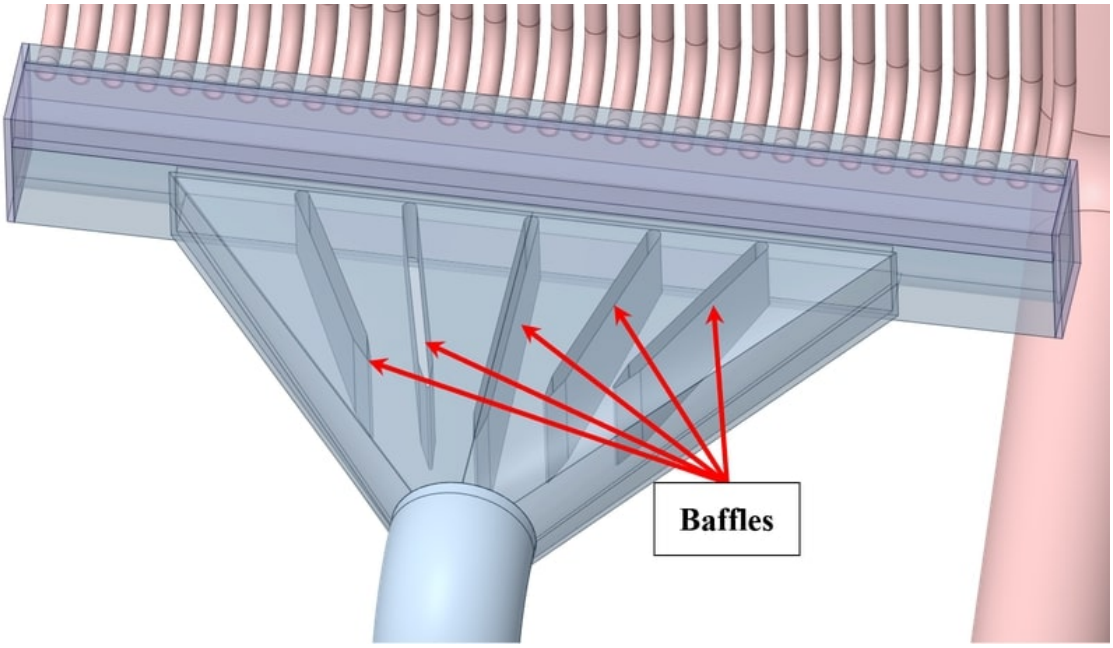

Figure 1.11: Details of the IVT distributor showing the internal baffles.

1.4.3 Shielding Liner

A protection system for shielding from thermal and particle loads the CB, the TF coils, PF6, and VV, this latter related to particle and radiation transport through the vacuum pumping hole, has been introduced in the divertor design in 2018 [20]. This system, namely the SL, consists of a linear plate mounted above the vacuum pumping hole, covering almost the entire CB length and width, as depicted in figure 1.12.

The SL is composed of three Eurofer97 layers. From bottom to top, the first layer is a 210 mm thick plate crossed by semi-circle-shaped slots for coolant flow. Both second and third layers are 5 mm thick plates joined together to form an array of 8 mm circular cooling channels to remove the significant plasma surface heat load. The front face of the steel heat sink plate is armoured with a tungsten coating (2 mm) to ensure physical compatibility with the plasma and to protect the steel structure from neutron flux, radiation and gas particles.

To allow for differential thermal expansions along the radial direction and,

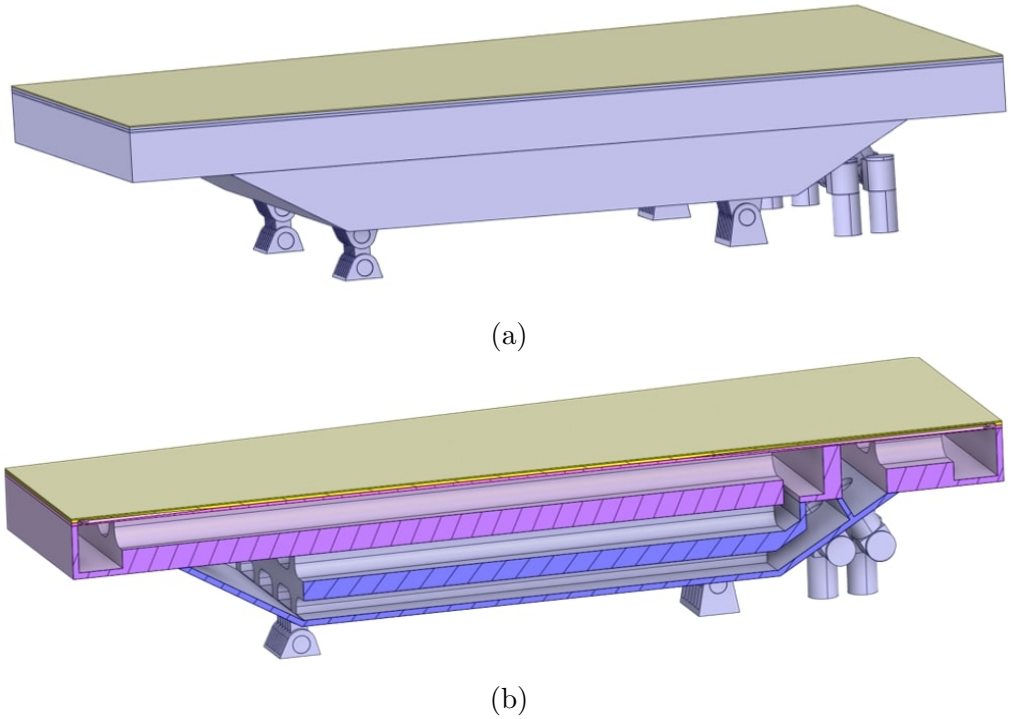

(a)

(b)

Figure 1.12: Divertor SL and its supports, (a), and details of its cross section, (b).

consequently, to avoid high secondary stresses, the SL is connected to the CB through a system consisting of four multilink/link supports welded to the CB. These supports consist of two single hinges on the outboard side and two double hinges on the inboard side, and their shape and size were optimized to avoid the occurrence of thermal hot spots caused by nuclear heating.

The dimensioning of the SL was made considering the capability to handle particle and radiation heat loads at which the component is exposed, the necessity to provide adequate shielding capacity to the underlying components, to be structurally resilient against impact loads and thermal stresses, as well as to guarantee a sufficient gas conductance for the plasma exhausts.

1.4.4 Reflector Plates

RPs, depicted in figure 1.13, are additional shielding components, introduced in 2019 [14] aiming to protect the VTs cooling distributors depicted in figure 1.11 from neutron irradiation. They are Eurofer97 components that have the same internal configuration as the SL, are provided with a 2 mm tungsten armour, and are connected to the CB with a system of two single hinges on the side closer to the SL and two double hinges on the side closer to the targets.

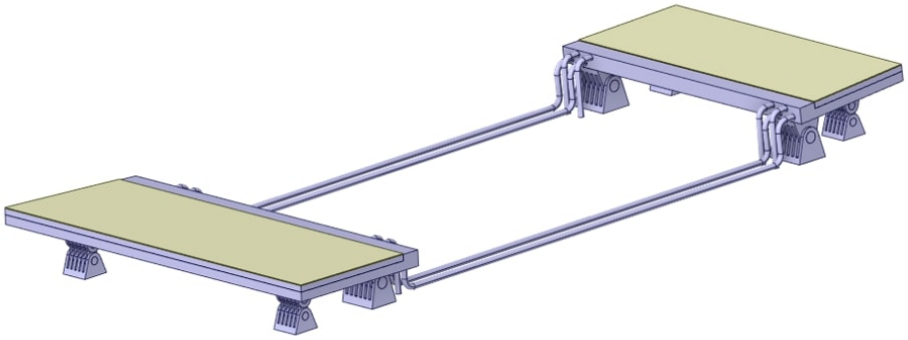

Figure 1.13: Details of the divertor RPs and their supports.

1.5 The EU DEMO divertor 2019 cooling circuits

Two separate and independent cooling circuits, one for the PFCs and the other for CB, SL and RPs (this latter is referred to in the following simply as CB cooling circuit) are foreseen for the 2019 EU DEMO divertor design, and both the cooling circuits are actively cooled by adopting sub-cooled pressurized water. In the following sections 1.5.1 and 1.5.2, the details of each cooling circuit layout and the operative conditions selected within the EUROfusion project will be discussed in detail.

1.5.1 The PFC cooling circuit

As far as the PFCs cooling circuit is concerned, IVT and OVT are connected in parallel by three-way branching to the inlet and outlet manifolds supplying water to their PFU assemblies.

The PFCs cooling circuit is designed to withstand the exceptional heat fluxes expected from the plasma, assuming a nominal peaked heat flux values at the strike point in the order of 20 MW/m^2 during normal and off-normal operation transient conditions. The component thus requires high mass flow rates of low-temperature water, resulting in average velocities inside the PFU cooling channels in the range of 12 to 15 m/s [21], so to guarantee a sufficient margin against the CHF occurrence to avoid dry-out phenomena that could jeopardize the structural integrity of the component itself.

The PFCs cooling circuit is depicted in figure 1.14, with a detail of the STs, while its schematic flowchart is shown in figure 1.15, with the indications of coolant temperatures, pressures, and mass flow rates, according to the results reported in [21]. The design of the DEMO divertor PFCs cooling circuit was the result of a long thermal-hydraulic research campaign, which began in 2015 and was performed mainly by adopting a numerical approach based on the Finite Volume Method (FVM) [22, 23, 24, 25].

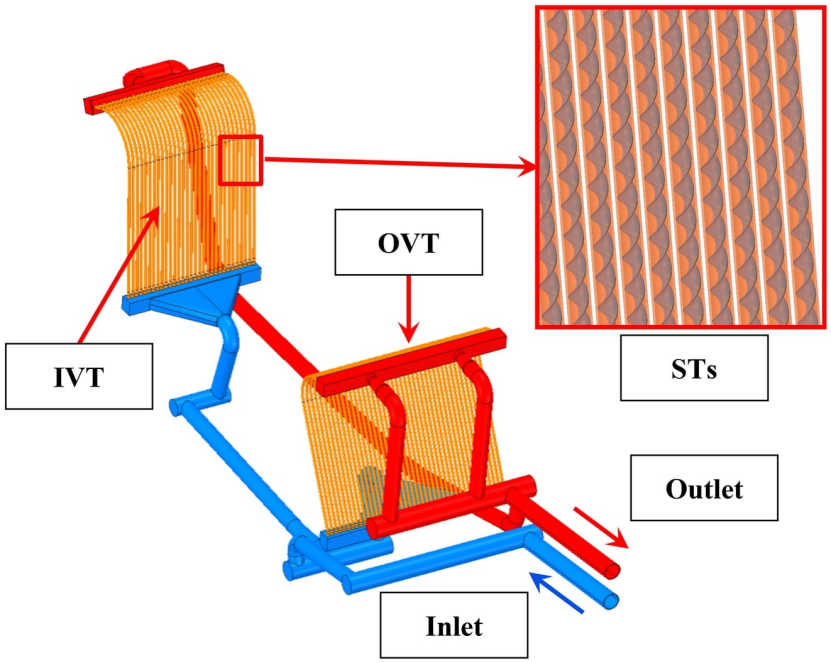

Figure 1.14: DEMO divertor PFCs cooling circuit (2019 design) [21].

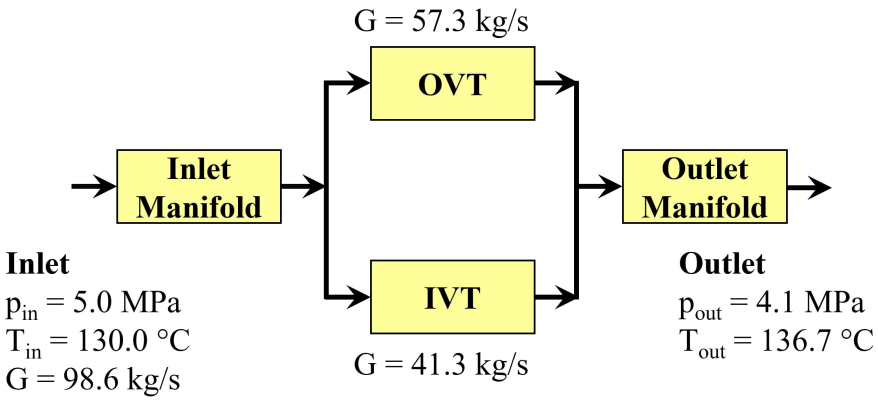

Figure 1.15: DEMO divertor PFCs cooling circuit flowchart (2019 design).

1.5.2 The CB cooling circuit

Regarding the CB cooling circuit, its layout is shown in figure 1.16, while its flowchart is visible, with coolant temperature, pressure and flow rate indications, in figure 1.17, according to the results reported in [26].

As can be argued from figure 1.17, the CB cooling circuit is supplied with water at a higher temperature than the PFCs cooling circuit, while both mass flow rate and inlet pressure are lower. These conditions are suggested by both the significantly lower surface power density to which the sub-components of the CB [26, 27] are exposed and the choice to adopt Eurofer97 as structural material, requiring higher operating temperatures to comply with resilience requirements for the expected lifetime.

The individual components supported by the CB are themselves cooled by a

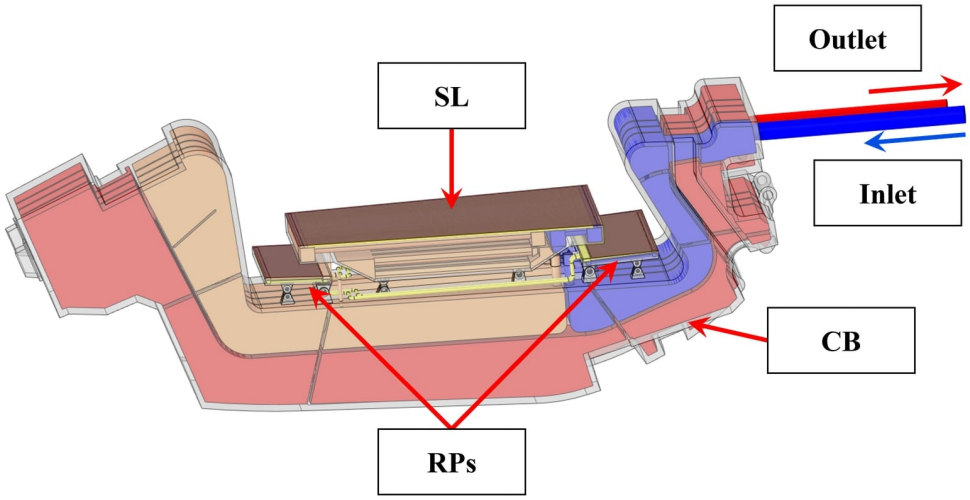

Figure 1.16: DEMO divertor CB cooling circuit (2019 design).

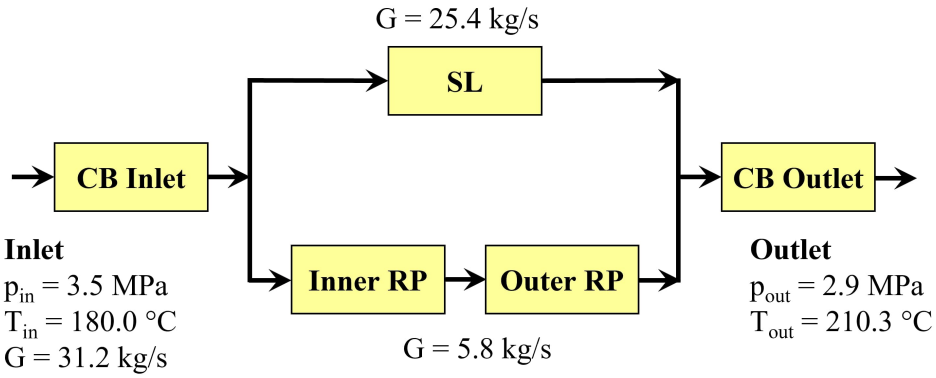

Figure 1.17: DEMO divertor CB cooling circuit flowchart (2019 design).

rather complex system of cooling channel arrays arranged in series and parallel to each other. In particular, the SL cooling circuit consists of four layers of cooling channels connected in series to each other. The cooling water coming from the CB is routed, at first, to the SL First Wall (FW) channel layer, composed of a parallel arrangement of 52 small circular cooling channels with a diameter of 12 mm, then to the other three layers, cooled by quasi-rectangular large cooling channels, 8 for each layer, and in the end, it is collected back to the CB. Concerning the RPs cooling circuit instead, it is composed of two layers of cooling channels connected in series. Inboard and outboard RPs FW channels are composed of a parallel arrangement of 62 and 49 circular cooling channels with a diameter of 12 mm, respectively. The other layer is cooled by semi-circular large cooling channels both in the case of inboard and outboard RPs. The two RPs are hydraulically connected in series by a set of four connection pipes, as visible in figure 1.13.

As for the PFC cooling circuit, the design of the CB cooling circuit was supported by a thermal-hydraulic research campaign, reported in [28, 29, 30, 31].

1.6 EU DEMO divertor 2021

During the entire PCD phase, which ended in 2020 [32], attention was focussed on the study of a double-circuit divertor concept, in which two independent cooling circuits served by two different PHTSs were used to cool the PFCs and the CB. The 2019 configuration, discussed in section 1.4, represents the final design of this divertor concept achieved at the end of the PCD phase.

The possibility to adopt a single cooling circuit to serve both PFCs and CB, suggested during the divertor final design review meeting of the PCD phase, led to the definition of a new divertor concept, namely the single-circuit cooling option, first developed in 2020 [33] and then improved in 2021 [34]. This solution was proposed with the aim to both ease the remote maintenance, as only one inlet and one outlet pipe should be cut and reweld for each divertor cassette during replacement operations, and to allow for a simpler balance of plant design and integration [35], as it would require a single PHTS. Compared to the previous design, the following main changes were introduced together with the integration of the two cooling circuits:

- an ITER-like fixation system between the PFCs and the CB was introduced to ease maintenance operation;
- an additional neutron shielding system inside the CB vacuum pumping hole was designed to improve the VV protection from neutron damage;
- a revised version of the wishbone was introduced in the divertor design.

The EU DEMO divertor 2021 configuration is depicted in figure 1.18, while a detailed description of all its main components is given in the following subsections.

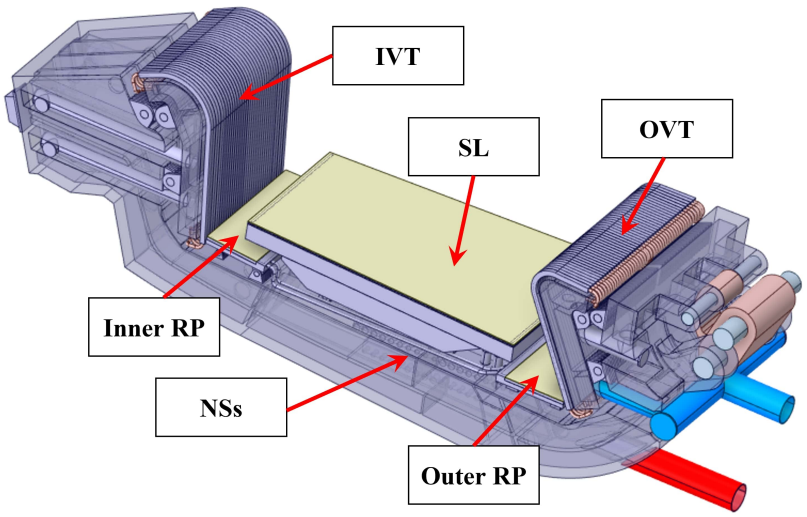

Figure 1.18: DEMO divertor cassette (2021 design).

1.6.1 Cassette body

As can be argued figure 1.19, the design of the 2021 divertor cassette is conceptually identical to that of the 2019 configuration. In fact, it is a Eurofer97 box-like structure consisting of external plates with a thickness of 40 mm and internal ribs of 20 mm, supporting all the other divertor sub-components. Its shape was modified with respect to 2019 configuration to accommodate the presence of the new ITER-like fixation system between the VTs and the CB and to comply with revised in-vessel space reservation constraints.

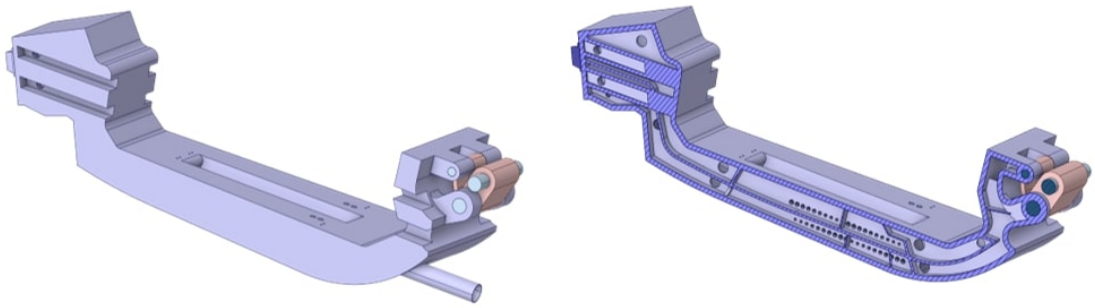

(a) (b)

Figure 1.19: EU DEMO divertor CB (a) with the details of its internal structure (b), 2021 design.

Concerning the fixation system, the same socket-nose solution already foreseen for the 2019 cassette has been selected, while on the outboard side, the wishbone design was revised to improve its mechanical performance, ensuring the component integrity under EM loads [36]. The revised wishbone design is depicted in figure 1.20, also showing the novel bridge-like removable system connected to the VV to which the central cassette is locked.

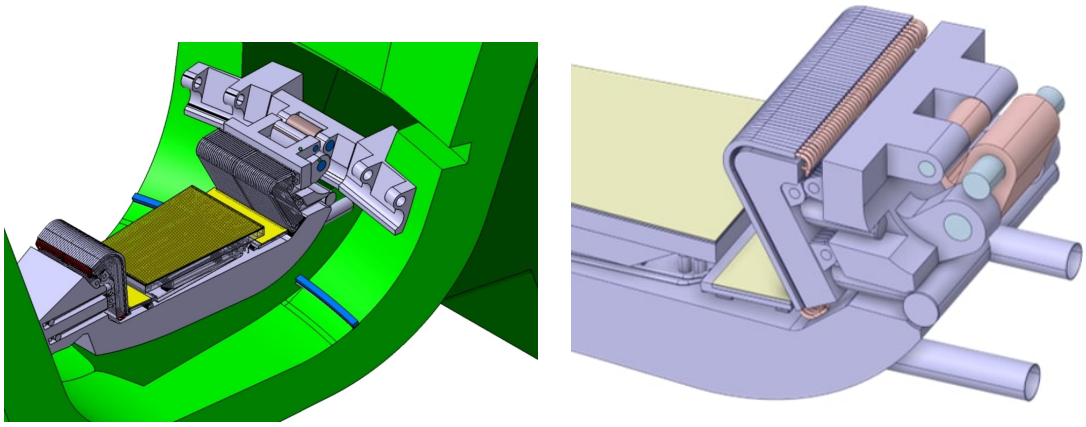

(a) (b)

Figure 1.20: Cassette in locked position (a) and details of the revised wishbone design (b).

1.6.2 Vertical Targets

One of the major novelties introduced in the 2020 design is the adoption of an ITER-like fixation system between the VTs and the CB. In particular, the VTs were provided with their own bodies, namely Target Bodys (TBs), with a structure similar to that used for the CB, connected to this latter with a multi-link fixation system consisting of hinges and double hinges, similarly to the solution employed for SL and RPs. The material selected for the TBs will probably be Eurofer97, although other options are currently being considered.

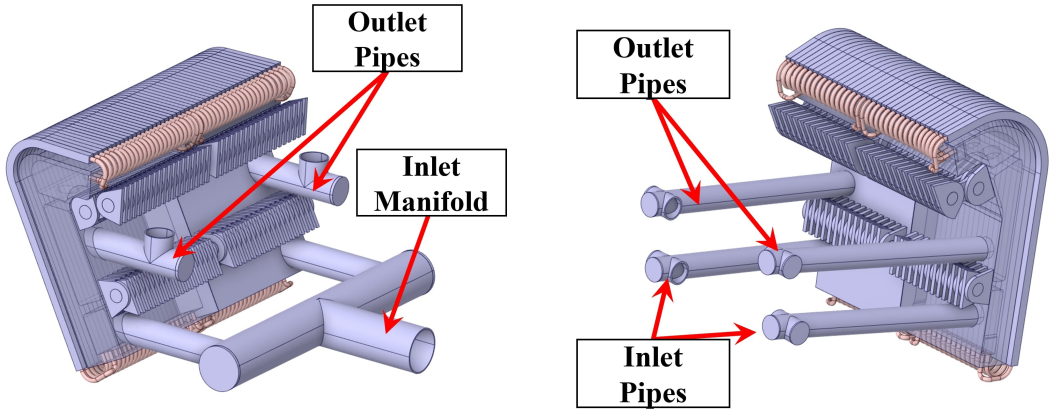

(a) (b)

Figure 1.21: OVT (a) and IVT (b) assemblies with supports, TB, and feeding pipes.

Each TB moreover comprises two toroidal-symmetrical units requiring two separate inlet and outlet pipes for each part of the target, located on the cassette side in such a way to ease the pipe cutting and rewelding.

Figure 1.21a shows the OVT assembly with its supports, TB, and cooling pipes. Since the cooling water is fed to the entire divertor cassette by routing it firstly through the OVT, it is provided with a single feeding pipe coming from the lower port, then requiring an inlet manifold to distribute the coolant to the two units. Similarly, the IVT assembly is depicted in figure 1.21b.

Each OVT TB unit hosts 23 PFU assemblies, for a total of 46 elements, while each IVT TB unit hosts 17 PFU assemblies, for a total of 34 elements, whose details are unchanged with respect to 2019 configuration. It is worth noting how the same system of connecting the PFU assemblies with the CB discussed in section 1.4.2 is now used to connect the PFUs to the TBs.

1.6.3 Shielding Liner

During 2020 and 2021, the design of the SL underwent very few changes compared to the 2019 layout. In particular, minor adjustments were made to the cooling circuit, in order to eliminate regions of coolant stagnation [37], and to the dimensions of the supports.

1.6.4 Reflector Plates

As for the SL, also the RPs were marginally changed during 2020 and 2021. More in detail, the RPs were brought closer to the CB, as the PFCs distributors were no longer present, resulting in a change in the size of the supports and, at the same time, improving the pumping performances through the gap between the SL and the RPs. Additionally, in 2021 some improvements were made to the cooling circuit [37] by increasing the volume of the internal manifolds in order to improve the distribution of coolant among the RPs FW channels, considered unacceptably uneven in the 2019 configuration [26].

The possibility of removing the RPs in the future divertor designs is currently being investigated within the EUROfusion project, once the elements that were in charge of shielding, i.e. the PFCs distributors, are no longer present.

1.6.5 Neutron Shields

The Neutron Shields (NSs) consist of two 60 mm thick Eurofer97 plates positioned inside the vacuum pumping hole and connected directly to the cooling circuit of the cassette, namely upper and lower NSs. They were introduced in the 2020 design to improve the VV protection from neutron damage and optimised in 2021 based on the results of preliminary fluid-dynamic analyses [37].

The NSs position is depicted in figure 1.22, showing the cooling channels inside the lower NS.

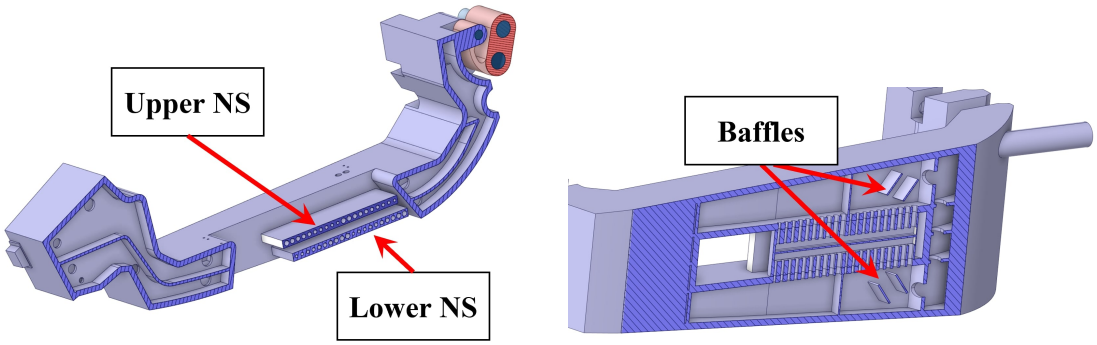

(a) (b)

Figure 1.22: DEMO divertor NSs (2021 configuration, a) with a detail of their internal cooling layout (b).

It should also be pointed out that the current NS design presents some manufacturability issues and, therefore, different geometric solutions are being considered and will be included in the future DEMO divertor design.

1.7 The EU DEMO divertor 2021 cooling circuits

The integration of the PFCs and CB cooling circuits, together with the inclusion of the NSs, leads to a significant increase in the complexity of the cooling circuit layout, which can be schematised as shown in figure 1.23 with reference to the region nomenclature depicted in figure 1.24, showing the coolant volume only. The 2021 divertor design foresees the adoption of pressurised water as a coolant, the operating conditions of which are still under discussion and will be detailed in part of this dissertation.

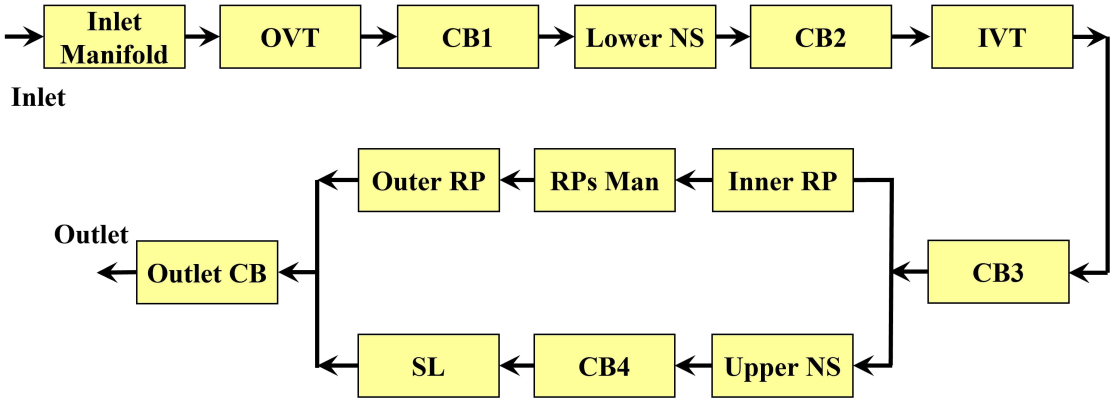

Figure 1.23: DEMO single-circuit cooling option divertor cassette cooling scheme.

Specifically, the coolant is routed to the divertor through an inlet pipe whose internal diameter is 142 mm, which is directly connected to the OVT distribution manifold, as shown in figure 1.21a. At the inlet manifold, the fluid splits and independently feeds the two TB units through two 87 mm pipes. The TBs have toroidal-radial internal ribs not provided with communicating holes, forcing the coolant to flow through the 46 PFU cooling channels of the OVT, from bottom to top. The straight part of these channels is equipped with STs, 637 mm in length, which improves the fluid cooling capabilities in the region around which the strike point is established. The coolant is then collected in the upper part of the TBs and is routed to the cassette through two pipes with an internal diameter of 87 mm.

The CB has ribs with no communication holes running along the entire toroidal-radial plane, defining two non-communicating environments, one upper and one lower. The water is channelled from the OVT into the lower part of the CB and flows in the radial direction until it encounters a poloidal-radial rib, which forces it to move from the first region of the box (CB1 in figure 1.24) to the lower NS.

The lower NS (the same applies to the upper one) cooling circuit comprises two independent cooling circuits, each one consisting of an array of 10 inlet and 10 outlet channels arranged in a toroidal direction, interconnected by a central radial manifold. A simplified description of the flow field inside the NS cooling channels is given in figure 1.25 both for lower and upper NSs.

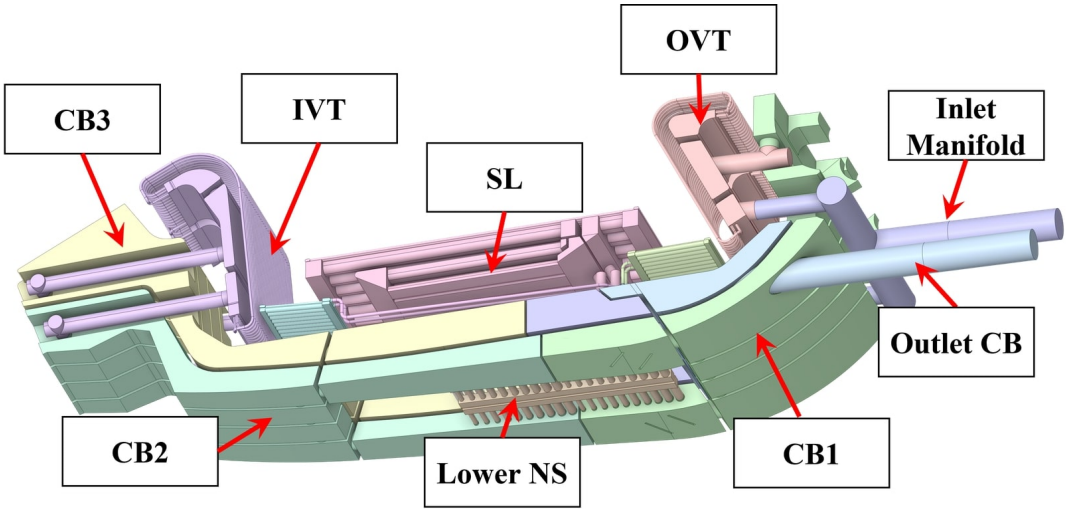

(a)

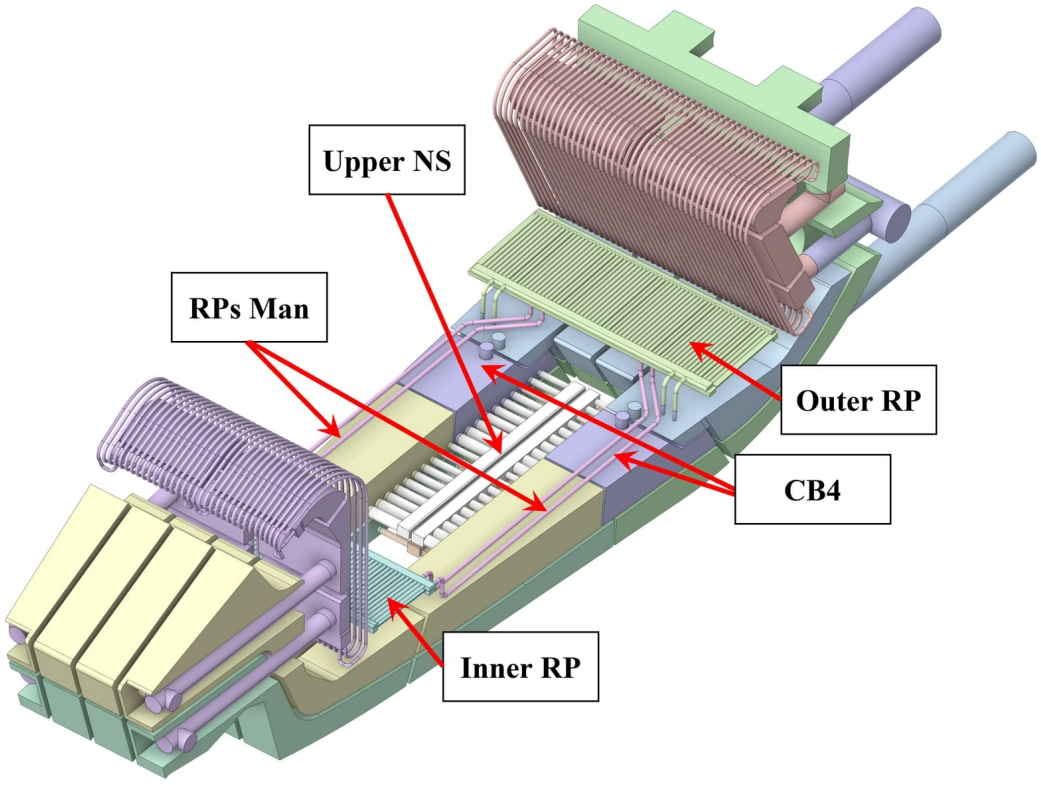

(b)

Figure 1.24: DEMO divertor cooling circuit main regions (2021 design), bottom (a) and top (b) views.

Additionally, as visible in figure 1.22, the diameter of these cooling channels is variable along the radial direction, as a result of a preliminary fluid-dynamic optimisation campaign reported in [37], which also guided the design of the baffles also visible in figure 1.22.

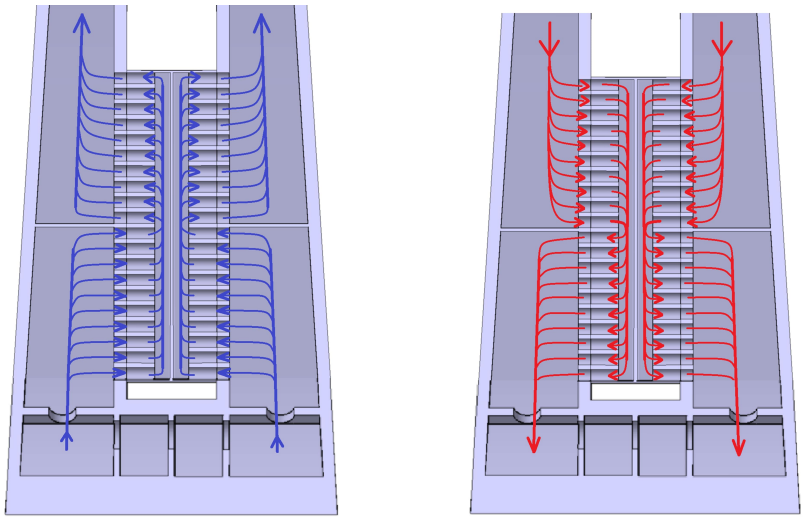

(a) (b)

Figure 1.25: Coolant routing inside the lower (a) and upper (b) NSs.

Once out of the lower NS, the cooling water continues flowing inside the lower part of the cassette (CB2 in figure 1.24), until it reaches the inboard side. Here it is conveyed to the IVT, through two pipes with an internal diameter of 70 mm, visible in figure 1.21b, following a similar fluid path as for the OVT. In particular, the coolant is routed to the lower part of the TBs, then to the 34 PFU cooling channels encompassed with 660 mm long STs and finally to the upper part of the TBs, where it is collected and routed to the upper segmentation of the CB via other two pipes with the same size of the inlet ones.

From the upper part of the cassette (CB3), the coolant flows back to the outboard of the divertor. Here, there is a branching of the coolant: part of it is routed to the RPs system, while the other to the SL and the upper NS.

Regarding the first branch in parallel, i.e. the one of the RPs, the coolant is spilt from the CB from four small pipes (internal diameter of 15 mm) placed in the upper part of the cassette and is routed to the inner RP. Inside this component, the fluid is firstly collected inside one toroidal manifold, then it moves back to the inboard side through a parallel array of 23 semi-circular Rear Channels (RCs) with a diameter of 30 mm, collected back into another toroidal manifold and then routed to 49 12 mm FW channels towards the outboard. The coolant is collected in a final toroidal manifold and from there sent to the outer RP, through four 15 mm inner diameter tubes (referred to as *RPs manifolds*) running along the flat part of the cassette in the space between the CB and the SL, for a length of about 1.6 m each. Within the outer RP, water routing is similar to that of the inner RP, the only difference

being the number of RCs, equal to 29, and FW channels, equal to 61. Finally, the coolant is again fed into the cassette through four pipes with an internal diameter of 15 mm.

Concerning the second branch, the one comprising the SL, the coolant is routed at first inside the upper NS following the path depicted in figure 1.25, and then it is collected back to some small CB volumes, the ones referred to as CB4 in figure 1.24. From here, water is routed to the SL, at first to the three levels of RCs, eight for each level, and then is fed to 53 toroidally-parallel FWs channels. The connection between the different levels of RCs and the FW channels is ensured by the presence of toroidal manifolds, collecting and distributing the water inside the SL. Additionally, it should be noticed how, with respect to the 2019 design, the water is fed in the opposite direction inside the SL.

Finally, the coolant is collected back to the CB from the two branches and leaves the divertor through a 70 mm inner diameter pipe directly connected to the CB (Outlet CB in figure 1.24).

The routing of the fluid within the entire divertor cassette is sketched in figure 1.26.

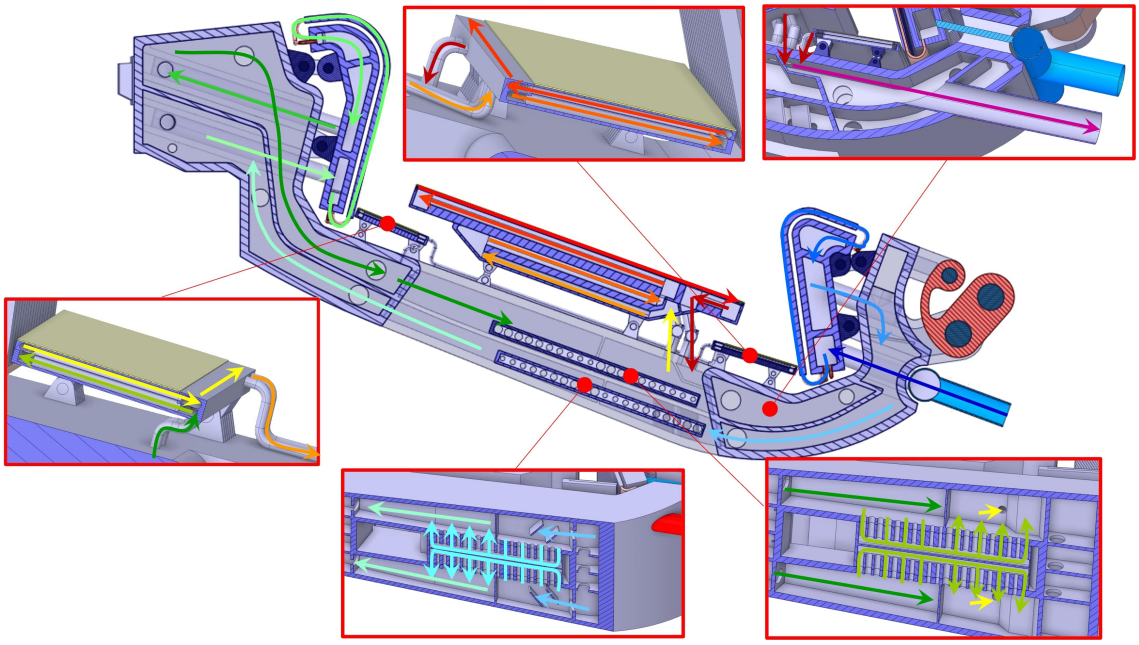

Figure 1.26: Coolant routing inside the entire divertor cassette.

As can be seen, the geometric complexity of the single-circuit cooling option divertor cassette is remarkable, given the lack of symmetries (the outlet pipe is not positioned on the centre plane of the component but is displaced to the side) and due to its multiscale nature, characterized by an overall length of more than 4 m, and featuring around 400 channels with diameters of the order of ≈1 cm.

1.8 Thermal and thermal-hydraulic constraints

As already discussed, the correct DEMO divertor cooling circuit design should prevent the structural and functional materials from working outside their operative limits, avoid excessive pressure drops, ensure that the coolant temperature is as high as possible in order to maximise the thermodynamic cycle efficiency, and allow the component to fulfil its functions for the desired lifetime.

With regard to the first aspect, i.e. the necessity to operate structural materials inside their temperature limits, a complete discussion is beyond the scope of this dissertation. Nevertheless, the temperature distribution within the structures plays an essential role in determining both the thermo-structural performance of the divertor cassette and its lifetime. Therefore, some aspects will be mentioned here, as they are essential for the next chapters. Given that the link among temperature, thermo-structural performance and lifetime is not trivial and a complete picture can only be obtained from the detailed thermo-mechanical analysis of the component once the thermal field and the neutron-induced effects on materials have been determined (requiring a multiphysics approach), it is yet possible to draw conclusions from knowledge of the thermal field alone, allowing a first screening of unacceptable cooling circuit configurations or unsuitable coolant operating conditions. In the following, all the constraints and relevant indications that can be directly derived from the knowledge of the temperature field alone are provided for the structural and functional materials foreseen for the EU DEMO divertor.

Eurofer97

As far as the Eurofer97 is concerned, the optimum operating temperature range is 300-550°C [6]. The upper limit is dictated by creep and creep-fatigue considerations, while the lower is related to the possibility to keep the structural material in a range of temperatures that allows for a sufficient ductile behaviour during both plant operation and maintenance [38], for the entire DEMO lifetime. However, the design of the DEMO divertor has been carried out during the PCD phase considering a minimum acceptable temperature of Eurofer97 equal to the coolant temperature, i.e. 180°C, according to the rationale described in [39]. Given the effects of neutron-induced damage and transmutation on materials, it is in fact possible to select an operating temperature that is just sufficient to guarantee a minimum divertor lifetime, lower than that of the entire plant. This approach is reasonable because the divertor lifetime can be dictated by other aspects, such as the erosion of the VTs due to interaction with the plasma, thus requiring its replacement in any case. In particular, the structural material behaviour can be assessed by determining the effects of temperature, irradiation and helium production on the Ductile-to-Brittle Transition Temperature (DBTT) and the Fracture Toughness

Transition Temperature (FTTT), as investigated at the DEMO PCD stage, and the relationship between the operating temperature and the component lifetime can be assessed as reported in the following.

1. Starting from the results of dedicated neutronic analyses of the divertor, such as those reported in [40, 41], it is possible to obtain an indication of the radiation damage due to neutron bombardment, expressed in Displacement per Atom (dpa) for Full Power Year (FPY) of operation of the machine, and helium production in Eurofer97 per FPY. A maximum radiation damage of ≈5 dpa/FPY is in particular reached in the upper part of the SL, while lower values are obtained in the CB. The helium production can be estimated at roughly 110 appm/FPY for the SL.
2. Supposing a component lifetime τ expressed in FPY, it is possible to calculate the total radiation damage and the total amount of helium accumulated at the end of the component life, simply by multiplying τ by the values reported in the previous point.
3. The shifts in DBTT and in FTTT due to neutron damage and He production can be then evaluated from figure 1.27, based on the data reported in [42], adopting the neutron damage and helium production values of the previous point.

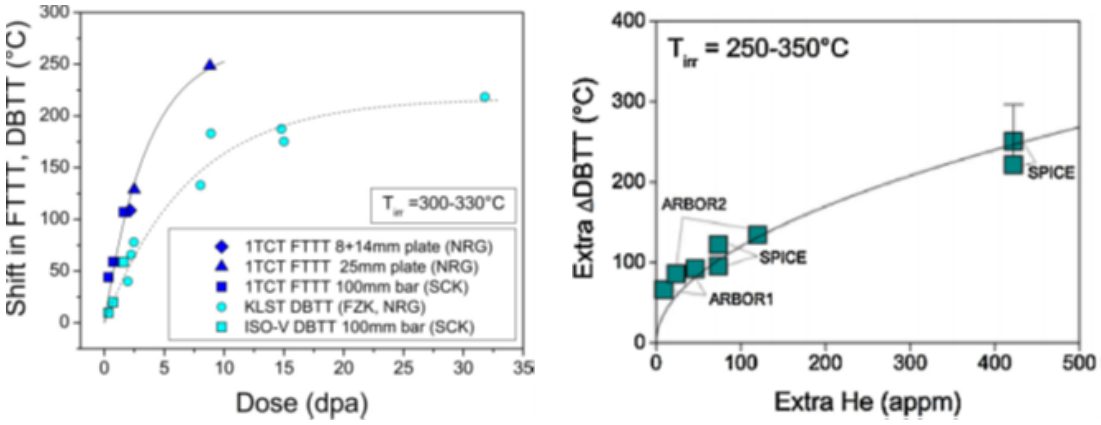

(a) (b)

Figure 1.27: Irradiation induced shift in FTTT and DBTT for Eurofer, (a) and He-induced extra embrittlement for irradiated boron doped steels, (b), from [42]

4. Starting from DBTT and the FTTT of Eurofer in the unirradiated condition, being respectively equal to -80 and -108°C [39, 42], it is possible to obtain the DBTT and the FTTT after τ FPY of operation from equation (1.2) and equation (1.3).

$$FTTT = -108°C + \Delta FTTT_n(\tau) + \Delta FTTT_{He}(\tau) \tag{1.2}$$

$$DBTT = -80°C + \Delta DBTT_n(\tau) + \Delta DBTT_{He}(\tau) \tag{1.3}$$

5. Since the material temperature should remain above the DBTT and FTTT during operation and maintenance, it is reasonable to suppose that, by keeping always the coolant at a minimum temperature of at least 5°C higher than these two temperature thresholds, this condition is met at least for the operation phase.

By following these steps, it is possible to construct by points the curve of divertor lifetime τ expressed in FPY against the coolant operating temperature, as depicted in figure 1.28.

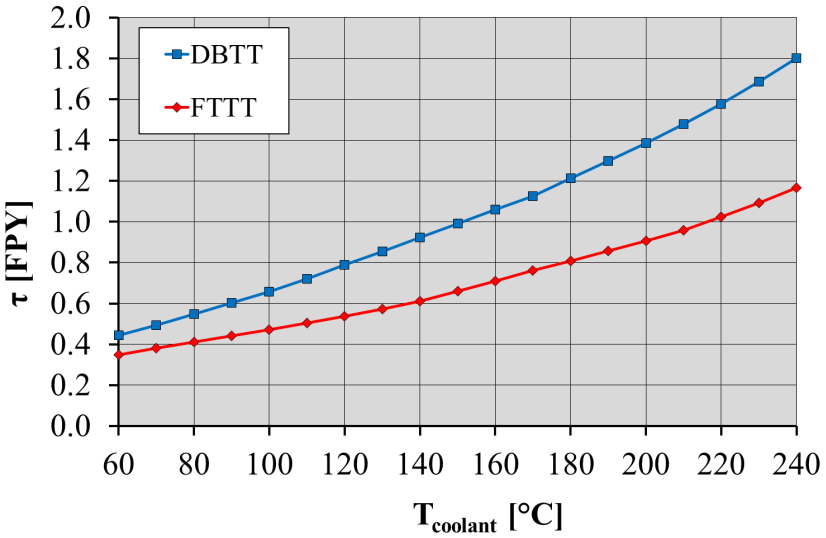

Figure 1.28: Divertor lifetime as a function of coolant temperature considering DBTT and FTTT.

It can be noted from the figure that every increase in the divertor coolant temperature would lead to an increase in the lifetime of the component and, vice versa, every reduction in coolant temperature would lead to a reduction of the component lifetime.

To avoid unduly conservative results, differently from what is reported in [39], DBTT can be adopted to assess the component lifetime, as agreed with the material experts in EUROfusion Work Package Divertor (WP-DIV) and consistently with the results reported in [6]. In fact, for the case of coolant inlet temperature of 180°C, as for the case of the CB cooling circuit, it is possible to estimate a cassette life of ≈0.8 FPY considering the FTTT as the limiting parameter, while a τ value of ≈1.2 FPY is obtained considering the DBTT.

It should be furthermore pointed out that the selection of the low operating temperature for the CB cooling circuit was done based on not well-grounded data, since the shifts in FTTT and DBTT versus dose and He production were evaluated

on experimental tests carried out at an irradiation temperature of 300-330°C, according to the data presented in [42], and thus they are not fully applicable at temperatures lower than 300°C. Nevertheless, in the absence of more relevant experimental data, the only possible estimates of the lifetime of the components made of Eurofer can be made by adopting this procedure.

Tungsten

Regarding tungsten, no indication is given within the project in terms of the optimal temperature window. Nevertheless, two constraints can be derived just by evaluating the temperature. The first one is the melting temperature, equal to 3422°C, which clearly cannot be overcome to avoid loss of control over the shape and thickness of the plasma-facing components. A 200°C margin against melting can be moreover considered, as suggested by [43], to cope with the uncertainties related to plasma physics.

An additional temperature constraint that could be easily verified and considered is the tungsten recrystallization limit. It is the temperature at which the recrystallization and grain growth occur in the material, accompanied by a change in its mechanical properties, such as a decrease in hardness and strength, that strongly affects the tungsten thermal shock resistance and can favour the appearance of deep macrocracks. The exact value of this threshold temperature typically depends on the level of cold deformation applied during manufacturing and values in the range 1100–1500°C can be found in literature [44]. However, recent experiments [45] have shown that, even in the presence of tungsten recrystallisation, the structural integrity of the component is not compromised and, therefore, this constraint will not be extensively considered in this dissertation.

CuCrZr

For CuCrZr, the optimal temperature range is between 150 and 350°C, as reported in [6]. The lower temperature limit can be set between 150 and 250°C, but the exact value depends on the specific structural design criterion selected to verify the design. At lower temperature values, the CuCrZr experiences loss of ductility, while, overcoming the upper limit, strength loss due to thermal softening and irradiation creep is observed. As for the Eurofer, the current DEMO divertor design foresees the operation of CuCrZr outside these limits, due to the need to find a compromise between material properties and thermal-hydraulic constraints, as detailed in [6]. The definition of clear limits based on these considerations is therefore not straightforward by relying only on temperature distribution.

Different constraints that can be easily applied are instead presented in [43], derived specifically for the PFU cooling channels, and temperature limits are given

to obtain negligible creep. In particular, the thickness-averaged temperature of the pipes should not exceed 300°C at 10 MW/m^2 and 450°C at 20 MW/m^2.

Copper

As far as copper is concerned, it is possible to define an upper temperature limit of 1085°C due to melting. As for the tungsten, a temperature margin of 200°C can be considered to cope with uncertainties, as suggested in [43].

Ti-6Al-4V

No temperature ranges or limits are usually considered for this material.

AISI 316

No temperature ranges or limits are usually considered for this material.

Apart from the aspects closely related to material and component temperatures, additional constraints must be taken into account to obtain the desired cooling circuit thermal-hydraulic performance. During the PCD phase, the following list of design constraints was developed for the EU DEMO divertor [14]:

- coolant total pressure drop lower than 14 bar for both the CB and PFC cooling circuits, calculated only for the in-vessel components;
- Maximum water axial velocity in PFU cooling pipes lower than 16 m/s to limit potential corrosion, erosion and fretting issues;
- minimum margin against bulk saturation greater than 20°C for both the cooling circuits;
- a CHF margin greater than 1.4 for the PFC cooling channels, under the nominal heat flux of 20 MW/m^2.

Regarding the last cooling circuit constraint, it is worth mentioning that the CHF margin is defined as the ratio between the *incident* CHF, a definition of which can be found in [46], and the actual heat flux on the plasma-facing walls.

Although the design of the divertor cooling circuit must comply with all the constraints listed above, this only defines necessary and not sufficient conditions for the proper functioning of the entire divertor, which must be able to fulfil all the other requirements and functions already described in section 1.2.

1.9 Study objective and methodologies

Within the framework of the Work Package DIV 1 - "Divertor Cassette Design and Integration" of the EUROfusion action, a research campaign has been carried out at the University of Palermo since 2020 to theoretically assess the steady-state thermal-hydraulic performances of the DEMO divertor cooling system, focussing the attention on the single-circuit cooling concept. This thesis work is framed within this context and describes the methodologies developed and analyses performed to evaluate the thermal and thermal-hydraulic performance of this newly-introduced divertor concept, by identifying suitable coolant operating conditions, and aiming to assess the compliance with the constraints discussed in the previous section. In chapter 2, the steady-state thermal-hydraulic performance of this divertor cooling option is assessed by means of preliminary parametric analyses, adopting the dedicated coupled lumped-parameters-FEM code ADRANOS. The code has been developed in MATLAB [47] environment as part of the Ph.D. research activities, and is able to provide the steady-state coolant temperature, pressure and mass flow rate distribution among the main divertor sub-components, and allows for evaluating 2D thermal fields within selected structures, relying on its FEM module. It has been developed and tailored to perform quick and preliminary screening studies, to assess whether a given layout of the DEMO divertor cooling circuit is capable of working in compliance with several constraints and to select suitable coolant operating conditions. ADRANOS has been conceived with an object-oriented approach, in order to have a flexible tool that can automatically handle different cooling circuit layouts and is optimized for parallel computing, allowing for a significant reduction of the calculation time. Moreover, the tool relies on the MATLAB built-in FEM module [48], directly executed within the code to evaluate the steady-state temperature distribution in the VT monoblocks exposed to the highest thermal loads. To carry out these preliminary analyses, the following list of actions is required:

- cooling circuit volume discretization;
- volumes characterization and connection;
- operating condition range selection;
- constraint definition;
- results post-processing.

As far as the first step is concerned, the divertor cooling circuit is subdivided into different volumes, each one generally representing one of its major sub-components, even if more detailed 1D analyses can be performed. Each volume must then be characterized by providing its typology, the total deposited power and a characteristic function curve, drawn from 3D-CFD calculations. Additional data should be provided for special volumes, such as those representing the VTs. The

volumes are thus connected in series and parallel, and the cooling circuit connectivity is provided in a simple text file format. ADRANOS is then set by selecting the range of operating conditions and the constraints to be taken into account, and after the calculations are completed, the data can be post-processed with a dedicated post-processing script.

Chapters 3 and 4 rely instead on the adoption of the FVM to perform the detailed fluid-dynamic assessment of the divertor cooling circuit, adopting the well-known and qualified commercial 3D-CFD code Ansys CFX [49].

To investigate numerically the steady-state thermofluid-dynamic behaviour of the DEMO divertor cassette cooling circuit, fully-3D steady state CFD analyses were performed to assess the total pressure drop required for the coolant circulation, to assess the uniformity of flow distribution inside the parallelly-arranged cooling channels of the cassette sub-components and to determine the temperature field within the coolant and cassette structures. To this purpose, specific 3D finite volume models were set up, to realistically reproduce the divertor and its cooling circuit, whose development can be schematised in the following steps:

- geometry cleaning, defeaturing and preparation;
- flow and solid domains discretization;
- constitutive model definition;
- loads and Boundary Conditions (BCs) selection;
- turbulence modelling.

As far as the first step is concerned, it was carried out by adopting the Ansys SpaceClaim 3D Computer Aided Design (CAD) modelling software [50]. The CAD model, provided by the WP-DIV EUROfusion CAD designers are imported into the modelling software, allowing the geometry to be manipulated by cleaning some issues related to CAD format conversions, some details whose sizes are small and that can be safely neglected in the calculation are removed, the fluid domain is extracted, and macro-regions are defined, aiming at easing the successive mesh preparation and pre-processing phases.

The second step, domain discretization, was carried out by adopting the Ansys Mesh tool [51]. During this phase, the named selections are defined and a suitable mesh is produced for each domain region. As a general strategy, it was decided to opt for hybrid structured-unstructured meshes: whenever the geometry allowed it (simple geometries or extrusion bodies), structured meshes were employed, while unstructured meshes were used for complex shapes. In addition, an attempt was made, where possible, to ensure conformal meshes between the different grid regions. The only general exception was at the solid-fluid interfaces, where sometimes considerably less dense meshes were used for the solids.

As far as the constitutive model is concerned, water coolant transport and thermofluid-dynamic properties defined in the IAPWS IF97 library [52] were

adopted, while, for the different solid materials, temperature-dependent values of density, specific heat and thermal conductivity were considered [53, 54].

Concerning the loads and BC definition, a suitable set of values is mandatory to obtain realistic predictions. As far as the coolant is concerned, pressure, mass flow rate and temperature conditions were agreed upon with the engineers responsible for the divertor and the PHTS. Additionally, the thermal loads were drawn from dedicated neutronic analyses and plasma simulations.

Regarding the turbulence modelling, the $k - \omega$-based Shear Stress Transport (SST) Reynolds Averaged Navier Stokes (RANS) model was generally selected, giving a more accurate description of the near-wall region, especially in the case of flow separation. It is a hybrid model that uses a transformation of the $k - \epsilon$ model into a $k - \omega$ model in the near-wall region and the standard $k - \epsilon$ model in the fully turbulent region far from the wall. In CFX, this model adopts the *automatic wall treatment*, which automatically switches from wall functions to a low-Re near-wall formulation as the mesh is refined. The choice of the turbulence model is a topical matter in a CFD simulation, highly depending on the flow regime predicted in the flow domain as well as on the robustness of its parameters and, as a consequence, it should be selected on a base case.

Once the setup is complete, the code solves the Navier-Stokes equations numerically by adopting suitable algorithms and discretization schemes and, finally, the results can be post-processed.

Chapter 2

Parametric Analyses and Operational Limits of the Divertor Cooling Circuit

During the years 2020 and 2021, the thermal-hydraulic performances of the single-circuit cooling option divertor cassette were preliminarily assessed by means of 3D-CFD isothermal calculations [37, 55]. The results of these analyses are not reported here for the sake of brevity and the preliminary nature of the assessments made. However, the results obtained showed how the CHF margin resulted always lower than the prescribed limit of 1.4 considering a coolant inlet pressure of 50 bar and inlet temperatures higher than 70°C, even assuming high values of coolant mass flow rates, compatible with the constraint on maximum pressure drop.

Moreover, these analyses shed light on two fundamental aspects of the study of this divertor concept. The first is the need to define new operating conditions for the coolant, necessarily different from those employed for the cooling circuits of the double-circuit cooling option divertor, due to the larger set of constraints to be considered, and the second is the impossibility of making this selection relying on 3D-CFD calculations, that would result in unduly high computational costs.

It is interesting to highlight how the compliance with most of the constraints listed in section 1.8 can be verified by adopting rather simple calculations by applying the First Principle of Thermodynamics and employing appropriate correlations, for example following the procedure described in [25]. The only exception is the evaluation of the temperature distribution in solids, which are determined by the complex geometrical shape of the components and which, therefore, compulsorily require the use of 3D coupled fluid-structure thermofluid-dynamics simulations in most of the cases.

Although this statement is strictly true for most of the cassette sub-components, it is possible to evaluate the temperature distribution inside the PFUs by carrying out 2D steady-state thermal simulations of a section of the PFU located at the strike

point. This is possible thanks to their relatively simple geometry, together with the peaked shape of the surface power density, as can be observed in figure 2.1, showing the heat flux expected over the plasma-facing surfaces of the divertor under normal operating conditions (detached plasma). The peak value of 5 MW/m^2 visible in the figure is highly localized and strongly dependent on the considered plasma scenario, as it is affected by the fraction of energy that can be radiated before reaching the divertor targets.

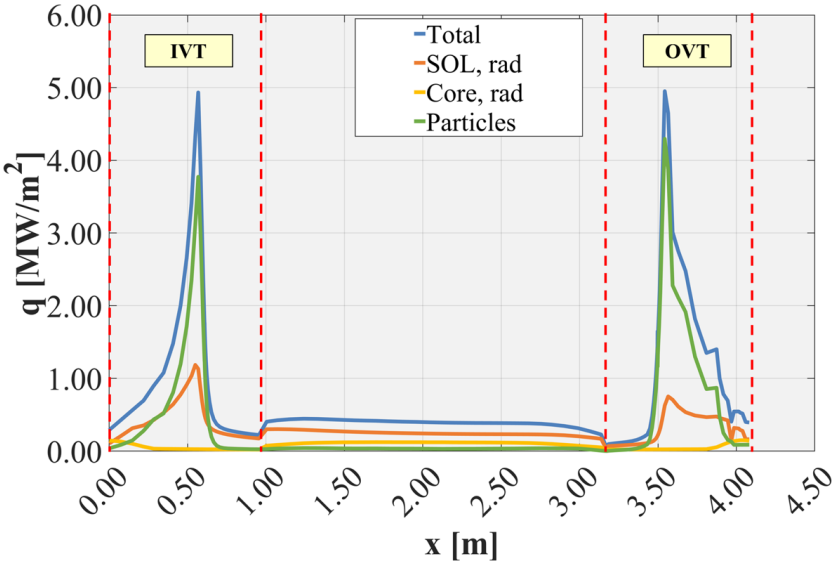

Figure 2.1: Heat flux profile for the different regions of the divertor, from [56].

Based on this reasoning, a novel numerical tool, namely ADRANOS, has been developed in order to predict, with a reduced computational effort, the divertor thermal-hydraulic performance map as the topology of the cooling circuit, the coolant inlet conditions and mass flow rate vary, with the final aim to assess the feasibility of the DEMO divertor cooling circuits integration foreseen with the single-circuit concept. The development of this calculation tool initiated several research campaigns, which will be described in the final part of this chapter, focusing on the operating condition limits of the different divertor cooling circuits.

It should be noted that the results obtained with ADRANOS are only able to assess most of the thermal and thermo-hydraulic performance of the divertor cooling circuit. Therefore, other aspects, such as the verification of the thermo-structural performance, should be addressed separately. This aspect is of great importance and is strictly linked to the choice of coolant operating conditions, due to the variation of mechanical properties with the combined effect of temperature and neutron-induced damage. It follows that additional analyses must be performed to check whether selected configurations or operating conditions are able to comply with additional constraints, not considered in ADRANOS. Nevertheless, any configuration or operating condition that is discarded by ADRANOS will certainly be not suitable for the DEMO divertor, as some of the design constraints are not met.

2.1 ADRANOS development

2.1.1 Overview

ADRANOS is a coupled lumped-parameter/2D FEM simulation tool originally created with the aim of evaluating the steady-state performance map of the DEMO divertor cooling circuit, to be intended as the domain of the phase space of coolant inlet mass flow rate, pressure and temperature conditions that allow the cooling system to safely perform its target mission under steady-state conditions. In particular, it allows parametric analyses to be carried out over a large number of different configurations and inlet coolant conditions with an acceptable computational effort, evaluating the compliance of the component's thermal-hydraulic operating conditions with the set of constraints already discussed in section 1.8. The code has been developed in MATLAB [47] with an object-oriented approach, to make it extremely flexible in evaluating different cooling system topologies, and it has been optimised for parallel computing, so to potentially reduce the overall time required for simulations, depending on the available computational resources.

The code takes advantage of the FEA toolbox [48] FEM solver available in the MATLAB package, with the aim to perform 2D steady-state thermal analyses of the PFU monoblocks located at the IVT and OVT strike points, to evaluate the temperature distribution in the most critical region of the PFCs.

The code relies on preliminary thermofluid-dynamic analyses performed with dedicated 3D-CFD calculations, whenever the geometric complexity of the sub-components constituting the divertor is too great to allow characteristic curves to be defined on the basis of simple correlations.

It is also important to point out that the methodologies and procedures implemented in the ADRANOS tool are inspired by and based on the efforts of [57, 58, 59, 60]. The element of novelty introduced in the present work is the coupling between the lumped-parameter simulation of the entire DEMO divertor cooling circuit and the FEM module, as well as the adoption of this methodology as a screening tool capable of quickly assessing whether a given layout of the DEMO divertor cooling circuit is capable of working in compliance with several constraints, and if so, for which ranges of coolant temperature, pressure and mass flow rates.

2.1.2 Methodology - Lumped parameters module

The code is grounded on a calculation module that evaluates the steady-state coolant temperature and pressure distribution within the considered cooling circuit, as well as the mass flow rate distribution among the main sub-components connected in parallel, by adopting a theoretical approach based on the lumped-parameter

method. The cooling circuit must be at first subdivided into different volumes, each one representing a relevant sub-component to be analysed in detail, as it will be detailed in section 2.1.4. The volumes can be then arranged in series or parallel, and it is furthermore possible to group them into higher-level assemblies, so to ease the circuit definition, as well as to perform more detailed 1D assessments (e.g. if it is required to obtain pressure and/or temperature profiles). The layout of the input cooling circuit is thus provided to the code in the form of a cooling scheme, similar to those reported in figures 1.15, 1.17 and 1.23.

Each volume requires the knowledge of its hydraulic characteristic function, which can be determined by suitable correlations for simple components. However, whenever the geometrical complexity of the cooling circuit embedded in the selected volume is too great, it is necessary to rely on the results of preliminary 3D-CFD calculations. In these cases, the hydraulic characteristic function can be defined according to equation (2.1), where Δp is the total pressure drop, ρ is the average density calculated starting from the average values of temperature $\overline{T}$ and pressure $\overline{p}$ inside the volume (arithmetic averages between inlet and outlet conditions), $\dot{m}$ is the mass flow rate, while a and b are the fitting parameters and ρ_{ref} is the reference density of the CFD simulation.

$$\Delta p = \frac{\rho_{ref}}{\rho\left(\overline{T}, \overline{p}\right)} a \dot{m}^b \tag{2.1}$$

More in detail, starting from a dataset containing different Δp values at different mass flow rates, a curve with the general form $\Delta p = a\dot{m}^b$ is fitted by choosing optimal a and b values. To take then into account the variation of pressure drop with the coolant temperature, the density correction $\rho_{ref}/\rho\left(\overline{T}, \overline{p}\right)$ is introduced, where the reference density is calculated from the CFD simulations as a proper volume-averaged density value.

For simplicity, the volumetric kinetic energy density terms are generally neglected in the pressure drop equation but are taken into account when dealing with special volumes, such as those representing the VTs, as will be discussed later in this section.

The code solves sequentially the cooling circuit, starting from the inlet volume and proceeding downstream to the outlet of the circuit. For each volume, for a given set of inlet conditions T_{in}, p_{in} and a given $\dot{m}$, energy conservation in steady-state conditions equation (2.2) and pressure drop equation (2.3) are solved iteratively to calculate the outlet fluid conditions, where c_p is the fluid heat capacity under isobaric conditions calculated at the volume average values of pressure and temperature, while W is the total deposited power, sum of integral surface and volumetric heat loads.

All the thermodynamic and transport properties of water are evaluated by adopting a MATLAB implementation [61] of the IAPWS IF97 water library [52].

$$T_{out}^{j} = T_{in} + \frac{W}{\dot{m} c_p \left(\overline{T}^{j-1}, \overline{p}^{j-1} \right)} \tag{2.2}$$

$$p_{out}^{j} = p_{in} - \frac{\rho_{ref}}{\rho \left(\overline{T}^{j-1}, \overline{p}^{j-1} \right)} a \dot{m}^{b} \tag{2.3}$$

At each iteration j, outlet temperature and pressure values are updated adopting the fluid properties obtained from the previous iteration, and the calculation proceeds until relative errors of outlet temperature and pressures calculated at two consecutive iterations result lower than a given tolerance, set equal to 0.01%.

Special attention has to be paid when two blocks are arranged in parallel. The code is currently able to handle only the parallel connection of two components (referred to as A and B in the following) by performing an additional outer loop, adopting an optimization algorithm to find the value of the branching factor χ such that the difference between the pressure drops in the two branches is the same.

$$\chi = \frac{\dot{m}_A}{\dot{m}} \tag{2.4}$$

The factor χ, defined according to equation (2.4) and given $\dot{m}_A$ the mass flow rate flowing inside the branch A of the parallel, is iteratively updated by adopting the Golden-section search algorithm [62] until the ratio between the pressure drop unbalances between the branches and the average pressure drop reaches values below a given tolerance, chosen equal to 0.01%. The mass flow rate fed to branch B of the parallel is calculated simply as $\dot{m}_B = (1 - \chi)\, \dot{m}$. Each optimization outer iteration of mass flow rate branching requires an inner loop to obtain consistent values of pressure and temperature, according to equations (2.2) and (2.3).

Once the iterative procedure converges, outlet pressure (the same for the two branches) is adopted as the input value for the following volume, while the temperature to be passed downstream is obtained by solving the energy conservation law for two mixing flows, according to equation (2.5), where i is the fluid specific enthalpy.

$$\dot{m} i_{out} \left(T_{out}, p_{out} \right) = \chi \dot{m} i_{out,A} \left(T_{out,A}, p_{out} \right) + (1 - \chi)\, \dot{m} i_{out,B} \left(T_{out,B}, p_{out} \right) \tag{2.5}$$

When average temperature and pressure values are available for all the components, the lowest margin against saturation is assessed according to equation (2.6), where T_{sat} is the saturation temperature calculated at the outlet pressure of the volume. This variable is calculated and stored for each volume, and the minimum value over the entire cooling circuit is successively compared with the applicable constraint.

$$\Delta T_{sat} = T_{sat}\left(p_{out}\right) - T_{out} \tag{2.6}$$

Special attention is moreover paid to the VT volumes, which require an estimation of the CHF margin and maximum velocity according to the procedure detailed in the following. For these additional assessments, the VT volumes must be provided with the number and geometrical details of the PFU cooling channels, i.e. the channel diameter, the thickness and the twist ratio of the ST.

Firstly, the average coolant axial velocity $\overline{v}$ along PFU cooling channels is determined according to equation (2.7), where A is the net cross-section of each cooling channel, considering the presence of the ST, while n is the number of PFU cooling channels of the selected VT.

$$\overline{v} = \frac{\dot{m}}{nA\rho\left(\overline{T}, \overline{p}\right)} \tag{2.7}$$

Given the axial fluid velocity, the fluid average thermodynamic conditions and the geometrical details of the PFU cooling channels, the CHF margin can be derived according to the procedure described in [46], by adopting the well-known Tong-75 correlation of equation (2.8) to calculate the *incident* CHF, where the Fanning friction factor is calculated according to equation (2.9), r is the enthalpy of vaporization, p_{crit} is the water critical pressure of 220.64 bar, Re is the Reynolds number, calculated according to equation (2.10), Ja is the Jacob number, calculated as per equation (2.11), and finally C_f is a factor to account for the specific geometrical configuration, that, for the case of ST-equipped channel can be assumed equal to 1.67.

$$CHF = 0.23 f \frac{\dot{m}}{A} r C_f \left[1 + 0.00216\left(\frac{\overline{p}}{p_{crit}}\right)^{1.8} Re^{0.5} Ja\right] \tag{2.8}$$

$$f = 8Re^{-0.6}\left(\frac{d_h}{d_{ref}}\right)^{0.32} \tag{2.9}$$

$$Re = \frac{\overline{v} d_h \rho\left(\overline{T}, \overline{p}\right)}{\mu_b\left(\overline{T}, \overline{p}\right)} \tag{2.10}$$

$$Ja = \frac{\rho\left(\overline{T}, \overline{p}\right)}{\rho_v} \cdot \frac{c_p\left(T_{sat} - \overline{T}\right)}{r} \tag{2.11}$$

With reference to equations (2.8) to (2.11), d_h is the PFU channel hydraulic diameter defined according to equation (2.12), being d_0 the channel inner diameter and δ the ST thickness, d_{ref} is a reference diameter equal to 12.7 mm, μ_b is the water bulk dynamic viscosity, while ρ_v is the water vapour saturation density calculated at the fluid pressure. Moreover, the average volume static pressure $\overline{p}$ is calculated

net of the fluid dynamic pressure $\frac{1}{2}\rho\left(\overline{T},\overline{p}\right)\overline{v}^2$, and the calculation of the CHF is made, according to the current implementation, assuming that at the strike point the coolant is at the average water thermodynamic conditions within the VT volume. However, it should be mentioned that by adopting a suitable discretization of the VTs with several volumes connected in series, it is possible to refine the calculation and obtain more precise values of the coolant static pressure and temperature at the strike point location to be employed for the CHF margin calculation.

$$d_h = \frac{\pi d_0 - 4\delta}{\pi + 2 - 2\delta/d_0} \tag{2.12}$$

Once the CHF is calculated, it is compared with the maximum heat flux $q_{w,max}$ expected at the interface between the PFU channel and the coolant, calculated according to equation (2.13),

$$q_{w,max} = q_w f_p, \tag{2.13}$$

where q_w is the nominal heat flux onto the armour plasma-facing surface (e.g. 20 MW/m^2), while f_p is a peaking factor (equal to 1.60 for the considered monoblock geometry) to take into account the uneven distribution of the heat flux around the channel diameter. The CHF margin definition is given in equation (2.14), where the factor 0.95 is required to take into account the uneven flow distribution among PFU channels, supposing a 5% deviation from average CHF value, conservatively taken on the basis of the 3D-CFD calculation results of the entire EU-DEMO divertor PFC cooling circuit of the past years [21, 37].

$$M_{CHF} = 0.95\frac{CHF}{q_{w,max}} \tag{2.14}$$

Finally, concerning the maximum velocity in the PFU cooling channels, it is calculated for each VT by increasing the average velocity of equation (2.7) of 5% (again in accordance with the results of the 3D-CFD simulations).

The ADRANOS tool performs all the calculations described above in order to assess, for each triplet $(p_{in}, T_{in}, \dot{m})$, whether the cooling circuit is able to provide results compatible with the constraints of maximum pressure drop, minimum saturation margin, adequate CHF margin and maximum PFU cooling channel coolant velocities for both IVT and OVT, in accordance with the applicable limits.

If the verification is successful, the tool performs further 2D steady-state thermal analyses to verify that the PFC temperature constraints are met. This condition significantly reduces the overall calculation time, as the more computationally-intensive 2D-FEM simulations are only performed when necessary.

2.1.3 Methodology - 2D steady-state FEM thermal analyses module

As anticipated, the ADRANOS FEM module performs 2D steady-state thermal simulations of a section of the monoblock located at the strike point. The calculations are performed both for IVT and OVT, and considering surface heat loads under normal operation and during slow transient conditions, according to the values indicated in [6].

The geometrical details of the domain considered are those of figure 1.9a while the mesh adopted for the 2D simulations is shown in figure 2.2 (only half domain has been taken into account for symmetry), showing the different regions characterized by different materials (tungsten, CuCrZr and copper), the boundaries between them, as well as the nomenclature adopted for the assignment of the BCs.

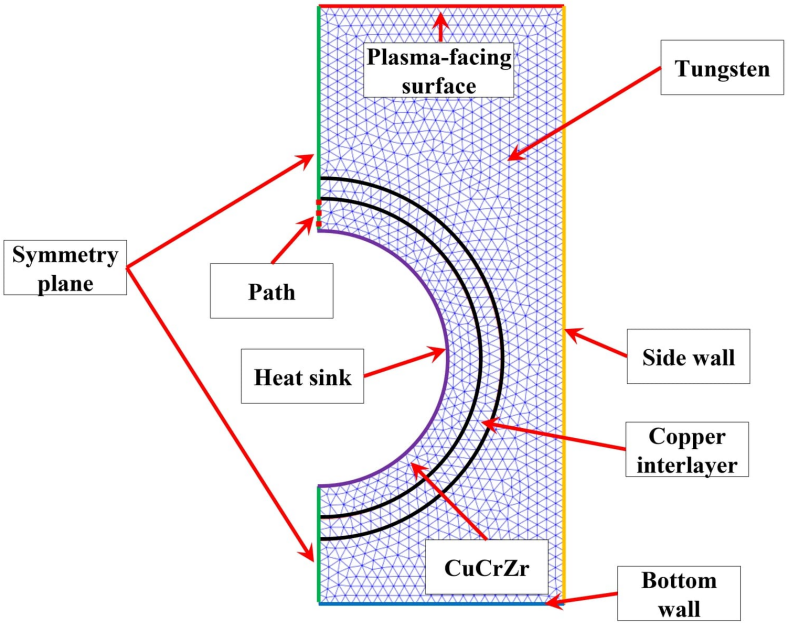

Figure 2.2: Mesh adopted for the monoblock steady-state thermal simulations with indications of the regions and boundary nomenclature.

Table 2.1: Summary of the main mesh parameters.

Mesh Parameter	**Value**
Nodes	1279
Elements	2384
Elements Order and Topology	Linear Tria
Maximum Element Size [mm]	0.5
Minimum Element Size [mm]	0.25
Mesh Growth Rate (GR)	1.5

The computational mesh, whose details are summarized in table 2.1, was selected by preliminary performing a grid-independence assessment considering both 10 and 20 MW/m^2 incident heat fluxes. In particular, this assessment was carried out by adopting the well-established Grid Convergence Index (GCI), derived in [63], and considering the Least-Square (LS) error estimation described in [64]. More in detail, given any monitored quantity ϕ, it is possible to define a dependence on the average mesh size by adopting equation (2.15), where ϕ_i is the measured value obtained with a selected mesh of average linear size h_i, ϕ_0 is the estimate of the asymptotic value, α is a constant and p is the observed order of convergence.

$$\phi_i = \phi_0 + \alpha h_i^p \tag{2.15}$$

Given the results obtained with a set of at least three meshes, it is then possible to obtain, by proper interpolation, the values of ϕ_0, α and p, e.g. by adopting the LS method. The GCI can be therefore calculated for the selected i-th grid, as follows

$$GCI_i = F_s \left| \frac{\phi_i - \phi_0}{\phi_i} \right| = F_s \left| \frac{\alpha}{\phi_i} \right| h_i^p, \tag{2.16}$$

where F_s can be interpreted as a safety factor, chosen here equal to 1.25 as suggested in [64], being the observed order of convergence close to the theoretical one, i.e. 2.

The results of the analysis campaign, summarized in figure 2.3, show how adopting the selected mesh (corresponding to the mesh M2 in figure), the GCIs are well below 1% for maximum temperatures in tungsten, copper, and CuCrZr, both under plasma heat fluxes of 10 and 20 MW/m^2. Moreover, the mesh M2 of figure 2.3, being the same described in table 2.1, was selected to obtain deviation with respect to asymptotic values below 1°C.

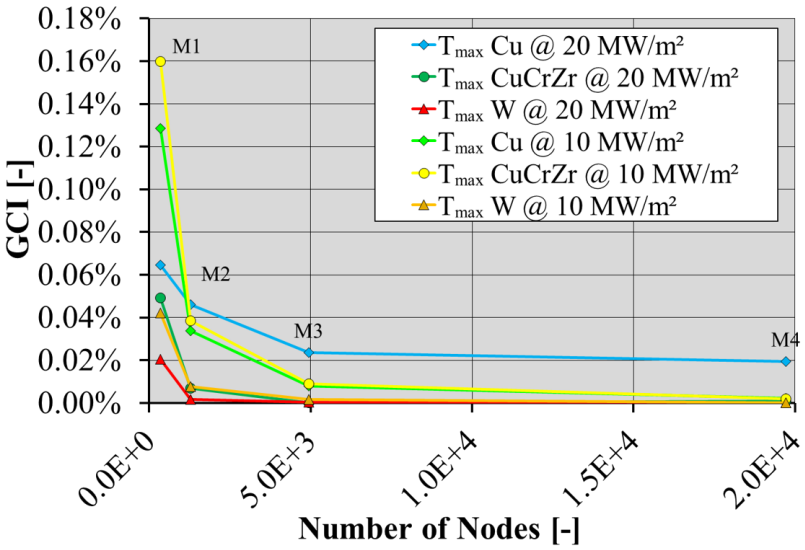

Figure 2.3: GCI results of the monoblock mesh independence assessment.

The 2D thermal steady-state simulations are carried out considering the BCs given in table 2.2. The volumetric heat loads are neglected, being the volumetric density of nuclear-deposited power significantly lower than the surface loads. Nevertheless, they are still considered in the lumped-parameter module of the ADRANOS tool. Concerning the materials, temperature-dependent properties are considered for tungsten, CuCrZr and copper interlayer, respectively taken from [65], [66] and [67].

Table 2.2: Summary of BCs adopted for the 2D FEM simulations.

Boundary	**Applied BC**
Plasma-facing wall	Heat flux of 10 and 20 MW/m^2
Bottom and side walls	Adiabatic
Symmetry plane	Symmetry
Heat sink	Robin BC

Regarding the BC adopted for the heat sink, a Robin BC, necessary for the well-posedness of the problem, is adopted. More in detail, an equivalent convective heat transfer coefficient is calculated, being dependent on the local CuCrZr temperature, as well as on the local pressure and bulk temperature values of the coolant, under both single-phase and two-phase heat transfer conditions. It is computed simply by dividing the heat flux calculated according to the procedure detailed in the next section by the temperature difference between the bulk of the fluid and the local wall temperature.

2.1.3.1 Heat Transfer Coefficient Calculation

In order to correctly assess the steady-state thermal response of the PFUs, it is necessary to accurately reproduce the convective heat transfer mechanisms involved. This is only possible if a model capable of predicting the Nukiyama boiling curve (see figure 2.4) under the conditions of interest is available.

To this purpose, the correlations reported in the following, calculated at each node of the heat sink boundary, have been implemented into the tool to properly predict the heat transfer coefficient in the various sub-regions of the Nukiyama curve.

Single-phase Forced Convection Heat Transfer

With regard to the correlations used for the calculation of the single-phase convective heat transfer coefficient, ADRANOS adopts the Sieder-Tate correlation [68] (valid for $Re > 10000$ and a broad range of Prandtl number Pr) with the Gambill correction factor [69] to take into account the presence of the ST, as reported in equation (2.17).

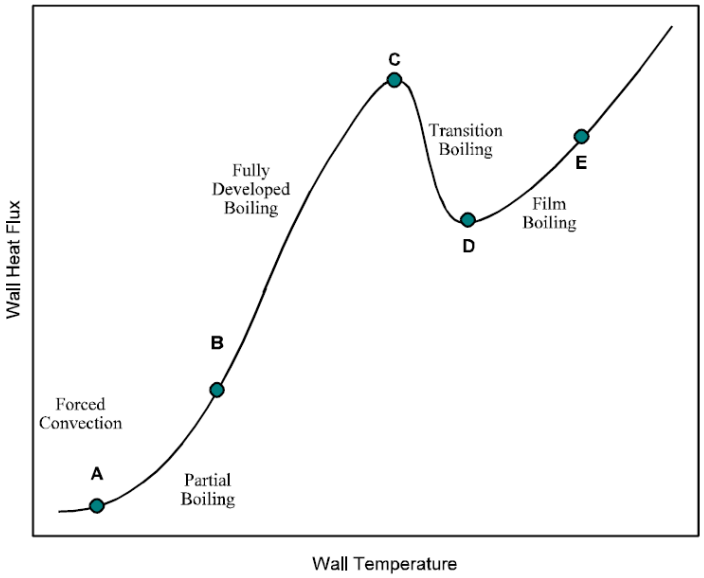

Figure 2.4: Nukiyama's Boiling Curve [58].

$$Nu = 0.027 Re^{0.8} Pr \left(\overline{T}, \overline{p}\right)^{1/3} \left(\frac{\mu_b \left(\overline{T}, \overline{p}\right)}{\mu_w \left(T_w, \overline{p}\right)} \right)^{0.14} \left(2.18 \gamma^{-0.09}\right) \tag{2.17}$$

With reference to equation (2.17), Nu is the Nusselt number, Pr is calculated at the coolant average pressure and temperature, γ is the dimensionless twist ratio (the ratio between the ST pitch and the cooling channel diameter), while μ_w is the water dynamic viscosity calculated at the average coolant pressure and considering the local wall temperature T_w. From equation (2.17) is then possible to calculate the heat transfer coefficient and thus to evaluate the local heat flux q_{sp}, according to equation (2.18), where λ is the bulk fluid thermal conductivity.

$$q_{sp} = \frac{Nu \lambda \left(\overline{T}, \overline{p}\right)}{d_h} \left(T_w - \overline{T}\right) \tag{2.18}$$

This latter equation is required to calculate the heat transfer coefficient in two-phase heat transfer conditions.

Two-phase Forced Convection Heat Transfer

The correlations used for the various regimes of the Nukiyama boiling curve are taken entirely from the procedure described in [58] and [70]. Boiling incipience is evaluated by adopting the Bergles-Rohsenow onset of nucleate boiling correlation [71], reported in equation (2.19), where the average pressure $\overline{p}$ is expressed in bar. The correlation is valid for water only, for a pressure range between 0.1 and 13.8 MPa [70].

$$q_{bi} = 1082 \overline{p}^{1.156} \left(1.799 \left(T_w - T_{sat}\right)\right)^{\frac{2.1598}{\overline{p}^{0.0234}}} \tag{2.19}$$

Fully developed nucleate boiling is evaluated with the Araki correlation [72], reported in equation (2.20), while the partially developed nucleate boiling is calculated with the Bergles-Rohsenow interpolation [71] of equation (2.21).

$$q_{fdnb} = 10^6 \left(\frac{T_w - T_{sat}}{\left(25.72 e^{\frac{-\bar{p}}{86}}\right)} \right)^3 \tag{2.20}$$

$$q_{pdnb} = \sqrt{q_{sp}^2 + \left(q_{fdnb} - q_{fdnb,bi}\right)^2} \tag{2.21}$$

Although Araki's correlation is derived from experiments conducted with inlet pressures up to 13 bar and temperatures up to 80°C, in [70] it is adopted up to significantly higher values of the two parameters, maintaining a very good agreement with the experimental data.

More in detail, according to the rationale defined in [71], the entire two-phase flow regime is calculated by adopting the partially developed nucleate boiling of equation (2.21). With this formulation, the heat flux asymptotically approaches fully developed boiling at high wall superheat. In particular, when the heat flux calculated with equation (2.18) is lower than the one of (2.19), the formulation given in (2.18) is applied, otherwise, the heat flux is evaluated by adopting equation (2.21).

Finally, as regards the calculation of the CHF and the estimation of the post-CHF heat transfer regime, it is interesting to note that the lumped-parameters module discussed in section 2.1.2 discards configurations characterised by a CHF margin lower than 1.4. Consequently, the FEM module will never operate under post-CHF heat transfer conditions and, therefore, the evaluation of this boiling regime of the Nukiyama curve has not been implemented. The code, in fact, is meant to operate only between the forced convection regime and the point C of figure 2.4.

2.1.4 Spatial discretization and input data

As anticipated, the layout of the input cooling circuit is thus provided to the code in the form of a cooling scheme, composed of several volumes connected in series or in parallel. The divertor single-circuit cooling option cooling scheme is reported in figure 2.5 as an example of typical spatial discretization to be provided to the code.

Each box in figure 2.5 represents a volume of the spatial discretization, and is generated as an instance of a Matlab class, named *GeneralVolume*. It entails being provided with the total deposited power W, the a and b parameters and the reference density ρ_{ref} required to define its characteristic function.

The boxes in green represent instead the volume assemblies. These are employed either to handle the parallel of different branches or to perform more detailed simulations with a 1D approach. These kinds of volumes should be provided with lists of W, a, b, and ρ_{ref}, each of those has as many elements as there are in the

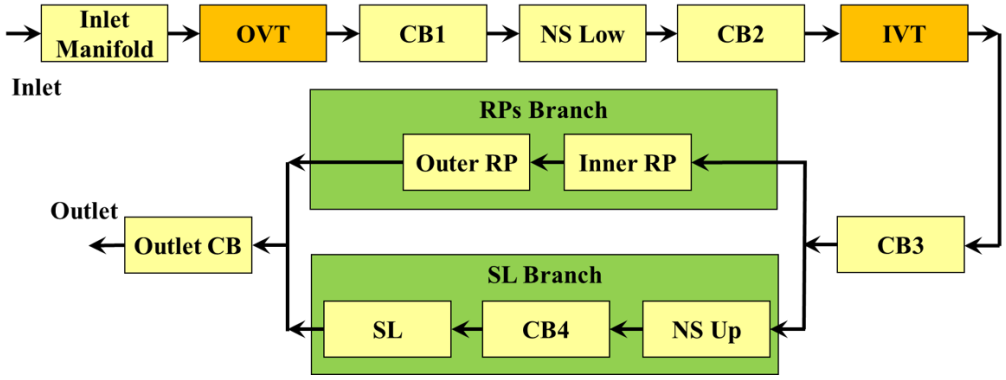

Figure 2.5: Example of ADRANOS input spatial discretization.

embedded sub-volume. Finally, the boxes in orange are those representing the VTs, named *VTVolume*. They are implemented as a sub-class of *GeneralVolume*, thus inheriting from this latter parameters and methods. The definition of the *VTVolume* objects require additionally to provide the number of PFU cooling channels, and additional parameters are hard-coded but can be superseded if required.

Table 2.3: Summary of input parameters and outputs for the different ADRANOS volumes.

	Required Input Param.	**Optional Input Param.**	**Upstream Input Param.**	**Output Results**
GeneralVolume	W a b ρ_{ref}		p_{in} T_{in} $\dot{m}$	p_{out} T_{out} $\dot{m}$ ΔT_{sat}
GeneralVolume Assembly	W (list) a (list) b (list) ρ_{ref} (list)		p_{in} T_{in} $\dot{m}$	p_{out} (list) T_{out} (list) $\dot{m}$ ΔT_{sat} (min)
VTVolume	W a b ρ_{ref} n	d_0 δ C_f f_p q_w Δ_v Δ_{CHF}	p_{in} T_{in} $\dot{m}$	p_{out} T_{out} $\dot{m}$ ΔT_{sat} M_{CHF} $\overline{v}$

A comprehensive list of the three volumes input and output data is provided in table 2.3, where are reported the input parameters required to create the objects, the optional input parameters that can be superseded, the data provided by upstream volumes, and finally, the output data. With reference to the table, Δ_v and Δ_{CHF} are the coefficients that take into account the non-uniform distributions of velocities and CHF margins, set by default equal to 0.95.

Moreover, a snippet of the ADRANOS input file is shown in figure 2.6, where it is possible to notice at the last line how the divertor cooling scheme layout is provided to the code.

```
%%%%%%%%%%%%%%%%%%%%%%%%%%%%%%%%%%%%%%%%%%%%%%%%%%%%%%%%%%%%%%%%%%%%%%%%%%%%
% CB0
%%%%%%%%%%%%%%%%%%%%%%%%%%%%%%%%%%%%%%%%%%%%%%%%%%%%%%%%%%%%%%%%%%%%%%%%%%%%
W=0; % [MW]
aa=1.941E-05; % [MPa s^b/kg^b]
bb=2; % [-]
rhoref=963.099; % [kg/m^3]

CB0=GeneralVolume(W,aa,bb,rhoref,'CB0');
%%%%%%%%%%%%%%%%%%%%%%%%%%%%%%%%%%%%%%%%%%%%%%%%%%%%%%%%%%%%%%%%%%%%%%%%%%%%
% OVT
%%%%%%%%%%%%%%%%%%%%%%%%%%%%%%%%%%%%%%%%%%%%%%%%%%%%%%%%%%%%%%%%%%%%%%%%%%%%
n=46; % [-]
W=2.018E+00; % [MW]
aa=1.338E-04; % [MPa s^b/kg^b]
bb=2; % [-]
rhoref=963.096; % [kg/m^3]

OVT=VTVolume(n,W,aa,bb,rhoref,'OVT');
% Optional
OVT.qw=20; % [MW/m^2]
%%%%%%%%%%%%%%%%%%%%%%%%%%%%%%%%%%%%%%%%%%%%%%%%%%%%%%%%%%%%%%%%%%%%%%%%%%%%
% CB1S
%%%%%%%%%%%%%%%%%%%%%%%%%%%%%%%%%%%%%%%%%%%%%%%%%%%%%%%%%%%%%%%%%%%%%%%%%%%%
% Series composed of CB1, NS (low), and CB2
W=[1.769E-01, 0.015, 1.769E-01]; % [MW]
aa=[4.687E-05, 3.117E-05, 6.041E-05]; % [MPa s^b/kg^b]
bb=[2, 2, 2]; % [-]
rhoref=[962.995, 962.988, 962.945]; % [kg/m^3]

CB1S=GeneralVolumeAssembly(W,aa,bb,rhoref,'CB1S');
%%%%%%%%%%%%%%%%%%%%%%%%%%%%%%%%%%%%%%%%%%%%%%%%%%%%%%%%%%%%%%%%%%%%%%%%%%%%
% Divertor Cooling Circuit Layout
%%%%%%%%%%%%%%%%%%%%%%%%%%%%%%%%%%%%%%%%%%%%%%%%%%%%%%%%%%%%%%%%%%%%%%%%%%%%
scheme={{CB0},{OVT},{CB1S},{IVT},{CB3},{LinerNSU,RPs},{CB4}};
```

Figure 2.6: ADRANOS input code snippet.

Finally, the ADRANOS tool should be supplied with the range and the number of sample points to be considered for inlet pressure, inlet temperature and mass flow rate to perform the parametric analyses.

2.1.5 Output data description

In this section, a typical output map obtained with ADRANOS is presented and discussed. Once the analysis step is completed, the outcomes of the simulation are stored in a dedicated text file and are post-processed with a dedicated Matlab script. During the post-processing stage, the compliance with the constraints listed in table 2.4, drawn from section 1.8, is checked for each coolant operating condition.

Table 2.4: List of constraints and their IDs considered for the simulations.

ID	Constraint	Region	Load
A	$M_{CHF} = 1.4$	OVT	20 MW/m^2
B	$M_{CHF} = 1.4$	IVT	20 MW/m^2
C	$\Delta p = 14$ bar	All	-
D	$v_{max} = 16$ m/s	OVT	-
E	$v_{max} = 16$ m/s	IVT	-
F	$\Delta T_{sat} = 20$°C	All	-
G	$T_{max} = 300$°C	OVT CuCrZr	10 MW/m^2
H	$T_{max} = 300$°C	IVT CuCrZr	10 MW/m^2
I	$T_{max} = 450$°C	OVT CuCrZr	20 MW/m^2
J	$T_{max} = 450$°C	IVT CuCrZr	20 MW/m^2
K	$T_{max} = 3222$°C	OVT tungsten	20 MW/m^2
L	$T_{max} = 3222$°C	IVT tungsten	20 MW/m^2
M	$T_{max} = 885$°C	OVT Cu	20 MW/m^2
N	$T_{max} = 885$°C	IVT Cu	20 MW/m^2

With regard to the maximum temperatures within the CuCrZr cooling pipe, these are calculated as average values along the path indicated in figure 2.2 with a red dashed line, as prescribed in [43].

A typical ADRANOS output is depicted in figure 2.7, showing the operating map at a given coolant inlet pressure, where the region in which the cooling circuit can operate being compliant with all the selected constraints is filled in green. Every constraint of table 2.4 is represented with a curve (the letter in the figure legend corresponds to the ID of the table), the locus of points where the monitored parameter is exactly equal to the limit value. The tags depicted in the figure are shown only for clarity and are not usually present in the tool output data.

The results relevant to the constraints A to F are calculated by the ADRANOS lumped-parameters module, and thus there is always an output value in terms of CHF margin, pressure drop, saturation margin, and maximum coolant axial velocity for each triplet of coolant inlet pressure, inlet temperature and mass flow rate. Constraints G to N are calculated instead by the ADRANOS FEM module, and they are evaluated only in a small portion of the selected phase space, the ones filled in orange and green in figure 2.7. The orange filling is usually omitted to avoid confusion, but its boundaries can be easily distinguished, being characterized

by jagged contours, which are precisely determined by the preliminary screening carried out by the lumped-parameter module. It follows that curves from G to N are physically meaningful only if they are inside the orange region, as for the case of temperature limits in CuCrZr in figure 2.7. When no orange region is reported, curves G to N should be considered only if they delimit the green region.

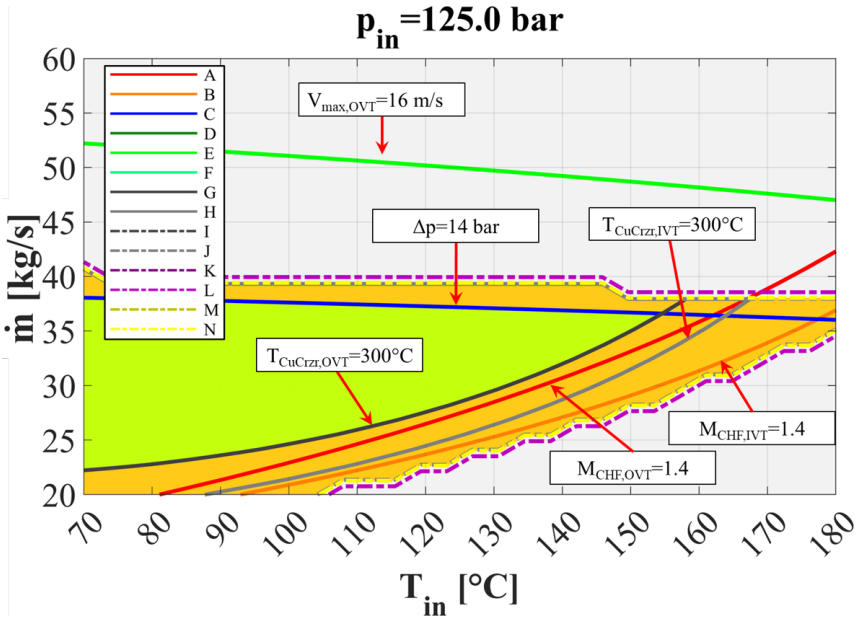

Figure 2.7: Example of ADRANOS output file.

It is interesting to note that the curves representing the different constraints can be grouped into two categories: those relevant to thermal aspects (curves A, B, and F to N) and those related to the coolant velocity (D and E, and indirectly the pressure drop curve C, being a function of the coolant mass flow rate). The curves belonging to the first category delimit the phase space in such a way that acceptable configurations can be obtained at higher values of mass flow rate and lower values of coolant temperature, so moving from the curve in the top-left direction. The curves of the second category, instead, are mainly affected by the coolant mass flow rate and less remarkably by coolant temperature. The acceptable configurations are thus below these curves. It follows that the green region is always delimited in the upper part by curves related to the coolant velocity (e.g. curve C in figure 2.7), and in the lower-right part by curves associated with temperature (curve G in figure 2.7). A comprehensive description of the dependence of all the ADRANOS monitored quantities on coolant inlet pressure, inlet temperature and mass flow rate is given in appendix A. It should also be pointed out that the 2D-FEM analyses are usually performed also for operating conditions slightly outside the limits A to F of table 2.4, in order to improve the graphical quality of the results and avoid the superposition of the green and orange regions. Further developments of the code are ongoing, with the aim to improve the graphical quality of the results by plotting the curves resulting

from FEM analyses only when they are truly representative of the temperature limits.

2.2 ADRANOS validation

To check the correctness of the implementation, the ADRANOS tool underwent a validation campaign of both the FEM and the lumped-parameters modules. First of all, the experimental setup of [73] was reproduced, and the outcomes of the stand-alone FEM module were compared to experimental data. Then, the divertor PFC cooling circuit of the double-circuit cooling option was studied, to check if the ADRANOS outputs under design operating conditions are in agreement with the CFD calculation and if the temperature distributions in the monoblocks are in line with the results of dedicated assessments.

2.2.1 FEM validation

The ADRANOS FEM module was validated by comparing the code predictions with the experimental results obtained by Mashall [74] and reported in [75]. The comparison was made by reproducing Marshall's experimental setup reported in [73], by looking at the temperature of the oxygen-free high-conductivity copper monoblock at the thermocouple location, i.e. 0.6 mm from the plasma-facing surface on the side of the monoblock, as shown in figure 2.8. The comparison between Marshall's experimental results and those obtained with ADRANOS are depicted in figure 2.9.

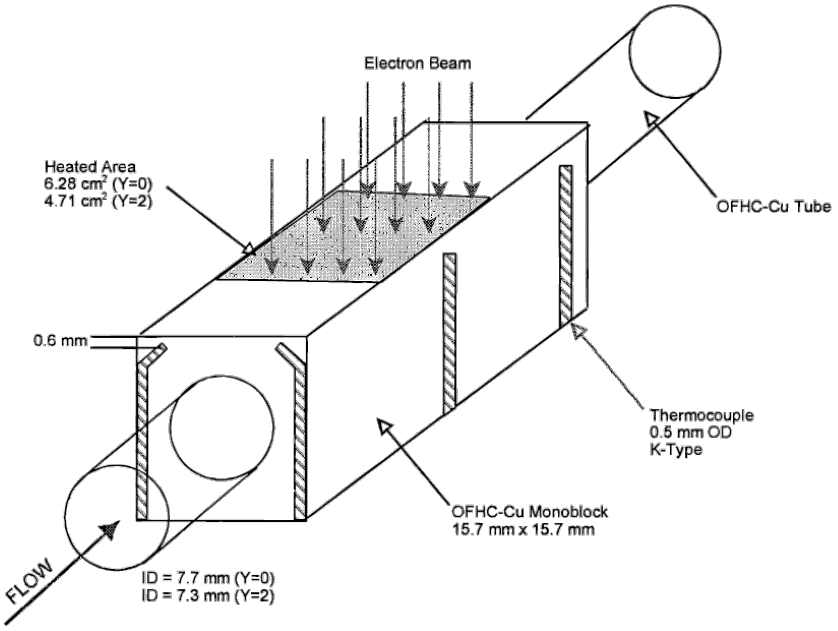

Figure 2.8: Experimental setup adopted by Marshall [73].

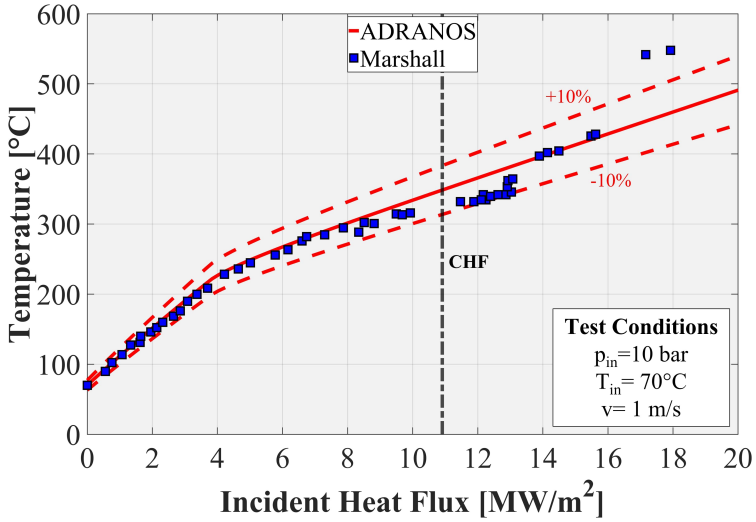

(a)

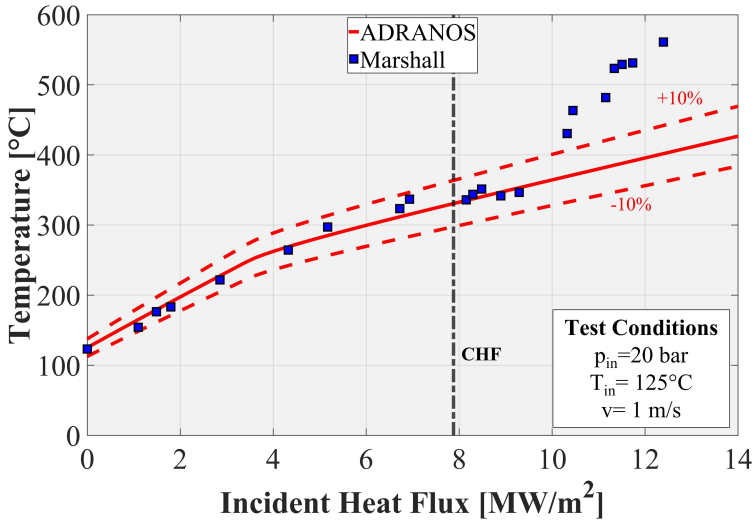

(b)

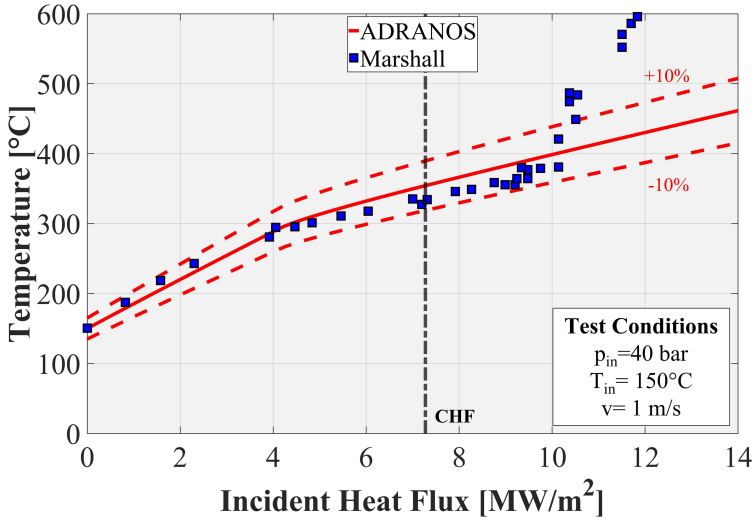

(c)

Figure 2.9: Comparison between ADRANOS and experimental results at inlet pressure of 10 (a), 20 (b) and 40 (c) bar.

As can be seen, there is a very good correspondence between the ADRANOS results and the experimental data, with errors in predicting thermocouple temperatures within the ±10% range. At high heat flux values, a significant deviation between the curves is observed, related to the occurrence of CHF and post-CHF heat transfer regimes, not predicted by the calculation tool. Nevertheless, as already pointed out in the previous section, this does not impair the code predictive potential, since the occurrence of these conditions is already excluded by the lumped-parameter module and the tool is not conceived to deal with a coolant experiencing such an extreme heat transfer mechanism.

2.2.2 DEMO divertor PFC cooling circuit validation case

The parametric study of the PFCs cooling circuit of the divertor double-circuit cooling option (2019 design) was carried out starting from the layout and volume discretization shown in figure 2.10, with the aim to evaluate the capability of the ADRANOS tool to reproduce the outcomes of CFD calculations under design operating conditions and to evaluate if the temperature distributions in the monoblocks are in line with the results of analyses available in literature.

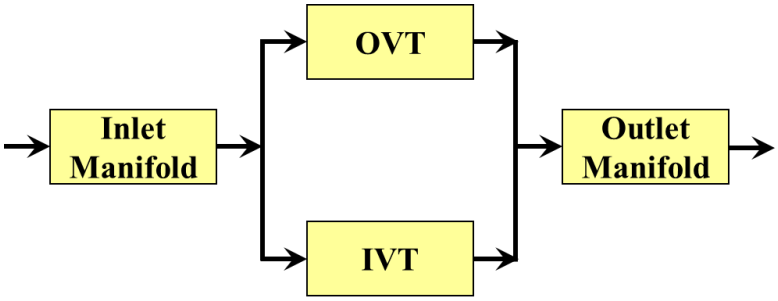

Figure 2.10: DEMO divertor PFCs cooling circuit ADRANOS volume discretization.

The ADRANOS volumes have been defined by considering integral surface and volumetric heat loads of 2.42 and 0.46 MW, respectively, drawn from [14], while as far as the characteristic curves are concerned, reference was made to the pressure drop breakdown reported in [21]. Since simulations of the PFC cooling circuit at different coolant mass flow rates are not available, a value of 2 was chosen for the b exponent of equation (2.1), taking into account that this coefficient has shown to be lower but reasonably close to 2 in similar components [76].

The analysis was therefore carried out by keeping the coolant inlet pressure fixed at 5 MPa while varying both the inlet temperature and the overall flow rate, respectively from 70 to 180°C and from 50 to 150 kg/s. The selected inlet temperature and mass flow rate ranges were discretized with 30 points each, for a total of 900 cases, while the overall run time to perform all the simulations was of approximately 7 minutes on a 3.00 GHz 18 core i9-9980XE workstation.

The results obtained are shown in figure 2.11, with reference to the constraints listed in table 2.4. The figure shows in red the PFCs cooling circuit design operating point, i.e. $\dot{m}$=98.58 kg/s and T_{in}=130°C, while the region in which the circuit can operate being compliant with all the selected constraints at the given inlet coolant pressure is filled in green.

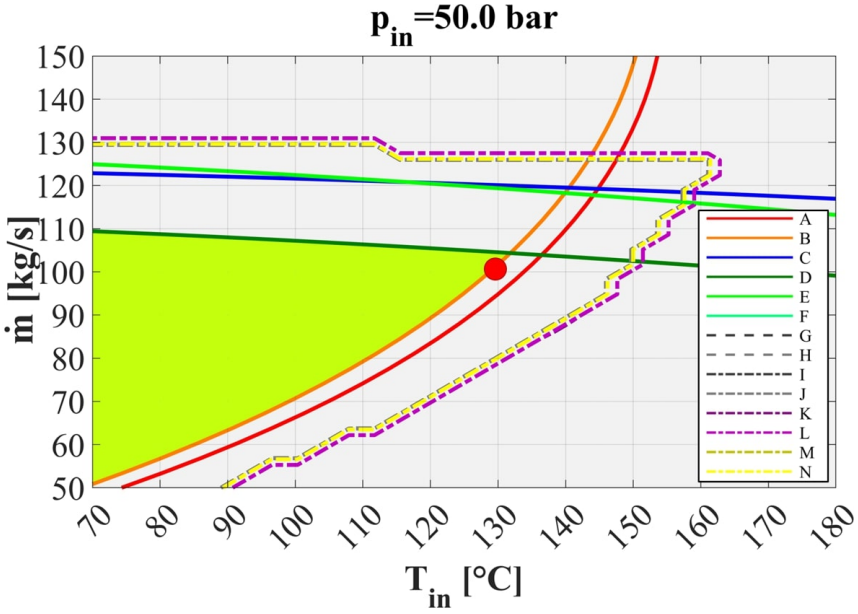

Figure 2.11: Range of acceptable operating conditions for the PFCs cooling circuit (2019 design, in green) and design operating point (in red).

A comparison between the results obtained by ADRANOS for the design operating point with those of the 3D-CFD analysis of [21] is reported in table 2.5. As it may be argued from the table, there is a very good prediction of the overall pressure drop, of the flow distribution between IVT and OVT, of the maximum fluid velocities that occur in the targets, and of the CHF margins, with maximum relative errors e_r below 3%. Furthermore, the results obtained with ADRANOS are conservative if compared to those of the detailed CFD calculations. These findings are not surprising since the ADRANOS simulations were set up on the basis of the results of the 3D-CFD analysis.

Table 2.5: Comparison between ADRANOS and CFD results.

	CFD	**ADRANOS**	**e_r [%]**
Δp_{tot} [bar]	9.40	9.43	0.32
$v_{max,OVT}$ [m/s]	14.91	15.09	1.21
$v_{max,IVT}$ [m/s]	13.18	13.22	0.30
$M_{CHF,OVT}$ [-]	1.47	1.43	-2.55
$M_{CHF,IVT}$ [-]	1.39	1.38	-1.15

It can also be argued that the design operating point is on the outer edge of the region in which the circuit can operate. The two constraints delimiting this region

are the CHF margin at the IVT and the maximum coolant velocity in the OVT PFU cooling channels. All other constraints are less relevant, including the temperatures in the PFUs, for which only approximate boundaries are shown in the figure, as the steady-state 2D thermal simulations were only performed in a small region of the $\dot{m} - T_{in}$ space, as already thoroughly discussed.

To further validate the FEM module, figure 2.12a shows the thermal field predicted by the ADRANOS tool for an OVT PFU considering the PFCs cooling circuit coolant under coolant design conditions and under an incident heat flux of 10 MW/m^2 (similar results are obtained for the IVT), with a maximum temperature value predicted in tungsten around 1100°C, in good agreement with the value reported in [6]. The temperature distribution inside an OVT PFU under an incident heat flux of 20 MW/m^2 is depicted instead in figure 2.12b (also in this case, a similar distribution is observed also for the IVT). Under this heat flux condition, the maximum temperature in tungsten is predicted to be approximately 2220°C.

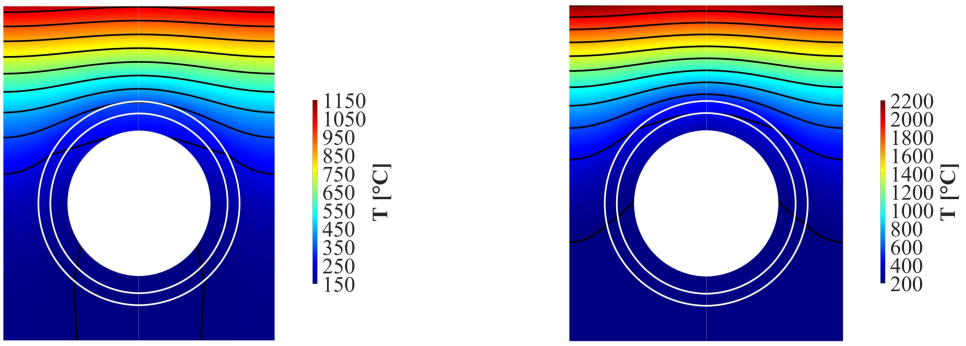

(a) (b)

Figure 2.12: Temperature distributions for an OVT PFU under an incident heat flux of 10 (a) and 20 (b) MW/m^2.

Further tests were carried out to assess how the results would change if PFUs with a height of 25 mm (and not 28 mm as in the reference case, so decreasing the thickness of tungsten in the plasma-facing region of 3 mm) were considered, in order to have additional validation tests to compare the results with. The maximum temperature values predicted in tungsten in this case were of approximately 830°C as visible in figure 2.13a, with a ≈6% deviation with respect to the results reported in [77]. For completeness, the results obtained with the 25 mm thick monoblock under the incident heat flux of 20 MW/m^2 are depicted in figure 2.13b, showing a maximum temperature in tungsten of around 1650°C.

As can be argued from the results shown in figure 2.12 and figure 2.13, increasing the monoblock thickness from 25 to 28 mm increases the maximum temperature by approximately 300°C for the 10 MW/m^2 case and approximately 600°C for the 20 MW/m^2 case.

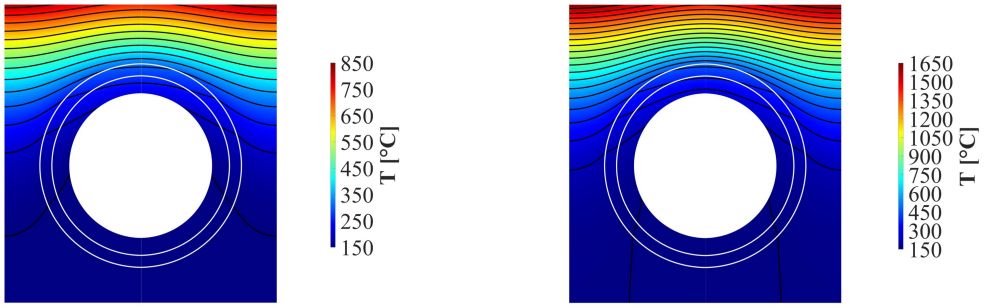

(a) (b)

Figure 2.13: Temperature distributions for a 25 mm OVT PFU under an incident heat flux of 10 (a) and 20 (b) MW/m^2.

Additionally, it can be noticed that under the 10 MW/m^2 heat flux condition, the maximum temperatures in the tungsten remain below the recrystallisation limit, being in the range of 1100-1500°C as reported in section 1.8, except for the sides of the plasma-facing surface.

2.3 Application of ADRANOS to the DEMO divertor cooling options

The ADRANOS tool was employed to study the performance map of both the DEMO divertor single-circuit cooling option and the PFCs circuit of the double-circuit cooling option with target connected both in series and in parallel.

As far as the CB cooling circuit relevant to the double-circuit cooling option is concerned, the results obtained with the ADRANOS tool are not reported here as they are of minor interest. In fact, for this specific cooling circuit, only the constraints on maximum pressure drop and minimum saturation margin apply. This latter parameter determines the possible range of acceptable coolant operating conditions, at least considering low coolant pressures. Additionally, the analyses of the CB cooling circuit showed that, with an inlet pressure of 35 bar, it is possible to go up to maximum inlet temperatures only slightly higher than 180 °C, highlighting how the cooling circuit is already working close to the best operating conditions compatible with the current design.

Moreover, to provide a reference scenario to compare the divertor cooling circuit thermal-hydraulic performance, a theoretical assessment of the limit coolant operating conditions is presented first, providing an indication of the highest coolant temperatures and mass flow rate values that can be selected for PFC cooling circuit, valid for both the single and double circuit concepts.

2.3.1 Theoretical assessment of limit operating conditions for VTs

Assuming that the considered cooling circuit has no hydraulic resistances, that the coolant is always at its inlet temperature, and that the fluid is distributed uniformly between the various PFU assemblies (this is the most favourable possible scenario, as the maximum available cooling potential is considered), it is possible to reformulate the CHF margin equation (2.8), taking into account the definition of the various terms as given in equations (2.9) to (2.11) and (2.14). Under the hypotheses of isothermal flow and no hydraulic losses, the only relevant constraints are the maximum coolant axial velocity inside the PFU cooling channels and the CHF margin. Substituting the limits on M_{CHF} and $\overline{v}$, it is thus possible to obtain a function $f(p,T) = 0$ that relates coolant pressure and temperature at which are met at the same time the conditions of $\overline{v} = \overline{v}_{limit}$ and $M_{CHF} = M_{CHF,limit}$. The resulting formulation is the following, where pressure and temperature are present both explicitly and implicitly, the latter through the dependence of water properties from p and T:

$$\rho^{0.4}\mu^{0.6}r + \Gamma_2 p^{1.8}\rho^{1.9}\mu^{0.1}\rho_v^{-1}c_p\left(T_{sat} - T\right) - \Gamma_1 = 0 \tag{2.22}$$

where

$$\Gamma_1 = \left(\frac{M_{CHF,limit}}{\overline{v}_{limit}^{0.4}}\right) q_w \left(\frac{0.132 f_p d_h^{0.28}}{C_f}\right), \tag{2.23}$$

and

$$\Gamma_2 = 1.302 \cdot 10^{-7}\overline{v}_{limit}^{0.5} d_h^{0.5}. \tag{2.24}$$

Equation (2.22) has two parameters, Γ_1 and Γ_2, which are not dependent on p and T and take into account the considered constraints, the design heat flux of the divertor PFCs, and the geometry of the monoblock.

Equation (2.22) is valid for a single target but it is still applicable when having two or more VTs in parallel, as it is analogous to increasing the number of PFU assemblies in parallel to each other. When, on the other hand, there are several targets in series, it should be noted that the margin against CHF should be calculated on the target with the largest number of PFU assemblies, where the fluid velocity is lower, while the constraint on the maximum axial velocity should be evaluated on the target with the smallest number of PFU assemblies, simply for the mass conservation constraint. It follows that the axial velocity at the VT with the lower number of PFU assemblies is equal to

$$\overline{v}_{limit}^{*} = \overline{v}_{limit}\frac{n_{min}}{n_{max}}, \tag{2.25}$$

where n_{min} and n_{max} are the minimum and maximum number of PFUs in the targets. By replacing $\overline{v}_{limit}$ with $\overline{v}^{*}_{limit}$ in equations (2.23) and (2.24), it is possible to obtain the temperature limits with targets in series, which is then achieved simply by reducing the coolant maximum axial velocity. By plotting this function, it is possible to derive the maximum inlet temperature of the coolant as its inlet pressure varies both for targets connected in series and in parallel, as depicted in the following pictures. It is moreover possible to study how the results vary as the model parameters change. In particular, figure 2.14 shows the trend of the maximum inlet temperature of the coolant as a function of its pressure at various heat flux values, both for the configuration with targets in parallel and in series.

As it can be argued from figure 2.14a, the maximum inlet coolant temperature value for the VTs in parallel, considering the current geometry and then nominal constraints, is approximately 150°C when considering water at 50 bar and 190°C at 75 bar. Concerning the targets in series, calculated considering the number of PFUs assemblies of the VTs for the 2021 divertor design, a limit temperature of 130°C is obtained when considering water at 50 bar and 160°C at 75 bar, as depicted in figure 2.14b. The reduction of the maximum coolant inlet temperature in this latter case can be derived from the condition of equation (2.25): for two VTs in series, the maximum velocity condition is reached at the IVT, while the limit CHF margin is reached at the OVT, due to the different number of PFU assemblies. To take into account both these conditions, equation (2.22) is applied to the OVT, and the maximum PFU cooling channel axial velocity in the OVT cooling channels is properly reduced. As an example, considering the number of PFUs assemblies for the VTs of the 2021 DEMO divertor and supposing a uniform coolant distribution among the different PFU assemblies for each target, a maximum coolant axial velocity of 16 m/s in the IVT would result in a coolant axial velocity of 11.83 m/s in the OVT, significantly lower than the original velocity limit.

It can also be noted that an increase in the maximum heat flux leads to a significant reduction in the maximum coolant inlet temperature. The same type of trend is expected by varying the f_p and the $M_{CHF,limit}$, as they are also present in the Γ_1 term with a unitary exponent. This can be easily interpreted as the product of the three terms $M_{CHF,limit} f_p q_w$ is equal to the incident critical heat flux. Additionally, it should be mentioned that these results are only qualitative, as it is possible to expect that at very high flux values, other constraints may come into play, e.g. the melting temperature in tungsten.

Figure 2.15 shows how the maximum coolant inlet temperature varies with the maximum coolant axial velocity, while figure 2.16 shows how the maximum temperature varies as the diameter of the PFUs cooling channels changes, keeping the f_p, and the ST thickness δ constant.

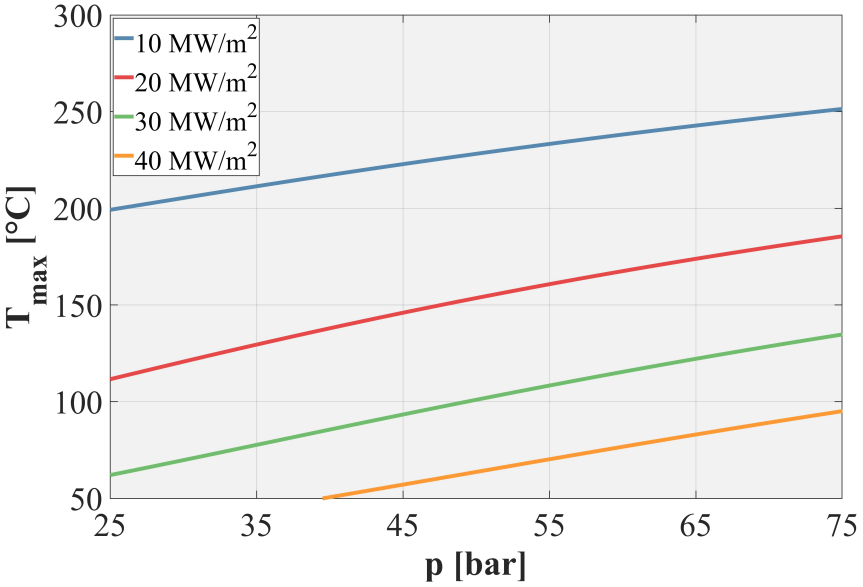

(a)

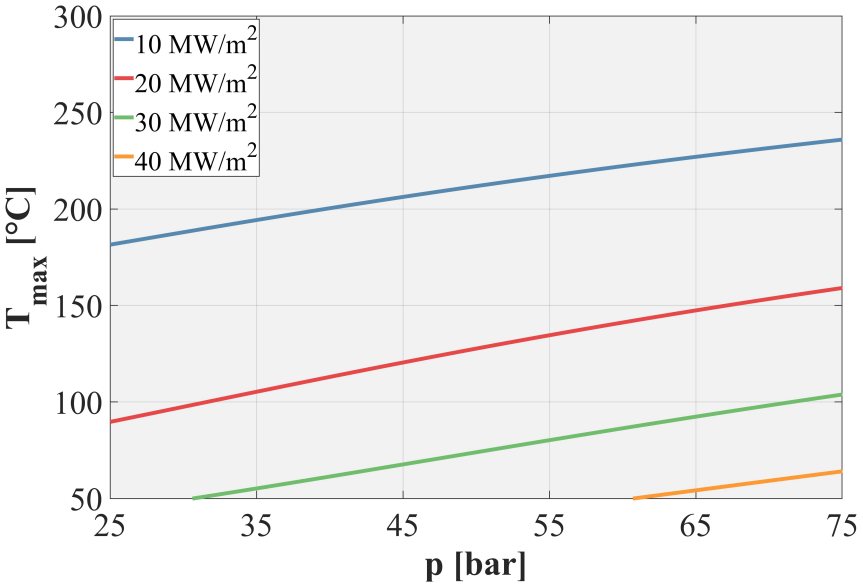

(b)

Figure 2.14: Maximum allowable inlet coolant temperature as a function of inlet coolant pressure for VTs connected in parallel (a) and in series (b), calculated at different maximum heat fluxes.

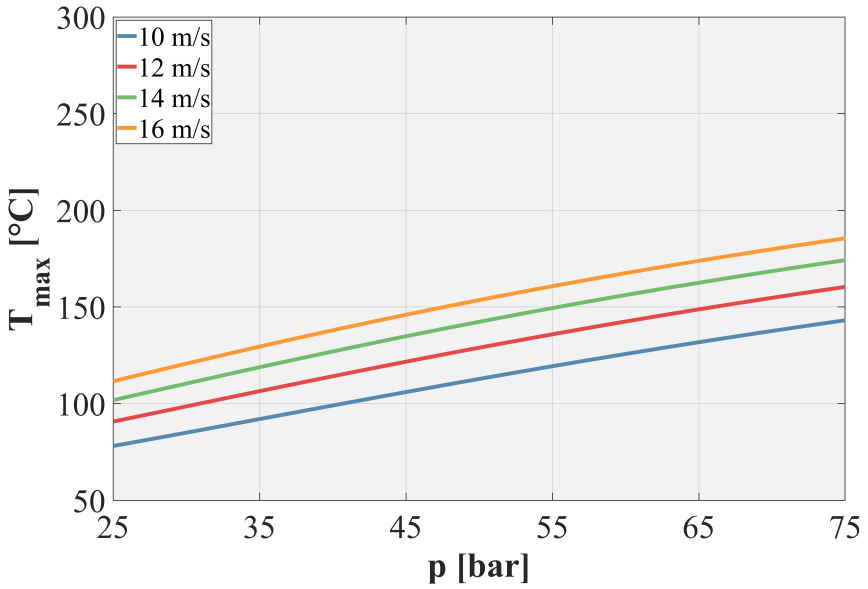

(a)

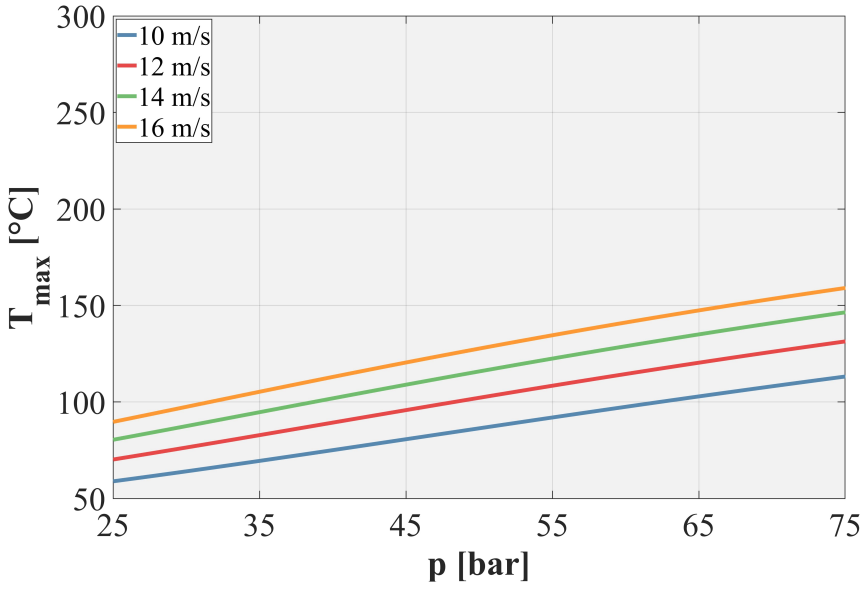

(b)

Figure 2.15: Maximum allowable inlet coolant temperature as a function of inlet coolant pressure for VTs connected in parallel (a) and in series (b), calculated at different maximum coolant axial velocities.

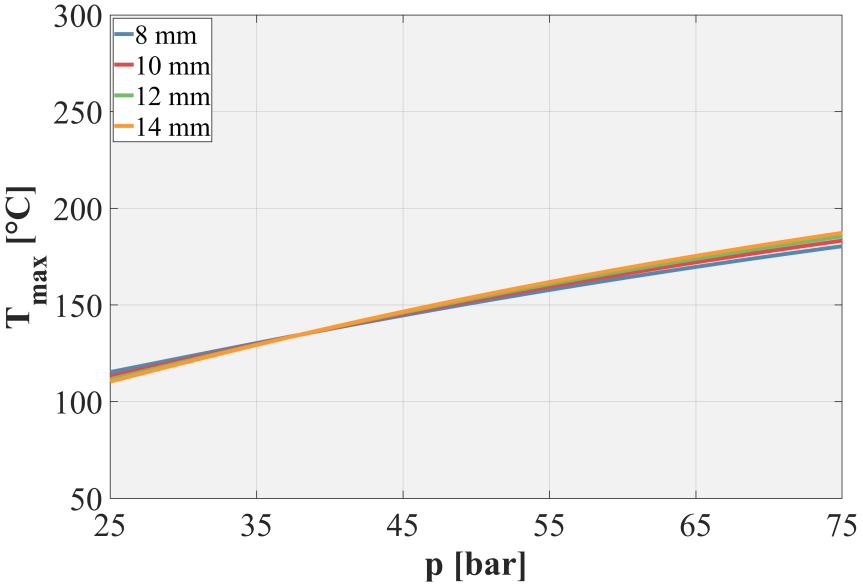

(a)

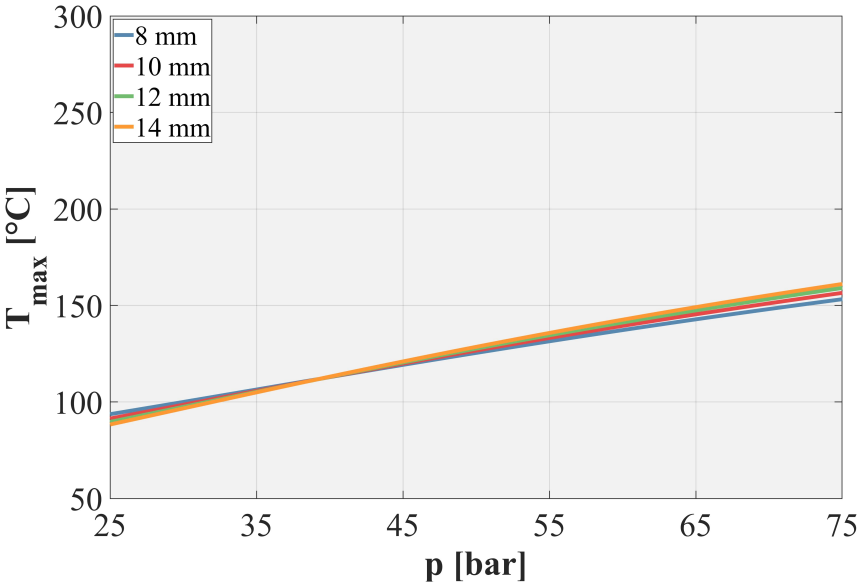

(b)

Figure 2.16: Maximum allowable inlet coolant temperature as a function of inlet coolant pressure for VTs connected in parallel (a) and in series (b), calculated at different PFUs cooling channels diameters.

The dependence on these parameters is more complex than the dependence on the heat flux, as it is present in both terms Γ_1 and Γ_2. It can be observed that a reduction in maximum coolant axial velocity always leads to a reduction in maximum coolant temperature, while for the diameter of PFUs cooling channels, the behaviour is much more complex, and it is found that for inlet pressure values below approximately 40 bar the use of cooling channels with smaller diameters is favoured to increase the coolant inlet temperature, while it is reversed at higher pressures. The same behaviour is observed for both VTs connected in series and in parallel. However, the sensitivity of the results from the latter parameter is very low compared to those analysed previously.

It should be pointed out that, under the hypothesis of no pressure loss for the cooling circuit and by taking into account only the constraints on maximum coolant axial velocity inside the PFU cooling channels and CHF margins, the other components of the divertor, i.e. CB, SL, RPs, and eventually NSs are not relevant, and thus the results drawn here for the VTs can be applied also to the single-circuit cooling option divertor.

2.3.2 DEMO divertor single-circuit cooling option

The parametric study of the DEMO divertor single-circuit cooling option was carried out starting from the cooling circuit layout and discretization shown in figure 2.17, referring to the results reported in [37] for the hydraulic characterisation.

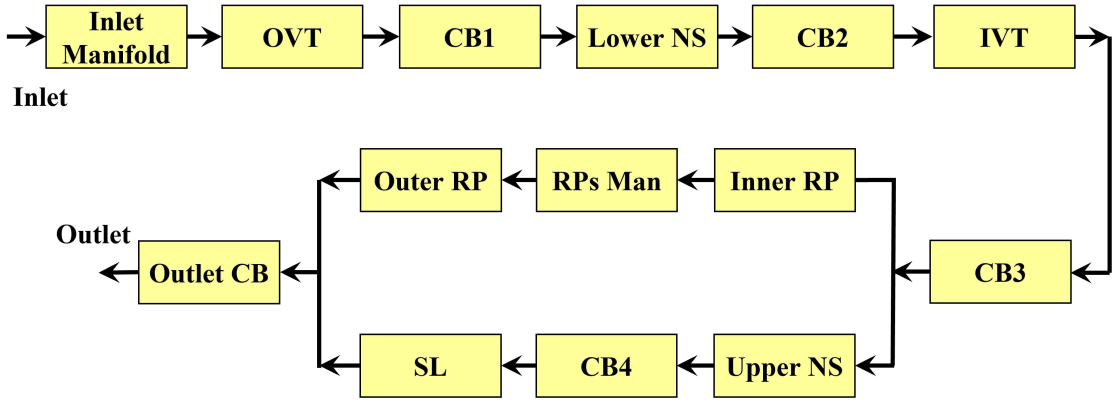

Figure 2.17: DEMO single-circuit cooling option divertor cassette ADRANOS volume discretization.

As for the validation case performed on the 2019 design, since the results were not available at different values of coolant mass flow rate, it was decided to adopt an exponent b for the characteristic function equal to 2. Regarding thermal loads, the same integral surface loads considered for the 2019 divertor were adopted, while volumetric loads obtained from dedicated neutronic analyses of the 2021 divertor design [40] were considered, whose breakdown is reported in table 2.6.

Table 2.6: Deposited volumetric power breakdown for each divertor cassette.

Component	**Power [MW]**
CB	0.717
SL	1.558
RPs	0.150
NSs	0.030
IVT	0.620
OVT	0.633
TOTAL	**3.707**

The analysis was performed considering the coolant inlet pressure at 50, 75, 100, and 150 bar varying the overall flow rate from 20 to 60 kg/s and the inlet temperature from 70 to 180°C. The selected inlet temperature and mass flow rate ranges were discretized with 30 points each, for a total of 3600 cases, while the overall run time to perform all the simulations was of approximately 24 minutes on a 3.00 GHz 18 core i9-9980XE workstation.

The results obtained are shown in figures 2.18 to 2.21, with reference to the constraints listed in table 2.4.

Many interesting conclusions can be drawn from the analysis of the results obtained. First of all, up to about 100 bar of coolant inlet pressure, the operating range of the cooling circuit is limited solely by the pressure drop and the CHF margin of the OVT. Unlike the PFCs circuit discussed in the previous section, in this case, the OVT is the critical component, as the two targets are now connected in series and the same mass flow rate is distributed across a greater number of PFUs cooling channels within the OVT, resulting in lower velocities (and thus lower heat transfer coefficients). At even higher pressures, however, the constraint on maximum CuCrZr temperature for the OVT at 10 MW/m^2 comes into play, which is more stringent than the CHF margin, ultimately limiting the maximum coolant inlet temperature to around 154°C.

It should be noted, however, that these results are only qualitative, as such a significant increase in coolant inlet pressure would certainly require a thorough overhaul of the entire DEMO divertor cassette, thus reducing the reliability of the maps presented here.

As it may be argued from the results, if the single-circuit cooling divertor option is chosen to work at lower pressures, i.e. 50 and 75 bar (possibly with no or minor changes in the component design), it would be possible to work with maximum inlet coolant temperatures of 85 and 115°C, respectively. Using the same reasoning on the maximum irradiation dose damage discussed in section 1.8 and the curves plotted in figure 1.28, it is therefore possible to estimate a component lifetime of approximately 0.6 and 0.8 FPY, respectively, which would clearly lead to an unduly reduction of the

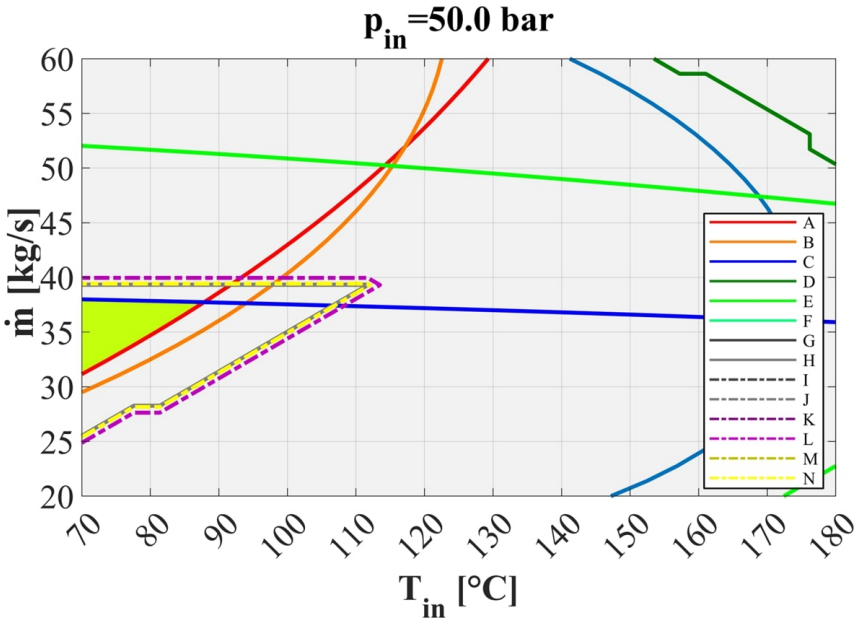

Figure 2.18: Range of acceptable operating conditions for the divertor single-circuit cooling option (in green) for an inlet pressure of 50 bar.

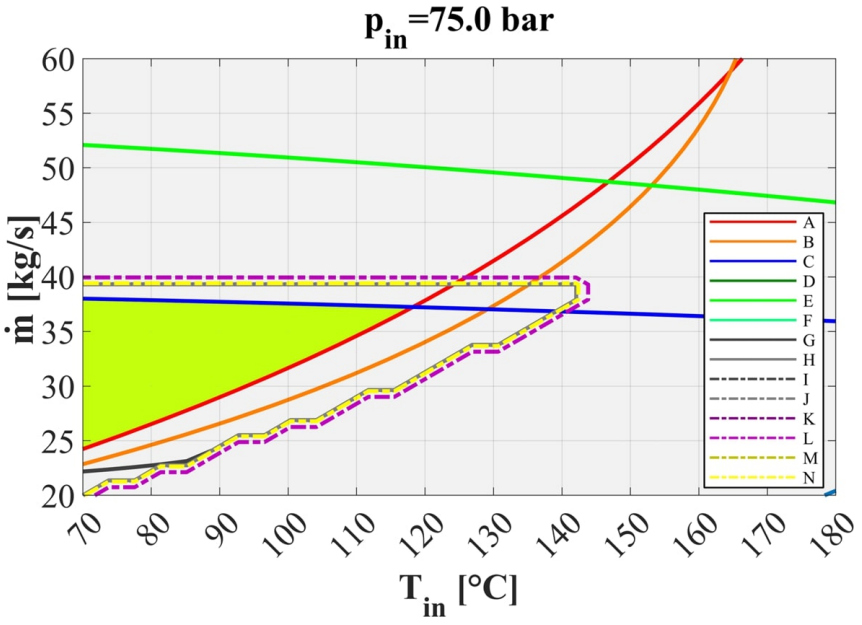

Figure 2.19: Range of acceptable operating conditions for the divertor single-circuit cooling option (in green) for an inlet pressure of 75 bar.

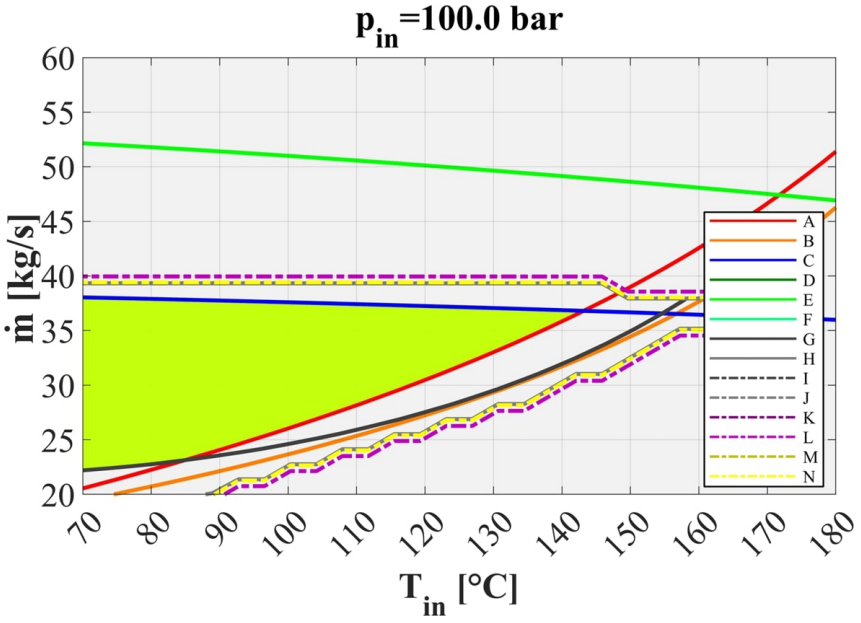

Figure 2.20: Range of acceptable operating conditions for the divertor single-circuit cooling option (in green) for an inlet pressure of 100 bar.

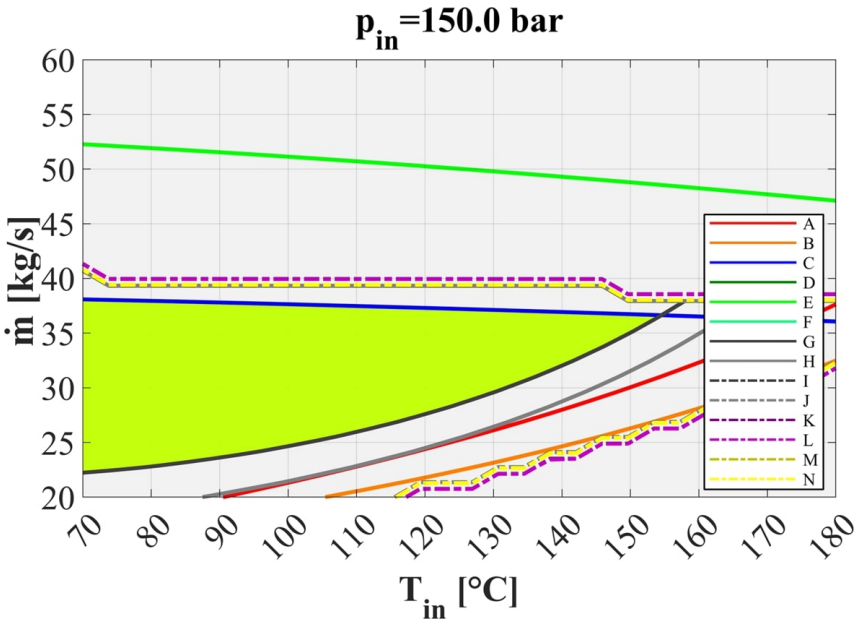

Figure 2.21: Range of acceptable operating conditions for the divertor single-circuit cooling option (in green) for an inlet pressure of 150 bar.

plant availability due to the frequent divertor cassettes replacements, an increased amount of nuclear waste, thus higher costs.

In order to provide an additional basis for assessing the feasibility of the single-circuit cooling option, four additional scenarios were evaluated, listed in the following.

Cooling circuit optimization

The first scenario foresees an optimisation of the cooling circuit to drastically reduce the total pressure drop. This scenario is highly unlikely, as most of the pressure drop occurs in the components directly exposed to the plasma (VTs, SL and RPs), which require high coolant velocities and small channel and channel sizes (thus resulting in high pressure drop) to handle the surface and volumetric loads to which they are subjected.

According to the results obtained, shown in the previous section, the maximum coolant operating temperature can certainly be increased, but only to a small extent. In fact, looking at figure 2.18 and figure 2.19, it can be seen how, in the absence of the pressure drop constraint, the acceptable operating region of the circuit would be delimited by the OVT CHF margin curve and the maximum velocity in the IVT PFU channels (curve E), as it was for the theoretical assessment of section 2.3.1.

This constraint was investigated by considering the limiting condition of a zero-loss cooling circuit but, differently from the theoretical case of section 2.3.1, here the coolant temperature increase is taken into account, together with the 5% non-uniformity of coolant velocity and CHF distributions in VTs The results obtained, depicted in figures 2.22 to 2.25, highlighted how at an inlet pressure of 50 bar it would be possible to reach up to 115°C coolant inlet temperature, and up to ≈150°C at 75 bar, while it is not possible in any case to overcome the maximum inlet temperature limit of 175°C due to CuCrZr constraints.

By performing additional parametric analyses, it is possible to assess the dependency of the results respectively on the two deviations from the theoretical model. The results obtained are not reported here, as they are very similar to those depicted in the following figures, but it can be observed that the heat loads have less influence on results than the non-uniformity in coolant distribution. This result is not surprising, as non-uniformities lead to a direct shift in both the CHF margin and maximum coolant axial velocity curves, while the effect of thermal loads is less pronounced. In fact, the coolant axial velocity inside the IVT PFU cooling channels increases due to density variations with temperature (low in the case of high mass flow rates), while the OVT CHF margin is affected uniquely by the power deposited on the OVT, being the first component exposed to high thermal loads in the divertor cassette cooling circuit. More realistically, an optimisation of the hydraulic circuit could allow an increase in operating temperature of only a few degrees, not solving

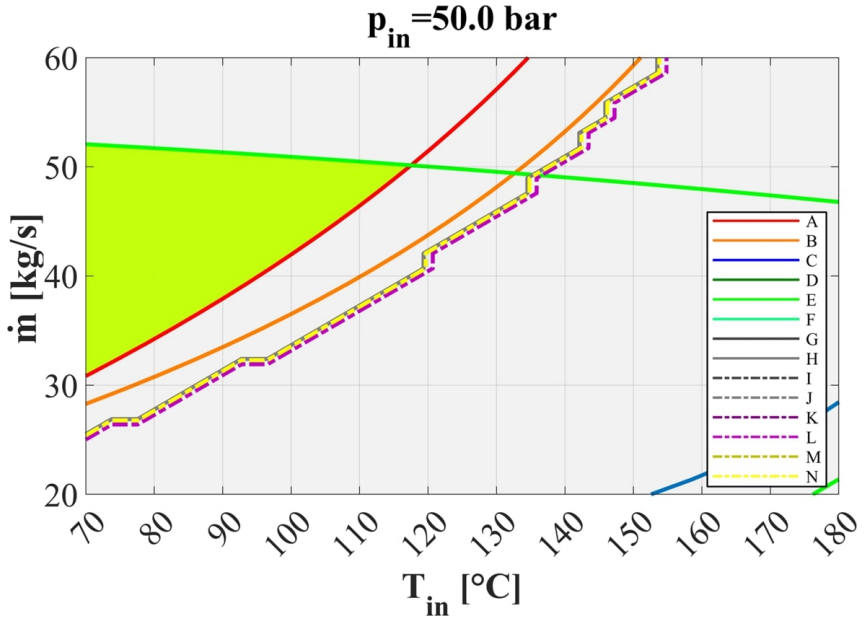

Figure 2.22: Range of acceptable operating conditions for the no-loss divertor single-circuit cooling option (in green) for an inlet pressure of 50 bar.

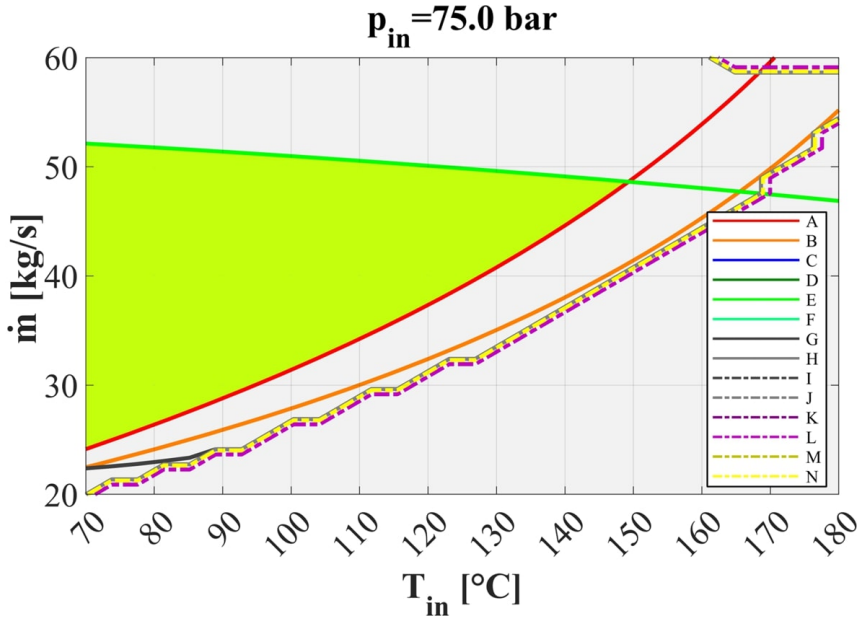

Figure 2.23: Range of acceptable operating conditions for the no-loss divertor single-circuit cooling option (in green) for an inlet pressure of 75 bar.

the issues related to the component lifetime. Additionally, it is interesting to note the shift in the CHF margin curves (A and B) from their analogues seen in the previous section, due to the dependence of CHF on pressure, detailed in equation (2.8). In particular, the CHF margin curves are shifted towards higher temperatures, and the effect is particularly visible for the IVT, characterized by a lower coolant pressure due to its position inside the cooling circuit (downstream the OVT and part of the CB).

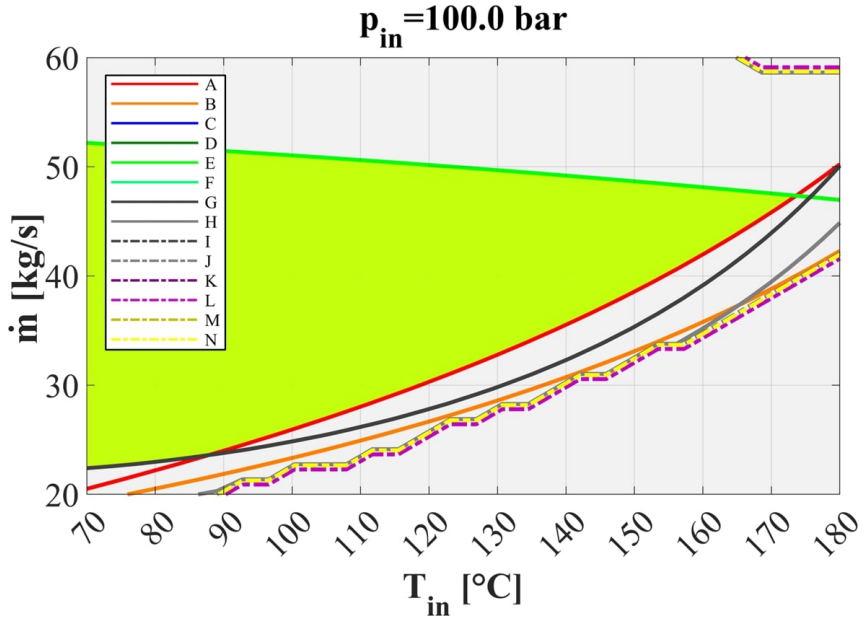

Figure 2.24: Range of acceptable operating conditions for the no-loss divertor single-circuit cooling option (in green) for an inlet pressure of 100 bar.

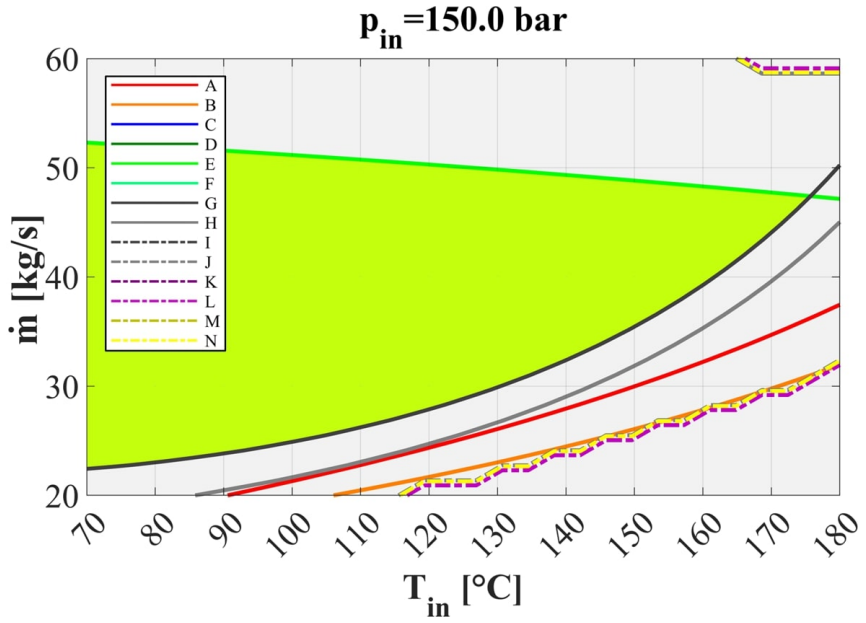

Figure 2.25: Range of acceptable operating conditions for the no-loss divertor single-circuit cooling option (in green) for an inlet pressure of 150 bar.

VTs in parallel

The second scenario investigated relies on the adoption of a parallel connection between the two VTs, as in the case of the PFC cooling circuit of the 2019 DEMO divertor double-circuit cooling option design. The cooling scheme adopted as reference is shown in figure 2.26, while loads, characteristic curves and assumptions are the same as those used for the single-circuit cooling option calculation with the divertor targets in series.

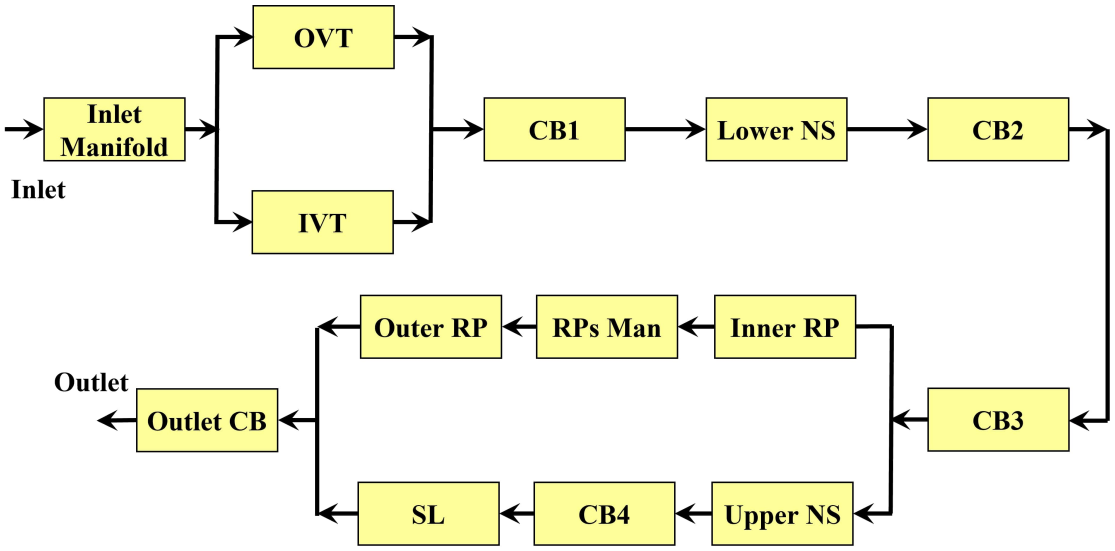

Figure 2.26: Cooling scheme and ADRANOS volume discretization of the DEMO divertor single-circuit cooling option with VTs in parallel.

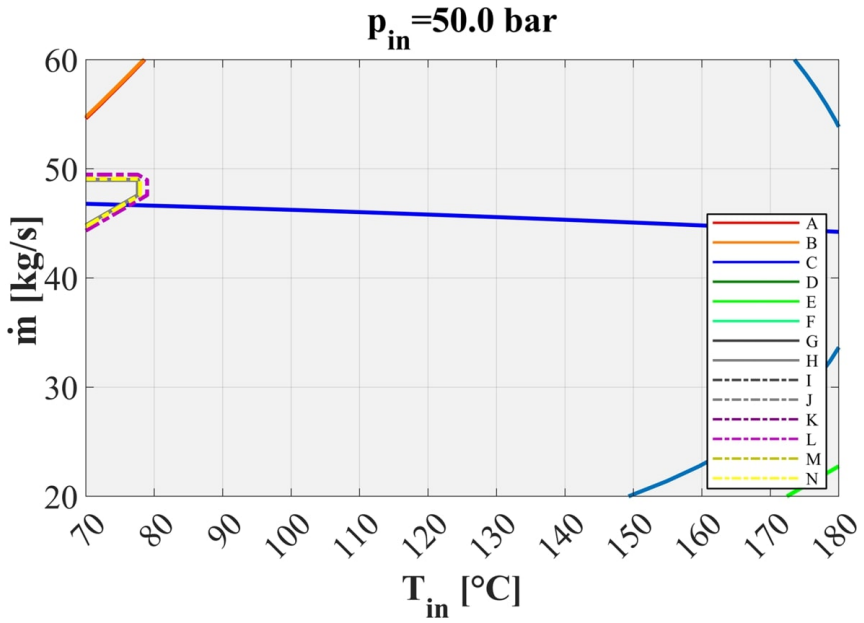

Figure 2.27: Range of acceptable operating conditions for the single-circuit cooling option divertor with VTs in parallel (in green) for an inlet pressure of 50 bar.

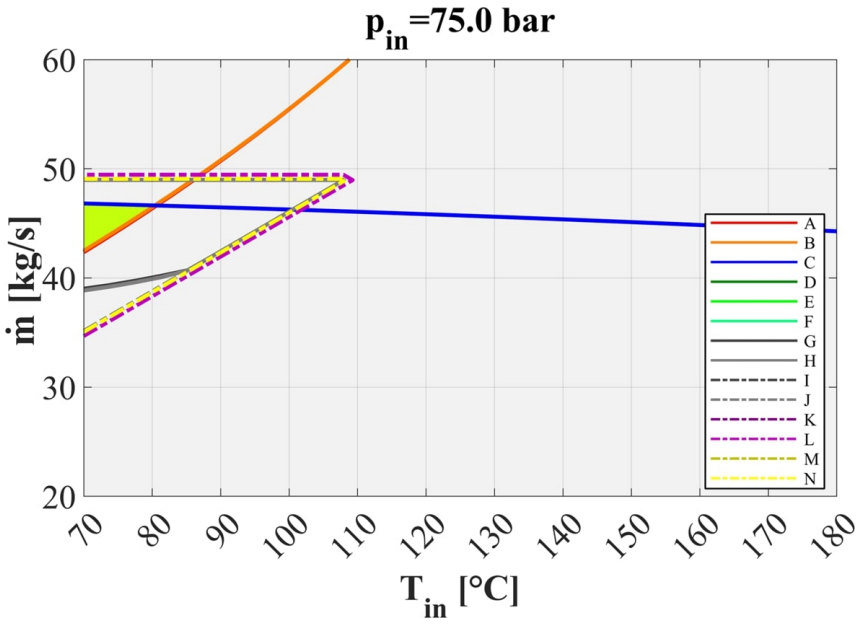

Figure 2.28: Range of acceptable operating conditions for the single-circuit cooling option divertor with VTs in parallel (in green) for an inlet pressure of 75 bar.

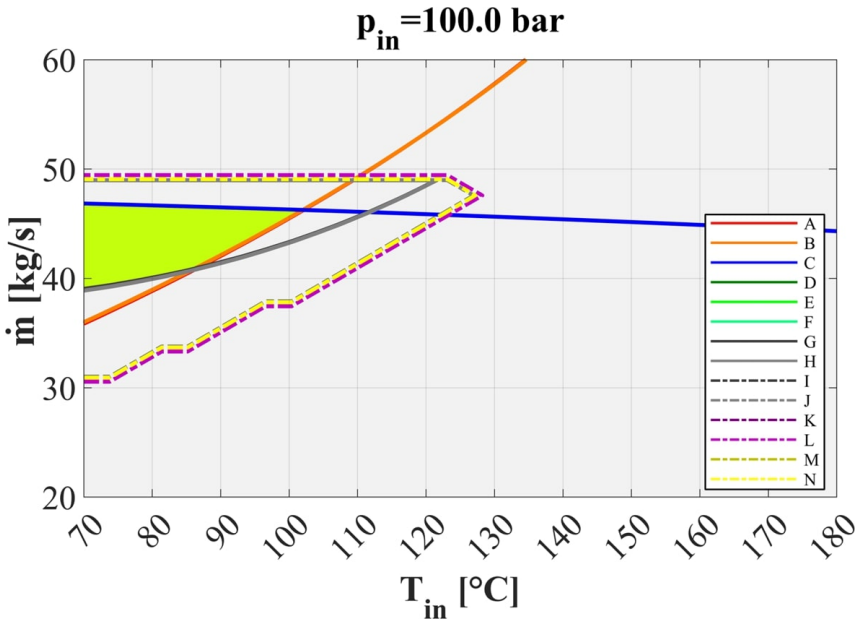

Figure 2.29: Range of acceptable operating conditions for the single-circuit cooling option divertor with VTs in parallel (in green) for an inlet pressure of 100 bar.

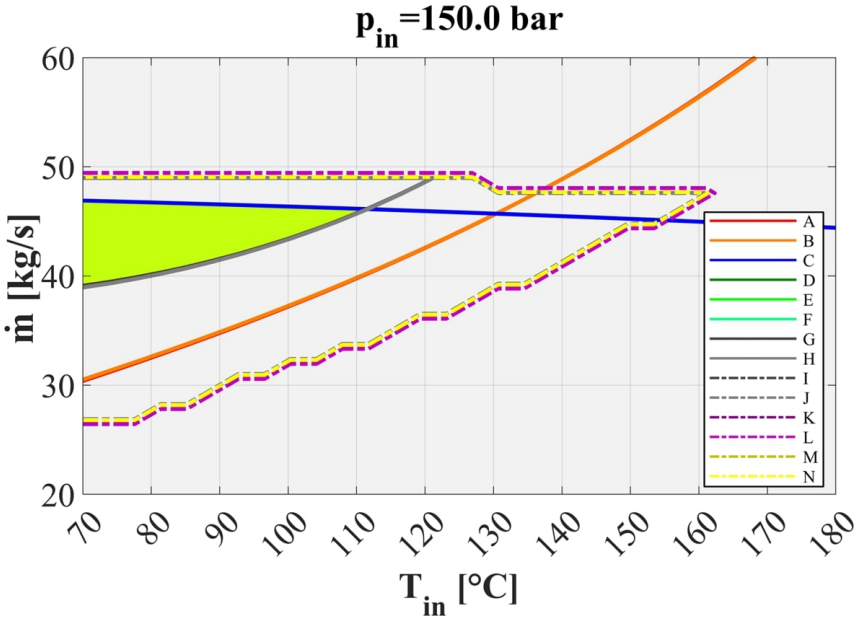

Figure 2.30: Range of acceptable operating conditions for the single-circuit cooling option divertor with VTs in parallel (in green) for an inlet pressure of 150 bar.

The results obtained showed that considering an inlet coolant pressure of 50 bar, no acceptable operating condition can be found for the circuit, as visible in figure 2.27. The results relevant to the inlet coolant pressure of 75, 100, and 150 bar condition are depicted in figure 2.28, figure 2.29, and figure 2.30.

As can be seen from the pictures, the single-circuit cooling option with VTs in parallel allows operation only at even lower coolant temperatures with respect to the configuration with targets in series. By further increasing the inlet pressure of the coolant up to 150 bar, it is possible to increase the inlet temperature up to a maximum of about 115°C, beyond which the constraint of the maximum temperature in the CuCrZr comes into play.

CB bypass

The third scenario analysed involves the presence of a bypass line which ensures that only part of the coolant mass flow rate is fed to the CB, while maintaining full flow rate at the VTs, in order to prevent the CHF limit curves from moving further to the left (with reference to the previous maps), reducing the region in which the cooling circuit can operate.

In the case of series-connected VTs, this is equivalent to a relaxation of the maximum pressure drop constraint, so the results obtained are similar to those of the first scenario, i.e. the cooling circuit optimization, thus no further investigations were performed. In the case of targets in parallel, on the other hand, reference is made to the cooling scheme shown in figure 2.31, where the bypass line is shown in red.

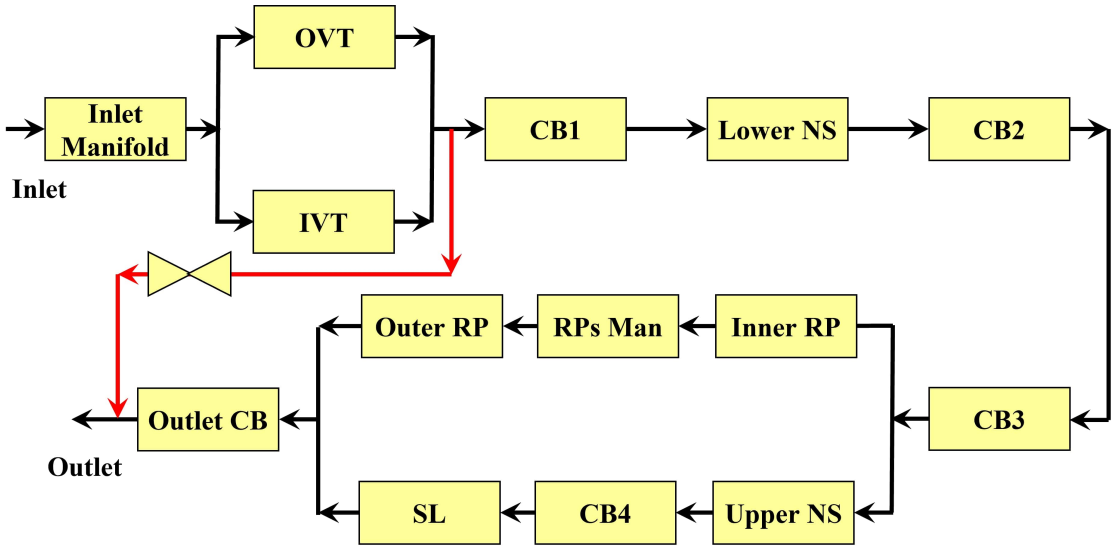

Figure 2.31: Cooling scheme and ADRANOS volume discretization of the DEMO divertor single-circuit cooling option with VTs in parallel and CB bypass.

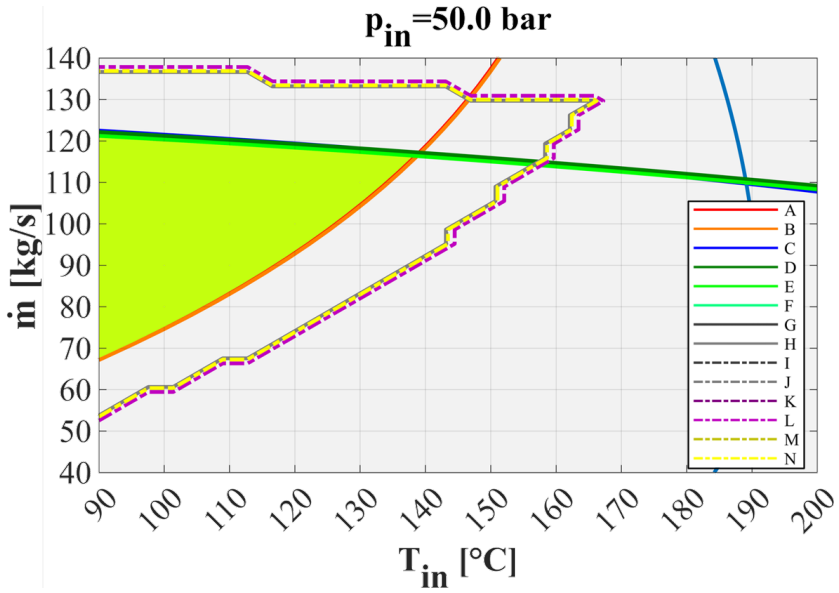

Figure 2.32: Range of acceptable operating conditions for the single-circuit cooling option divertor with VTs in parallel and CB bypass (in green) for an inlet pressure of 50 bar.

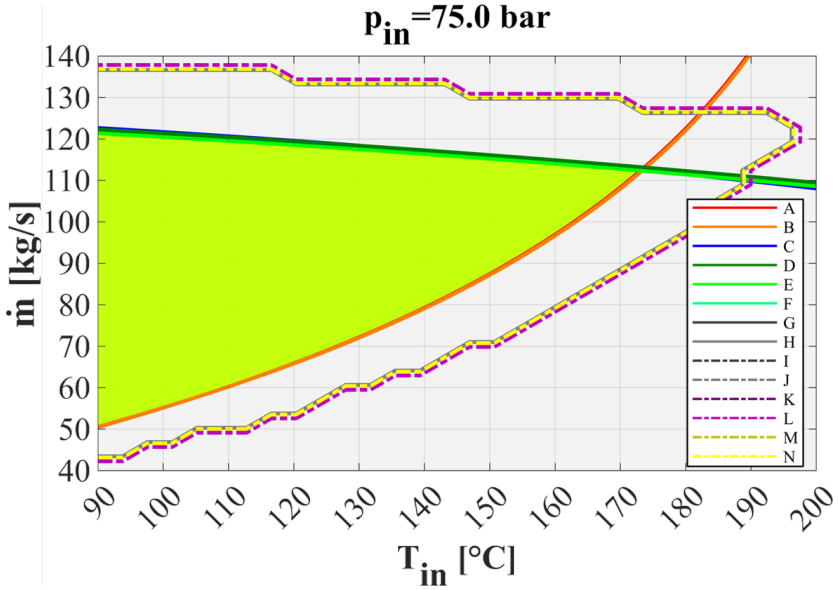

Figure 2.33: Range of acceptable operating conditions for the single-circuit cooling option divertor with VTs in parallel and CB bypass (in green) for an inlet pressure of 75 bar.

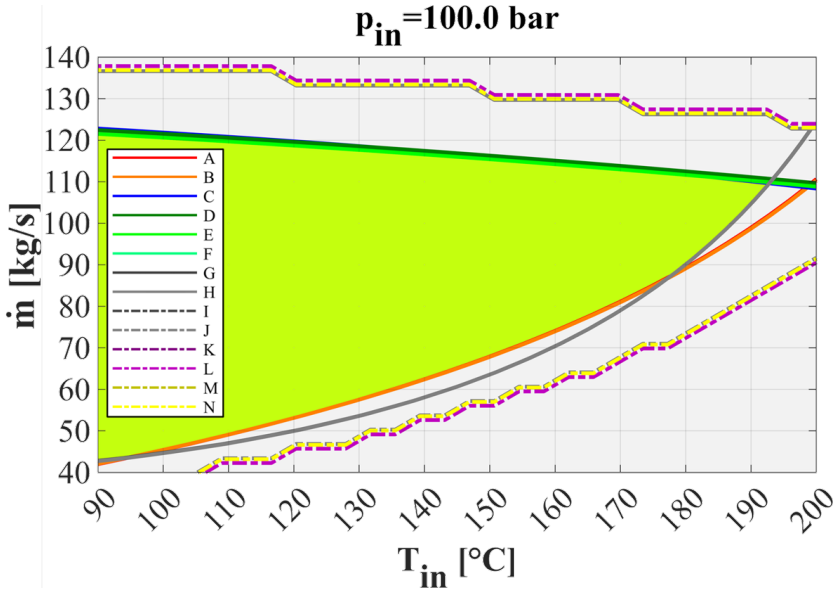

Figure 2.34: Range of acceptable operating conditions for the single-circuit cooling option divertor with VTs in parallel and CB bypass (in green) for an inlet pressure of 100 bar.

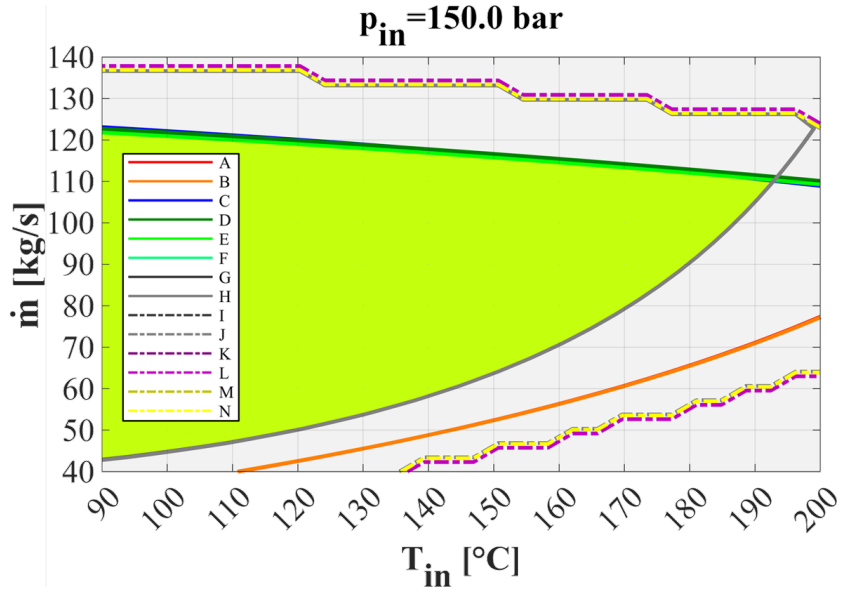

Figure 2.35: Range of acceptable operating conditions for the single-circuit cooling option divertor with VTs in parallel and CB bypass (in green) for an inlet pressure of 150 bar.

The bypass line was modelled by imposing a fixed mass flow rate through the CB equal to 35 kg/s for all the operating conditions of the map, a value close to the one adopted for the double-circuit cooling option divertor CB [26], so to provide adequate cooling to the components.

The results obtained are reported in figures 2.32 to 2.35. As can be seen, comparing the results shown here with those of the previous section, the gain obtained with the CB bypass is remarkable, with a maximum value of coolant inlet temperature of about 135°C at 50 bar, 175°C at 75 bar, and 195°C at higher coolant inlet pressure values due to CuCrZr temperature constraints. Although this configuration appears promising, some additional issues should be considered: it is necessary to provide for the adoption of properly sized orifices downstream of the targets, capable of producing a localized pressure loss of ≈7 bar, resulting in high localized coolant velocities that could cause erosion problems. Moreover, considering the coolant operating point at the maximum allowable coolant inlet temperature of figure 2.34, the orifice alone would result in a loss of fluid mechanical power in the order of ≈60 kW per cassette (approximately equal to the 50% of the pumping power required by both the CB and PFC cooling circuit of the double-circuit configuration [6]), which would have to be supplied to the fluid by the circulation pumps. Finally, it should be further investigated the behaviour of the cooling circuit under transient conditions, and the possibility to establish flow distribution instabilities between the CB and the bypass line, which could potentially pose a risk for the structural integrity of the cassette.

Cooling circuit optimization with VTs in parallel

Finally, the last scenario focussed on a hypothetical optimization of the cooling circuit with the VTs in parallel, aimed at reducing the total pressure drop. As for the case of targets in series, the limiting condition of a zero-loss cooling circuit was considered.

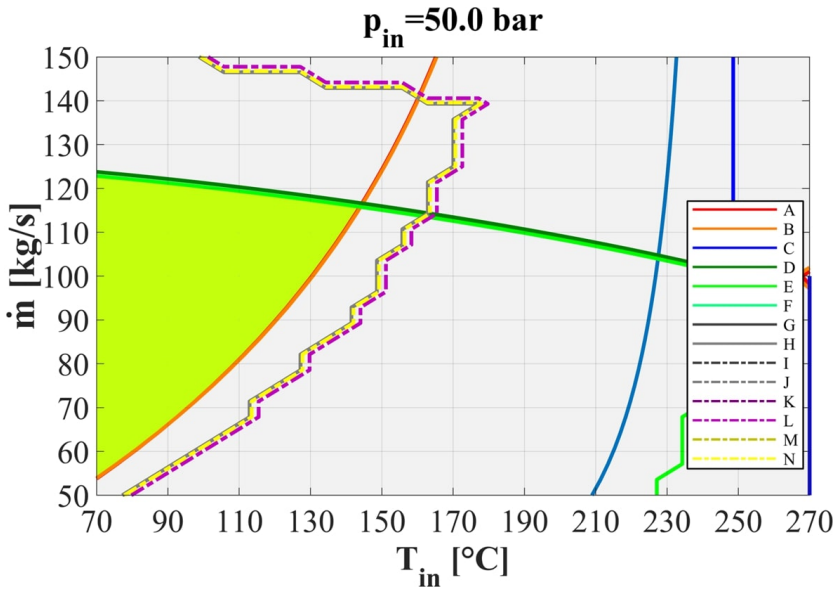

Figure 2.36: Range of acceptable operating conditions for the no-loss single-circuit cooling option divertor with VTs in parallel (in green) for an inlet pressure of 50 bar.

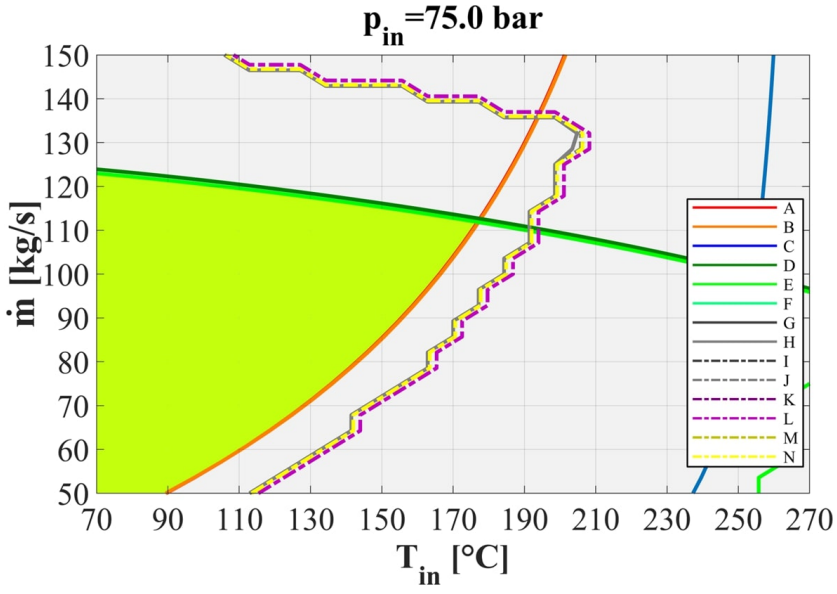

Figure 2.37: Range of acceptable operating conditions for the no-loss single-circuit cooling option divertor with VTs in parallel (in green) for an inlet pressure of 75 bar.

The results obtained, depicted in figures 2.36 to 2.39, show that considering an inlet pressure of 50 bar it would be possible to reach up to 145°C coolant inlet

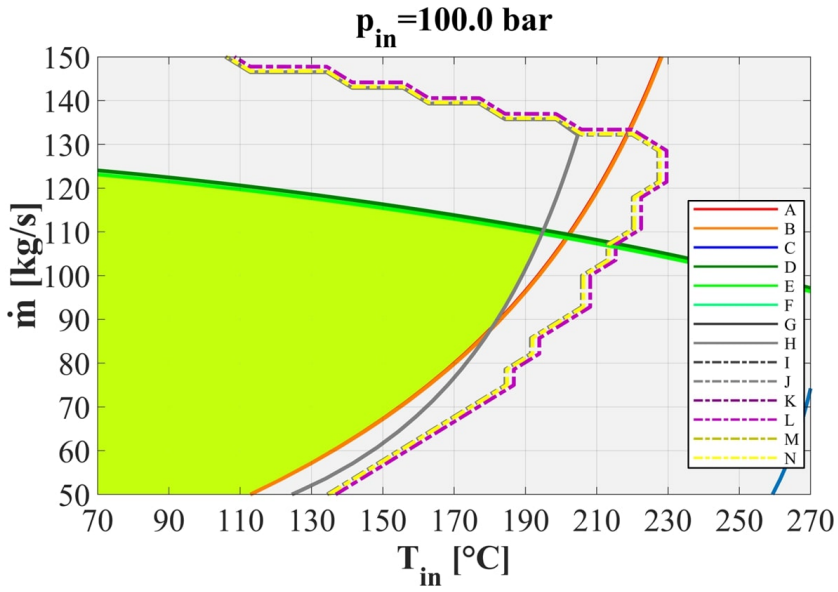

Figure 2.38: Range of acceptable operating conditions for the no-loss single-circuit cooling option divertor with VTs in parallel (in green) for an inlet pressure of 100 bar.

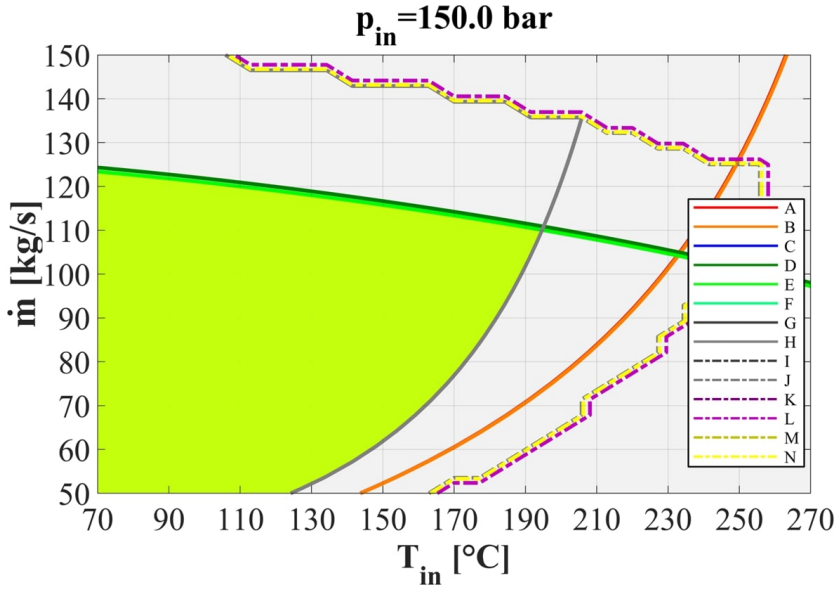

Figure 2.39: Range of acceptable operating conditions for the no-loss single-circuit cooling option divertor with VTs in parallel (in green) for an inlet pressure of 150 bar.

temperature, and up to ≈180°C at 75 bar, while it is not possible in any case to overcome the maximum inlet temperature limit of 195°C due to CuCrZr constraints, as for the case discussed in the previous sections.

These results shown here are in line with the theoretical limits discussed in section 2.3.1. Moreover, as for the scenario of cooling circuit optimization with targets in series, the reduction of coolant maximum inlet temperature is mainly related to the 5% coolant velocity and CHF margin distribution non-uniformities, while the effects of the heat loads are practically negligible.

In summary, the results obtained in terms of maximum coolant inlet temperature considering the baseline topology of the DEMO divertor single-circuit cooling option and the four additional scenarios discussed above are summarised in table 2.7, together with the pertaining theoretical limits.

Table 2.7: Summary of the results obtained for the different DEMO divertor single-circuit cooling option cooling circuit topologies.

Maximum coolant inlet temperature			
Scenario	p_{in}=50 bar	p_{in}=75 bar	Max
Theoretical series	≈128°C	≈159°C	-
Baseline	≈85°C	≈115°C	≈155°C
Baseline optimization	≈115°C	≈145°C	≈175°C
Theoretical parallel	≈154°C	≈186°C	-
Parallel VTs	-	≈80°C	≈115°C
Parallel VTs and Bypass	≈135°C	≈175°C	≈190°C
Parallel VTs optimization	≈145°C	≈180°C	≈195°C

The cooling circuit optimisation scenarios return excessively optimistic outcomes and are reported only to allow for simple comparison with the pertaining theoretical limits. Concerning the different cooling circuit arrangements, excepting for the scenario with targets connected in parallel and CB bypass, it can be clearly observed that it is not possible to exceed a maximum coolant inlet temperature of 120°C for coolant inlet pressures up to 75 bar, while temperatures lower than 85°C are required at 50 bar inlet pressure. Under these conditions, according to the lifetime estimation described in section 1.8, the divertor cassette needs replacement every 0.6 and 0.8 FPY, respectively considering 50 and 75 bar as inlet coolant pressure conditions.

The most promising single-circuit divertor cooling circuit arrangement is the one with targets in parallel and CB bypass, which permits to adoption of coolant conditions close to the theoretical limits, allowing for a coolant maximum inlet temperatures approximately of 135 and 175°C, respectively for an inlet pressure of 50 and 75 bar. Under these conditions, the lifetime of the divertor cassette can be extended up to 0.9 and 1.1 FPY, depending on the coolant inlet pressure.

At higher pressures it is feasible to increase these values, but, as can be argued

from the summary table, it is never possible to obtain the same inlet temperature of the CB circuit as in the double-circuit cooling option configuration, except for the configuration with VTs in parallel and CB bypass, which would entail the criticality of providing suitable orifices to reduce the pressure in the bypass line, with potential issues in terms of erosion and coolant distribution instabilities, as well as an increase in pumping power.

As already pointed out, the analyses carried out only take into account aspects of thermal-hydraulics and, therefore, increases in coolant inlet pressure must necessarily be accompanied by a review of the design of the divertor to ensure its structural integrity. It is reasonable to argue that if a coolant pressure much higher than the current one (e.g. 100 bar or above) is considered, the results obtained would lose their relevance, as modifications would be required to the PFUs cooling channels which would change their thermal and hydraulic behaviour.

Focusing on a narrower pressure range (e.g. below 75 bar), it can be seen that the maximum coolant temperature is solely determined by three constraints, i.e. the pressure drop, the CHF margin, and the maximum velocity in the PFUs cooling channels, while in the case of assuming a no-pressure-loss cooling circuit, solely by the last two conditions.

2.3.3 DEMO divertor double-circuit cooling option - PFC cooling circuit

The last topic dealt with in this chapter is the analysis of the operational map of the PFCs cooling circuit of the divertor double-circuit cooling option, considering two different layouts: the one with the VTs connected in parallel, i.e. the 2019 layout already discussed in the chapter 1, and a new design, presented in 2022, which is characterised by the series connection of the two targets. The analysis was carried out using ADRANOS, with the aim of defining a rationale for the selection of acceptable operating conditions for the divertor cooling circuit, questioning the constraints used to date and assuming a possible increase in heat flux under slow-transient conditions to which the component could be subjected.

The parametric analyses took into account realistic thermal loads of the divertor VTs, based on the latest DEMO energy map, reported in [78]. Additionally, the analyses considered the realistic pressure drops of both the VTs cooling circuits drawn from dedicated 3D-CFD analyses ([21] and [79]) and of the PFCs PHTS. Regarding the VT power distribution, a steady-state peaked plasma heat flux of 10 MW/m^2 was considered, representative of normal operating conditions, while three different slow-transient heat load scenarios were evaluated, namely 20, 25 and 30 MW/m^2, to assess how the maximum plasma heat fluxes expected during plasma operation may influence the operating map.

As already discussed, the ADRANOS code provides necessary but not sufficient conditions to assess the complete performance of the component, which must be successively verified in terms of structural response and expected lifetime due to neutron-induced damage of the PFUs and their supporting structures.

The attention was at first focused on the 2022 PFCs divertor cooling circuit design, described in [80], which features a dedicated cooling circuit for the two VTs, which are connected in series. The analyses were performed by considering the list of constraints already discussed in section 1.8, also taking into account the additional aspects summarized in the following.

- Maximum CHF margins higher than 1.4 were checked both for the IVT and the OVT, considering the incident heat flux selected for the specific scenario (20, 25 and 30 MW/m^2). Additionally, a scenario with CHF margins higher than 1.2 was included, to reduce the conservativeness of this constraint, allowing the component to operate at higher heat fluxes, otherwise unachievable. The CHF margins are conservatively calculated at the outlet of the ST section of the VTs, so as to account for possible controlled or uncontrolled displacements of the strike point.
- A maximum allowable total pressure drop curve, to be considered as the maximum net value that can be spent inside the VTs cooling circuit, as reported in figure 2.40, was obtained supposing a pump head water column for the PFCs PHTS of 230 m and taking into account the pressure drop inside the PHTS itself. The data reported in figure 2.40 were obtained by considering the PHTS layout reported in [56], calculated according to the methodology presented in [81]. It should be noted that, at low mass flow rates, a reduction of the size of the various pipes and equipment of the PHTS was performed, maintaining a minimum PHTS pressure drop of ≈5 bar while ensuring a reduction in water inventory, as depicted in figure 2.41.
- A maximum coolant axial velocity inside the PFUs cooling channels of 16, 12 and 10 m/s was considered. These three values were selected to provide potential limits, in the case fretting issues and flow-induced corrosion are proven to pose a risk to the component integrity and are calculated both for the IVT and OVT.
- A maximum temperatures for CuCrZr cooling channels lower than 450°C was considered also for heat fluxes higher than 20 MW/m^2.
- The temperature limit of tungsten has been selected equal to its melting temperature, i.e. 3422°C, to avoid unduly conservative results.

The operating map of the PFCs cooling circuit with targets connected in series was calculated by considering the inlet coolant temperature ranging between 70 and 180°C, the coolant mass flow rate between 10 and 60 kg/s, and the coolant inlet

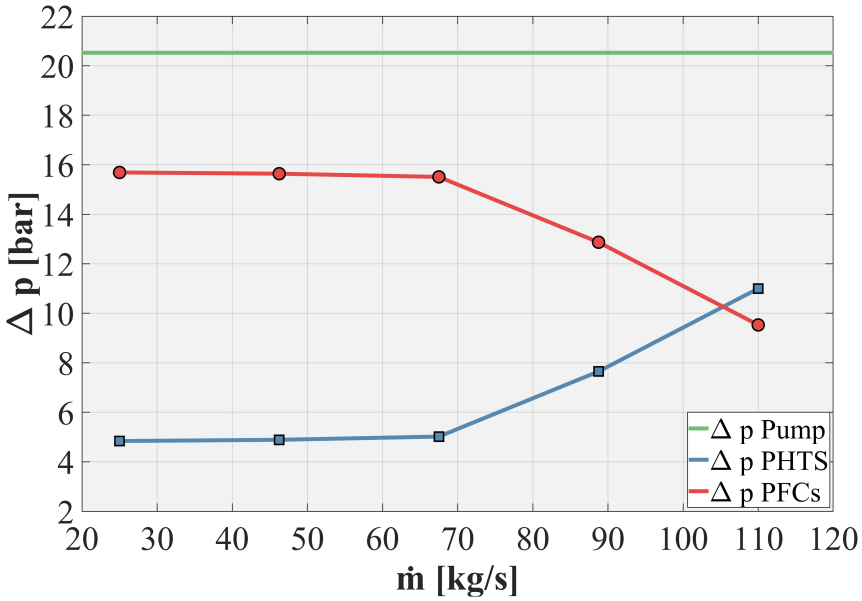

Figure 2.40: Curves of maximum pressure drop provided by the pump (green), pressure drop due to PHTS losses (blue) and pressure drop available for the PFCs cooling circuit (red). The mass flow rates are relevant to a single divertor cassette.

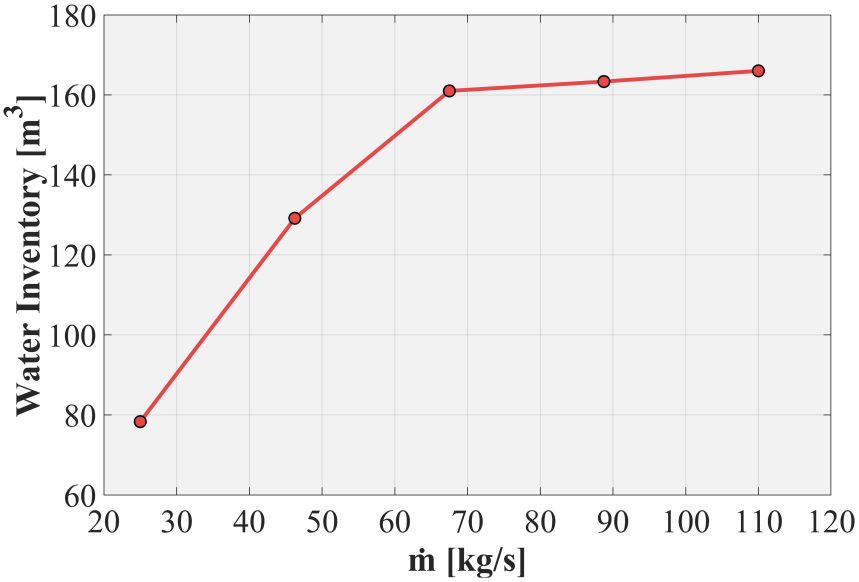

Figure 2.41: Total PFC PHTS water inventory for the different mass flow rates considered. The mass flow rates are relevant to a single divertor cassette.

pressure between 50 and 75 bar. The results obtained are depicted in figure 2.42 and figure 2.43 for the 20 MW/m^2 case, where it is possible to distinguish a green region, in which the cooling circuit can operate in compliance with all the constraints and with a CHF margin higher or equal to 1.4 and a yellow region, in which the cooling circuit can operate with a CHF margin between 1.2 and 1.4.

The results are presented for two different values of inlet pressure (50 and 75 bar) and for the three maximum axial coolant velocities inside the PFU cooling channels of 16, 12 and 10 m/s (top, middle and bottom rows, respectively). Additionally, the curve CHF equal to 1 has been included with a dashed line and should be intended as an indication to evaluate whether the loss of coolant event from one of the pumps of the PFC PHTS may lead the system to a mass flow rate value that could start thermal crisis of the cooling channels.

As may be argued from the results, the green and yellow regions of the maps are delimited uniquely by the CHF margin at the OVT (red curve) and by the maximum axial coolant velocity inside the IVT PFU cooling channels (light green curve), analogously to the results of the single-circuit cooling option.

It is also interesting to note that although the IVT is fed with a coolant that is at a lower pressure and higher temperature, this does not constitute a critical issue for the circuit, as the critical target in terms of margin against CHF remains the OVT. Note also in figure 2.42 how, at low coolant inlet pressure values, there is a crossing of the CHF margin curves of the IVT and OVT, linked precisely to the phenomenon just described, i.e. the degradation of the cooling performance of the IVT cooling circuit related to variations in coolant pressure and temperature.

In case fretting and flow-induced corrosion phenomena are not critical for the component, or at least not critical with respect to the expected lifetime of the divertor, the green and yellow regions of the map would be still limited by the pressure drop curve (blue line), which is only slightly higher than the maximum velocity in the PFU cooling channels of 16 m/s.

As can be argued from the picture, the green and yellow regions decrease in amplitude as the maximum coolant PFU cooling channel axial velocity decreases (the green region disappears completely at 50 bar coolant inlet pressure and 10 m/s) and become more extended as the coolant inlet pressure increases. In particular, considering the intermediate limit value of the maximum PFU coolant axial velocity (12 m/s), at 20 MW/m^2 it is possible to operate in the green area at all the coolant inlet pressure values in a range of mass flow rates between 26 and 39 kg/s and a temperature lower than 112°C, while in the yellow area at all the considered pressures (50 to 75 bar) at temperatures lower than 130°C and mass flow rates in between 22 and 39 kg/s.

The choice of operating conditions within the green region then has to be based on several additional considerations, herewith summarized.

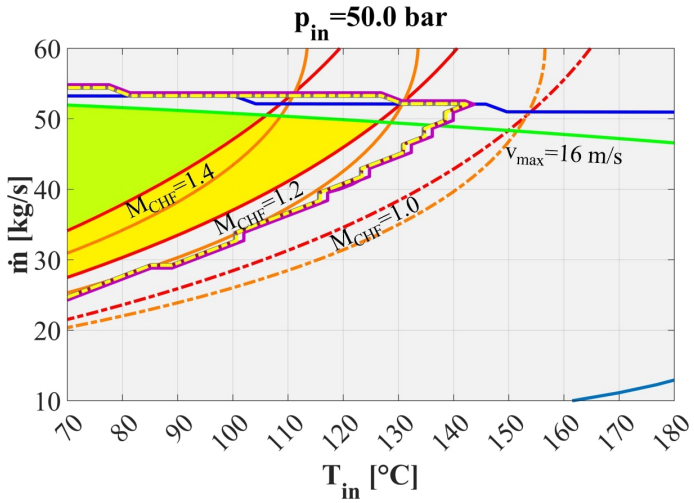

(a)

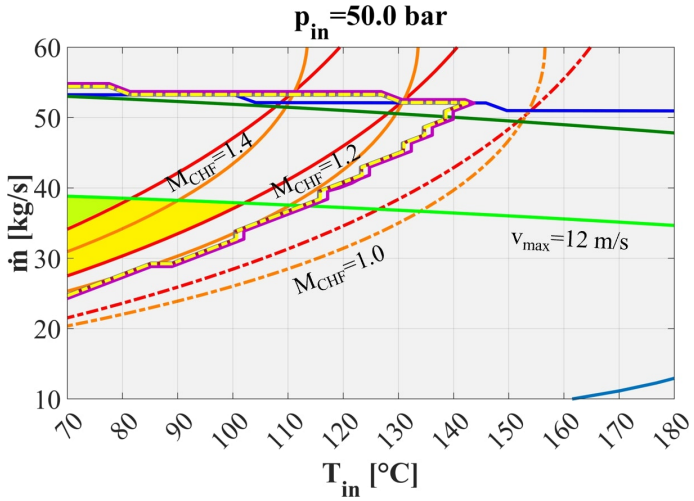

(b)

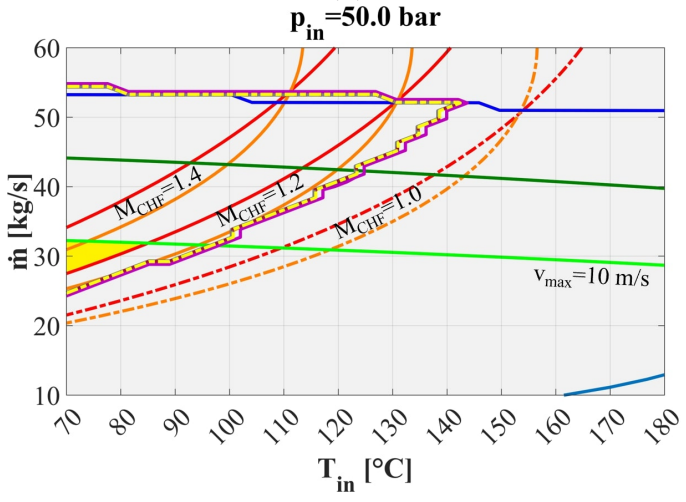

(c)

Figure 2.42: Map of divertor (VTs in series) cooling circuit operating conditions for a maximum plasma heat flux of 20 MW/m^2 considering 50 bar inlet pressure and three different maximum PFU cooling channel axial coolant velocities (16, 12 and 10 m/s, respectively first, second and third row).

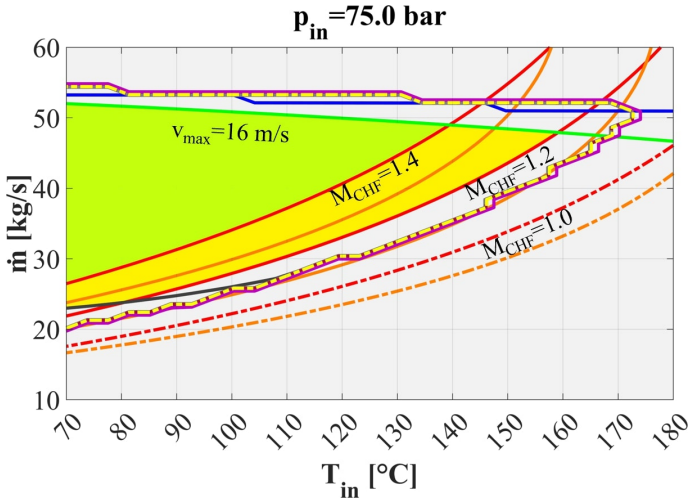

(a)

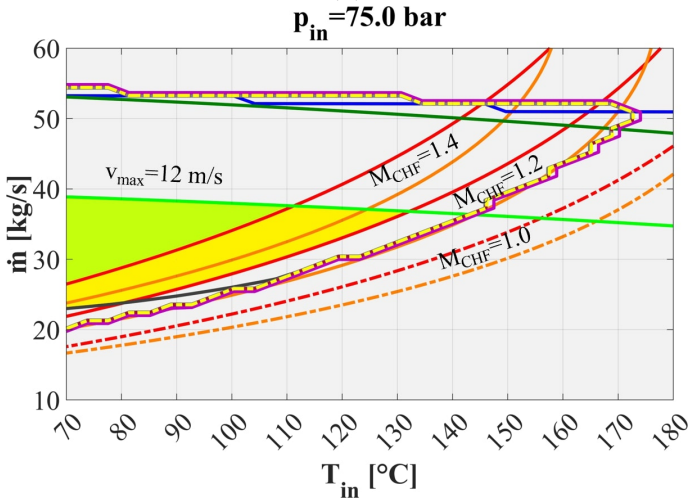

(b)

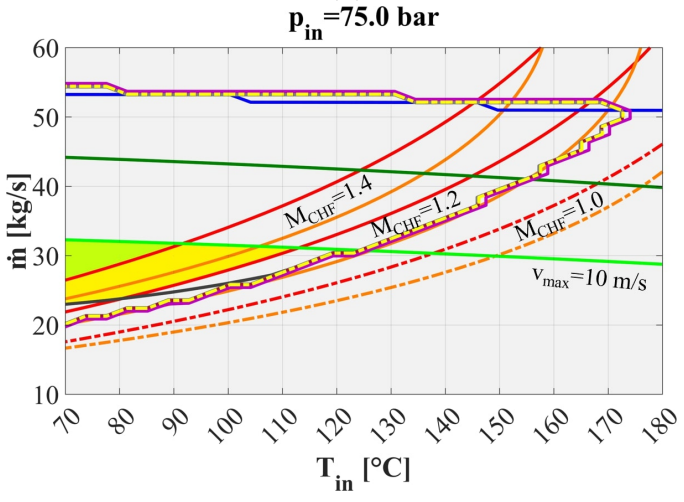

(c)

Figure 2.43: Map of divertor (VTs in series) cooling circuit operating conditions for a maximum plasma heat flux of 20 MW/m^2 considering 75 bar inlet pressure and three different maximum PFU cooling channel axial coolant velocities (16, 12 and 10 m/s, respectively first, second and third row).

- It must be verified that the PFUs can withstand the thermo-mechanical stresses that result from the particular choice of coolant operating conditions since the calculations made do not take into account the mechanical problem. In particular, the variation in the mechanical properties of the irradiated materials should be considered. Consequently, additional analyses must be performed to provide a complete picture of the operating map.
- An operating point characterized by low mass flow rates would be beneficial in terms of water inventory, as clearly visible in figure 2.41.
- By operating the cooling circuit with a high mass flow rate, on the contrary, the divertor is more likely to survive off-normal conditions induced by the plasma and the PHTS.
- By operating the cooling circuit with a high inlet temperature, it can be beneficial for the lifetime of the supporting structures of the PFUs, i.e. its manifolds or the target bodies. Additionally, it is known that at temperatures lower than 150°C, irradiated CuCrZr undergoes hardening. This effect should be properly accounted for by performing dedicated thermo-mechanical analyses.

By increasing the plasma heat flux to 25 MW/m^2, the results obtained are qualitatively identical, but all green and yellow areas are reduced, as depicted in figure 2.44 and figure 2.45. Under these conditions and considering the intermediate limit value of the maximum PFU coolant axial velocity (12 m/s), it is possible to operate in a range of mass flow rates between 35 and 39 kg/s, a temperature lower than 80°C and a pressure higher than 65 bar within the green area, while in the yellow area for all the considered coolant inlet pressure values, for a coolant inlet temperature lower than 100°C and a mass flow rate within the range 29-39 kg/s.

Finally, by increasing the plasma heat flux to 30 MW/m^2, tungsten melting phenomena occur in the OVT, as depicted in figure 2.46 and figure 2.47. Acceptable conditions at intermediate pressures (65-70 bar) are available for a very narrow range of flow rates and inlet temperatures and have therefore not been reported here, due to the very small extent of the yellow and green regions. Moreover, these regions are accessible only if a maximum coolant axial velocity of 16 m/s is considered inside the PFU cooling channels.

A second parametric analysis campaign was then carried out, once again considering the plasma heat flux scenarios previously described, focusing the attention on the 2019 divertor cooling circuit design described in section 1.4. The operating map of the PFCs cooling circuit was calculated by considering the inlet coolant temperature ranging between 70 and 180°C, the coolant mass flow rate between 25 and 150 kg/s, and the coolant inlet pressure between 50 and 75 bar.

As may be argued from the following results, the green and yellow regions of the maps are delimited uniquely by the CHF margin at the IVT (orange curve), by the

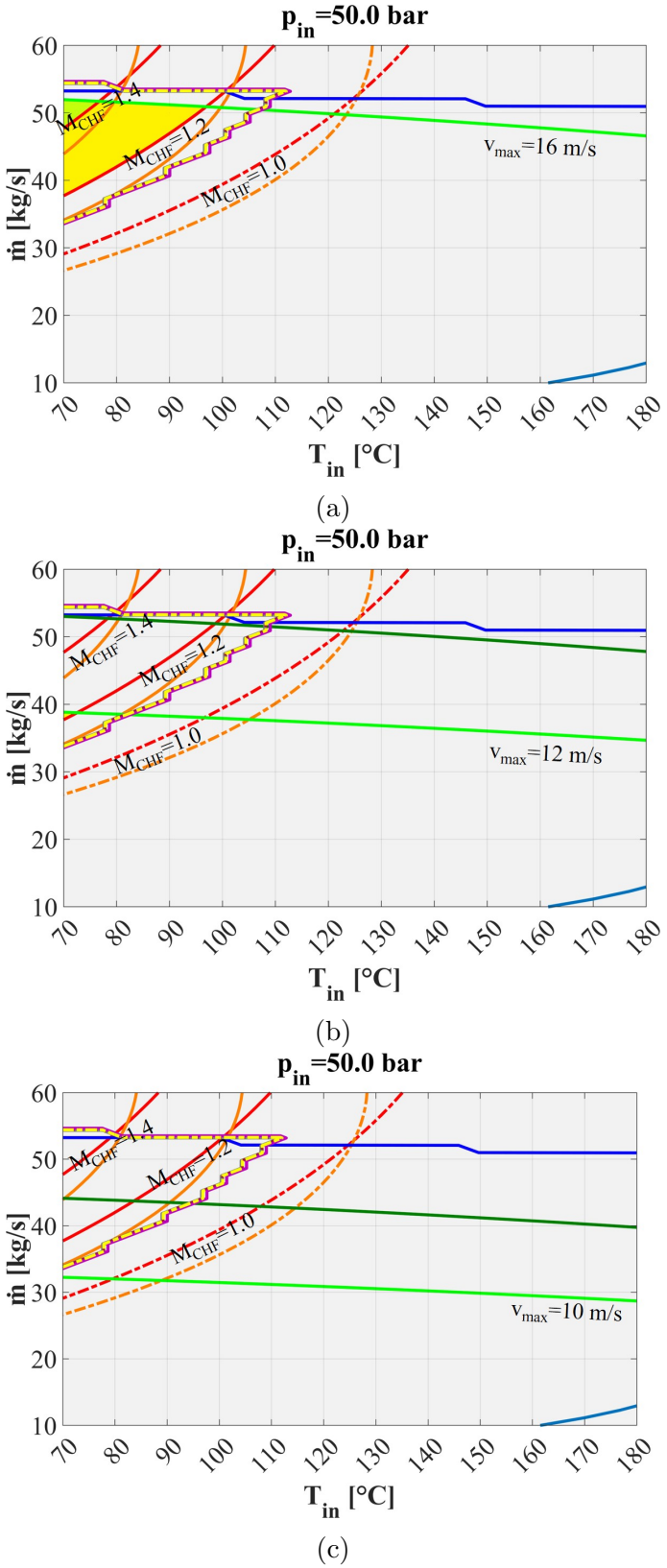

Figure 2.44: Map of divertor (VTs in series) cooling circuit operating conditions for a maximum plasma heat flux of 25 MW/m^2 considering 50 bar inlet pressure and three different maximum PFU cooling channel axial coolant velocities (16, 12 and 10 m/s, respectively first, second and third row).

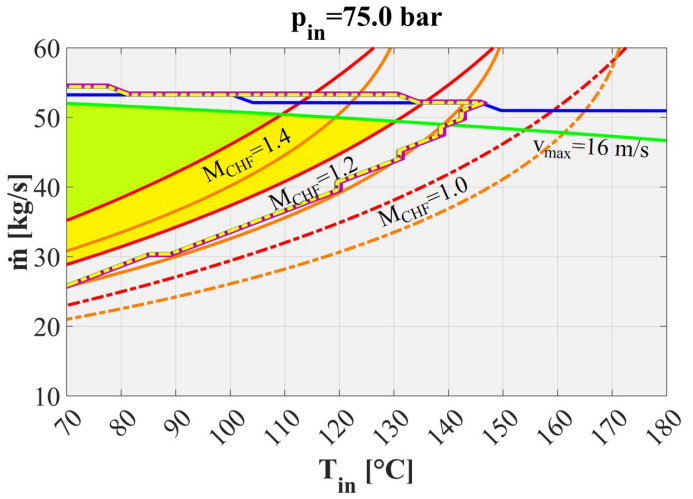

(a)

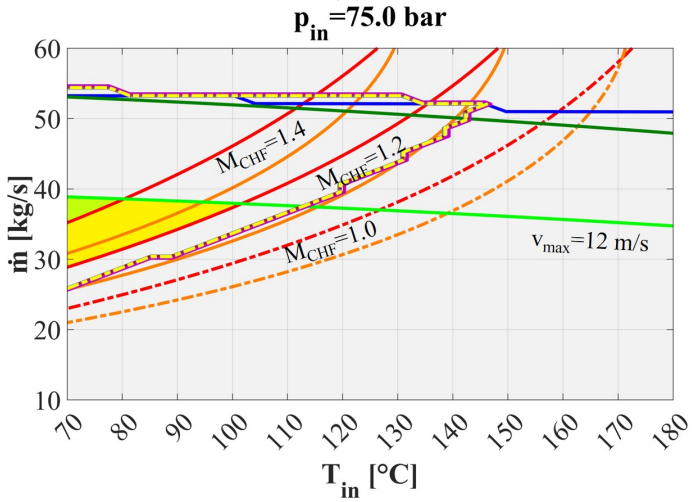

(b)

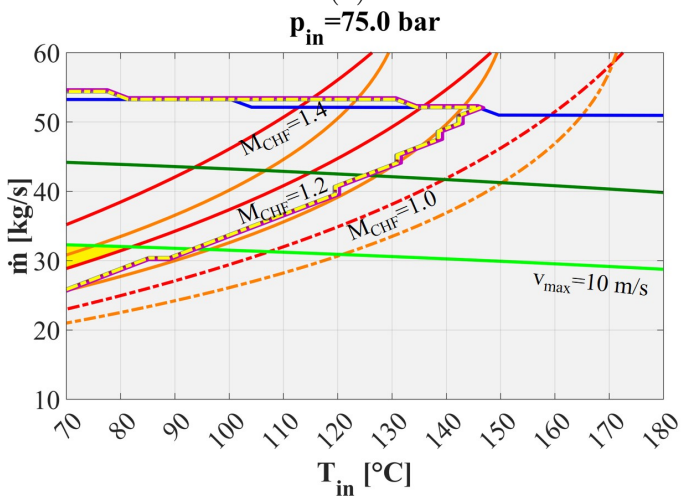

(c)

Figure 2.45: Map of divertor (VTs in series) cooling circuit operating conditions for a maximum plasma heat flux of 25 MW/m^2 considering 75 bar inlet pressure and three different maximum PFU cooling channel axial coolant velocities (16, 12 and 10 m/s, respectively first, second and third row).

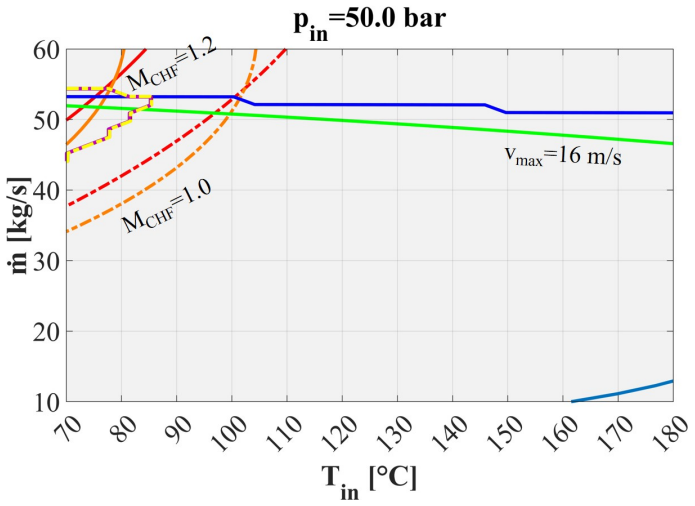

(a)

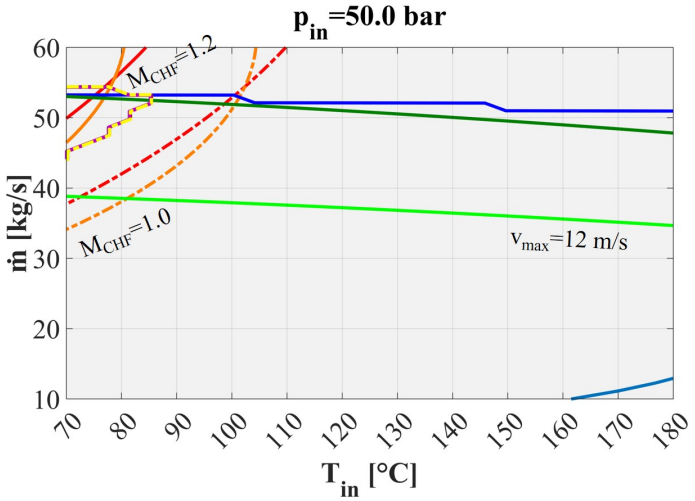

(b)

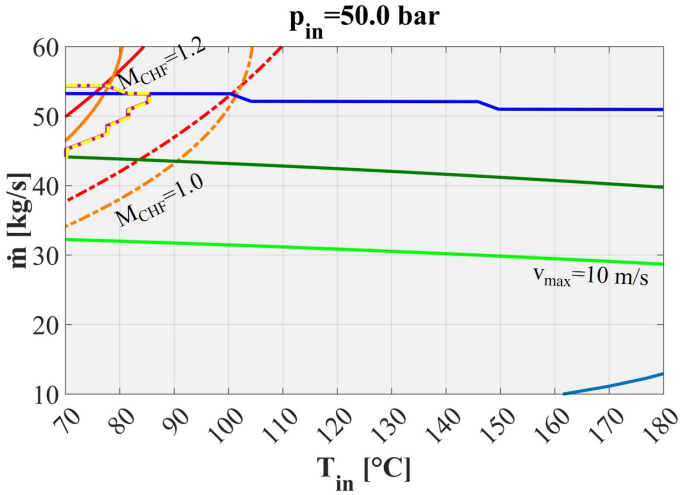

(c)

Figure 2.46: Map of divertor (VTs in series) cooling circuit operating conditions for a maximum plasma heat flux of 30 MW/m^2 considering 50 bar inlet pressure and three different maximum PFU cooling channel axial coolant velocities (16, 12 and 10 m/s, respectively first, second and third row).

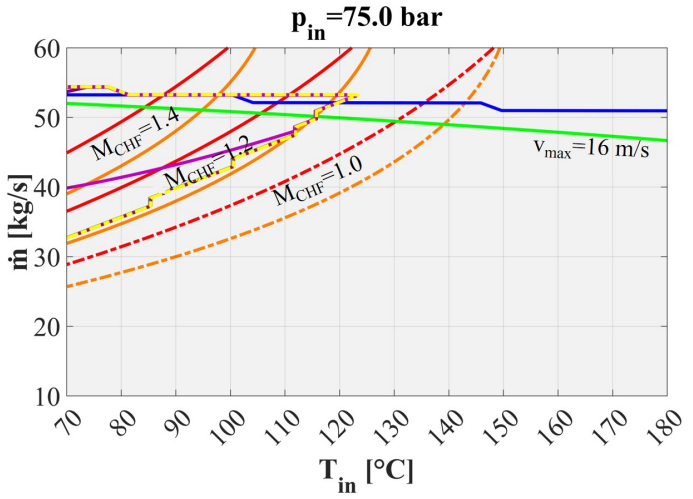

(a)

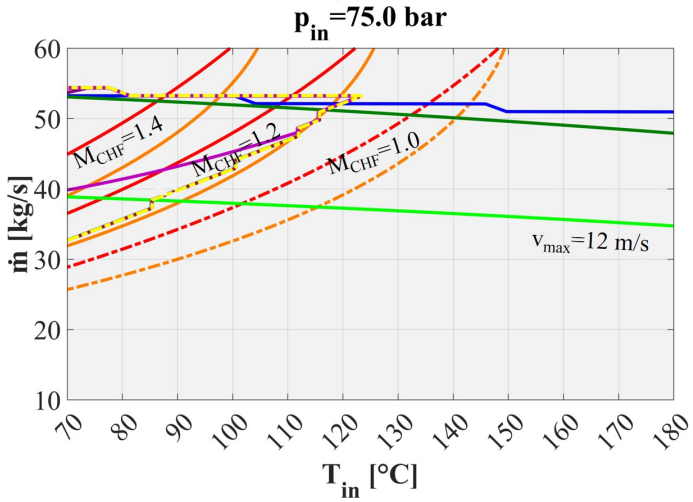

(b)

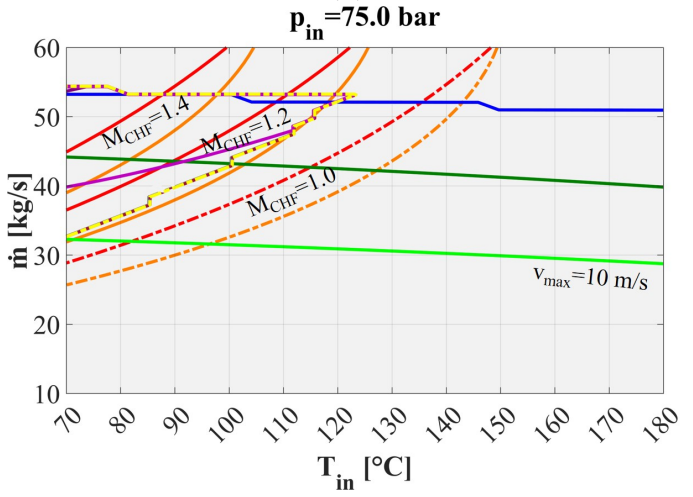

(c)

Figure 2.47: Map of divertor (VTs in series) cooling circuit operating conditions for a maximum plasma heat flux of 30 MW/m^2 considering 75 bar inlet pressure and three different maximum PFU cooling channel axial coolant velocities (16, 12 and 10 m/s, respectively first, second and third row).

maximum axial coolant velocity inside the OVT PFU cooling channels (dark green curve), and by the pressure drop (blue curve) at higher values of maximum PFU cooling channel axial velocity.

The results obtained considering a plasma heat flux of 20 MW/m^2 are depicted in figure 2.48 and figure 2.49. In particular, a comparison with figure 2.42 and figure 2.43 highlights how connecting the VTs in parallel it is possible to obtain a broadening of green and yellow areas. Considering the intermediate limit value of the maximum PFU coolant axial velocity (12 m/s), it is possible to operate in the green area in a range of mass flow rates between 43 and 82 kg/s, a temperature lower than 135°C and at all the considered pressure values, while in the yellow area at all the considered pressures (50 to 75 bar) at temperatures lower than 155°C and mass flow rates in between 36 and 82 kg/s. Comparing the results with those shown in figure 2.42 and figure 2.43, it can be seen that the maximum coolant inlet temperatures for both green and yellow areas are increased by approximately 25°C.

It is worth pointing out that, with reference to figure 2.48, the inlet coolant working conditions depicted in figure 1.15 is characterised by a CHF margin lower than 1.4, thus not meeting all the requirements. The discrepancy with the results reported in [21] is related to the CHF margin calculation, here performed at the outlet section of the PFU cooling channel section equipped with the swirl tapes to take into account any displacement of the strike point on the target, while in [21] this margin was calculated assuming a fixed strike point located at the central section of the target.

By increasing the plasma heat flux to 25 MW/m^2, the results obtained are qualitatively identical to those reported above, but all green and yellow areas are reduced, as visible in figure 2.50 and figure 2.51. Under these conditions and considering the intermediate limit value of the maximum PFU coolant axial velocity (12 m/s), it is possible to operate in the green area in a range of mass flow rates between 56 and 82 kg/s, a temperature lower than 105°C and a pressure higher than 55 bar, while in the yellow area at all the considered pressures (50 to 75 bar) at temperatures lower than 125°C and mass flow rates in between 48 and 82 kg/s. Comparing the results with those relevant to the 20 MW/m^2 condition, it can be seen that the maximum coolant inlet temperatures for both green and yellow areas are increased by approximately 25°C.

Finally, by increasing the plasma heat flux to 30 MW/m^2, the operation is allowed inside small regions, due to the occurrence of tungsten melting of the IVT, as depicted in figure 2.50 and figure 2.51.

More in detail, the yellow region of the operating map is shown for six pressure values between 50 and 75 bar in figure 2.54 and figure 2.55, considering a maximum coolant velocity of 12 m/s. As can be seen, it is not possible to work at low pressures due to the constraint on the CHF margin, while as the coolant inlet pressure

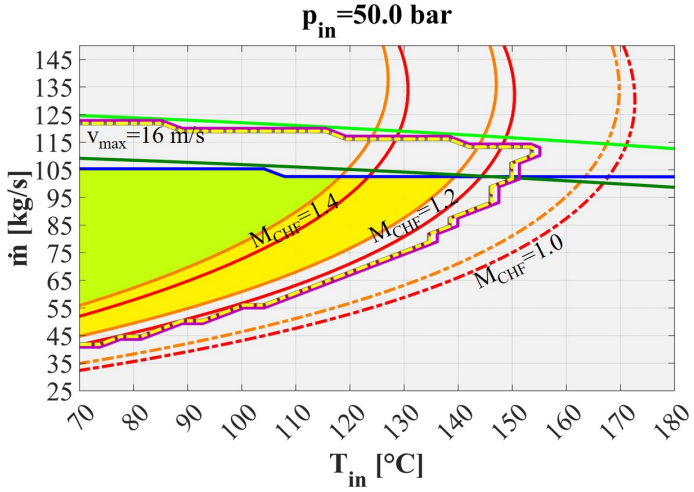

(a)

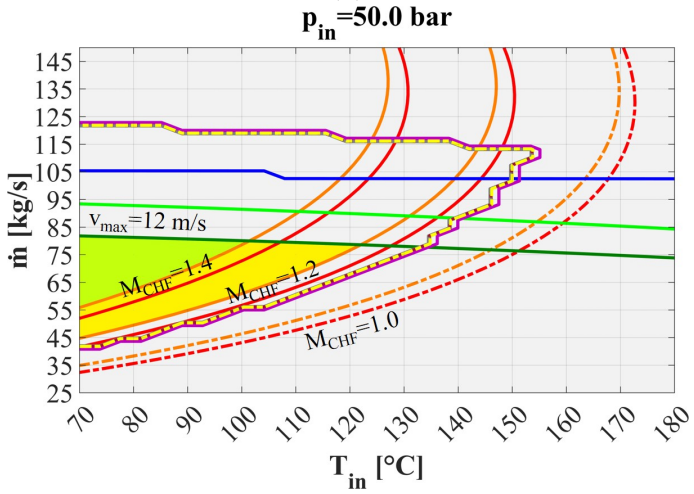

(b)

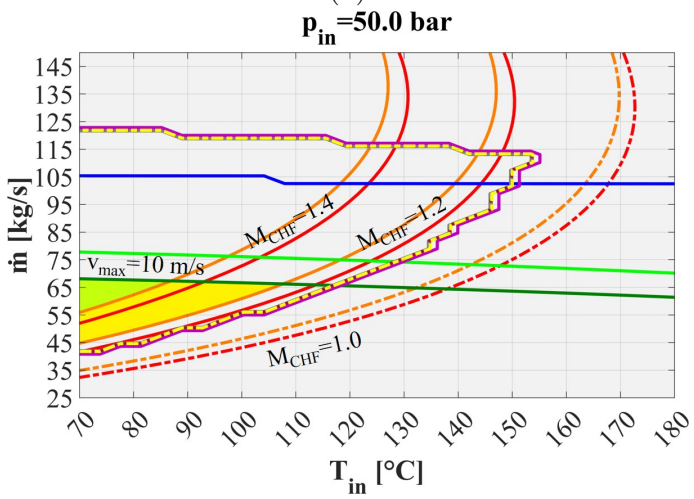

(c)

Figure 2.48: Map of divertor (VTs in parallel) cooling circuit operating conditions for a maximum plasma heat flux of 20 MW/m^2 considering 50 bar inlet pressure and three different maximum PFU cooling channel axial coolant velocities (16, 12 and 10 m/s, respectively first, second and third row).

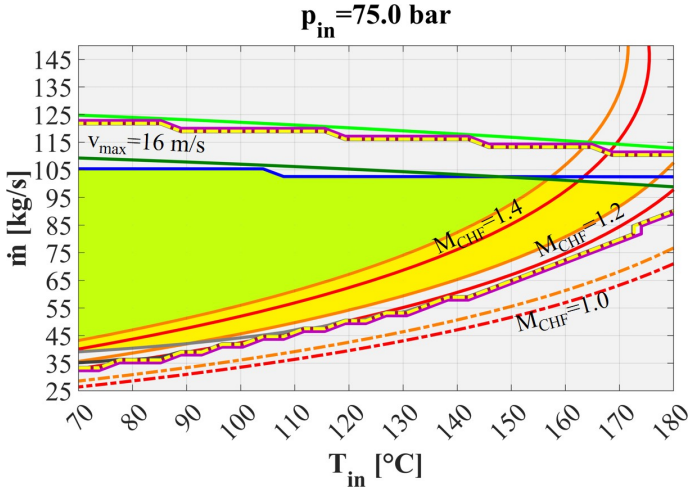

(a)

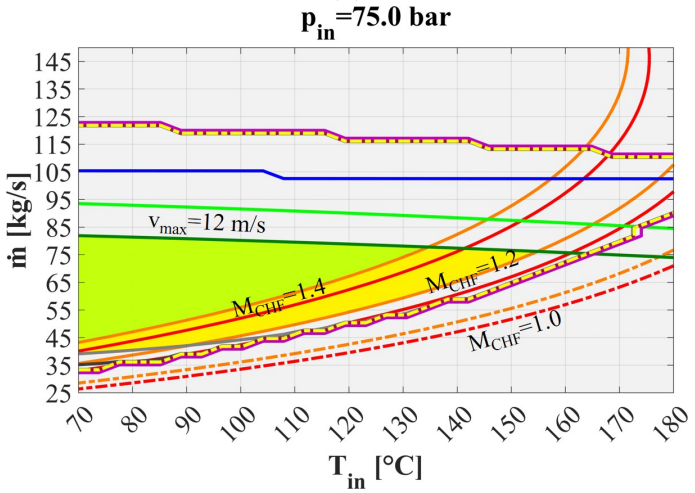

(b)

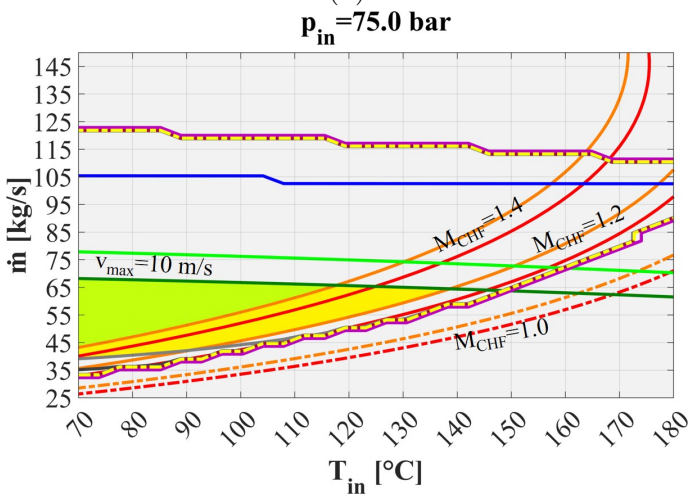

(c)

Figure 2.49: Map of divertor (VTs in parallel) cooling circuit operating conditions for a maximum plasma heat flux of 20 MW/m^2 considering 75 bar inlet pressure and three different maximum PFU cooling channel axial coolant velocities (16, 12 and 10 m/s, respectively first, second and third row).

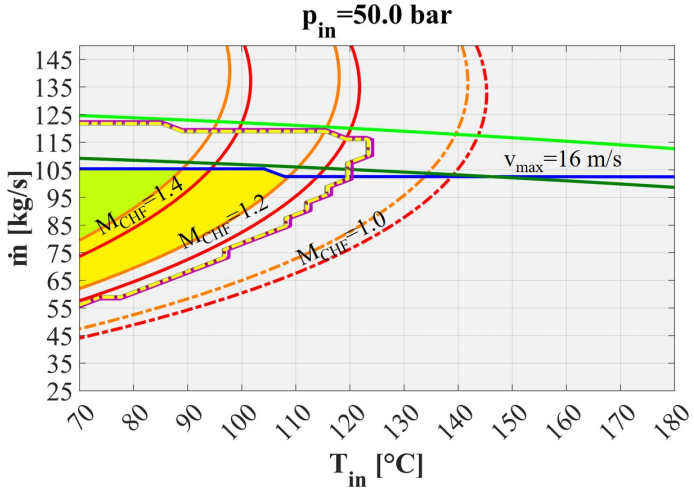

(a)

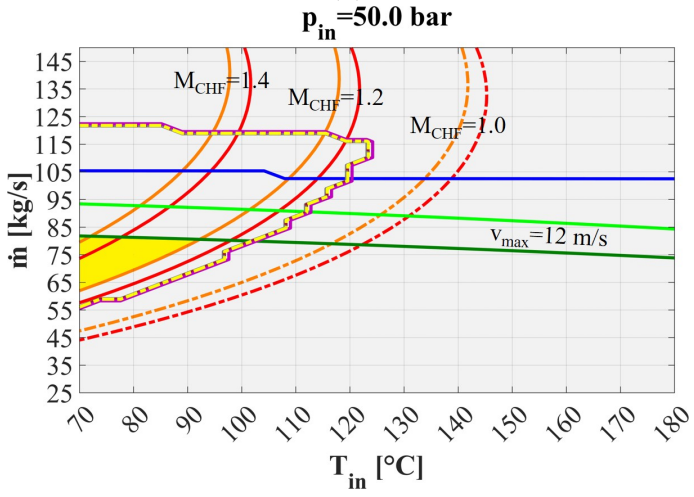

(b)

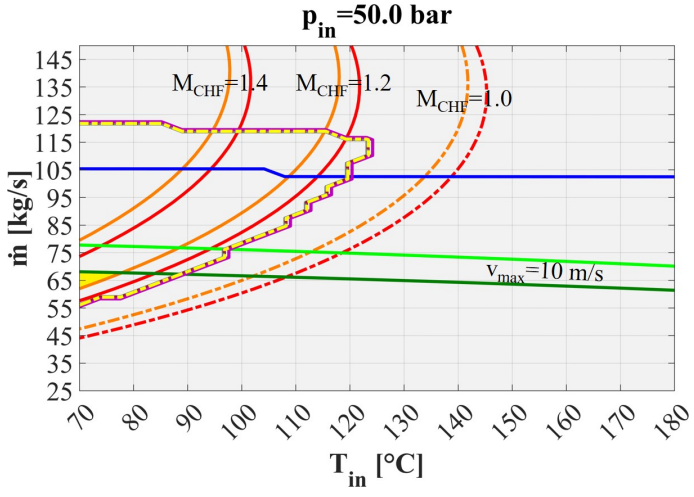

(c)

Figure 2.50: Map of divertor (VTs in parallel) cooling circuit operating conditions for a maximum plasma heat flux of 25 MW/m^2 considering 50 bar inlet pressure and three different maximum PFU cooling channel axial coolant velocities (16, 12 and 10 m/s, respectively first, second and third row).

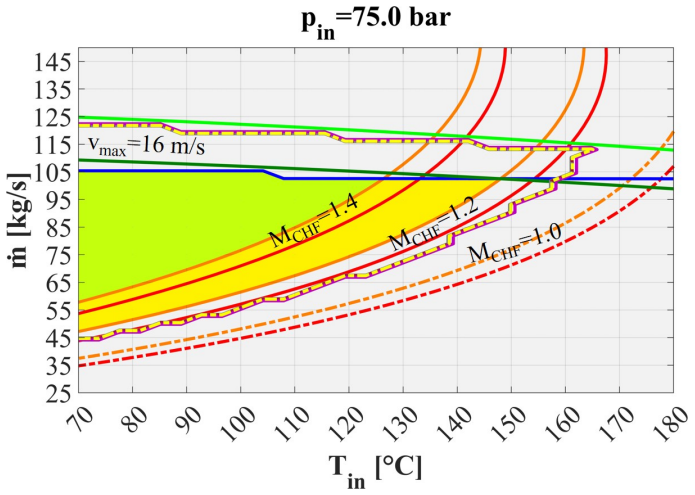

(a)

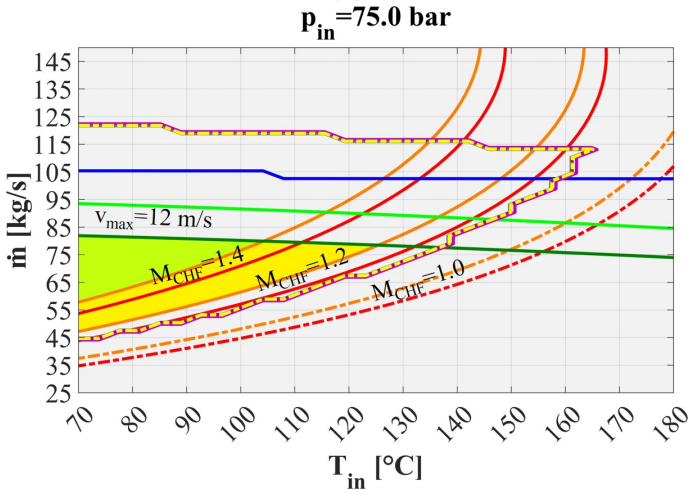

(b)

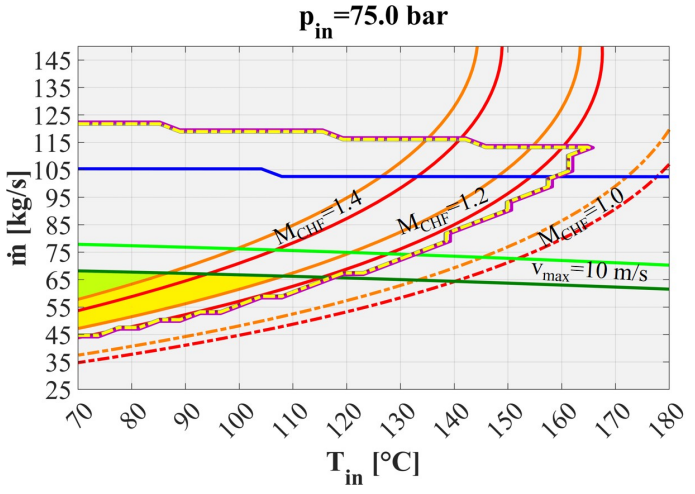

(c)

Figure 2.51: Map of divertor (VTs in parallel) cooling circuit operating conditions for a maximum plasma heat flux of 25 MW/m^2 considering 75 bar inlet pressure and three different maximum PFU cooling channel axial coolant velocities (16, 12 and 10 m/s, respectively first, second and third row).

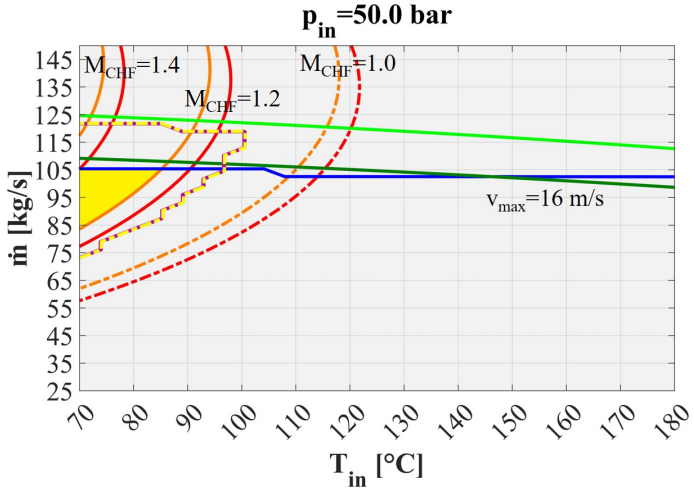

(a)

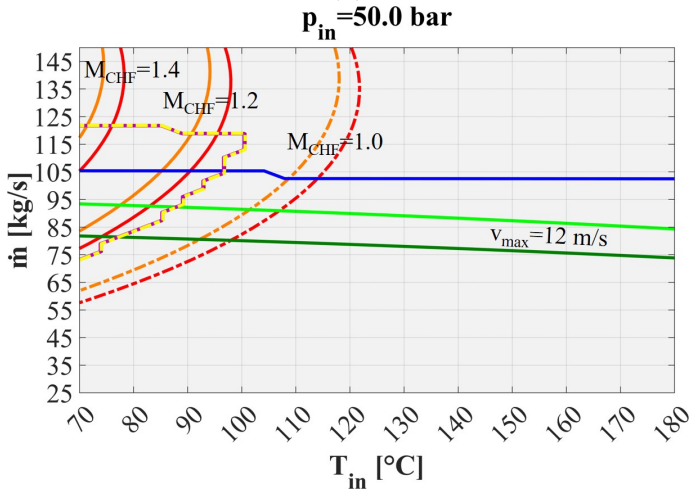

(b)

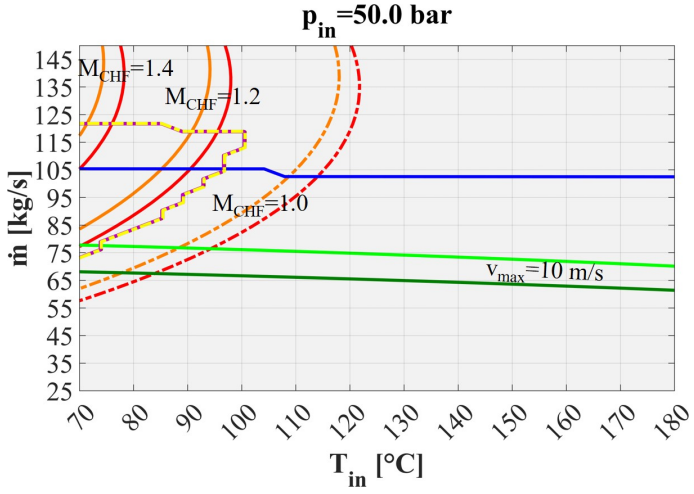

(c)

Figure 2.52: Map of divertor (VTs in parallel) cooling circuit operating conditions for a maximum plasma heat flux of 30 MW/m^2 considering 50 bar inlet pressure and three different maximum PFU cooling channel axial coolant velocities (16, 12 and 10 m/s, respectively first, second and third row).

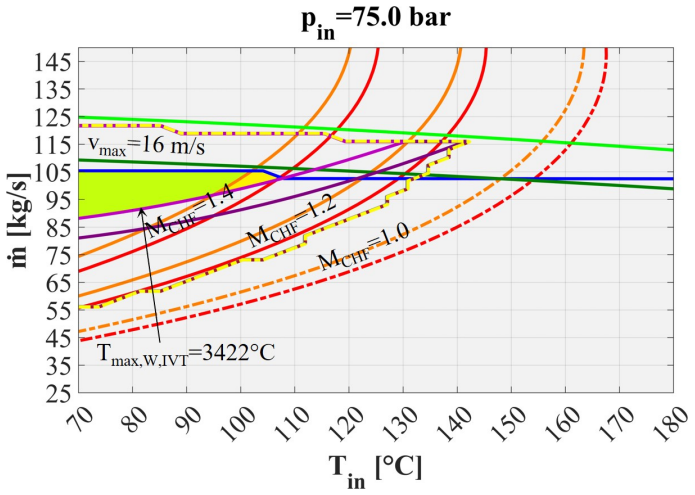

(a)

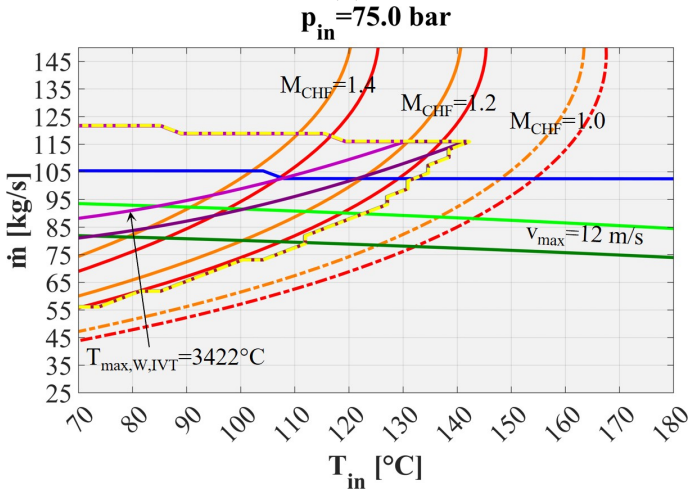

(b)

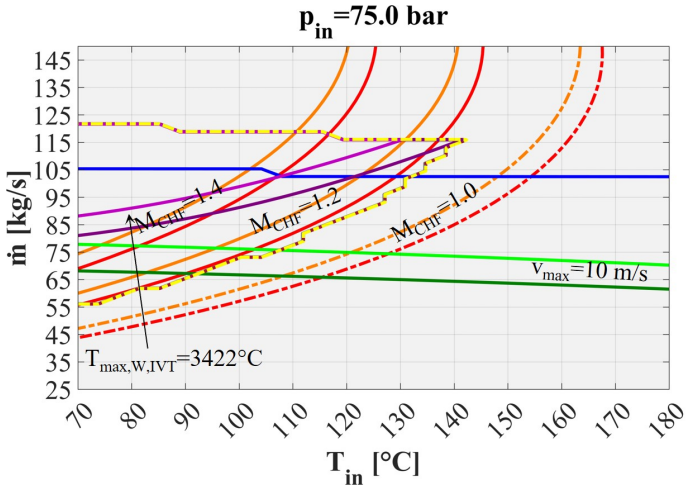

(c)

Figure 2.53: Map of divertor (VTs in parallel) cooling circuit operating conditions for a maximum plasma heat flux of 30 MW/m^2 considering 75 bar inlet pressure and three different maximum PFU cooling channel axial coolant velocities (16, 12 and 10 m/s, respectively first, second and third row).

increases, a shift of the tungsten melting curves upwards is observed. This is related to the increase in water saturation temperature with pressure, which determines the heat sink temperature for the PFUs. The resulting range of operating conditions that could be considered is between 55 and 65 bar of water inlet pressure, a coolant mass flow rate between 70 and 82 kg/s and a coolant inlet temperature lower than 88°C.

Moreover, as can be easily deduced, a further increase in plasma heat flux quickly leads to the total disappearance of the yellow region due to the melting temperature constraint, and no acceptable operating condition can be found. Furthermore, it is interesting to note how the results obtained are not far from those reported in [45], documenting 31-32MW/m^2 as the heat flux value at which tungsten melting begins to take place.

In conclusion, the results of the parametric analysis on the PFCs cooling circuit revealed some limitations on the coolant operating conditions that can be selected to guarantee the correct operation of the component, in compliance with the thermal and hydraulic constraints.

The maximum coolant inlet temperatures are summarized in tables 2.8 to 2.10 for the different maximum axial coolant velocity of 16, 12, and 10 m/s, supposing a minimum CHF margin of 1.4, and in tables 2.11 to 2.13 supposing a CHF margin of 1.2. Moreover, all the results have been compared to the pertaining theoretical limits.

Finally, the most important outcomes are summarized in the following.

- The cooling circuit in which the VTs are connected in parallel has a higher thermal performance than the circuit in which the targets are connected in series. This results in a reduction of the maximum coolant inlet temperature in the order of 15-25°C, calculated considering all the coolant inlet pressure and incident heat flux values assessed.
- The potential occurrence of fretting and flow-accelerated corrosion problems, which impose constraints on the maximum coolant velocities within the cooling channels of the PFUs, is pivotal in determining the extension of the operating map. As a general trend, a reduction of the maximum coolant axial velocity from 16 to 12 m/s produces a lowering of the maximum coolant temperature up to 30°C, while a reduction from 16 to 10 m/s a lowering up to 50°C. These values are calculated considering the average values of maximum temperature reduction for all the cases considered (both series and parallel). This significantly limits the maximum heat flow that can be safely handled by the monoblocks and forces the adoption of a lower temperature and higher pressure coolant.
- If the monoblocks are expected to operate at high heat fluxes (higher than

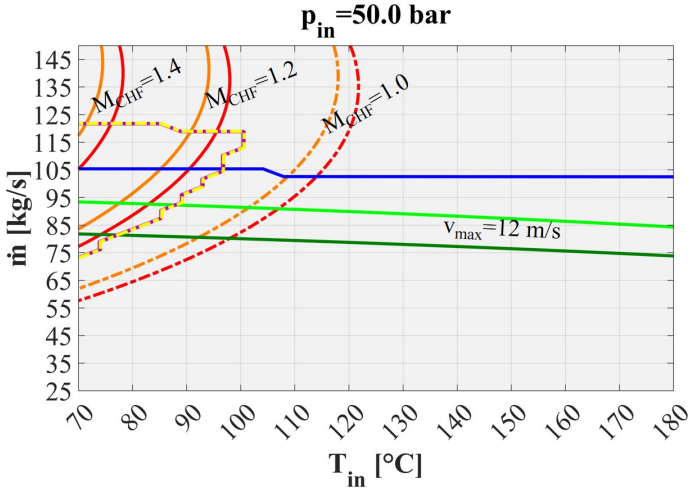

(a)

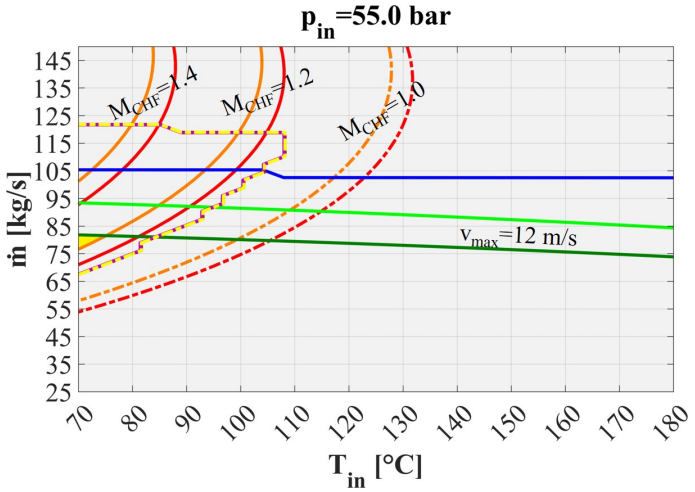

(b)

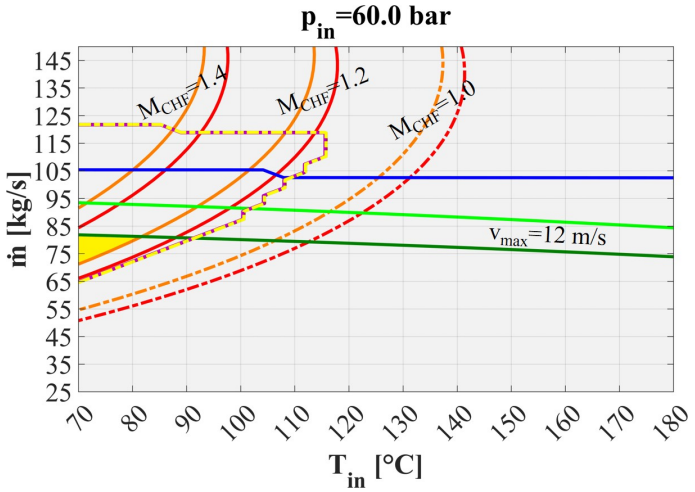

(c)

Figure 2.54: Map of divertor (VTs in parallel) cooling circuit operating conditions for a maximum plasma heat flux of 30 MW/m^2 considering increasing inlet coolant pressure values, from 50 to 60 bar.

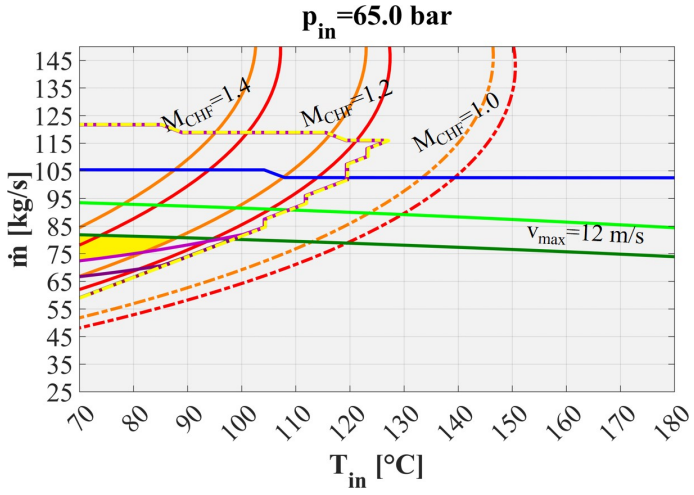

(a)

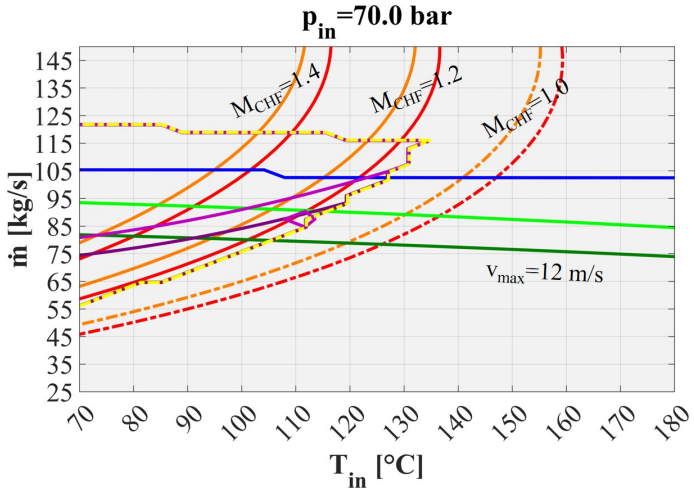

(b)

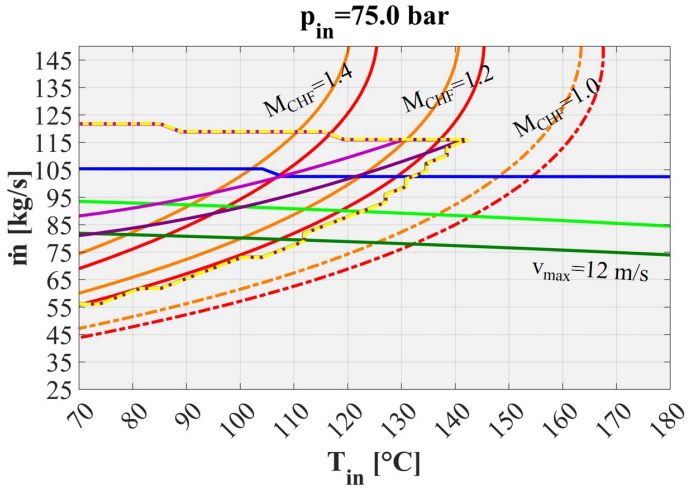

(c)

Figure 2.55: Map of divertor (VTs in parallel) cooling circuit operating conditions for a maximum plasma heat flux of 30 MW/m^2 considering increasing inlet coolant pressure values, from 65 to 75 bar.

Table 2.8: Summary of the results obtained for the different DEMO divertor PFC double-circuit cooling option cooling circuit topologies for a limit coolant axial velocity of 16 m/s and a minimum CHF margin of 1.4.

	Series VTs		**Parallel VTs**	
	p_{in}=50 bar	p_{in}=75 bar	p_{in}=50 bar	p_{in}=75 bar
		20 MW/m²		
Theoretical limit	≈128°C	≈159°C	≈154°C	≈186°C
DEMO PFC cooling circuit	≈105°C	≈140°C	≈118°C	≈155°C
		25 MW/m²		
Theoretical limit	≈98°C	≈129°C	≈125°C	≈159°C
DEMO PFC cooling circuit	≈75°C	≈110°C	≈90°C	≈125°C
		30 MW/m²		
Theoretical limit	≈74°C	≈104°C	≈101°C	≈135°C
DEMO PFC cooling circuit	≈55°C	≈60°C	≈65°C	≈100°C

Table 2.9: Summary of the results obtained for the different DEMO divertor PFC double-circuit cooling option cooling circuit topologies for a limit coolant axial velocity of 12 m/s and a minimum CHF margin of 1.4.

	Series VTs		**Parallel VTs**	
	p_{in}=50 bar	p_{in}=75 bar	p_{in}=50 bar	p_{in}=75 bar
		20 MW/m²		
Theoretical limit	≈102°C	≈131°C	≈129°C	≈160°C
DEMO PFC cooling circuit	≈80°C	≈110°C	≈100°C	≈135°C
		25 MW/m²		
Theoretical limit	≈73°C	≈100°C	≈99°C	≈131°C
DEMO PFC cooling circuit	≈50°C	≈80°C	≈70°C	≈105°C
		30 MW/m²		
Theoretical limit	≈51°C	≈75°C	≈75°C	≈105°C
DEMO PFC cooling circuit	≈30°C	-	≈50°C	-

Table 2.10: Summary of the results obtained for the different DEMO divertor PFC double-circuit cooling option cooling circuit topologies for a limit coolant axial velocity of 10 m/s and a minimum CHF margin of 1.4.

	Series VTs		**Parallel VTs**	
	p_{in}=50 bar	p_{in}=75 bar	p_{in}=50 bar	p_{in}=75 bar
		20 MW/m²		
Theoretical limit	≈86°C	≈113°C	≈113°C	≈143°C
DEMO PFC cooling circuit	≈65°C	≈90°C	≈85°C	≈115°C
		25 MW/m²		
Theoretical limit	≈58°C	≈82°C	≈83°C	≈112°C
DEMO PFC cooling circuit	≈35°C	≈60°C	≈55°C	≈85°C
		30 MW/m²		
Theoretical limit	≈38°C	≈57°C	≈60°C	≈87°C
DEMO PFC cooling circuit	≈15°C	-	≈35°C	-

Table 2.11: Summary of the results obtained for the different DEMO divertor PFC double-circuit cooling option cooling circuit topologies for a limit coolant axial velocity of 16 m/s and a minimum CHF margin of 1.2.

	Series VTs		**Parallel VTs**	
	p_{in}=50 bar	p_{in}=75 bar	p_{in}=50 bar	p_{in}=75 bar
		20 MW/m²		
Theoretical limit	≈148°C	≈178°C	≈172°C	≈202°C
DEMO PFC cooling circuit	≈125°C	≈160°C	≈140°C	≈175°C
		25 MW/m²		
Theoretical limit	≈118°C	≈150°C	≈145°C	≈178°C
DEMO PFC cooling circuit	≈95°C	≈130°C	≈105°C	≈145°C
		30 MW/m²		
Theoretical limit	≈94°C	≈125°C	≈121°C	≈155°C
DEMO PFC cooling circuit	≈70°C	≈60°C	≈85°C	≈105°C

Table 2.12: Summary of the results obtained for the different DEMO divertor PFC double-circuit cooling option cooling circuit topologies for a limit coolant axial velocity of 12 m/s and a minimum CHF margin of 1.2.

	Series VTs		**Parallel VTs**	
	p_{in}=50 bar	p_{in}=75 bar	p_{in}=50 bar	p_{in}=75 bar
		20 MW/m²		
Theoretical limit	≈123°C	≈152°C	≈149°C	≈180°C
DEMO PFC cooling circuit	≈100°C	≈130°C	≈120°C	≈155°C
		25 MW/m²		
Theoretical limit	≈93°C	≈122°C	≈120°C	≈151°C
DEMO PFC cooling circuit	≈70°C	≈100°C	≈90°C	≈125°C
		30 MW/m²		
Theoretical limit	≈69°C	≈96°C	≈95°C	≈127°C
DEMO PFC cooling circuit	≈51°C	-	≈65°C	-

Table 2.13: Summary of the results obtained for the different DEMO divertor PFC double-circuit cooling option cooling circuit topologies for a limit coolant axial velocity of 10 m/s and a minimum CHF margin of 1.2.

	Series VTs		**Parallel VTs**	
	p_{in}=50 bar	p_{in}=75 bar	p_{in}=50 bar	p_{in}=75 bar
		20 MW/m²		
Theoretical limit	≈107°C	≈135°C	≈134°C	≈164°C
DEMO PFC cooling circuit	≈85°C	≈110°C	≈105°C	≈140°C
		25 MW/m²		
Theoretical limit	≈77°C	≈103°C	≈104°C	≈134°C
DEMO PFC cooling circuit	≈55°C	≈80°C	≈75°C	≈105°C
		30 MW/m²		
Theoretical limit	≈55°C	≈78°C	≈79°C	≈108°C
DEMO PFC cooling circuit	≈35°C	-	≈55°C	-

20 MW/m^2) it is mandatory to increase the coolant inlet pressure or to significantly reduce the coolant inlet temperature.

- Operation at heat fluxes of 30 MW/m^2 is limited to small regions of the operating space, due to the occurrence of tungsten melting phenomena. Adopting even higher plasma heat fluxes is most likely not possible due to the limitations imposed by melting.
- The choice of operating conditions within the operating map may be dictated by different, often conflicting requirements:
  - working at lower flow rates may lead to benefits in terms of water inventory in the PFCs PHTS circuit. This effect is less accentuated in the case of parallel VTs due to the higher mass flow rates;
  - working at higher mass flow rates ensures that the system can avoid the occurrence of CHF phenomena in the event of a loss of flow of one of the circulators of the PFCs PHTS;
  - working at higher coolant temperatures is beneficial in terms of materials, possibly increasing the component lifetime;
  - working at lower coolant temperatures may allow the operation at higher heat fluxes.
- Further thermo-mechanical analyses are mandatory to verify that the selected operating conditions are acceptable from the structural standpoint, and the proper variation of mechanical properties due to irradiation should be properly taken into account.

Chapter 3

Preliminary Analyses and Criticalities in the Thermofluid-Dynamic Simulation of the EU DEMO Divertor Cassette

3.1 Introduction

In 2020, a mock-up of the OVT [82] of the EU DEMO divertor was built by ENEA research group. The mock-up was tested at ENEA Brasimone Labs with the aim to demonstrate the feasibility of the manufacturing procedures, to experimentally characterize the hydraulic behaviour of the OVT cooling circuit and to validate the CFD finite volume models developed at the University of Palermo against experimental data.

A research campaign was therefore carried out to experimentally and theoretically assess the steady-state hydraulic performances of the OVT mock-up, paying particular attention to the coolant mass flow rate distribution among the PFUs assemblies and the total pressure drop across the inlet and outlet sections of the mock-up.

The outcomes of this research activity, reported in [76], highlighted an overall good agreement between CFD calculations and experimental data, with an error on pressure drop estimation between -7.22% and -0.77% over a quite broad range of mass flow rates, between 12 and 35 kg/s. Similarly, a good agreement was obtained also for the coolant mass flow rate distributions among the PFUs cooling channels, with maximum deviations always below 10% between numerical and experimental data.

Additionally, in [76] it is stressed how the need to use a very fine calculation grid is mandatory for the specific OVT geometry to avoid the influence of the mesh on the results obtained: in particular, with a calculation mesh with a bulk size of 1.3 mm for the region of the PFU cooling channel (to be compared with the pipe internal diameter of 12 mm) and a less dense mesh for the manifolds and the rest of the pipes (10 mm), an error ranging between 8 and 10% is obtained with respect to the values obtained by means of a Richardson extrapolation procedure at the various mass flow rates considered. Furthermore, by adopting coarser meshes, the numerical results are significantly overestimated if compared to experimental outcomes, especially at high coolant mass flow rates.

The coarsest mesh that has been considered in the study mentioned above, i.e. the one with the largest errors, is still made up of around 20 million finite volumes, required to model a system that incorporates only 39 PFU cooling channels with a section occupied by the STs of only 470 mm, and a total length of the CuCrZr tubes of only 852 mm for each PFU cooling channel. Wanting to make a rough estimate of the number of cells that would be required to prepare a mesh of the same characteristics for the PFUs cooling channels of the 2021 divertor cassette, appropriately scaled to the total volume of water inside the PFUs (just to give an idea, the CuCrZr pipes of the IVT are almost 1.6 m long in the 2021 design), it can be conservatively assumed a number close to 60 million, without considering the TBs and especially neglecting the monoblock structures, which would entail a further and unmanageable computational burden. Instead, by adopting a mesh with similar features to the one reported in [76] to obtain errors with respect to mesh-independent results below 5%, this number of finite volumes would be in the order of 150 million only for the fluid domain.

Additionally, it should be considered the efforts required for the preparation of the geometry and the mesh, being the integration of the ST regions with the PFU cooling channel CAD the most time-consuming part of the pre-processing phase. In fact, the CAD files representing the divertor cooling circuit are provided without the STs, so it is required for each PFU assembly to align the ST geometry to the cooling channel, to merge the geometries and to fix the unavoidable issues that may arise from these operations. Furthermore, special care must be paid to the preparation of these geometries, since it is a common practice to define several mesh regions for each PFU cooling channel, in order to adopt structured mesh any time it is allowed by the geometry, with the final aim to reduce the overall number of finite volumes.

These preliminary considerations led to the decision to investigate the problem of fluid flow within the PFU cooling channels in greater detail, with the aim to:

- perform a mesh-independence study on the specific PFUs cooling channel geometry;
- check whether the minimum node density required to correctly simulate

STs with fairly mesh-independent results is affordable with the available computational resources, and estimate the errors related to mesh size;

- compare the numerical results with experimental findings in terms of integral quantities of interest, i.e. pressure drop and mass flow rates, in order to check if the adopted numerical methods are adequate to correctly predict fluid-dynamic features of pipes equipped with STs;
- investigate alternative modelling strategies to accurately simulate the PFUs cooling channels with reduced computational cost and time required to prepare the simulations.

The entire preliminary campaign was performed following a theoretical-numerical approach based on the FVM and adopting the Ansys CFX 2021 R1 commercial CFD code [49].

The models developed and the results obtained are herewith reported and critically discussed.

3.2 Preliminary mesh independence studies and validation campaign

The first preliminary analyses were carried out on a small portion of a cooling channel embedded with an ST turbulence promoter, whose characteristic dimensions, depicted in figure 3.1, are those currently selected for the EU DEMO divertor [6]. In particular, the main ST geometrical parameters, i.e. the internal diameter d_0 of the pipe, the ST thickness δ, and the ST pitch H are reported in table 3.1.

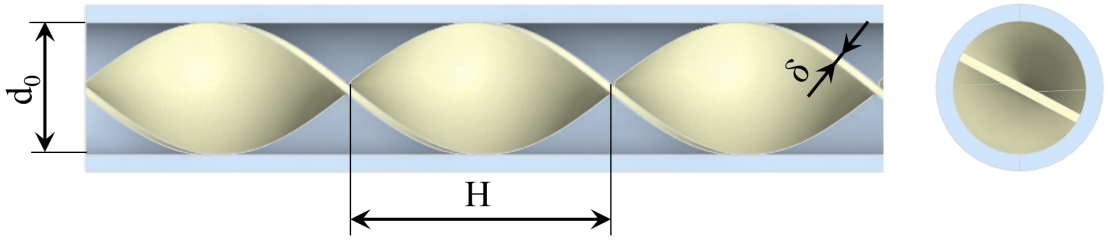

Figure 3.1: Schematics of the ST geometrical features.

This very simple geometry was selected as starting point because a large number of experimental data and correlations are available in the literature, making it possible to easily validate the numerical results.

Table 3.1: Main ST-equipped channel geometrical parameters.

Parameter	**Value**
d_0	12 mm
δ	0.8 mm
H	24 mm

3.2.1 Mesh independence

To perform the preliminary mesh-independence analysis and validation campaign, the attention was focused on the computational domain shown in figure 3.2. As can be noted, a section (a single 180° twist pitch) of the ST-equipped half channel was considered due to its symmetries.

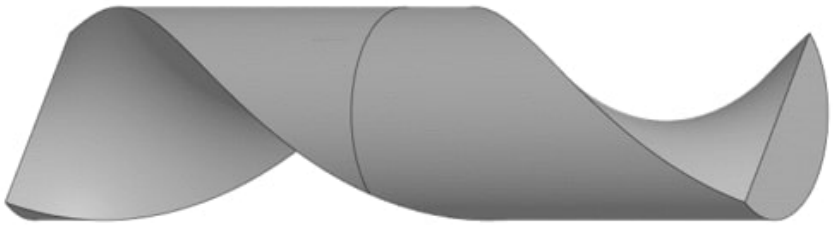

Figure 3.2: Half ST-equipped channel geometry selected for the preliminary analyses.

Six different meshes, whose details are reported in table 3.2, have been considered to assess the mesh independence of the results (the details of one of the finest meshes adopted, namely M5, are depicted in figure 3.3, while a comparison of the different meshes is visible in figure 3.4).

Table 3.2: Preliminary ST analyses mesh parameters.

	Mesh M1	**Mesh M2**	**Mesh M3**
Elements	$1.55{\cdot}10^4$	$2.30{\cdot}10^4$	$4.46{\cdot}10^4$
Element Size [mm]	1.30	1.00	0.77
Element Density [m^{-3}]	$6.24{\cdot}10^9$	$9.26{\cdot}10^9$	$1.79{\cdot}10^{10}$
	Mesh M4	**Mesh M5**	**Mesh M6**
Elements	$7.98{\cdot}10^4$	$1.37{\cdot}10^5$	$2.37{\cdot}10^5$
Element Size [mm]	0.59	0.46	0.35
Element Density [m^{-3}]	$3.21{\cdot}10^{10}$	$5.52{\cdot}10^{10}$	$9.54{\cdot}10^{10}$

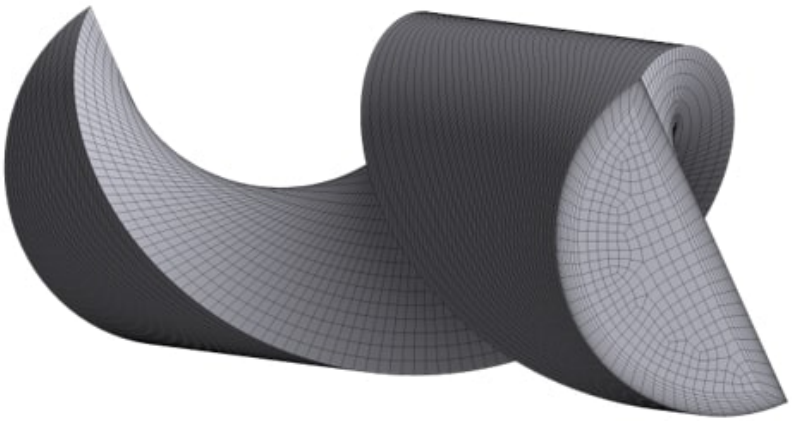

Figure 3.3: Mesh M5 adopted for the preliminary CFD analyses.

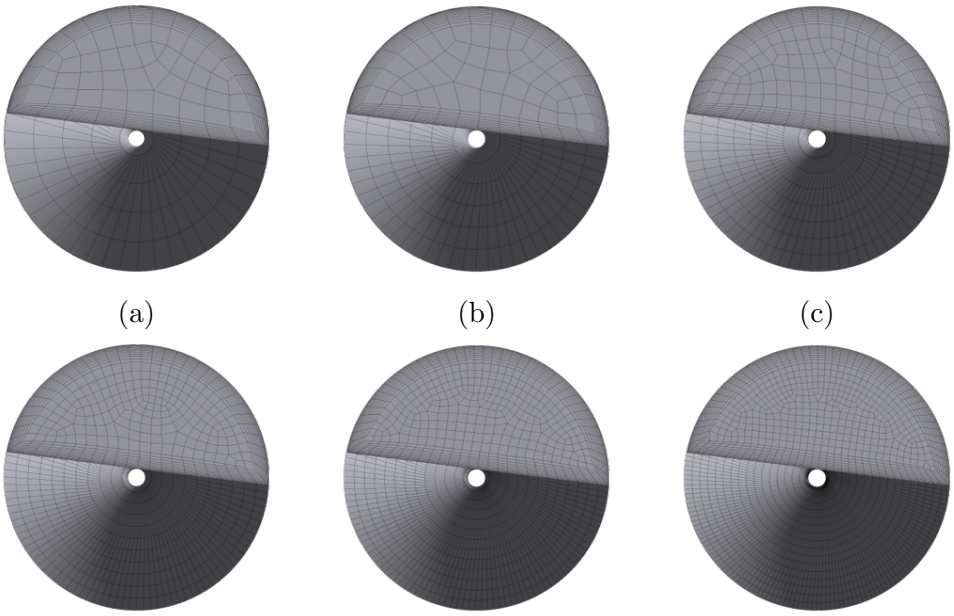

Figure 3.4: Comparison of the different meshes adopted for the mesh-independence assessment, M1 to M6 from (a) to (f).

All the meshes from M1 to M6 were produced with a sweeping algorithm, and are thus consisting of hexahedral and triangular prism elements. A fixed first-layer thickness of 20 μm and a total of 12 inflation layers was considered, while the inflation GR was fixed at 1.2.

The simulations were performed under the assumptions and considering the BCs and the models summarized in table 3.3. In particular, the k-ω SST turbulence model was chosen, being a good compromise between the accuracy of the results and the required overall computational time. Moreover, it should be noted that the assumption of isothermal flow is commonly adopted for the PFC cooling circuit, as reported for example in [21], since the coolant temperature rise between inlet and outlet sections is lower than 10°C, as already detailed in section 1.5.

Table 3.3: Summary of assumptions, models and BCs for the ST calculations.

Analysis Type	Steady-state isothermal
Material Library	Water (constant properties)
Reference temperature	133°C
Reference absolute pressure	45 bar
Turbulence Model	k-ω SST
Boundary Layer Modelling	Automatic Wall Functions
Pipe Roughness	1 μm [46]
ST Roughness	0.5 μm [46]
Inlet/Outlet BC	Cyclic (translational periodicity)
Imposed pressure drop values	see table 3.4

Table 3.4: List of pressure drop values.

	Imposed pressure drop [kPa]
Case #1	0.25
Case #2	0.50
Case #3	1.00
Case #4	2.00
Case #5	4.00
Case #6	8.00
Case #7	16.00
Case #8	32.00

Adopting the near-wall discretization previously described, the boundary layer is treated both with a High and Low Reynolds approach, based on the velocities values resulting from the analyses. Although this setting is not optimal for correctly capturing the fluid behaviour in the boundary layer, it was decided not to employ a fully Low Reynolds approach for all the mass flow rate values considered, as it would have required a significantly higher number of finite volumes, particularly for the simulations described in the next section.

As can be seen from table 3.3, the simulations were performed by imposing a periodicity condition between the inlet and outlet sections of the geometry and applying an imposed pressure drop, whose values are reported in table 3.4. By adopting this setup, it is possible to reproduce a fully-developed flow field without modelling several ST pitches. Additionally, the water properties were selected consistently with the selected pressure and temperature values, relevant to the 2019 divertor design.

A single Figure of Merit (FoM) was employed to assess the quality of the results, i.e. the Fanning friction factor f, defined according to equation (3.1), where Δp is the imposed pressure drop, ρ is the water density, L is the length of the pipe section, and u_0 is the *empty-pipe* flow velocity calculated as shown in equation (3.2), where

$\dot{m}$ is the coolant mass flow flowing inside the pipe.

$$f = \frac{d_0 \Delta p}{2 L \rho u_0^2} \tag{3.1}$$

$$u_0 = \frac{\dot{m}}{\rho \pi d_0^2 / 4} \tag{3.2}$$

It should be pointed out that the parameter f was selected as FoM because of the availability of different correlations in literature allowing easy validation of the numerical results, as will be detailed in the following section 3.2.2.

The results obtained for the eight different pressure drops considered were collected and elaborated, in order to obtain curves of Fanning friction factor as a function of the number of elements of the different meshes. The corresponding values of u_0 lie between approximately 1 (Case #1) and 16 m/s (Case #8).

In particular, the grid-convergence analysis was carried out by adopting the well-established GCI, derived in [63], and considering the LS error estimation described in [64], already discussed and employed in chapter 2. For each mesh and for each pressure drop value, the GCI together with the asymptotic values obtained with the generalized Richardson extrapolation (that will be referred to simply as asymptotic values in the following) were calculated.

Additionally, the safety factor F_s was conservatively chosen here equal to 3 being the observed order of convergence greater than 2, as prescribed in [64].

An example of the results of this procedure is depicted figure 3.5, reporting the FoM values obtained with the different meshes and the extrapolated asymptotic value (red dashed line), representing an estimate of a mesh-independent result, while the results in terms of GCI are reported for all the pressure drop investigated in figure 3.6, where the GCI is referred to the values of f.

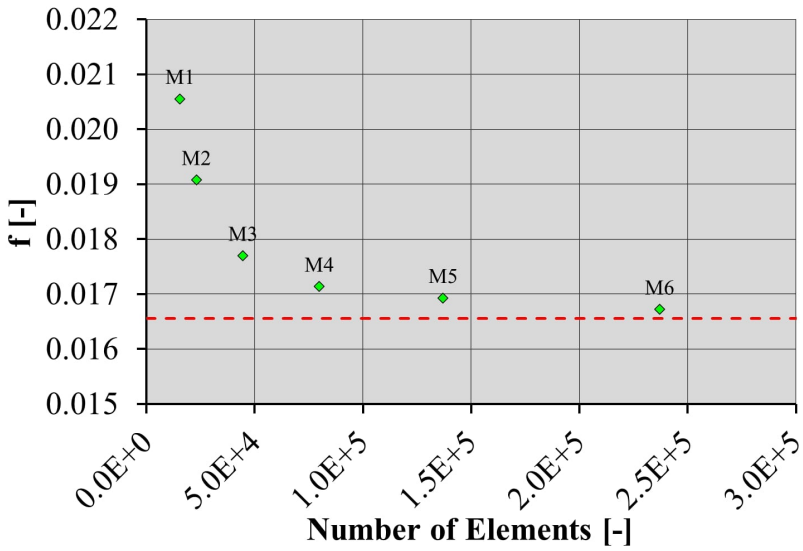

Figure 3.5: Grid independence results obtained for a pressure drop of 4.00 kPa.

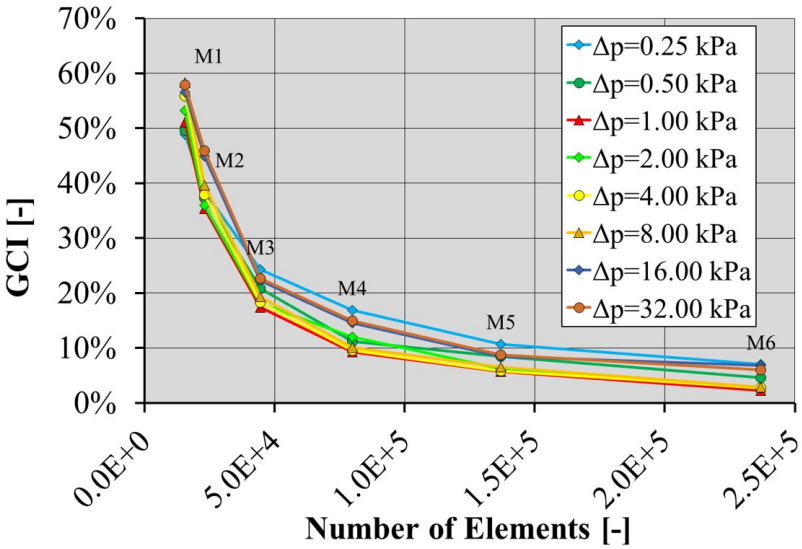

Figure 3.6: GCI results for all the considered pressure drop values.

Looking at the results depicted in figure 3.6, it is possible to notice how:

- the friction factor is always overestimated when considering coarse meshes, thus obtaining conservative results. Adopting the mesh M1, the resulting friction factor is overestimated, with a GCI in the order of 60%;
- only meshes M4, M5 and M6 are characterized by GCI values lower than 20% for all the considered pressure drop values, and below 15% for pressure drop higher or equal to 0.5 kPa;
- it is difficult to draw conclusions on the dependency of GCI on pressure drop, due to the effects of noisy convergence;
- high GCI values are obtained with the mesh independence assessment. This outcome is due to the FoM selected, being dependent quadratically on the real result of the simulation, i.e. the coolant mass flow rate.

From the outcomes of these analyses, it was decided to consider mesh M4 as the minimum size required to obtain fairly mesh-independent results, being the GCI values lower than 15% for almost all the pressure drop values considered, thus resulting in deviations lower than 5% with respect to the pertaining asymptotic values obtained by means of the Richardson extrapolation procedure.

3.2.2 Results validation

To further assess the quality of the results, the CFD outcomes were compared to literature data, selecting different correlations from [46, 83, 84]. To provide a common framework to compare the results of the different correlations, the formulation given by Manglik and Bergles [83], i.e. the friction factor expressed according to equation (3.1) and the Reynolds number according to equation (3.3), was considered.

$$Re_0 = \frac{\rho u_0 d_0}{\mu} \tag{3.3}$$

By employing this formulation, reference is made to quantities calculated considering an empty pipe, i.e. the tape envelope and the effects of swirl on velocity are not taken into account, making it straightforward a comparison with straight pipe results. Some preliminary definitions are given in the following, with reference to the geometrical features of the ST, depicted in figure 3.1. In particular, it is possible to define the dimensionless twist ratio parameter γ, defined as

$$\gamma = \frac{H}{d_0}, \tag{3.4}$$

the dimensionless area ratio A_r, that can be interpreted as the ratio between the empty cooling channel without ST area and the actual ST-equipped pipe area, i.e.

$$A_r = \frac{\pi}{\pi - (4\delta/d_0)}, \tag{3.5}$$

and d_r, the dimensionless diameter ratio, given in equation (3.6), representing the ratio between the hydraulic diameter and the inner pipe diameter.

$$d_r = \frac{\pi + 2 - (2\delta/d_0)}{\pi - (4\delta/d_0)}, \tag{3.6}$$

Considering the geometrical features of the PFU cooling channels relevant to the DEMO divertor, it can be possible to calculate $\gamma = 2.00$, $A_r = 1.09$, and $d_r = 1.74$.

With reference to the definitions given in the previous equations, it is possible to assume a general formulation of the friction factor formula as follows:

$$f = \alpha \, \mathrm{Re}_0^{\beta} \, d_r^{\eta} A_r^{\theta} g\left(\gamma\right), \tag{3.7}$$

where the coefficients α, β, η, θ, and the function $g(\gamma)$ depend on the specific correlation selected. This expression is valid for all the considered correlations, with the only exception of the one proposed by Dedov [84], for which the formula of equation (3.8) applies (which cannot be reduced to the given functional form of equation (3.7)).

$$f = \frac{1}{4}\left[1.82 \log \mathrm{Re}_0 + 1.82 \log\left(\frac{A_r\sqrt{1+\gamma^2}}{d_r}\right) - 1.64\right]^{-2} d_r A_r^2 \left(1+\gamma^2\right)^{1.5} \tag{3.8}$$

A summary of the coefficients of all the selected correlations is reported in table 3.5. It has to be moreover underlined how it is possible to usually find an

additional term in equation (3.7), to take into account the effects of temperature distribution inside the pipe cross-section on the pressure drop calculation. This term has been neglected here since all the simulations have been performed under isothermal conditions.

Table 3.5: Summary of the different coefficients of equation (3.7)

Correlation	α	β	η	θ	$f(\gamma)$
Manglik & Bergles [83, 85]	0.0791	-0.25	1.25	1.75	$1 + 2.752/\gamma^{1.29}$
Lopina & Bergles [83, 86]	0.1265	-0.2	1.2	1.8	$\gamma^{-0.406}$
Ibragimov [83, 87]	0.0791	-0.25	1.25	1.75	$1 + 14.375/\gamma^{4}$
Donevski & Kulesza [83, 88]	0.0791	-0.25	1.25	1.75	$1 + 3.813/\gamma^{1.61}$
Watanabe [83, 89]	0.046	-0.2	1.2	1.8	$1 + 3.65/(2\gamma/\pi)^{2}$
Raffray [46]	0.0525	-0.2	1.2	1.8	$\left(1 + (\pi/2\gamma)^{2}\right)^{-1.4}$
Dedov [84]	Not applicable, see equation (3.8)				

A comparison between the numerical results obtained with the mesh M4 and the correlations described above is shown in figure 3.7, reporting the 10% error bars with respect to numerical results. As can be noted, there is a very good agreement between numerical outcomes and experimental results.

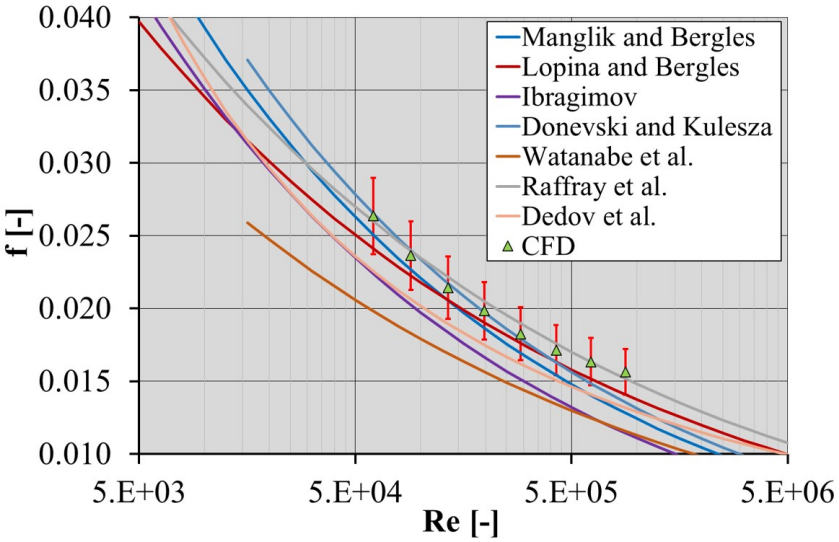

Figure 3.7: Comparison between numerical outcomes and experimental correlations (Mesh M4).

If the same validation procedure is repeated considering the M1 mesh described above, the results obtained are those shown in figure 3.8, where it is possible to clearly realize the magnitude of the pressure drop overestimation due to the conservative simulation of the Fanning friction factor. The results are reported with 10% error bars with respect to numerical results.

The results for the M1 mesh are reported here because the same size was used in the preliminary simulations of the 2021 divertor reported in [55], due to limitations

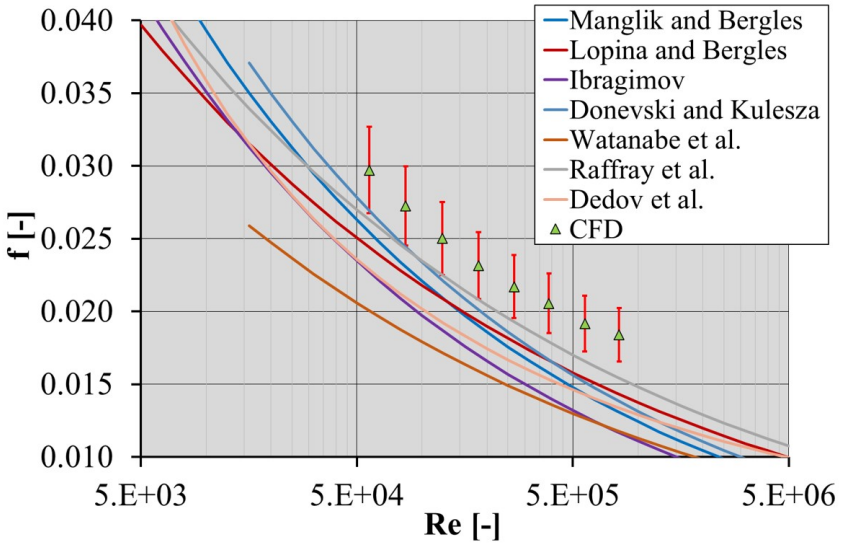

Figure 3.8: Comparison between numerical outcomes and experimental correlations (Mesh M1).

on the available computational resources.

Finally, figure 3.9 reports the results obtained with meshes M1, M4, and M6, showing the small differences between M4 and M6, an indication of acceptable mesh independence of the results.

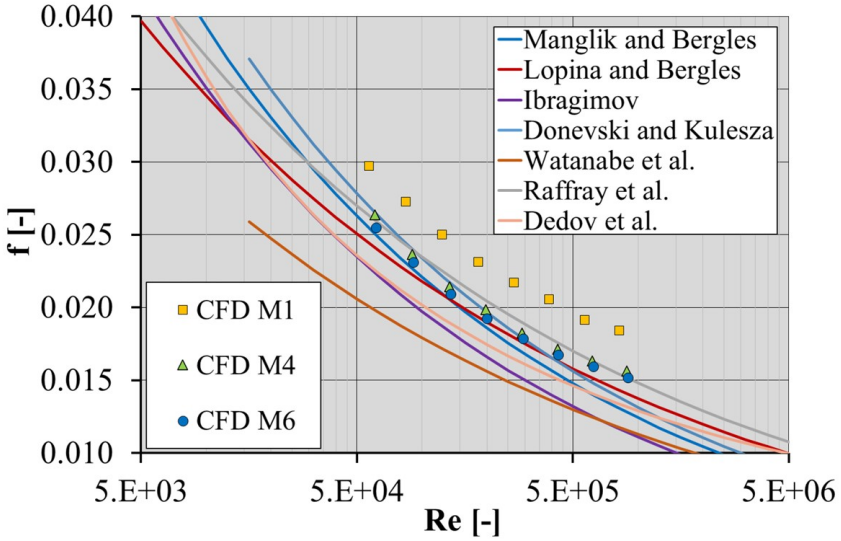

Figure 3.9: Comparison between numerical outcomes and experimental correlations for meshes M1, M4, and M6.

3.2.3 Sensitivity on turbulence modelling approach

Finally, the effect of employing different turbulence models was considered, and the results obtained are reported in figure 3.10. In particular, one additional from the k-ω family, i.e. the Ansys Generalized $k-\omega$ (GEKO) model, and two from the k-ϵ family, i.e. the standard and Re-Normalisation Group (RNG), details of

which can be found in [49]. For all the cases, the mesh M6 was considered to safely assume all the simulations to be close enough to their asymptotic values, and a grid with a coarser first layer was taken into account for the k-ϵ models, so to be compliant with the requirements of the near-wall treatment. It should be noted that, by changing the turbulence model, it should be necessary to repeat the entire grid-independence procedure. To check whether the mesh M6 is fine enough to obtain mesh-independent results without performing the complete procedure, an additional set of analyses was performed with the mesh M4, showing how variations in the order of 5% are obtained between M4 and M6 for all the turbulence models, thus confirming that the results presented in the following are fairly independent on the selected mesh.

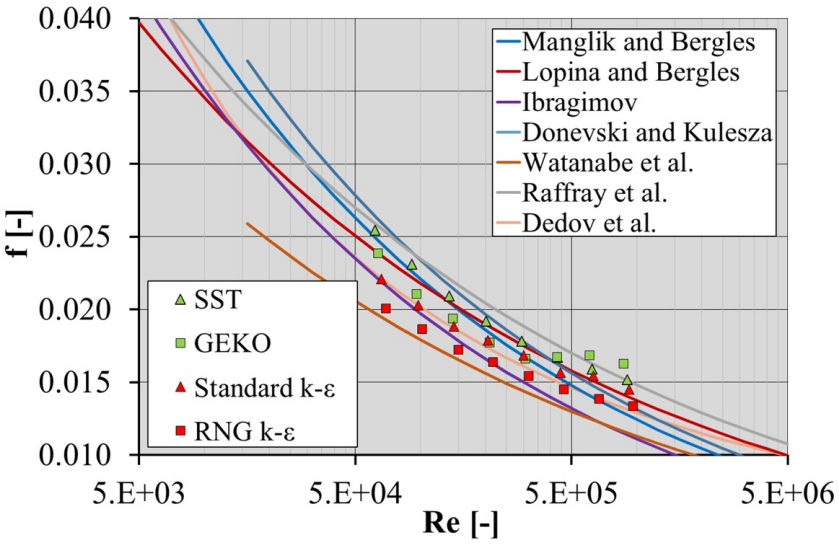

Figure 3.10: Comparison between numerical outcomes and experimental correlations for different turbulence models (Mesh M6).

As can be noted, the use of different turbulence models leads to significant variations in the outcomes of the analyses. Nevertheless, the results always lie within the region delimited by the different correlations (except for the GEKO model at high Reynolds numbers), and the most conservative turbulence model among those considered appears to be the SST for most of the pressure drop values considered. Despite the significant variation in the results, no over-conservative outcomes as for figure 3.8 are predicted with different turbulence models.

In conclusion, the results obtained here confirm what was already highlighted in [76] and add other aspects to be accounted for when performing CFD calculations of the PFU cooling channels. In particular it was found that:

- particularly dense calculation grids are required to correctly predict the fluid-dynamic behaviour of the ST-equipped PFU cooling channels. At least $\approx 3 \cdot 10^{10}$ elements per cubic meter are required to have a GCI lower than 15-20% for the Fanning friction factor in a reasonable range of empty pipe

coolant velocities, between 1 and 16 m/s, resulting in ≈5% deviation from the asymptotic values obtained by means of Richardson extrapolation;

- coarser meshes, such as the M1 described previously (resulting in a grid density of $\approx 6 \cdot 10^9$ elements per cubic meter), exhibit a significant overestimation of the Fanning friction factor, with a GCI in the order of 60%, thus resulting in a poor prediction of the characteristic function curve;
- the adoption of different turbulence models certainly affects significantly the results, but outcomes obtained with different modelling approaches always lie within the range delimited by the different correlations;
- among the considered turbulence modelling approaches, k-ω SST provides the most conservative results in most of the cases.

Unfortunately, employing such fine meshes results prohibitive, and it was then deemed necessary to find an alternative approach to reduce the computational and pre-processing efforts required to correctly simulate these components. Moreover, comparing the results obtained with those of [76], it can be argued how a finer mesh is required to correctly reproduce the pressure drop of the single PFU cooling channel, compared to the one adopted for the complete OVT mock-up. This discrepancy can be probably justified by the fact that having several PFU cooling channels in parallel, if their pressure drop is overestimated due to an insufficiently fine mesh, the fluid-dynamic system responds by flattening the flow distribution between the various PFU assemblies, thus reducing the total pressure drop. In fact, the distribution of mass flow rate is determined by the combined effect of hydraulic resistances of the PFU cooling channels, the distributor and the collector. Being the resistance of all the PFU almost the same for all the channels in parallel to each other, if the hydraulic resistance of these latter is small, the coolant mass flow rate distribution is uneven and strongly affected by the resistances of the non-ideal distributor and collector. Increasing the resistance of the PFU cooling channels, the effect of collector and distributor becomes less important, and the distribution tends to flatten, due to the non-linear dependency of the pressure drop on the coolant mass flow rate. Furthermore, it should be considered the uncertainty on the surface roughness values of CuCrZr tubes, STs, and manifold, which most likely hide the effects related to the selection of the mesh size.

3.3 Detailed simulation of a single PFU channel

The problem of reducing the computational cost of simulating the PFU cooling channels equipped with the STs was already addressed in the first studies on the fluid-dynamic behaviour of DEMO divertor PFC cooling circuit. The methodology adopted in [22] and discussed more in detail in [90] foresaw the simulation through CFD of the simple cylindrical pipe without inserting the STs and leaving the

evaluation of their effect on the pressure drop to a post-analysis hand-made correction performed by means of proper correlations.

More in detail, this approach was based on the assumption that the pressure drop inside the ST-equipped PFU cooling channel can be calculated as the sum of the pressure drop occurring inside the empty pipe, not considering the presence of the ST, and an additional correction term, that is in turn composed of three contributions:

- a concentrated sudden contraction loss, whose loss coefficient K_c is calculated according to:

$$K_c = 0.5 A_r \left(A_r - 1\right), \tag{3.9}$$

  rearranged from [91], where the loss coefficient is referred to the empty pipe velocity, i.e. the pressure drop can be calculated as:

$$\Delta p = K_c \frac{1}{2} \rho u_0^2, \tag{3.10}$$

  representing the pressure loss related to the change of section occurring at the beginning of the ST section;
- a distributed pressure drop estimated in terms of Fanning friction factor correction, simply calculated as the difference between a proper correlation valid for ST-equipped channels, as those of equation (3.7), and a suitable correlation for empty pipes;
- a concentrated Borda-Carnot loss, whose loss coefficient K_e is calculated according to:

$$K_e = \left(A_r - 1\right)^2, \tag{3.11}$$

  rearranged from [91], representing the change of section occurring at the end of the ST section.

This methodology, although promising, was shortly abandoned as soon as computing resources allowed the complete simulation of the cooling circuit with the inclusion of the STs [24]. However, by adopting this approach it was not possible to correctly estimate the pressure drop of the entire PFU cooling channel, as will become clear throughout this section, so it would have been necessary to abandon it anyway.

The analyses discussed in this section take this methodology as a starting point, assess its limitations and lay the foundations for the implementation of pressure drop correction through the use of an equivalent porous medium, which will be dealt with

in detail in the following sections, in such a way as to avoid the correction being carried out a-posteriori, that would result in particular in a distortion of the coolant mass flow rate distribution among the different PFU cooling channels connected in parallel.

First of all, a detailed 3D-CFD simulation of the flow field inside a complete PFU cooling channel was carried out. The activity was performed focussing the attention on the 2021 DEMO divertor OVT and IVT PFU channel geometry, already detailed in chapter 1 but, for the sake of brevity, only the results relevant to the complete OVT channel are reported here, being the phenomenology involved the same. The geometry considered for the analyses is the one depicted in figure 3.11, which has been simulated under the coolant operative conditions, models, and assumptions summarized in table 3.6.

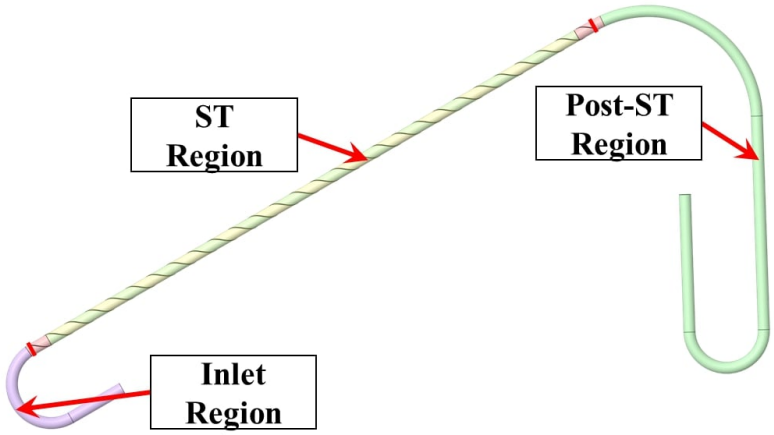

Figure 3.11: ST-equipped PFU cooling channel computational domain.

Table 3.6: Summary of PFU cooling channel CFD analysis setup.

Analysis Type	Steady-state isothermal
Material Library	Water (constant properties)
Reference temperature	133°C
Reference absolute pressure	45 bar
Turbulence Model	k-ω SST
Boundary Layer Modelling	Automatic Wall Functions
Pipe roughness	1 μm [46]
ST roughness	0.5 μm [46]
Inlet velocity	6 m/s
Outlet relative static pressure	0 Pa

The mesh features selected for the PFU cooling channel are reported in table 3.7, selecting the parameters relevant to mesh M4 discussed in the previous section, while some details of the mesh set up for the PFU analysis are shown in figure 3.12.

Table 3.7: PFU cooling channel analysis mesh parameters.

Mesh Parameter	**Value**
Mesh Type	Hybrid Hexa - Tetra
Nodes	$4.86 \cdot 10^6$
Elements	$5.06 \cdot 10^6$
Inflation Layers Number	12
First Cell Height [μm]	20
Layers GR	1.2
Target Element Size [mm]	0.59
Surface with y^+>100 [%]	0

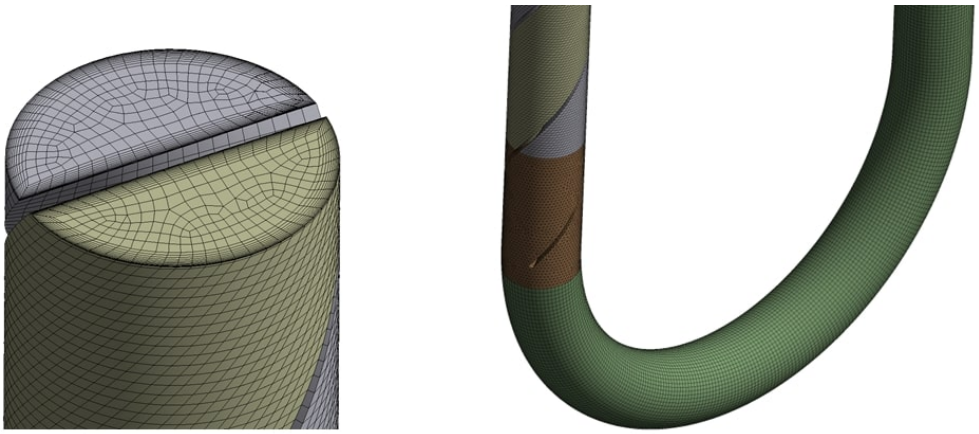

Figure 3.12: Mesh adopted for the PFU cooling channel CFD analysis.

The results obtained for the divertor OVT PFU cooling channel in terms of local Fanning friction factor along s, the curvilinear abscissa of the pipe axial line, are shown in figure 3.13, also reporting the comparison with Manglik and Bergles correlation valid for ST-equipped pipes, given in table 3.5, and Haaland correlation [92] valid for straight *empty* pipes, detailed in equation (3.12), where ϵ is the sand-grain equivalent surface roughness.

$$\frac{1}{\sqrt{f}} = -3.6 \log \left(\frac{6.9}{\mathrm{Re}} + \left(\frac{\epsilon}{3.7 d_0} \right)^{1.11} \right), \tag{3.12}$$

It should be pointed out that the local Fanning friction factor is simply obtained from the simulation starting from the average pressure measured at two monitoring sections, p_1 and p_2, and the distance l between these two sections, by adopting equation (3.13).

$$f_{CFD} = \frac{p_1 - p_2}{2\rho u_0^2 \left(l/d_0 \right)} \tag{3.13}$$

As can be noted from figure 3.13, there are two main deviations from the relevant

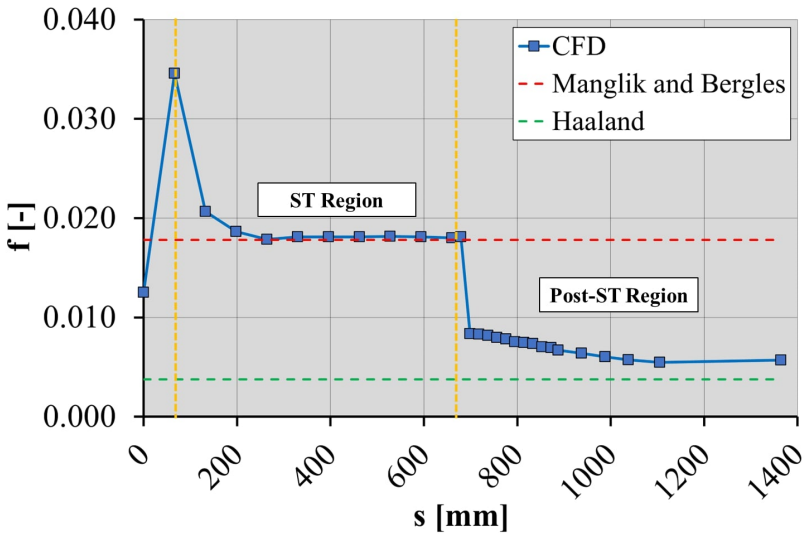

Figure 3.13: Local Fanning friction factor along the PFU cooling channel curvilinear abscissa.

correlations: an initial peak, corresponding to the inlet section of the ST region, and a higher friction factor value in the post-ST region, decaying along the curvilinear abscissa.

To better understand these two deviations, two further fluid-dynamic analyses were carried out. In particular, the same results were reproduced considering the cooling channel without the addition of the ST and the cooling channel with a no-twist ST, which corresponds to the $\gamma = \infty$ condition. These analyses were performed using table 3.6 settings and mesh parameters similar to those shown in table 3.7. The results of this comparison are shown in figure 3.14.

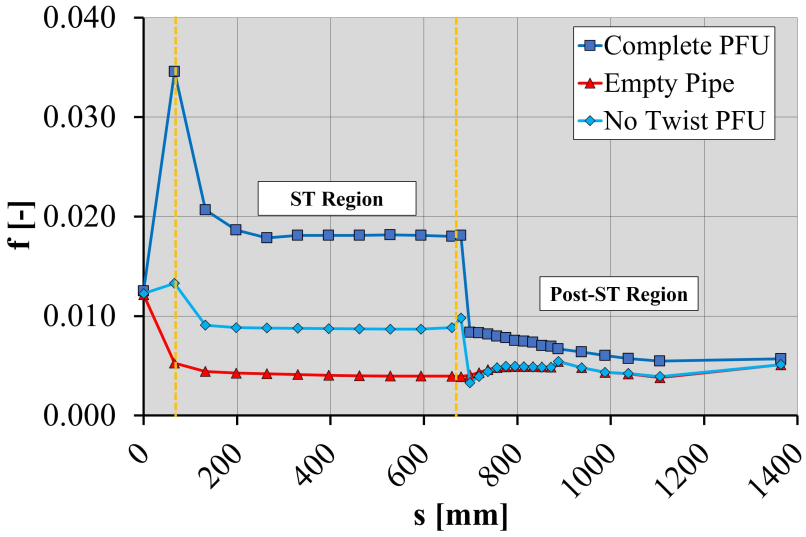

Figure 3.14: Comparison of local Fanning friction factor along the PFU cooling channel curvilinear abscissa.

Regarding the initial peak, its occurrence is related to section restriction at the

entrance of the ST region, as correctly defined already in [90]. This can be confirmed by looking at figure 3.14 because the same effect is encountered when no-twist ST is embedded in the cooling channel, while it is not observed in the case of empty pipe. However, it can be also argued from figure 3.14 that the concentrated loss of the pipe with a no-twist ST is significantly lower than in the case of the complete PFU cooling channel.

A more detailed analysis highlights that this effect is related to the presence of strong flow separation at the entrance of the ST region, as clearly visible in figure 3.15. The separation occurs only on one side of the ST, far from the axis of the cooling channel, mainly promoted by the local unfavourable curvature of the ST. Even if it is localized on a length scale of a half ST pitch (H), it results in a localized pressure drop amounting to $\approx$7% of the overall pressure drop inside the entire PFU cooling channel. Moreover, it has to be highlighted how the height of the resulting pressure peak is most likely to depend on the orientation of the ST inside the PFU cooling channel, as well as on the curvature of the pipe bend in the PFU inlet region of figure 3.11.

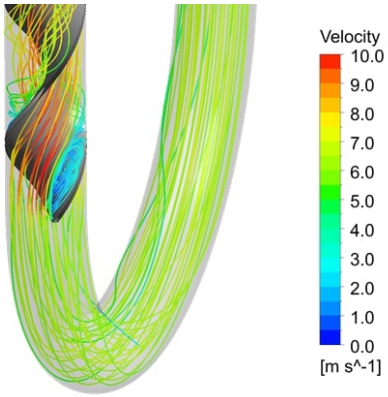

Figure 3.15: Details of the flow field at the entrance of the ST region.

Concerning the second effect, i.e. a higher pressure drop in the post-ST region, some considerations can be drawn from the comparison of figure 3.14. In particular, the effect is not related to the curvature of the post-ST part of the PFU cooling channel, since no similar phenomenon is observed for the empty pipe case (red line). Moreover, it cannot be neither related to the sudden expansion of the flow, since the same behaviour is not observed for the cooling channel with the no-twist ST (light blue line), where the expansion is clearly identifiable as a small "spike" corresponding to the outlet section of the ST.

The effect is instead due to the persistence of the swirling motion in the region downstream of the ST, as clearly visible in figure 3.16.

As may be argued from the picture, the swirling motion decays moving towards the outlet, resulting in a straightening of the fluid flow inside the pipe, due to the occurrence of viscous effects. The effect is almost completely lost after the sharp bend in the final part of the PFU channel. The magnitude of this second effect

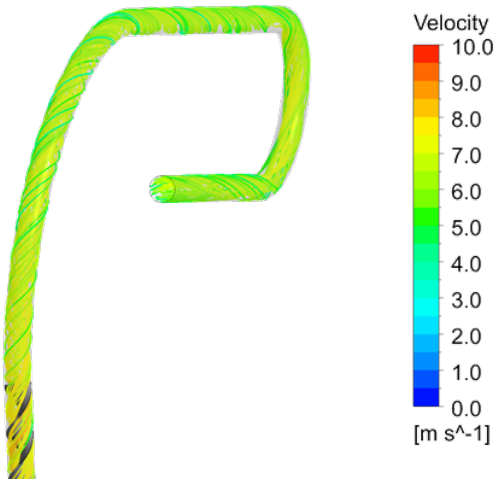

Figure 3.16: Persistence of the swirling motion in the post-ST region.

is estimated to account for ≈2% of the total pressure drop inside the entire PFU channel, resulting in a lower importance if compared to the initial peak. Nonetheless, the importance of this second effect may become more relevant if, for example, shorter STs are equipped, or if the shape of the post-ST region of the cooling channel is different.

Summing up these two effects, they result in a ≈10% of the overall pressure drop inside the PFU cooling channel, and thus they must be taken into account to avoid an unduly underestimation of the pressure drop.

Furthermore, similar results are obtained by varying the coolant inlet velocity, as suggested by the results of dedicated numerical analyses. In particular, by adopting the same setup summarized in table 3.6 and the same mesh whose details are provided in table 3.7, the results obtained for coolant inlet velocities from 6 to 16 m/s are reported in figure 3.17. It should be moreover noted that the preliminary analyses reported in section 3.2 showed how a fair mesh-independence of the results is obtained for all the coolant velocities considered for the mesh M4, whose features are identical to those of the mesh employed for the analysis of the entire PFU cooling channel.

As can be argued from the figure, the initial peak and the post-ST decay are observed for all the values of coolant inlet velocity considered, while the friction factors decrease as the inlet coolant velocity increase, in agreement with the correlations presented in section 3.2.

From the analysis of the results obtained, it can be argued that the adoption of concentrated losses at the inlet and outlet of the ST section of the cooling channel cannot be addressed by using sudden contraction and Borda expansion coefficients reported in the first part of this section, as they would result in an underestimation of the total pressure drop. The adoption of an a-posteriori correction of the pressure loss would thus require a definition of more suitable loss coefficients, but this choice

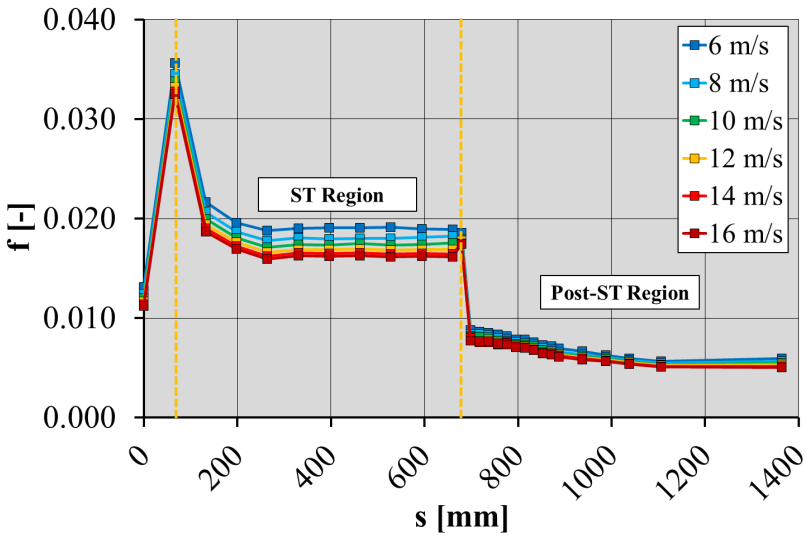

Figure 3.17: Local Fanning friction factor along the PFU cooling channel curvilinear abscissa for different coolant inlet velocity values.

would definitely impair the possibility of realistically predicting the mass flow rate distribution among the different PFU cooling channels and, hence, the margin against CHF.

3.4 The virtual swirl tape approach

The development of a numerical model relying on the adoption of porous media domains to reproduce the effect that the ST has on the flow field, in particular in terms of pressure drop, was thus pursued. This approach, called VST, was developed following two parallel research lines, which led to the development of two different modelling techniques, namely the Isotropic Virtual Swirl Tape (IVST) and the Orthotropic Virtual Swirl Tape (OVST), that will be detailed in the following.

3.4.1 The isotropic virtual swirl tape approach

The IVST approach is the simplest model that has been developed, and it is based on the adoption of two distinct porous regions, one aimed at reproducing the pressure drop inside the ST (accounting for both the initial flow separation-induced peak and the fully-developed swirling motion inside the ST-equipped pipe), and the other simulating the additional losses encountered inside the post-ST region, that are only due to the swirling motion decay already thoroughly discussed in the previous section. These two porous regions are shown in figure 3.18, respectively in red and in blue. As can be noted from the figure, the blue porous region is extended up to the upper straight part of the PFU cooling channel, before the last bend, coherently with the results discussed in section 3.3.

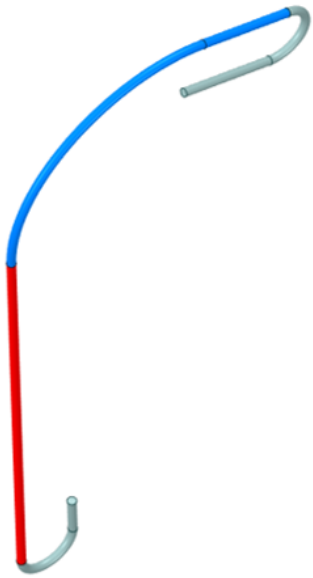

Figure 3.18: Porous regions adopted in the IVST approach.

It is worth mentioning that two porous media are considered instead of a single one with the aim to obtain an indication of the static pressure at the outlet section of the PFU cooling channel equipped with the ST. A good prediction of the coolant absolute pressure along the entire ST is required to correctly predict the CHF margin of the component.

Each one of the two regions is simulated taking into account a properly calibrated isotropic momentum sink term acting as a source term in the Navier-Stokes equations, defined according to equation (3.14), where $\underline{u}$ is the local velocity vector and $\|\cdot\|$ is the norm operator.

$$\underline{S} = -K_{loss}\frac{\rho}{2}\|\underline{u}\|\,\underline{u} \tag{3.14}$$

According to this equation, the force per unit volume acting on the fluid $\underline{S}$ is oriented along the same direction as the velocity vector $\underline{u}$ due to the isotropy of the loss coefficient, here reported as a scalar quantity for simplicity.

The K_{loss} coefficients relevant to the two porous regions can be determined with a staged approach:

1. detailed 3D-CFD simulations of the PFU cooling channels, as the one presented in section 3.3, are performed. The overall total pressure drop and the total pressure drop relevant to the ST region only can be calculated and collected considering a single mass flow rate relevant to the considered PFU cooling channels;
2. the K_{loss} coefficients are obtained by means of dedicated optimization studies, performed by adopting the Ansys Direct Optimization tool [93], aimed at finding a couple of K_{loss} coefficients for the two porous regions such that the

overall pressure drop and the pressure drop of the ST region are reproduced with the smallest error. With this approach, relying on the adoption of an optimization algorithm, it is possible to easily define the required porous media domains, with a very limited computational effort;

3. the results obtained at step 1. are compared with those of the IVST PFU cooling channel, considering mass flow rates within a certain range from the calibration value, to evaluate if it is able to maintain a good predicting capability when limited mass flow rate deviations are considered.

An advantage of the VST approach is the possibility, aiming at reducing the computational grid, to select arbitrarily coarse elements for the porous media, allowing for a reduction of the computational cost of both the optimization phase and when adopting VSTs in more complex simulations. In fact, mesh-related errors can be compensated by an optimal selection of the parameters, provided that the same mesh used for calibration is later employed for the following analyses.

For the analysis, a mesh bulk size of 1.3 mm was selected, and the mesh was generated with the same layer parameters reported in table 3.7. The resulting mesh was composed only of hexa and prism elements, resulting in $5.8 \cdot 10^5$ finite volumes and $5.6 \cdot 10^5$ nodes, with a reduction in the overall number of cells and nodes by a factor of 10 compared to the detailed simulation discussed in the previous section.

To test the performance of the IVST approach, the calibration procedure was performed considering 12 m/s as the reference coolant velocity, and the selection of the K_{loss} coefficients was performed with the Multi-Objective Genetic Algorithm (MOGA) optimizer. The optimization phase took 182 iterations to converge, resulting in a K_{loss} of 4.91 m^{-1} for the ST region and 0.89 m^{-1} for the post-ST porous medium, with an error with respect to the reference values of pressure drop lower than 1%. The comparison of the local Fanning friction factor along the PFU cooling channel curvilinear abscissa is provided in figure 3.19, while the pressure evolution along the cooling channel is depicted in figure 3.20.

As it may be argued from the figures, the initial peak is significantly underestimated by the IVST approach, conversely, its effect on pressure drop is compensated by a constant and increased loss coefficient along the entire ST region, thus resulting in a pressure value at the outlet of the ST region close to the one of the complete PFU cooling channel calculation. The post ST region instead presents some fluctuations in the Fanning friction factor profile, and it is not able to compensate for the lack of swirling flow, thus resulting in a lower pressure drop. The overall behaviour of this approach is however acceptable, and the pressure drop values deviate by a small amount from the desired target values. In particular, relative errors on pressure drops with respect to the complete PFU cooling channel simulation are reported in table 3.8, where the ST mid section is a probing section placed in the middle of the straight part of the PFU cooling channel, where the

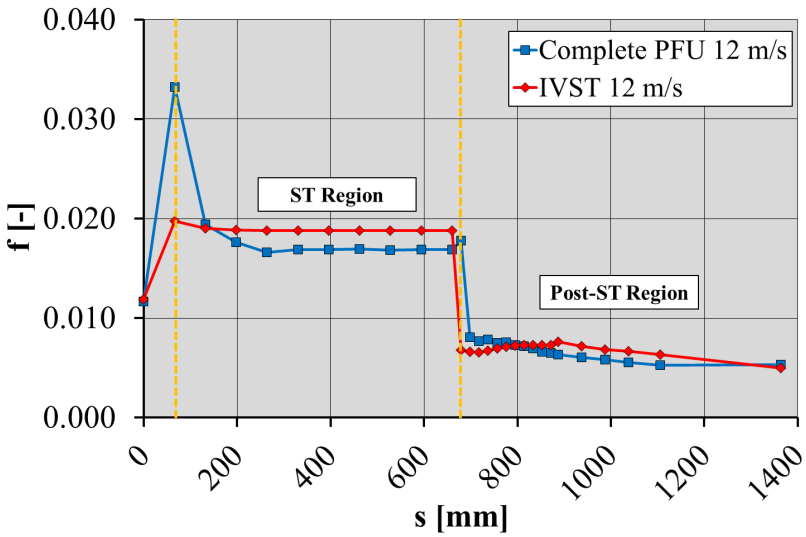

Figure 3.19: Comparison of local Fanning friction factor along the PFU cooling channel curvilinear abscissa between complete simulation and IVST approach.

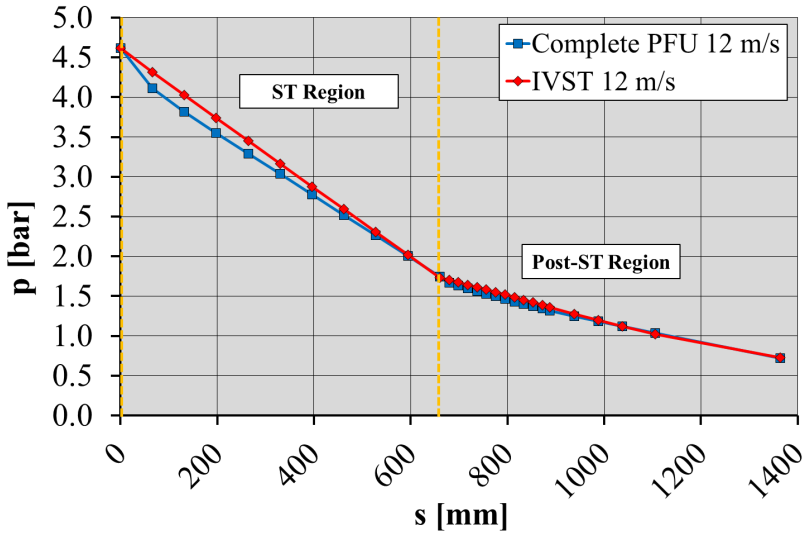

Figure 3.20: Comparison of pressure evolution along the PFU cooling channel curvilinear abscissa between complete simulation and IVST approach.

strike point is supposed to be located. As it may be argued from the table, the pressure drops of the entire cooling channel and of the ST region alone are predicted with good accuracy, while the pressure drop between the inlet and the location of the strike point is underestimated by 7%.

Table 3.8: Pressure drop relative errors of the IVST approach.

Probing sections	**Value** [%]
Inlet - Outlet	-0.1
Inlet - ST Outlet	+0.6
Inlet - ST mid section	-7.0

As anticipated, an additional test to be performed is related to the capability of the approach to maintain bounded errors when the coolant mass flow rate deviates from the value adopted for the calibration of the porous media. To this purpose, a set of analyses was performed by changing the inlet velocity from 6 to 16 m/s and comparing the results with those presented in section 3.3. The outcomes obtained are reported in figure 3.21, showing the pressure drop predicted for the entire PFU cooling channel and for the ST region only by the complete CFD model and by the IVST modelling approach, together with 10% error bars for the results of the complete model. As it may be argued from the figure, there is a really good agreement between the curves, showing that by adopting this approach it is possible to correctly predict the pressure losses over a broad range of coolant inlet velocities. In particular, the maximum deviations occur for the points characterized by the lower velocities, for which a relative error of 7% is measured between the complete and the IVST model.

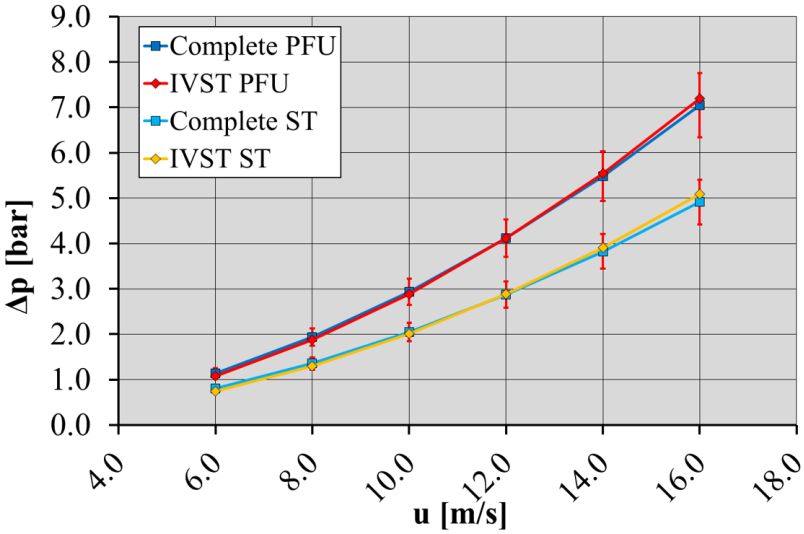

Figure 3.21: Comparison of pressure drop prediction between complete simulation and IVST approach.

In conclusion, the IVST approach allows for a reduction in the overall number of elements of the computational grid almost up to a factor of 10, while maintaining a good accuracy in the prediction of the pressure drop, being the relative errors lower than a few per cent. The main drawback related to this method is due to its lack of generality: in fact, each PFU channel type requires a dedicated calibration campaign for both regions. Moreover, the swirling motion is not simulated with this approach, posing some limitations in the adoption of the methodology to perform non-isothermal simulations, as will be discussed in section 3.4.3.

3.4.2 The orthotropic virtual swirl tape approach

The idea behind the definition of a second VST approach, different from the IVST, is to reproduce the pressure drop of the ST region and of the entire PFU cooling channel by adopting a single porous domain with a properly defined momentum source term, possibly corresponding to the ST region, as depicted in figure 3.22.

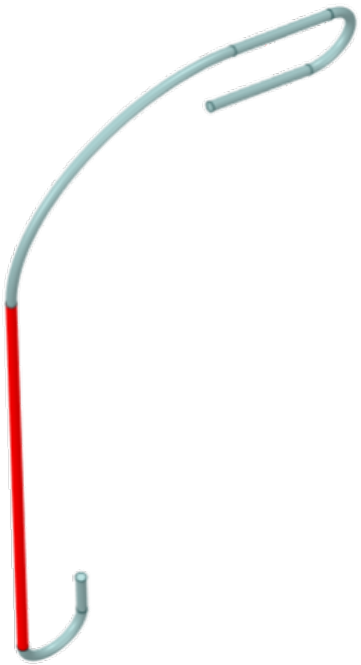

Figure 3.22: Porous region adopted in the OVST approach.

As can be expected, a single isotropic and uniform porous medium should be in principle able to determine a pressure loss only inside its domain, marginally affecting the flow field outside this region, and making difficult the realistic simulation of the local pressure at the outlet sections of both the ST and the entire PFU cooling channel at the same time. However, if this single porous medium is defined such as to determine a swirling motion of the fluid, it would be possible to realistically predict the desired pressure profile.

To this purpose, the porous medium should be able to determine a preferred direction of fluid motion within its domain, requiring the definition of a non-isotropic momentum source term in the Navier-Stokes equations.

It should be noted that a momentum source term can be defined directly inside the ST region of the PFU cooling channel without any need to implement a porous medium, so to provide a tangential velocity component to the coolant, and to virtually reproduce the target swirling flow. However, this approach (which was initially investigated for its simplicity) was soon abandoned because it determined the feeding of kinetic energy to the fluid, thus resulting in an artificial compensation of the pressure loss.

According to the rotating slug flow model proposed by Gambill [69], the tangential velocity component u_θ inside a pipe equipped with a ST can be related to the axial velocity u_z by the relation given in equation (3.15), where r is the radial coordinate of the cylindrical coordinate system aligned with the axis of the cooling channel.

$$u_\theta = u_z \frac{\pi}{2\gamma} \frac{r}{d_0/2} \tag{3.15}$$

From this equation, it is possible to calculate the preferred flow direction angle θ with respect to the axial direction, given in equation (3.16).

$$\theta = arctan\left(\frac{\pi}{2\gamma} \frac{r}{d_0/2}\right) \tag{3.16}$$

As it can be argued from the equation, the preferred flow direction is characterized by a varying angle θ that is a function of the radial coordinate. It is then possible to determine the directional cosines of this preferred direction of the fluid $\underline{n}_1$, referred to the local cylindrical coordinate system reported in equation (3.17), where the three components are given respectively along the radial, tangential, and axial directions.

$$\underline{n}_1(r) = \begin{bmatrix} 0 \\ \dfrac{\frac{\pi}{2\gamma}\frac{r}{d_0/2}}{\sqrt{1+\left(\frac{\pi}{2\gamma}\frac{r}{d_0/2}\right)^2}} \\ \dfrac{1}{\sqrt{1+\left(\frac{\pi}{2\gamma}\frac{r}{d_0/2}\right)^2}} \end{bmatrix} \tag{3.17}$$

For clarity, the main directions adopted for the OVST modelling are reported in figure 3.23, together with the definition of the angle θ and an indication of the cylindrical coordinate system $(\underline{r}, \underline{\varphi}, \underline{z})$ of the single PFU cooling channel.

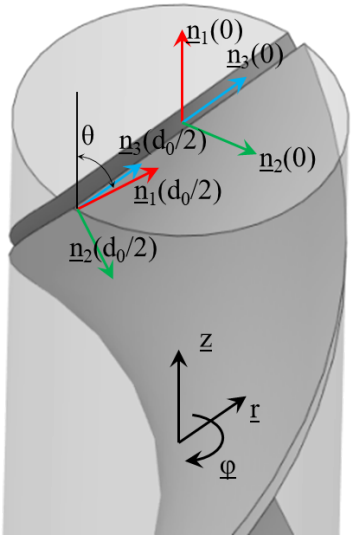

Figure 3.23: Main directions adopted for the OVST modelling.

A simple implementation of a numerical model relying on a single porous medium could be thus based on the adoption of an orthotropic sink term, in which two values of K_{loss} coefficients are given, one in the preferred direction $\underline{n}_1$, namely $K_{loss,1}$, and another (higher) along all the perpendicular directions, namely $K_{loss,2-3}$. It is interesting to note that, adopting a uniform value of $K_{loss,1}$ along the $\underline{n}_1$ direction, it is not possible to develop a strong swirling motion, as the fluid is most likely to flow at low values of r, due to the shortest path available. It is in fact possible to easily calculate that, for the rotating slug flow model, the distance travelled by the fluid L_{fluid} varies with the radius and is equal to:

$$L_{fluid} = l_{ST}\sqrt{1 + \left(\frac{\pi}{2\gamma}\frac{r}{d_0/2}\right)^2}, \tag{3.18}$$

where l_{ST} is the axial length of the ST. Consequently, to force the fluid to move far from the pipe axis, a non-uniform loss coefficient must be defined. The function $K_{loss,1}(r)$ should be a decreasing function with r, so as to have a maximum corresponding to $r = 0$. The loss coefficient function can be chosen arbitrarily, and the form of equation (3.19) was selected for its simplicity, where B, C and D are coefficients to be selected through the optimization procedure.

$$K_{loss,1} = (B - Cr)^D . \tag{3.19}$$

Concerning $K_{loss,2-3}$, a high value, equal to 100 m^{-1}, was selected, being a good compromise between the numerical stability of the simulation and the blockage of fluid motion along the direction perpendicular to the tape. The resulting source term to be adopted in the Navier-Stokes equations is thus defined according to equation (3.20).

$$\underline{S} = -\begin{bmatrix} (B - Cr)^D & 0 & 0 \\ 0 & 100m^{-1} & 0 \\ 0 & 0 & 100m^{-1} \end{bmatrix} \frac{\rho}{2} \|\underline{u}\| \, \underline{u} \tag{3.20}$$

This first OVST formulation suffers from the fact that the fluid is avoided from moving along all the directions perpendicular to $\underline{n}_1$, including the radial direction. It results that the coolant is forced to flow along the prefixed trajectory defined by the preferred direction, and thus any rearrangement of the fluid inside the section is forbidden by the high loss coefficient along the other directions. To overcome this issue, a different formulation can be given as follows: the high value of K_{loss} coefficient is assigned to a single direction, while all the directions perpendicular to it are provided by a suitable and lower value of the loss coefficient.

The possible choice of this direction is such that to be perpendicular to both the preferred direction of equation (3.17) and the radial direction. It results in the vector

reported in equation (3.21), that corresponds to the direction $\underline{n}_2$ of figure 3.23.

$$\underline{n}_2 = \begin{bmatrix} 0 \\ \frac{-1}{\sqrt{1+\left(\frac{\pi}{2\gamma}\frac{r}{d_0/2}\right)^2}} \\ \frac{\frac{\pi}{2\gamma}\frac{r}{d_0/2}}{\sqrt{1+\left(\frac{\pi}{2\gamma}\frac{r}{d_0/2}\right)^2}} \end{bmatrix} \tag{3.21}$$

The source term to be adopted in the Navier-Stokes equations is thus defined according to equation (3.22). As can be noted from equation (3.22), the loss coefficient matrix is diagonal, hence the name orthotropic VST.

$$\underline{S} = -\begin{bmatrix} (B-Cr)^D & 0 & 0 \\ 0 & 100m^{-1} & 0 \\ 0 & 0 & (B-Cr)^D \end{bmatrix} \frac{\rho}{2} \|\underline{u}\| \, \underline{u} \tag{3.22}$$

The constants to be adopted for the loss coefficient can be determined always with an optimization procedure. As can be argued, the OVST approach is in principle able to reproduce the swirling motion of the fluid, with two main advantages: it could be better suited to correctly capture the heat transfer coefficient of the fluid, and it does not require in principle a dedicated calibration depending on the geometry of the post-ST region. Nevertheless, the complexity of the numerical approach is significantly greater than that of the IVST model.

As for the IVST, to test the performance of the OVST approach, the results depicted in figure 3.17 relevant to the velocity value of 12 m/s were taken as a reference for the calibration of the porous medium, and the procedure for the calibration of the K_{loss} constants was performed with the MOGA optimizer. Moreover, differently from the procedure adopted for the IVST, also the static pressure drop across the ST-equipped region was selected as a target value to be obtained through the optimization procedure. Furthermore, the same mesh employed for the IVST was also selected for the OVST, so as to avoid any mesh-induced difference in the results.

The optimization phase took 116 iterations to converge, resulting in B, C and D coefficients as reported, in proper units, in table 3.9.

Table 3.9: Coefficients of the OVST porous medium.

Parameter	**Value**
B	3.21
C	1.99
D	1.45

The comparison of the local Fanning friction factor along the PFU cooling channel

curvilinear abscissa is provided in figure 3.24, while the pressure evolution along the cooling channel is depicted in figure 3.25.

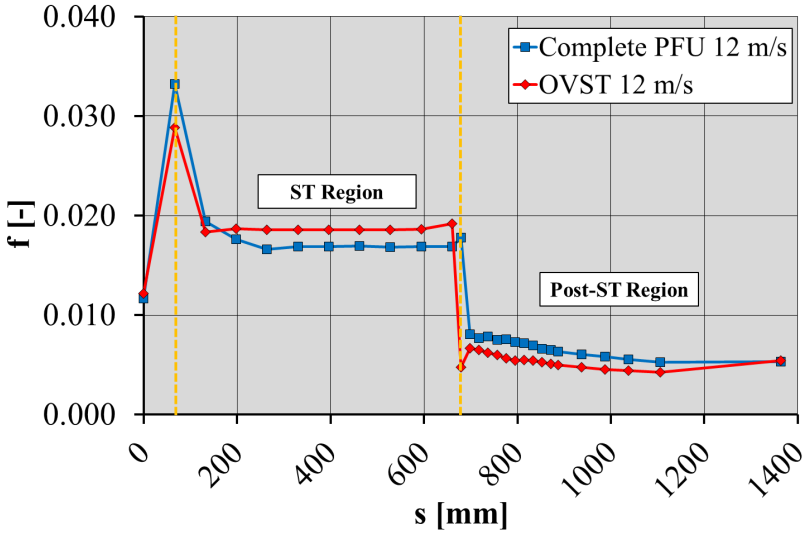

Figure 3.24: Comparison of local Fanning friction factor along the PFU cooling channel curvilinear abscissa between complete simulation and OVST approach.

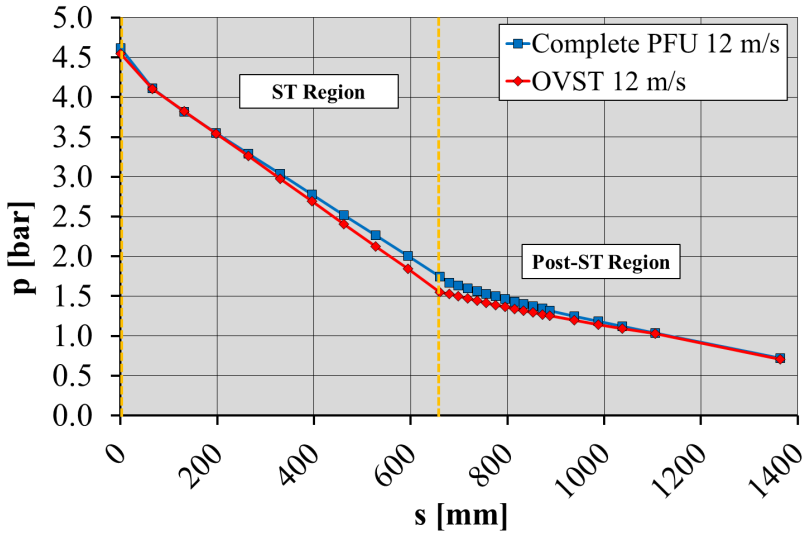

Figure 3.25: Comparison of pressure evolution along the PFU cooling channel curvilinear abscissa between complete simulation and OVST approach.

As it may be argued from the figures, the model can capture the initial peak of the Fanning friction factor, while the pressure drop along the ST region is slightly overestimated. Regarding the post-ST region, the pressure loss is underestimated with respect to the original profile, but the profile is similar between the correct curve and the one resulting from adopting the OVST. These results suggest that the swirling motion is correctly predicted, but its strength may be underestimated. More in general, it can be concluded that the pressure drop is overestimated in

the ST region to compensate for the inability of the model to fully capture all the features of the swirling motion in the post-ST region.

Relative errors on pressure drops with respect to the complete PFU cooling channel simulation are reported in table 3.10. As it may be argued from the table, the total pressure drop and the pressure drop up to the strike point are predicted with good accuracy, while the result in terms of ST pressure drop is overestimated by ≈4%, thus resulting in conservative outcomes.

Table 3.10: Pressure drop relative errors of the OVST approach.

Probing sections	**Value** [%]
Inlet - Outlet	-1.1
Inlet - ST Outlet	+4.5
Inlet - ST mid section	-0.1

The resulting flow field is depicted in figure 3.26, showing the fluid swirling motion induced by the OVST porous medium with a detail of the ST section inlet. It is interesting to observe from the figure that no flow separation is obviously observed since there is no solid wall inside the cooling channel. Therefore, the initial peak visible in figure 3.24 is produced by a different mechanism: it is in fact related to the fluid momentum that forces the coolant to move along the pipe axial direction, despite the higher resistance induced by the porous medium.

Afterwards, the OVST approach has been tested when the coolant mass flow rate deviates from the value adopted for the calibration of the porous media, as for the IVST approach. The results obtained are reported in figure 3.27, showing the pressure drop predicted by the complete CFD model and by the OVST for the entire PFU cooling channel and for the ST region only, together with 10% error bars for the results of the complete model.

As it may be argued from the figure, there is a fairly good agreement between the curves, showing that by adopting this approach it is possible to correctly predict the pressure losses over a broad range of coolant inlet velocities. In particular, as far as the overall pressure drop is concerned, the maximum deviations occur for the points characterized by the lower velocities, for which a relative error of 7% is measured between the complete and the OVST model, while the pressure drop of the ST region only is overestimated for the higher velocities, with errors up to 7%.

To further improve the quality of the predictions obtained with the OVST approach, an additional formulation was developed, namely OVST v2. This second model relies on a different definition of the K_{loss} coefficients in the directions of lower resistance, according to equation (3.23),

$$K_{loss,1} = K_{loss,3} = \begin{cases} A & \text{if } r < R_{crit} \\ B + \frac{C}{r^2} & \text{if } r \geq R_{crit} \end{cases}, \tag{3.23}$$

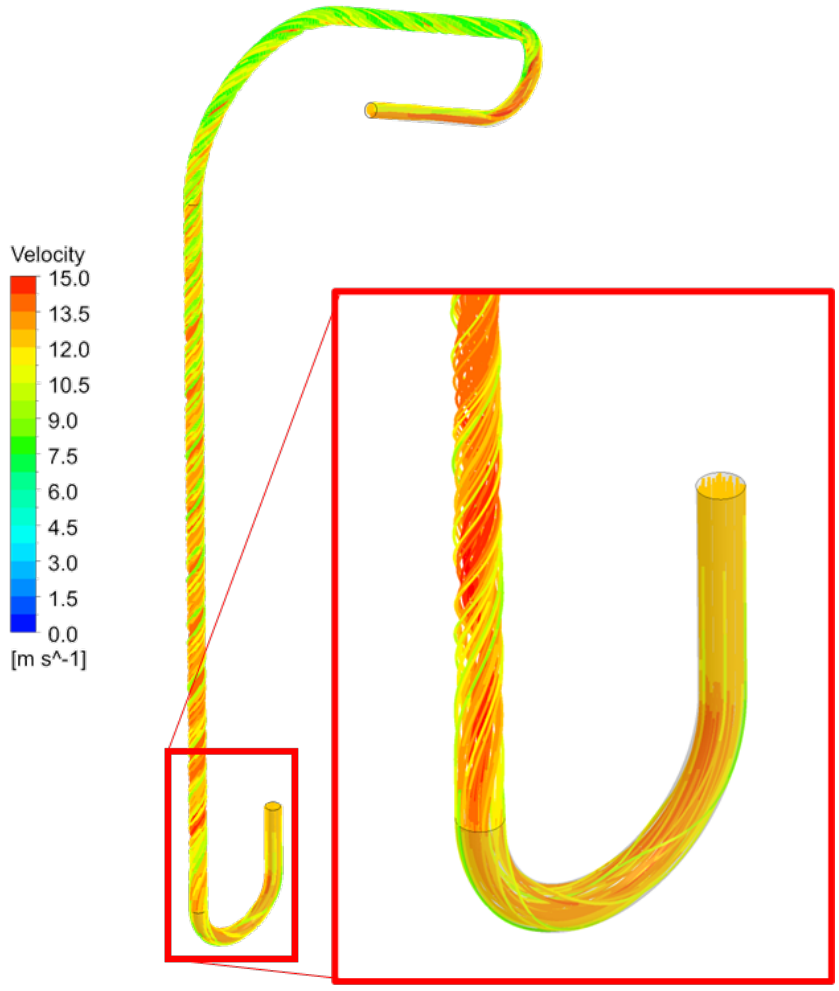

Figure 3.26: Details of the swirling motion induced by the OVST inside the PFU cooling channel.

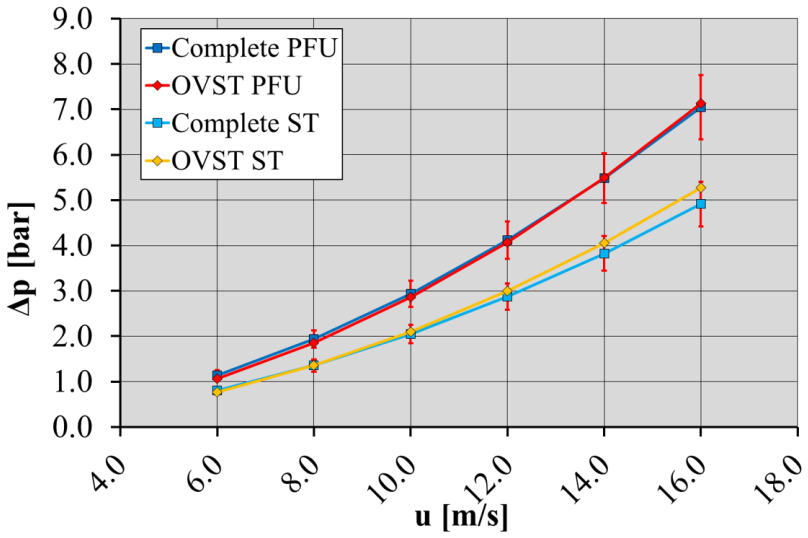

Figure 3.27: Comparison of pressure drop prediction between complete simulation and OVST approach.

where A, B, and C are properly defined parameters, while R_{crit} is a threshold radius value.

The rationale for the definition of this second formulation is to strengthen the swirling motion in the post-ST region of the PFU cooling channel, thus increasing the friction factor in this region. Improving the predictions in the post-ST region allows for improving the OVST predictive capability also in the ST region, because the porous medium is no longer required to compensate for the lower downstream pressure drop. To do so, the coolant is forbidden to flow in the innermost part of the cooling channel by adopting a suitably high value of A, chosen equal to 300 m^{-1}. In particular, this value was selected as the highest possible required to avoid numerical instabilities. For this model, the optimizer performed 213 iterations, aiming to find the optimal values of the parameters to be employed, reported in table 3.11.

Table 3.11: Coefficients of the OVST v2 porous medium.

Parameter	**Value**
A	300 m^{-1}
B	≈0 m^{-1}
C	$1.46 \cdot 10^{-7}$ m
R_{crit}	0.72 mm

The results obtained are depicted in figure 3.28 in terms of friction factor distribution and in figure 3.29 in terms of pressure profile.

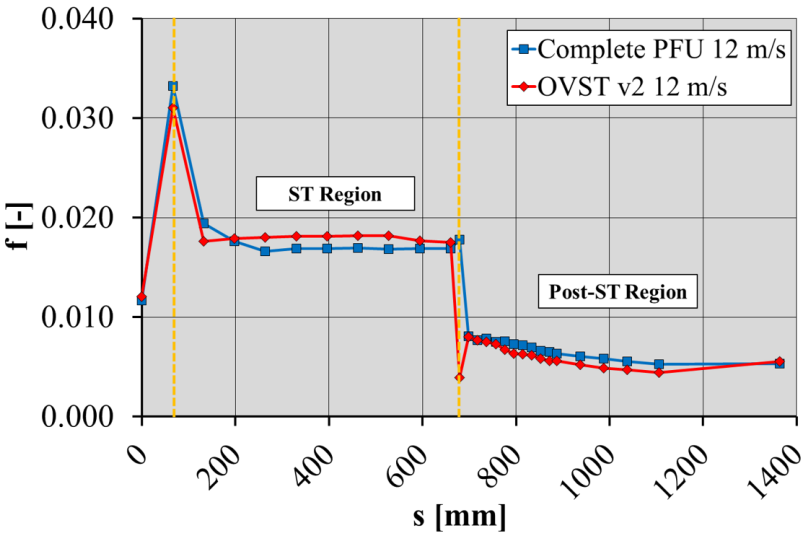

Figure 3.28: Comparison of local Fanning friction factor along the PFU cooling channel curvilinear abscissa between complete simulation and OVST v2 approach.

As can be argued from the results, the predictions obtained with the second OVST model are better than those of the first OVST definition, with a good improvement

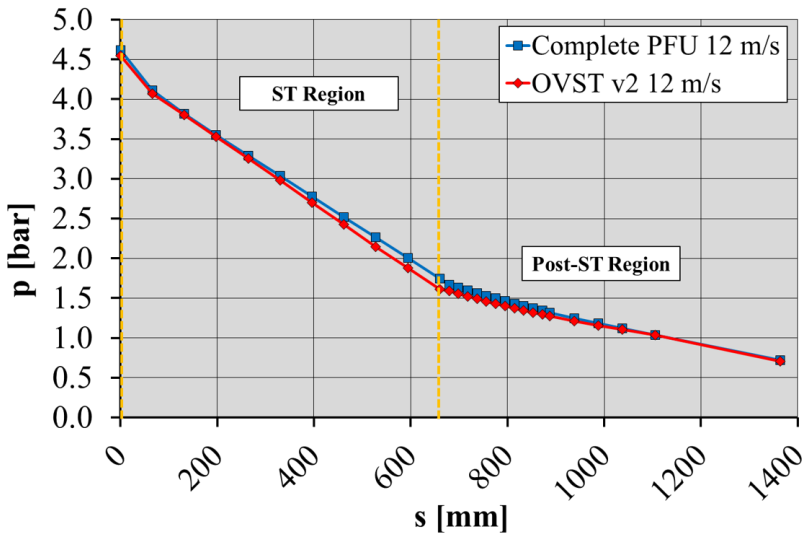

Figure 3.29: Comparison of pressure evolution along the PFU cooling channel curvilinear abscissa between complete simulation and OVST v2 approach.

in the post-ST region. The relative errors on pressure drops with respect to the complete PFU cooling channel simulation are reported in table 3.12, showing an improvement of the pressure drop estimation of the ST region with respect to the first OVST formulation (the error is reduced from 4.5 to 2.2%), maintaining a good accuracy for the other monitored quantities.

Table 3.12: Pressure drop relative errors of the OVST v2 approach.

Probing sections	**Value** [%]
Inlet - Outlet	-1.2
Inlet - ST Outlet	+2.2
Inlet - ST mid section	-0.4

Finally, the capability of the model to deviate from the calibration mass flow rate values was tested, and the results obtained are depicted in figure 3.30 with 10% error bars for the results of the complete model.

In this case, as far as the overall pressure drop is concerned, the maximum deviations occur for the points characterized by the lower velocities, for which a relative error lower than 7% is measured between the complete and the OVST model, while the pressure drop of the ST region only is underestimated for the lower velocity values, and overestimated for the higher, with errors ranging from -5% to 5%. These results are slightly better than those of the first OVST approach, as visible from a comparison with figure 3.27.

In conclusion, as for the IVST, the OVST approach allows for a reduction in the overall number of elements of the computational grid almost up to a factor of 10, while maintaining a good accuracy in the prediction of the pressure drop, being the relative errors lower than a few per cent.

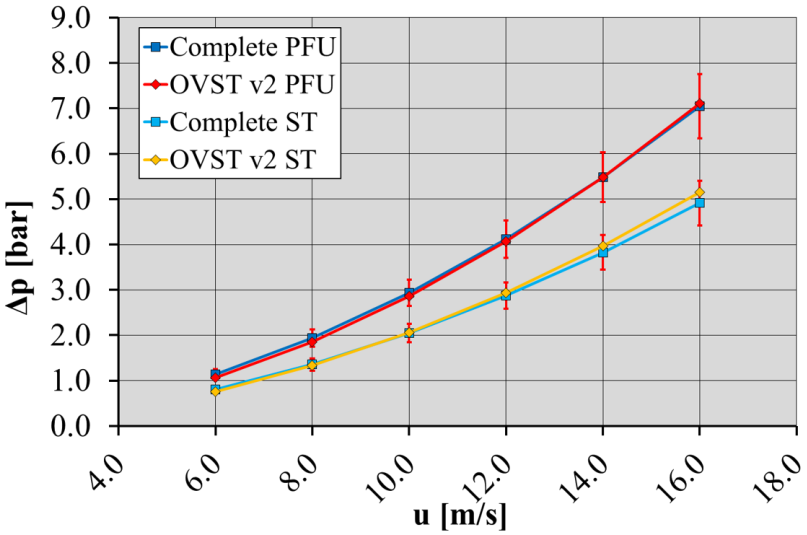

Figure 3.30: Comparison of pressure drop prediction between complete simulation and OVST v2 approach.

As it may be argued from the figures, compared to the IVST approach, the predictions are less accurate and the pressure value at the end of the ST region is underestimated for both the models, thus resulting in conservative outcomes.

Moreover, differently from the simpler IVST formulation, both the OVST approaches require a local cylindrical reference system to be defined for each PFU cooling channel, whereby the direction of the pipe axis and the centre must be reported for each PFU assembly. To overcome this limitation that would make the definition of OVST extremely time-consuming, a script was developed in the SpaceClaim-python language [50] to automatically calculate the directions of the PFU cooling channels and their centres to properly define the OVSTs porous media.

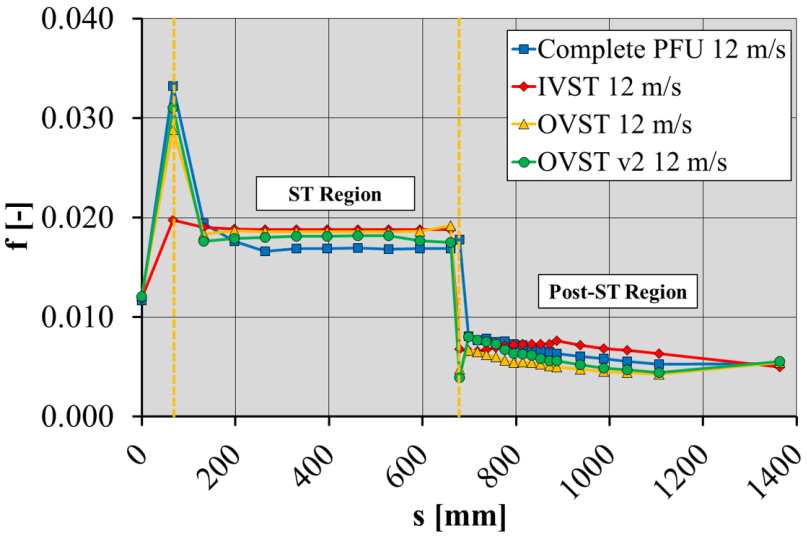

Figure 3.31: Comparison of local Fanning friction factor along the PFU cooling channel curvilinear abscissa with the different VST approaches.

A summary of the results obtained with the different VST approaches is provided in particular in figure 3.31, allowing an easy comparison of the different models.

3.4.3 Heat transfer prediction capabilities of the virtual swirl tape approaches

Finally, for the sake of completeness, the attention was focused on the heat transfer predicting potential of the different VST approaches discussed in the previous sections. The analyses presented here have to be intended as a preliminary evaluation of issues and potentials of these modelling techniques in terms of heat transfer performance. In particular, the analyses were performed considering the VST coefficients obtained with the calibration discussed in the previous sections, and no further optimization was carried out to improve the models to better predict the heat transfer coefficients.

As for the pressure drop assessment, a detailed PFU cooling channel analysis was performed, by adopting the same computational mesh of figure 3.12 and the settings of table 3.13.

Table 3.13: Summary of PFU cooling channel hot CFD analysis setup.

Analysis Type	Steady-state thermal
Material Library	Water IAPWS IF97 [52]
Reference absolute pressure	45 bar
Turbulence Model	k-ω SST
Boundary Layer Modelling	Automatic Wall Functions
Pipe roughness	1 μm [46]
ST roughness	0.5 μm [46]
Inlet velocity	6 to 16 m/s
Inlet temperature	130°C
Outlet relative static pressure	0 Pa
ST integral surface load	32 kW
Post-ST integral surface load	8 kW

As it may be argued from the table, the analyses were performed considering the fluid domain only and by assuming a total thermal power of 40 kW for the single PFU, being close to the thermal loads expected for this component for the single-circuit cooling option. The surface loads were supposed to be uniform and the breakdown of 32 to 8 kW, respectively for the ST and post-ST regions. These values were obtained from the surface power profiles on the OVT PFUs reported in [56], and have to be intended just as a rough indication to provide an order of magnitude to the loads. In fact, a more realistic assessment should take into account the non-uniformities of the heat flux both along the curvilinear abscissa and around the pipe circumference.

The cooling performances were estimated in terms of convective heat transfer coefficients h, calculated at different sections of the PFU cooling channel.

To check the soundness of the results obtained, the heat transfer coefficient values were compared to Manglik and Bergles correlation [85] for the ST region, and to Gnielinski correlation [94] for the empty pipe. The correlations adopted are in particular reported in equation (3.24) and equation (3.25), where f is calculated from equation (3.12).

$$h = \frac{\lambda}{d_0} 0.023 Re_0^{0.8} Pr^{0.4} \left(1 + \frac{0.769}{\gamma}\right) d_r^{0.2} A_r^{0.8} \left(\frac{\mu_b}{\mu_w}\right)^{0.3} \tag{3.24}$$

$$h = \frac{\lambda}{d_0} \frac{(f/2)\,(Re_0 - 1000)\,Pr}{1 + 12.7\,(f/2)^{1/2}\,(Pr^{2/3} - 1)} \tag{3.25}$$

Moreover, the local heat transfer coefficients are obtained from the CFD simulations on the same monitoring sections already employed for the estimation of the local Fanning friction factor. In particular, h values are locally calculated by adopting equation (3.26), where q and $T_{ave,ch}$ are respectively the average heat flux and the line average temperature evaluated at the circumference resulting from the intersection between the probing section and the cooling channel surface, while T_{bulk} is the coolant local bulk temperature.

$$h_{CFD} = \frac{q}{T_{ave,ch} - T_{bulk}} \tag{3.26}$$

The comparison between the numerical predictions and the correlations considered is depicted in figure 3.32, while the heat transfer coefficient values are reported in figure 3.33 for all the considered coolant velocities.

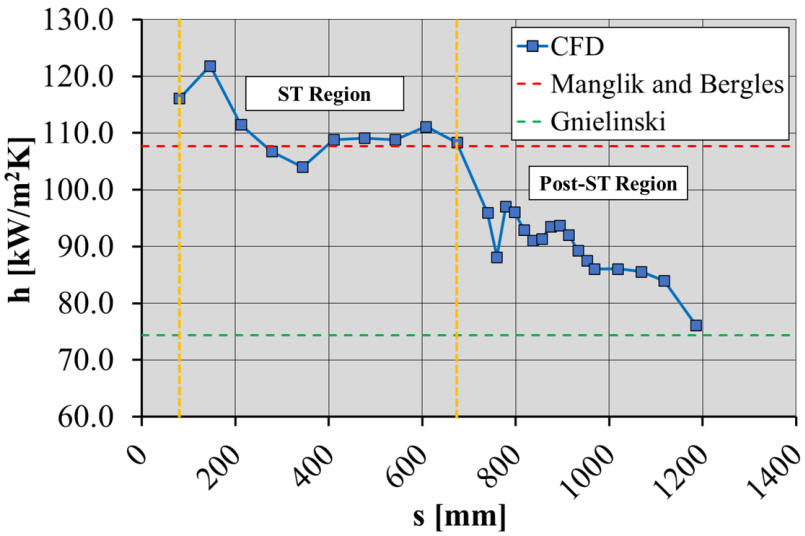

Figure 3.32: Heat transfer coefficient along the PFU cooling channel curvilinear abscissa for a coolant axial velocity of 12 m/s.

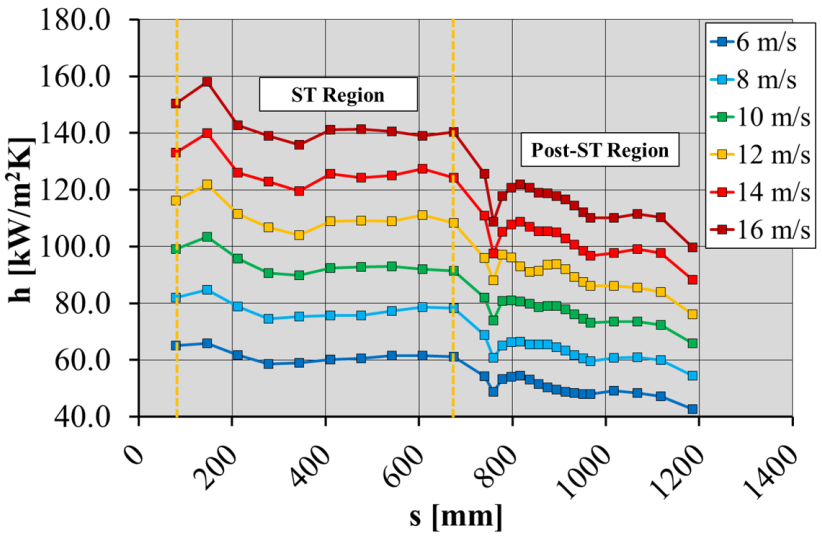

Figure 3.33: Heat transfer coefficient along the PFU cooling channel curvilinear abscissa for different coolant inlet velocity values.

As it may be argued from figure 3.32, the ST region heat transfer coefficient is predicted with a quite good accuracy, being the relative error between the Manglik and Bergles correlation and the average value among all the considered sections below 3%. Moreover, local deviations (e.g. due to the initial peak) determine variations of more than 10% with respect to the correlation. Regarding the post-ST region, instead, the heat transfer coefficient is always overestimated by the CFD simulation. This last result is not surprising, since Gnielinski's correlation is valid for straight pipe with a fully developed flow field, while the results obtained with the thermofluid-dynamic calculation embed several effects, i.e. the presence of bends and the swirling motion of the coolant, that increase the heat transfer coefficient compared to the reference correlation. However, the last point of the post-ST region (where the effects of the pipe bend and the swirling motion are almost completely lost) shows a good agreement with Gnielinski's correlation, being the relative error slightly higher than 2%. Moreover, a good agreement between numerical outcomes and correlations is observed for all the coolant inlet velocities considered, as briefly summarized in table 3.14.

The different VSTs were then tested under the same conditions to check their predictive capabilities in terms of heat transfer. In particular, the results relevant to the coolant inlet velocity of 12 m/s are taken as a reference and are reported in figure 3.34 for the IVST, in figure 3.35 for the first OVST formulation, and in figure 3.36 for the second OVST formulation presented in section 3.4.2.

As it may be argued from the results obtained, the IVST approach behaves poorly in terms of heat transfer coefficient distribution. The heat transfer coefficient h is underestimated on average by 34% in the ST region and by 16% in the post-ST region, but higher deviations are observed locally. Moreover, the heat transfer

Table 3.14: Heat transfer coefficient relative errors at different coolant axial velocities.

	6 m/s	**8 m/s**	**10 m/s**
Average error on ST section [%]	-0.5	0.3	1.0
Maximum error on initial peak [%]	6.5	8.9	11.1
Maximum error in post-ST region [%]	34.3	32.4	29.5
Minimum error in post-ST region [%]	5.7	4.8	4.1
	12 m/s	**14 m/s**	**16 m/s**
Average error on ST section [%]	2.7	4.1	5.4
Maximum error on initial peak [%]	13.1	14.9	16.6
Maximum error in post-ST region [%]	29.0	29.8	30.2
Minimum error in post-ST region [%]	2.3	3.3	3.3

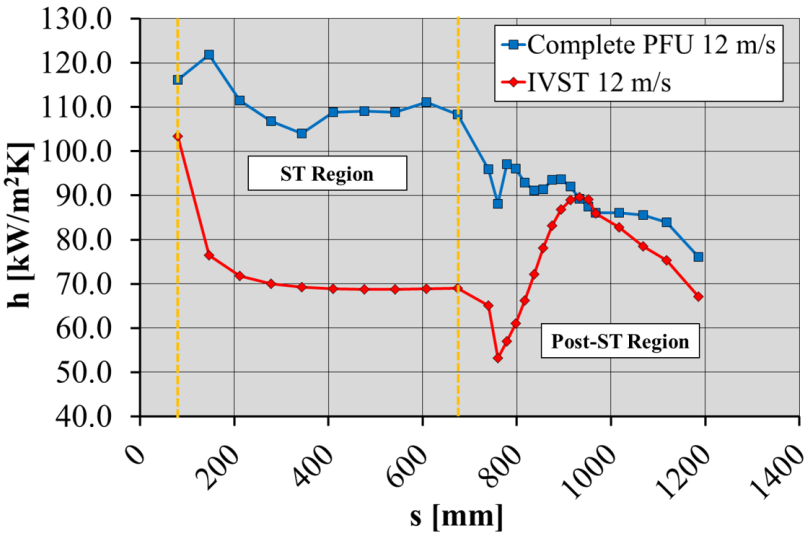

Figure 3.34: Comparison of heat transfer coefficient along the PFU cooling channel curvilinear abscissa between complete simulation and IVST approach.

distribution shows a remarkably different trend between the two curves, as can be expected by a model that is not able to reproduce the swirling motion of the fluid.

Similarly, the results obtained with the first OVST approach show a poor agreement with the complete simulation, and the heat transfer coefficient is underestimated on average by 31% in the ST region and by 30% in the post-ST. Compared to the IVST approach, the predictions are more accurate in the ST region but are worse downstream. This outcome can be justified by the occurrence of a swirling motion of lower strength if compared to the detailed simulation, and possibly by the lack of secondary flow inside the pipe cross-section, avoided by the highest loss coefficients in the direction perpendicular to the tape.

Regarding the second OVST model, the results obtained are significantly better both in terms of relative error, being equal to 21% in the ST region and 20% in

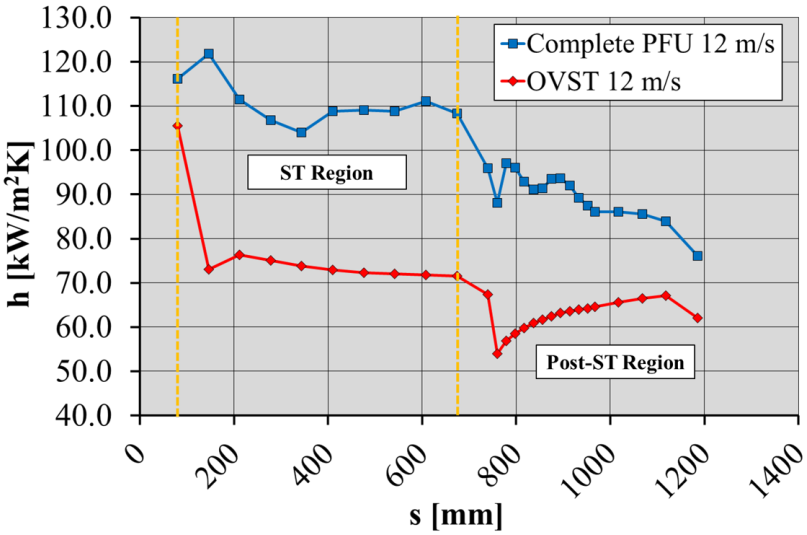

Figure 3.35: Comparison of heat transfer coefficient along the PFU cooling channel curvilinear abscissa between complete simulation and OVST approach.

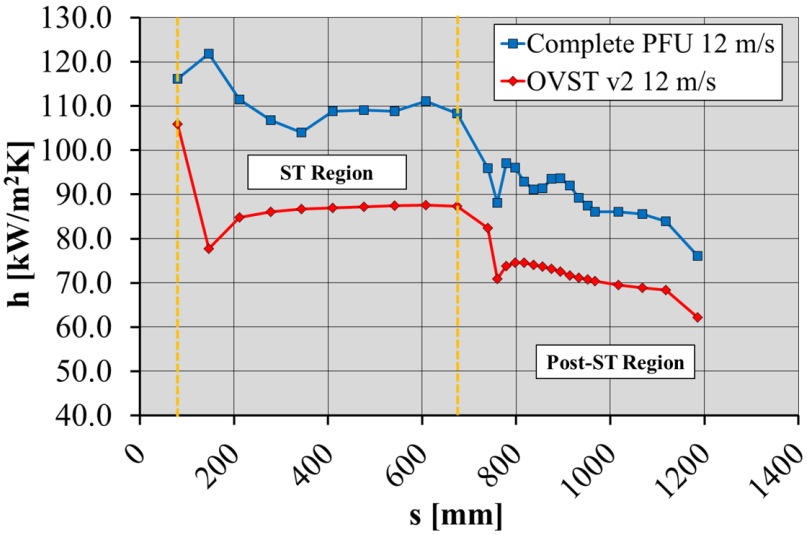

Figure 3.36: Comparison of heat transfer coefficient along the PFU cooling channel curvilinear abscissa between complete simulation and OVST v2 approach.

the post-ST region, and curve shape. As can be noted from figure 3.36, the model is able to capture the decaying trend of the heat transfer coefficient in the region downstream the tape, even if the predicted h values are lower than the detailed model along the entire curvilinear abscissa.

Finally, a comparison of the results obtained with the three VST models is depicted in figure 3.37.

As can be argued from the results, the heat transfer prediction capabilities of the VST approaches are not satisfactory, since it was not possible to obtain deviations lower than 20% from the complete PFU cooling channel model. Despite the most advanced OVST approach v2 has shown good predictions in terms of pressure drop and its breakdown between ST and post-ST region due to the presence of a strong

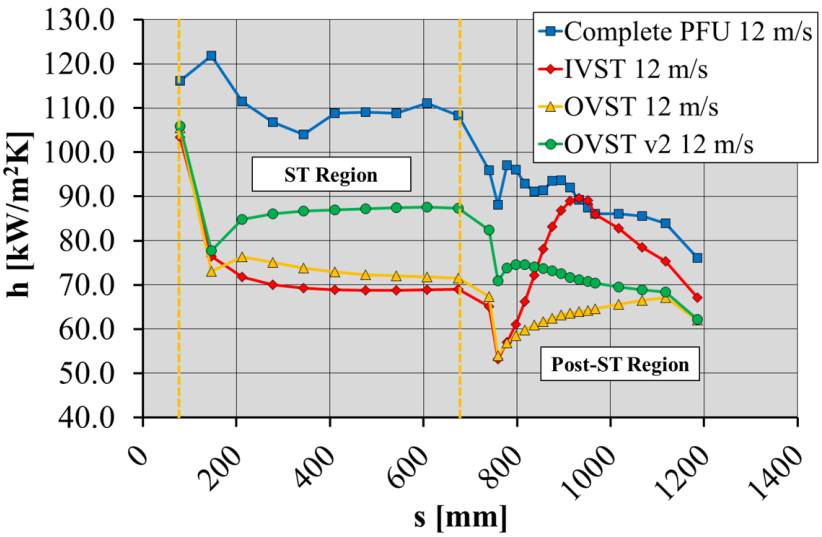

Figure 3.37: Comparison of heat transfer coefficient along the PFU cooling channel curvilinear abscissa with the different VST approaches.

swirling motion, the same results are not obtained in terms of heat transfer. It follows that the VST approach, according to the current formulations, is well-suited to perform purely hydraulic analyses, but it should be adopted with care when dealing with thermal analyses.

In particular, a possible solution to be adopted, that will be employed in the simulations of the next chapter, is to consider the PFU cooling channels with a VST model, without introducing the structure of the PFUs. To correctly deal with the deposited power, it is then possible to adopt an equivalent volumetric heat source term inside the coolant domain, accounting for both the surface and volumetric loads. Then, detailed simulations of the most critical PFU assemblies can be carried out with a sub-modelling approach in a second analysis step. It should be moreover pointed out that the OVST v2 approach introduces an additional level of complexity, since the coolant in the innermost part of the ST region, located at a distance from the axis lower than R_{crit} is completely still, and thus hot spots caused by the numerical approach can be obtained, possibly affecting the results. Therefore, the adoption of either IVST or the first OVST models is suggested.

Chapter 4

Thermofluid-Dynamic Assessment of the EU-DEMO Divertor Single-Circuit Cooling Option

4.1 Introduction

In this last chapter, the thermal-hydraulic performance of the single-circuit cooling option divertor was assessed by running steady-state, thermally fully-coupled (fluid-structure) 3D-CFD analyses, performed with the aim to assess:

- the coolant total pressure and total pressure drop distributions;
- the coolant mass flow rate branching between SL and RPs,
- the coolant flow velocity distribution among SL, RPs, PFUs and NSs cooling channels;
- the coolant temperature and sub-cooling margin distributions;
- the CHF margin distribution among SL, RPs, and PFUs cooling channels;
- the structure temperature field;

to check whether the considered divertor cooling circuits under the selected operating conditions might still provide a uniform and effective cooling of the structures, suitable to maintain the temperatures within their optimal ranges without incurring in coolant vaporization.

The analyses were performed considering the coolant operating conditions reported in table 4.1 in terms of coolant inlet temperature, inlet pressure and mass flow rate. These conditions were selected in agreement with the WP-DIV team in 2021 to test the thermofluid-dynamic performance of the divertor while avoiding too low temperatures that could unacceptably reduce the component lifetime due to neutron irradiation and He production effects, as already thoroughly described in

Table 4.1: Summary of coolant operative conditions.

	Operative Conditions
Inlet Pressure [bar]	70
Inlet Temperature [°C]	130
ΔT [°C]	≈46
ṁ per Cassette [kg/s]	36
ṁ for the entire divertor [kg/s]	1728

section 1.8. As a result, a minimum inlet coolant temperature of 130°C was agreed, allowing for a cassette lifetime slightly higher than 0.8 FPY, according to the results shown in figure 1.28.

At the same time, excessively high coolant pressures were avoided, which would require a deep design revision of the component, being the original design pressure equal to 50 bar. Therefore, an inlet coolant pressure of 70 bar was judged as an acceptable compromise value.

Concerning the coolant mass flow rate, it was selected, starting from dedicated ADRANOS analyses, in order to have the maximum allowable value that could be used to achieve a pressure drop slightly below the 14 bar limit, in order to guarantee the VTs maximum coolant velocity and, consequently, obtain the maximum CHF margin achievable.

However, the selected operating point is not compliant with all the divertor cooling circuit constraints as can be argued by the ADRANOS results depicted in figure 4.1, showing the selected operating conditions in red.

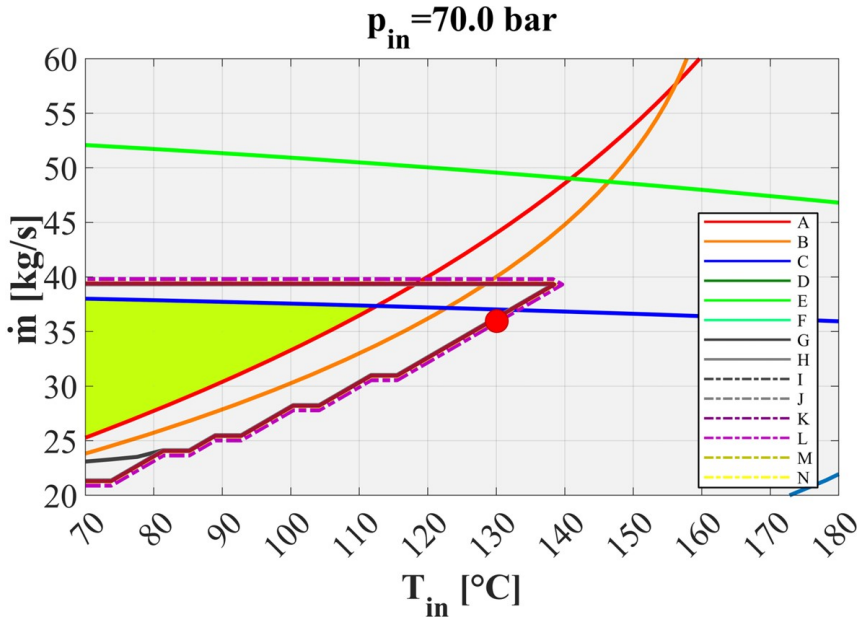

Figure 4.1: Range of acceptable operating conditions for the divertor single-circuit cooling option (in green) for an inlet pressure of 70 bar and design operating point (in red).

More in detail, the parametric analyses predict that, under these conditions, the divertor cooling circuit works at unduly low margins against CHF, respectively equal to 1.15 and 1.23 for OVT and IVT, while determining a pressure drop of 13.25 bar.

The CFD analyses presented in this chapter should therefore be intended both as an additional benchmark to assess the soundness of the ADRANOS predictions, and to determine the presence of further criticalities in the temperature distribution, e.g. in the Eurofer, which cannot be predicted other than by resorting to 3D thermal analysis.

The coolant temperature increase between the inlet and outlet sections of the divertor cooling circuit was calculated starting from the total deposited power (equal to the sum of surface and volumetric loads) of 6.97 MW per cassette, detailed in the following. The volumetric density of nuclear-deposited power was calculated by the ENEA Frascati Neutronics Team for the 2021 divertor design [40] and is depicted in figure 4.2, while the total power deposited in each divertor sub-component is detailed in table 4.2.

Table 4.2: Volumetric deposited power breakdown for each cassette.

Volumetric Heat Loads	
Component	**Power [MW]**
SL Armour	0.095
SL Structure	1.032
SL Coolant	0.430
RPs Armour	0.024
RPs Structure	0.085
RPs Coolant	0.041
CB Structure	0.547
CB Coolant	0.169
NSs Structure	0.025
NSs Coolant	0.005
VTs Armour	0.519
VTs Structure	0.597
VTs Coolant	0.137
TOTAL	**3.707**

In addition to the non-uniform volumetric nuclear power densities, surface heat loads representative of the steady-state normal operating conditions for VTs, SL, and RPs plasma-facing surfaces were considered. These surface loads were selected starting from the integral values drawn from [78] and the load distribution among VTs and the cassette presented in [56]. Since the loads calculated in [56] were assessed in a simplified divertor cassette geometry not equipped with SL and RPs, the same ratio between the nominal loads (1 MW/m^2 for the SL and 0.2 MW/m^2 for the RPs, so 5:1) was considered, and uniform surface heat fluxes were assumed

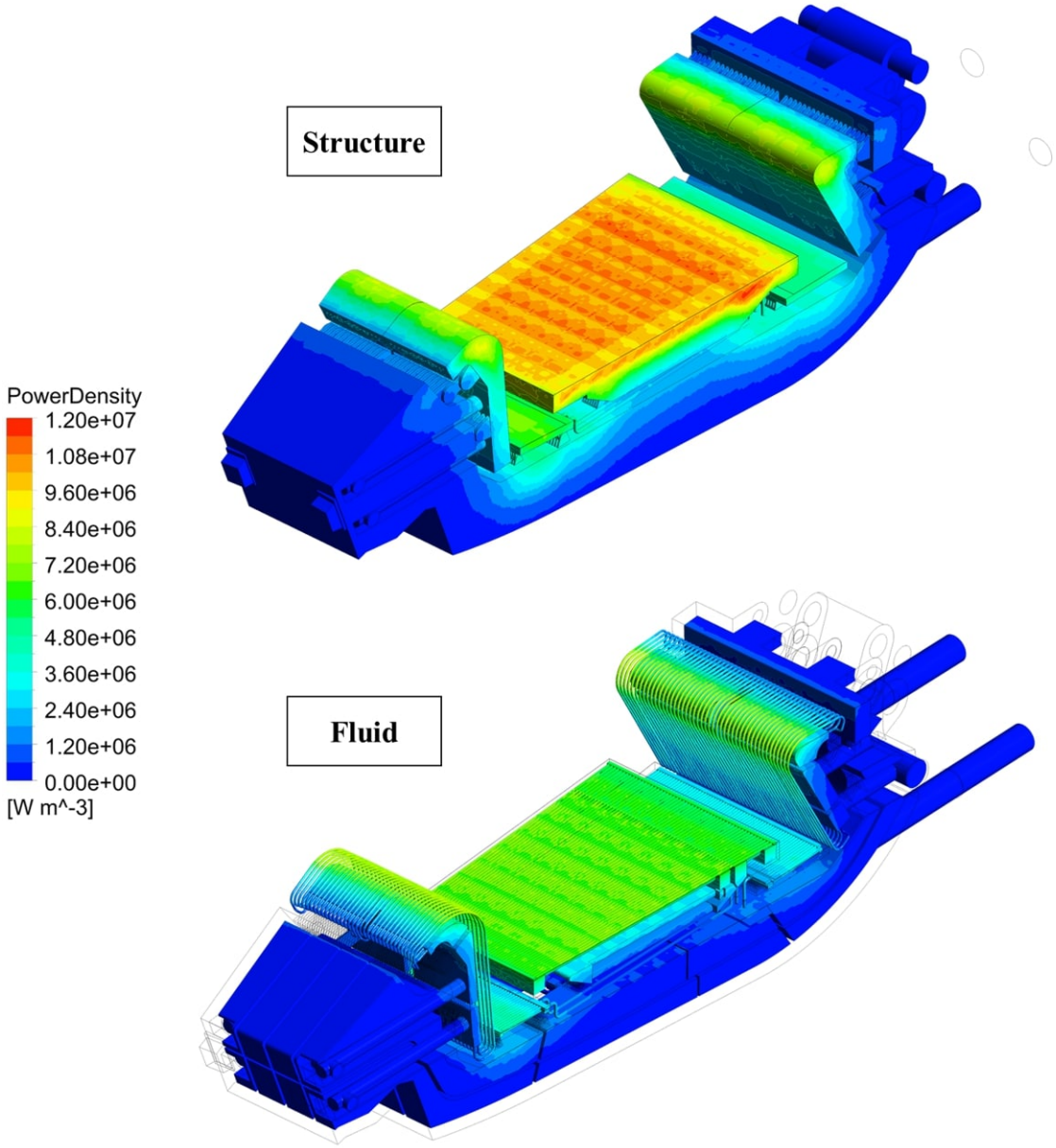

Figure 4.2: Nuclear heating distribution adopted for calculations.

over these components. Regarding the integral surface loads on the VTs, they were drawn entirely from [56]. Additionally, due to the modelling approach adopted for the PFCs, which will be detailed in the next section, no indication of the heat flux profile was necessary. The power breakdown of surface heat loads is summarized in table 4.3.

Table 4.3: Surface deposited power breakdown for each cassette.

Surface Heat Loads	
Component	**Power [MW]**
SL Surface	0.771
RPs Surface	0.062
VTs Surface	2.430
TOTAL	**3.263**

Considering these cooling circuit operating conditions and thermal loads, the resulting temperature increase between the inlet and outlet of the divertor cooling circuit, neglecting the radiative thermal losses to the VV, amounts to approximately 46°C.

It should be moreover pointed out that, differently from the procedure adopted in past simulations of the divertor cooling circuits [28, 29, 30, 31, 26], the coolant temperature rise inside the cassette was not decided a priori (thus requiring an adjustment of the mass flow rate), as it would have resulted most likely in unfeasible operating conditions, while the thermal-hydraulic assessment was performed with a two-step approach:

1. a detailed 3D-CFD simulation is carried out considering the thermal loads foreseen during steady-state normal operating conditions of the divertor cooling circuit, in order to properly set the mass flow rate to be fed to each divertor cassette;
2. an additional 3D-CFD simulation is performed to evaluate if the system is able, considering the same mass flow rate of the first step, to safely withstand the nominal loads selected for the SL and RPs, significantly higher than the values derived from plasma physics assessments [95].

It should be emphasised that this two-step approach is not expected to lead to surprising results here, as the operating point was chosen on the basis of the preliminary analyses, and not considering a fixed coolant temperature difference between the inlet and outlet sections of the divertor cooling circuit, as for the case of past cassette analyses. Additionally, in the case of the single-circuit solution, the relative overestimation of the total heat load (sum of surface and volumetric contributions) is lower, as the total power is indeed higher.

Nevertheless, this approach should be mandatory for future analyses of the divertor cassette where the coolant mass flow rate is determined based on a desired

coolant temperature rise: by adopting this approach is in fact possible to obtain more realistic results, since the mass flow rate of the cooling circuit is not unduly overestimated taking into account the nominal loads, and the cooling capability of the divertor cooling circuit is assessed conservatively.

4.2 Mesh and PFU modelling approach

The thermofluid-dynamic simulation of the divertor complex cooling circuit with 3D-CFD tools results difficult due to the multiscale nature of its geometry, characterized by an overall length of more than 4 m, and features around 400 channels with diameters of the order of ≈1 cm.

It is therefore evident how it is of paramount importance to select an optimal mesh size, which must be sufficiently fine to guarantee the mesh-independence at least of the integral engineering quantities of interest (e.g. the coolant total pressure drop and the maximum temperatures that various materials reach), and at the same time it should be manageable in terms of overall computational cost. Therefore, mesh-independence analyses were carried out on the individual divertor components, as will be detailed in section 4.2.2.

Concerning the PFU cooling channels, the difficulties that are encountered to reproduce with a high level of detail and with suitable accuracy the thermal behaviour of this component have been already discussed thoroughly in chapter 3. The OVST porous medium approach was thus selected to simulate the PFUs cooling channels in order to reduce the computational burden while keeping the quality of the results under control, although an inevitable loss of information is obtained, i.e. in terms of temperature distribution inside the coolant body and the structures of the PFU assemblies.

The details of the PFU modelling and of the mesh selection procedure are herewith reported.

4.2.1 PFU modelling

As anticipated in chapter 3, the most demanding components from the point of view of computational burden are the PFUs and their supports, which are composed of different materials, have very small geometric details and are subject to high thermal fluxes, which require a sufficient number of cells to correctly reconstruct the thermal gradients.

It was thus mandatory to renounce the simulation of these components in detail, analysing only the fluid-dynamic aspect through the use of the VST approach. Using this methodology, the possibility of predicting the thermal field within the PFUs and their supports is unavoidably lost. However, by identifying the most critical

region of VTs, detailed thermofluid-dynamic analyses could be carried out using a sub-modelling approach, adopting the results of the entire cassette as boundary conditions for a single PFU assembly simulation.

More in detail, the first OVST approach was employed, i.e. the one relying on the adoption of the source term defined in equation (3.22), as it is able to provide accurate results and does not have the criticality of inducing regions of stagnant fluid that can reach excessively high temperatures due to volumetric loads, as for the case of the OVST v2.

The workflow adopted for the definition of the porous media parameters is the same detailed in section 3.4.2:

- at first a detailed simulation of the flow field inside the individual PFU cooling channels was carried out for each of the two targets considering a very fine mesh with a bulk size able to guarantee results with an error lower than 5% with respect to the asymptotic values obtained through a Richardson extrapolation procedure (M4 of section 3.2.1) and selecting the nominal mass flow rate value, calculated as the ratio between the total mass flow rate and the number of PFU assemblies of each target;
- the OVST parameters were properly calibrated using the Ansys DesignXplorer optimization tool to ensure that the pressure drop is correctly reproduced at the nominal mass flow rate;
- the OVST is tested at different mass flow rates, deviating from the nominal value, in order to check whether the $\Delta p(\dot{m})$ curve is reproduced with acceptable errors.

Concerning the last point, the comparison between the complete model and the equivalent porous medium results is shown in figure 4.3 for a OVT PFU cooling channel, considering a mass flow rate within the range $\pm 20\%$ from its average nominal value to account for possible variations of mass flow rate due to the non-uniformities in the coolant distribution. The maximum relative error in terms of overall pressure drop between the two curves of figure 4.3 is below 2.5%, while it is lower than 1.5% within the range $\pm 10\%$ from the nominal mass flow rate (where realistically will operate the array of PFU cooling channels).

It has to be pointed out that the ability to reconstruct the pressure drop curve as a function of $\dot{m}$ over a fairly wide range of values around the nominal one allows having some confidence in the distribution of flow rates between the various PFU cooling channels when the complete simulation is performed, being the equivalent model capable of dealing with deviations from nominal values. Furthermore, the small temperature variations observed in the VTs (in the order of 10°C) reasonably allow to avoid the development and adoption of temperature corrections for the OVST.

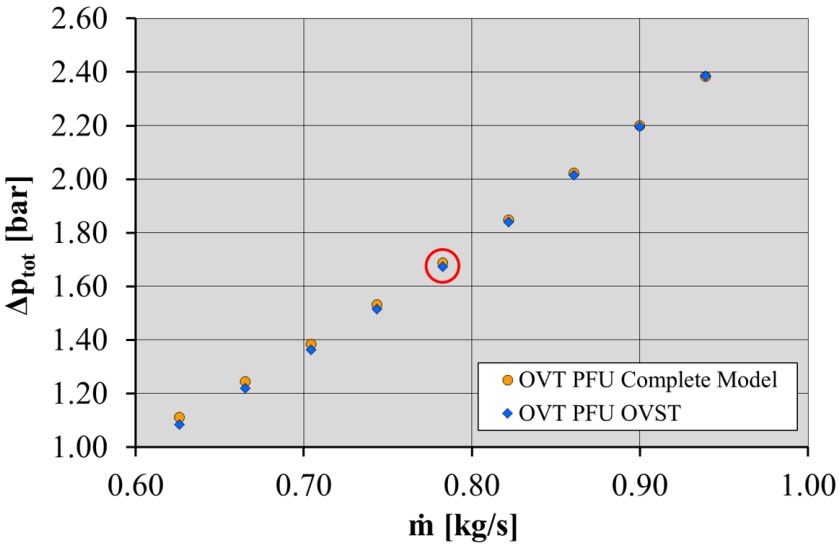

Figure 4.3: Comparison between complete OVT PFU cooling channel and OVST. The average nominal mass flow rate is circled in red.

To correctly reproduce the PFUs energy balance into account, a uniform volumetric heat source was considered inside the porous media, being equal to the sum of surface and volumetric contributions detailed in table 4.2.

Finally, to properly define the local reference frames for each different PFU cooling channel and the required porous media (90 in total), an automatic procedure was developed with the SpaceClaim-Python programming language, allowing to extract from each PFU cooling channel the principal direction, to correctly define the porous media, and to automatically arrange the case setup in the Ansys CFX-Pre environment.

4.2.2 Mesh independence studies

For all components except the PFUs, the optimal mesh size to be adopted to obtain fairly grid-independent results was assessed through dedicated mesh-independence studies. Several parametric analyses were carried out separately on the individual components, being a complete mesh-independence assessment of the entire divertor too much computationally expensive to be performed in a reasonable amount of time.

This resulted in a total of more than 50 3D-CFD steady-state thermofluid-dynamic simulations of the SL, inner RP, OVT TB, and CB with NSs under realistic operating conditions, allowing moreover to define optimum local mesh sizes for each component in a much more flexible manner. Moreover, for the outer RP and IVT TB, it was assumed that they could be dealt with computational grids with the same features as those adopted respectively for the inner RP and OVT TB. The analyses were carried out using the GCI as a FoM, evaluating the Richardson extrapolated values ϕ_0 for a generic quantity ϕ by means

of a LS approach, by adopting the procedure already detailed in section 3.2. The GCI was calculated according to the definition of equation (2.16), conservatively considering a safety factor $F_s = 3$ being the observed convergence order higher than the theoretical one, as prescribed in [64]. This approach was applied to several engineering quantities of interest for each component, namely the total coolant pressure drop, together with the maximum and average temperatures for each solid region. The results obtained from these analyses are briefly summarized in figure 4.4, from which it is interesting to note that the GCI value is always lower than 7%, with the only exception of the average Eurofer97 temperature in SL, resulting in a GCI of approximately 14%.

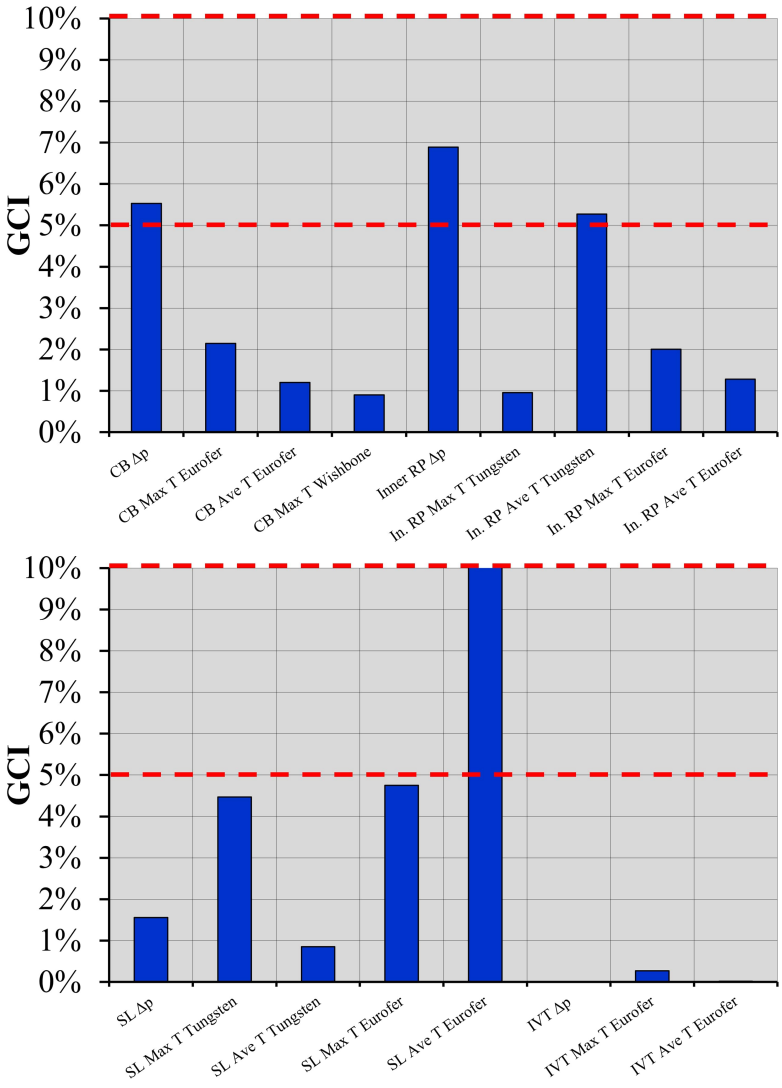

Figure 4.4: Summary of the GCI values obtained by the preliminary mesh independence analyses.

More in detail, a grid refinement of the SL solid was carried out until meshes of over 180 million volumes were achieved, without being able to obtain a clear convergence trend that could justify a mesh-independent result. For this quantity it

was observed, in fact, oscillatory behaviour of convergence, and, therefore, it wasn't possible to determine a clear trend, even adopting the LS approach. For the SL average temperature in Eurofer, the GCI was calculated according to:

$$GCI = F_s \frac{T_{Max} - T_{min}}{T_{ave}}, \tag{4.1}$$

where T_{Max}, T_{min}, and T_{ave} are respectively the maximum, the minimum and the arithmetic average among the results obtained with different meshes in terms of the volumetric average of Eurofer97 temperature in SL.

This effect can be explained by the fact that the total number of cells in the SL is mainly dictated by automatic local refinements due to curvatures and proximities, thus distorting the results of the analysis, together with disturbances introduced by the mapping between the different solid and fluid meshes at their interfaces.

Nevertheless, variations in average and maximum temperatures of the order of ±10°C were obtained in Eurofer97 and no significant changes in the thermal field features are observed. Therefore, it was decided to avoid further mesh-independence studies of the SL and a computational mesh of ≈50 million finite volumes was selected for the SL solid domain only, being a good compromise between computational cost and accuracy of the results.

4.2.3 Complete assembled mesh

Once the optimal grid sizes were selected for each component, an overall mesh was assembled, the details of which are depicted in figure 4.5 and figure 4.6, while its main parameters are summarized in table 4.4.

Concerning table 4.4, it is worth noting how the average mesh quality metrics relevant to Ansys CFX, i.e. orthogonality factor, expansion factor, and aspect ratio, are within the acceptable ranges prescribed in [49] and less than 1% of the overall number of cells is characterized by poor metrics. Consequently, the results are not expected to be significantly influenced by the mesh quality. Moreover, as can be argued from the table, the mesh was tailored so as to have y^+ values below 100 in most of the mesh surface (excepting for less than 1% of the total area), while it was not possible to guarantee at least $y^+ > 11$, due to the occurrence of several stagnation regions inside the cooling circuit, caused by the box-like shape of the cassette. As a result, more than 40% of the total mesh surface is treated with a low-Reynolds approach. Due to the exceptionally large size of the computational domain, which counts 120 million nodes and 245 million volumes, resulting in the most complex thermofluid-dynamic simulation ever performed for the EU DEMO divertor, it was necessary to rely on the computational resources of the CRESCO/ENEAGRID High Performance Computing infrastructure [96] to

perform the thermofluid-dynamics simulations.

Table 4.4: Summary of the main mesh parameters.

Region	Mesh Parameter	Value
Fluid	**Mesh Type**	Hybrid
	Nodes	$9.51 \cdot 10^7$
	Elements	$1.34 \cdot 10^8$
	Inflation Layers Number	12
	First Cell Height [μm]	$20 - 50$
	Layers GR	$1.2 - 1.35$
	Target Element Size [mm]	$1.3 - 10$
	Surface with y^+>100 [%]	0.76
Structure	**Mesh Type**	Hybrid
	Nodes	$2.48 \cdot 10^7$
	Elements	$1.11 \cdot 10^8$
	Target Element Size [mm]	$2.5 - 10$
Quality	**Orthogonality Factor (ave/min)**	0.80/0.01
	Expansion Factor (ave/max)	2.98/7597
	Aspect Ratio (ave/max)	15/1427

4.3 Results

In the following section 4.3.1 and section 4.3.2, the steady-state thermal-hydraulic performance of the divertor cooling circuit are presented for the two scenarios of normal operating conditions and nominal loads foreseen by the two-stages approach already discussed at the beginning of chapter 4, under the coolant operative conditions of table 4.1, with the aim to assess:

- coolant total pressure and total pressure drop distributions;
- mass flow rate branching between SL and RPs,
- coolant flow velocity distribution among SL, RPs, PFUs and NSs cooling channels and channels;
- coolant temperature and sub-cooling margin distributions;
- CHF margin distribution among SL, RPs, and PFUs cooling channels and channels;
- structure temperature field.

4.3.1 Normal operating conditions

For the case of normal operating conditions, the simulation was carried out considering the assumptions, models and BCs summarised in table 4.5. Moreover, in

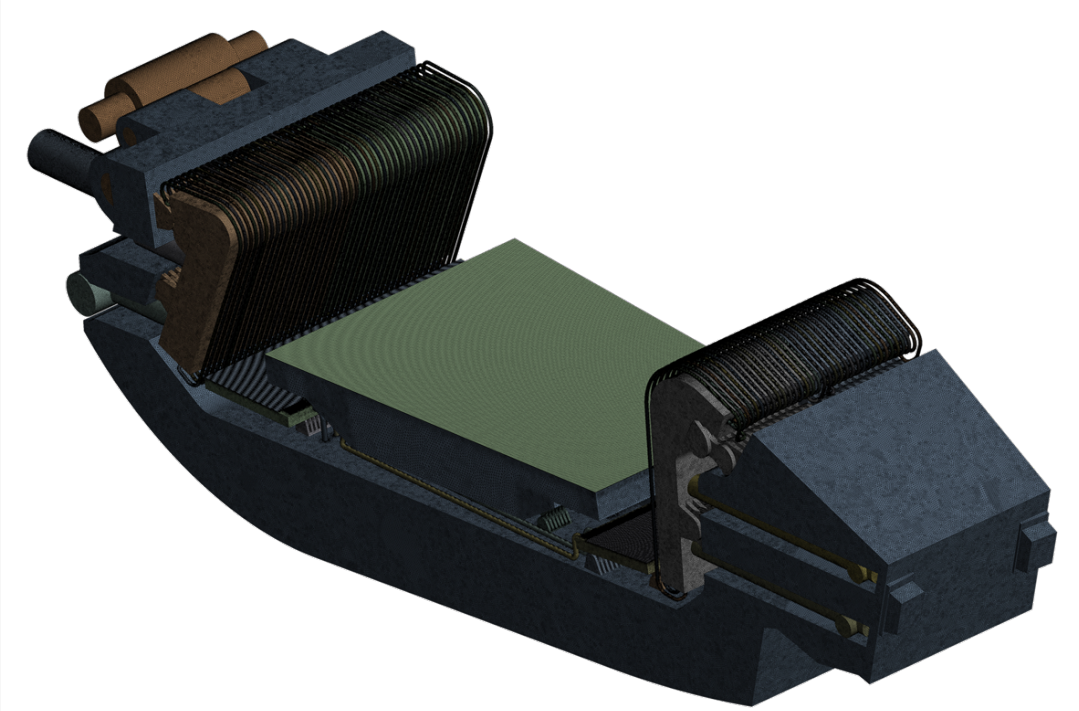

Figure 4.5: Mesh adopted for the thermofluid-dynamic CFD analysis.

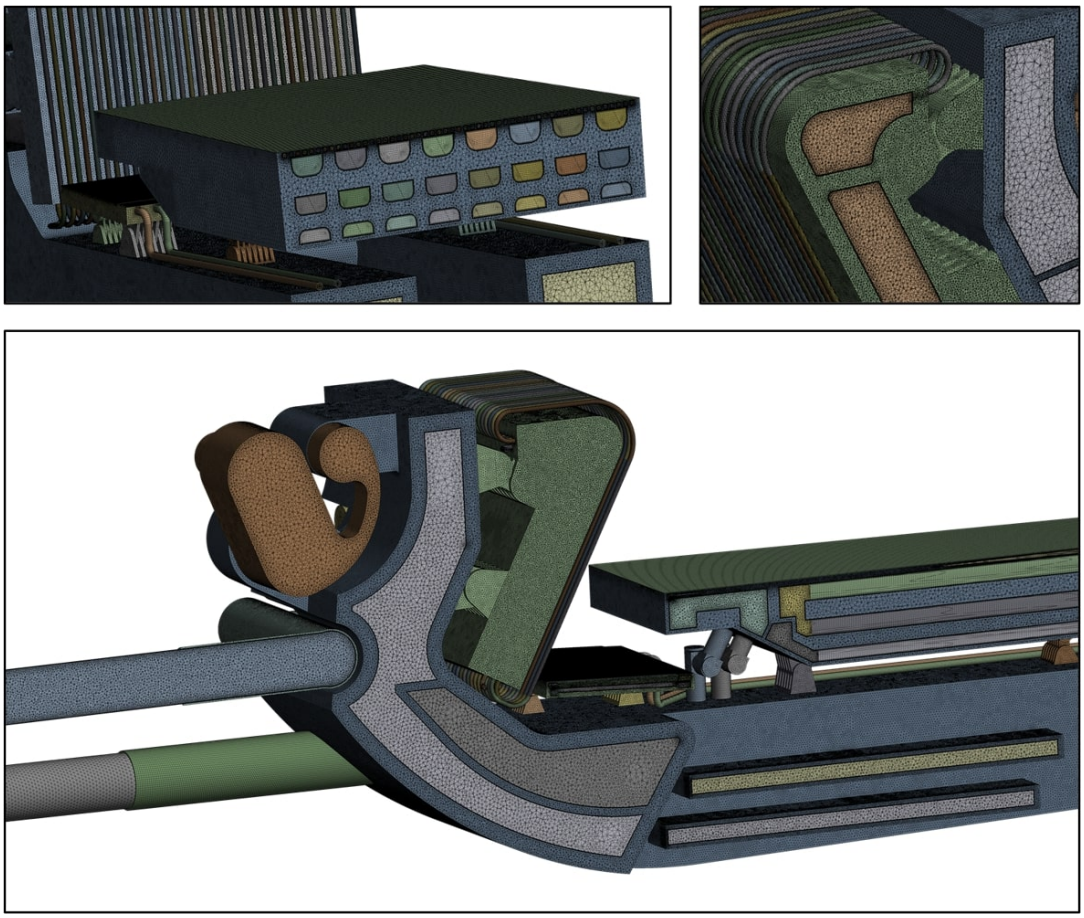

Figure 4.6: Details of the complete computational mesh.

order to avoid over-conservative evaluations of the cassette temperature distribution, a radiative heat transfer condition with the VV was considered, and this latter was supposed to operate at 40°C [97]. The selected radiative surfaces are depicted in red in figure 4.7.

Table 4.5: Summary of assumptions, models and BCs.

Analysis Type	Steady-state coupled thermal analysis
Material Library	Water IAPWS IF97 [52] Eurofer [53] W / Ti6Al4V [54]
SL / RPs Heat Flux	Uniform according to table 2.6
Nuclear Heating	From [40]
Radiative Heat Transfer	Towards VV @ 40°C
Turbulence Model	k-ω SST
Boundary Layer Modelling	Automatic Wall Functions
PFU Modelling	OVST approach with volumetric heat loads
Wall Roughness	15 μm
Wall Roughness PFUs	2 μm
Inlet BC	T=130°C / p_{tot}=70 bar
Outlet BC	$\dot{m}$=36.00 kg/s

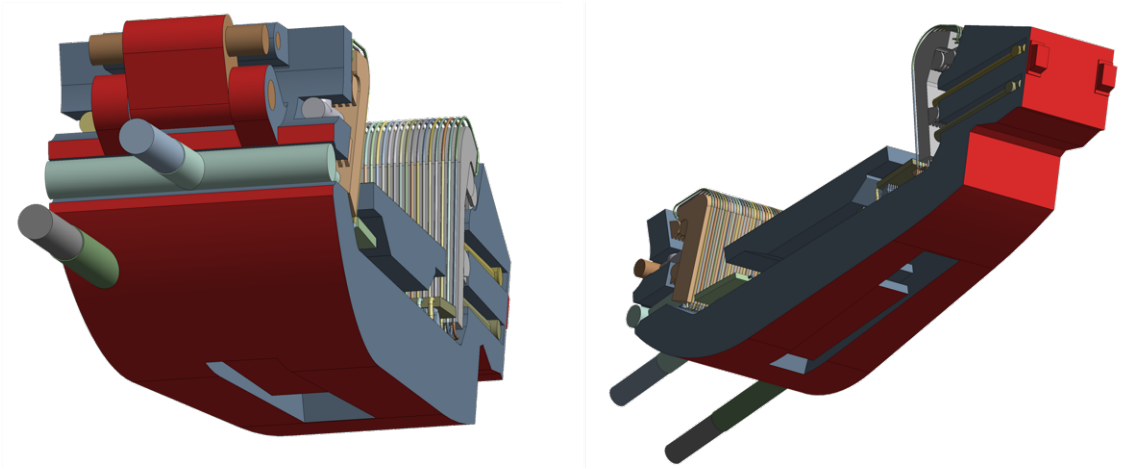

Figure 4.7: Divertor cassette radiative surfaces.

The analysis ran until all the residuals reached the iteration convergence control criterion of 10^{-4} and a second-order accurate numerical scheme was selected, as suggested by [98]. The CFD simulation required about 38 hours of calculation time to perform 1300 iterations on the ENEA CRESCO cluster, running on 240 Intel Xeon Platinum 8160 processors @2.10 GHz, equipped with a total of 960 GB of RAM.

Pressure drop and pumping power

The coolant pressure distribution and total pressure drop for the main CB components, adopting the nomenclature depicted in figure 1.24, are shown in figure 4.8 and table 4.6, respectively, while the calculated mass flow rate branching between SL and RPs cooling circuit is reported in table 4.7.

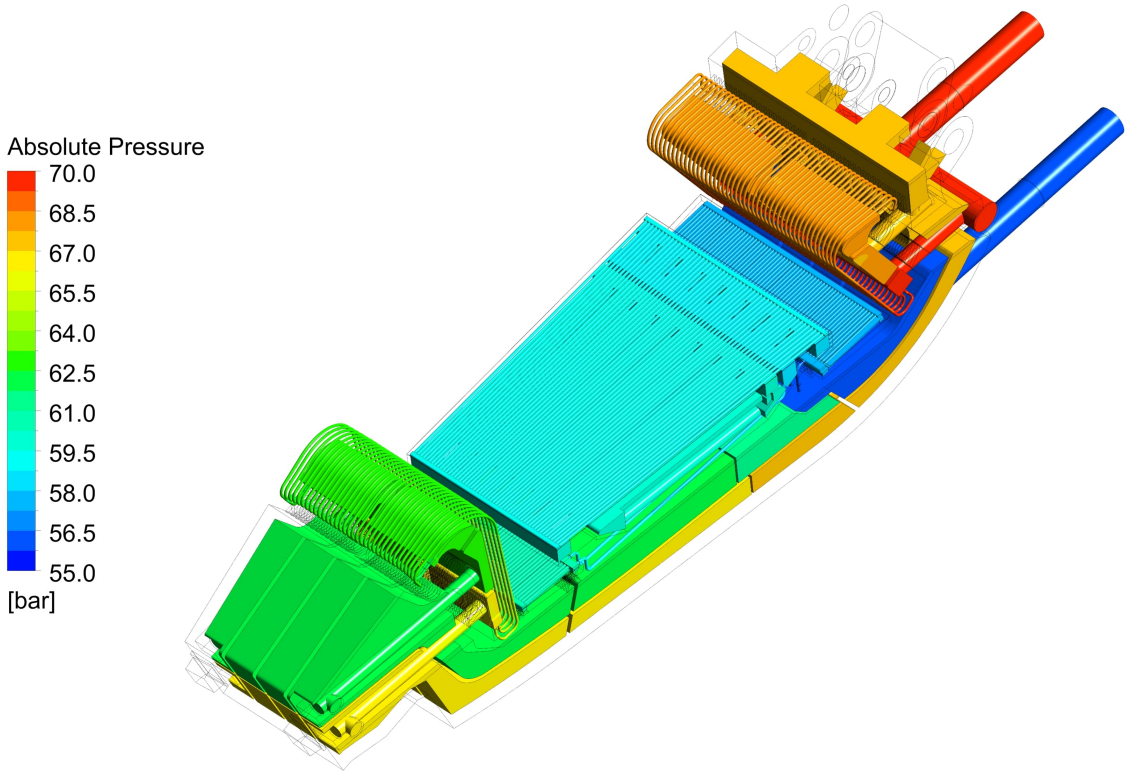

Figure 4.8: Divertor coolant absolute pressure field distribution.

As it may be argued from the results, the divertor cooling circuit's overall pressure drop amounts to ≈13.71 bar, being slightly lower than the prescribed limit of 14 bar, as anticipated in section 4.1. This result is close to the ADRANOS prediction of 13.25 bar, being the relative error of ≈3%. The components with the highest pressure loss are the VTs, due to the presence of the STs, and the SL, due to the FW channels and the S-shaped inlet and outlet pipes.

By combining the information on pressure drop and flow distribution, it is possible to calculate the required pumping power for each component, a breakdown of which is shown in figure 4.9, while the total pumping power required for each cassette amounts to 41.95 kW, calculated for each divertor block of figure 1.24, according to the definition of equation (4.2), where P is the pumping power, and then summed.

$$P = \Delta p \cdot \dot{m}/\rho. \tag{4.2}$$

Figure 4.9 highlights how the two VTs are responsible for the higher coolant

Table 4.6: Coolant total pressure drop distribution.

Divertor Component	**Δp [bar]**
Inlet CB	0.058
OVT	2.233
CB1	0.243
Lower NS	0.703
CB2	0.209
IVT	4.267
CB3	0.406
Upper NS	0.453
CB4	0.210
SL	4.630
Inner RP	1.559
RPs Manifold	1.842
Outer RP	1.315
Outlet CB	0.590
Total	**13.713**

Table 4.7: Divertor cooling circuit mass flow rate distribution.

Sections	$\dot{m}$ **[kg/s]**	$\dot{m}/\dot{m}_{tot}$
SL	27.95	77.6%
RPs	8.05	22.4%
Total	36.00	-

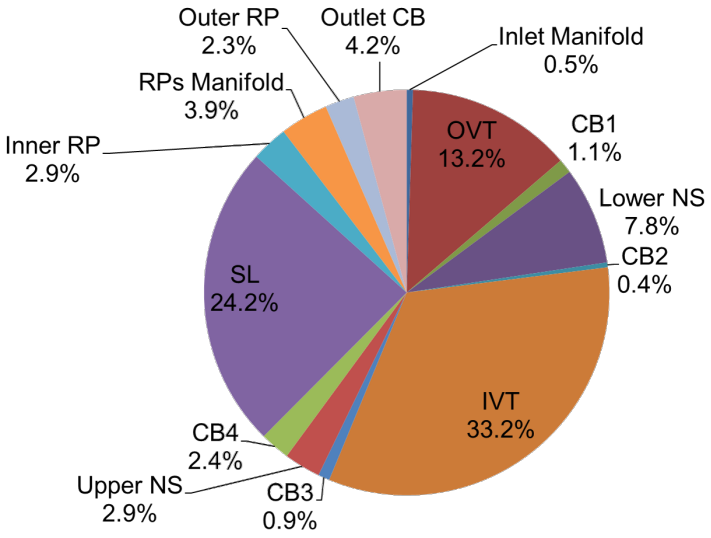

Figure 4.9: Divertor cooling circuit pumping power breakdown.

pumping losses, together amounting to almost 50% of the total value, SL for ≈24%, the entire RP system for 9%, the two NSs for the 11%, while the CB only for 9%.

These latter results together with those of table 4.6 reporting the pressure drop distribution, highlight that the potential for reducing the total pressure drop is limited, as it is significantly influenced by the presence of VTs, for which it is not possible to significantly change the design. Consequently, if an optimisation of the hydraulic circuit aimed at reducing pressure losses is attempted, it would be necessary to revise the SL cooling circuit, being characterized by high losses, then to adjust the RPs, so to rebalance the mass flow rate partition with the SL. In particular, it would be necessary to act on the pipework connecting the CB with these components, as well as to revise their manifolds, since both the RC and FW channels cannot be significantly changed to preserve their capability to handle the plasma heat loads.

Coolant distribution

In the following, it is reported the coolant distribution in all the divertor cassette cooling channels. With regard to all the components that have toroidal-parallel channels, i.e SL, RPs, and PFUs, they are numbered in a clockwise direction looking at the tokamak from above, as depicted in figure 4.10. The NSs channels instead are indicated with a letter representing the two separate cooling circuits for each NS, while the channels are numbered from inlet to outlet, thus resulting from outboard to inboard for the lower NS, and the opposite for the upper NS. Moreover, also concerning the NSs numbering, 1 to 10 are inlet channels, while 11 to 20 are outlet channels. The nomenclature adopted for NSs is reported for clarity in figure 4.11.

As far as the coolant distribution is concerned, in the following are reported the results relevant to axial velocity distributions among SL FW channels and RCs (figure 4.12 and figure 4.13), RPs FW channels and RCs (figure 4.14 and 4.15), PFU cooling channels (figure 4.16), and NSs channels (figure 4.17). The results statistics are moreover summarized in tables 4.8 to 4.13, where σ is the standard deviation relevant to the velocity distribution, ϵ is relative span, defined according to equation (4.3) for a generic quantity ϕ, and CV is the coefficient of variation, calculated as the ratio between the standard deviation and the average value.

$$\epsilon_\phi = \frac{\phi_{Max} - \phi_{min}}{\phi_{ave}}. \tag{4.3}$$

From the analysis of the results obtained, it may be argued that within the SL FW channels the distribution of coolant axial velocity is acceptably uniform, with maximum deviations of ±6% with respect to the average value. Regarding the distribution of coolant axial velocity in the SL RCs, it is supposed to be of lower importance due to the lower thermal loads they have to handle compared to the FW

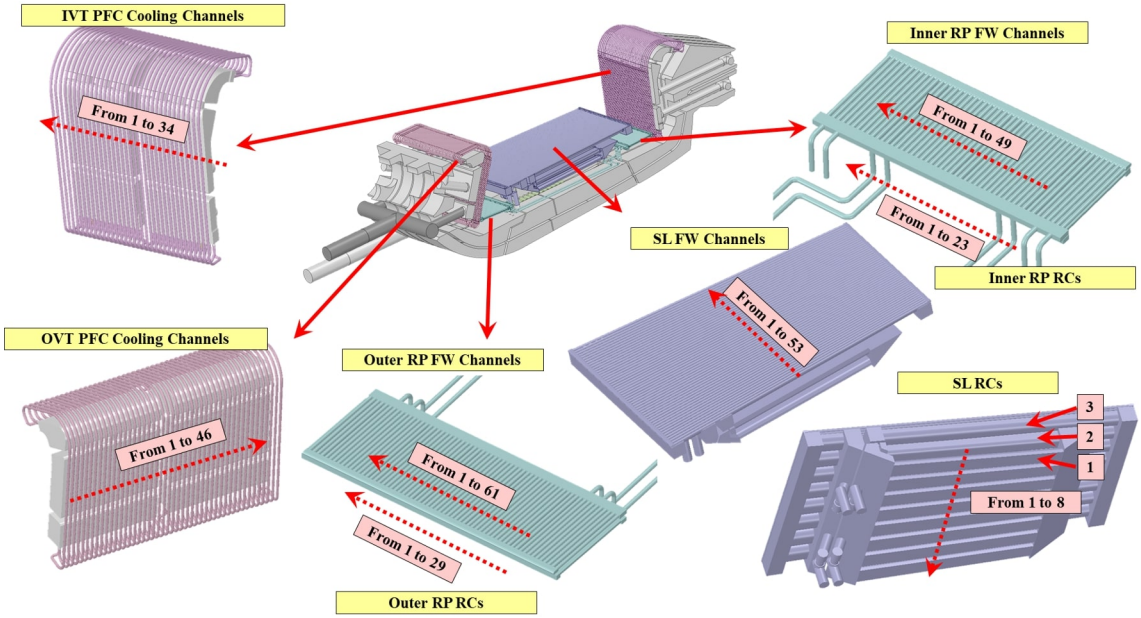

Figure 4.10: DEMO divertor cooling circuit SL, RPs, and PFU channels nomenclature.

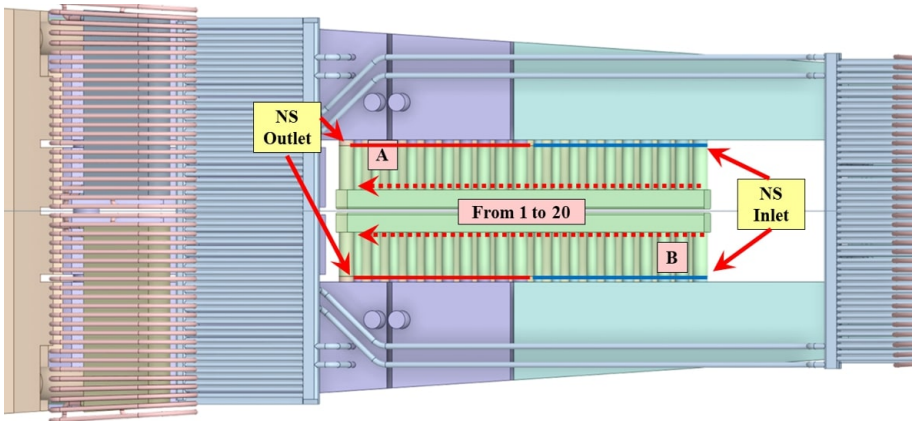

(a)

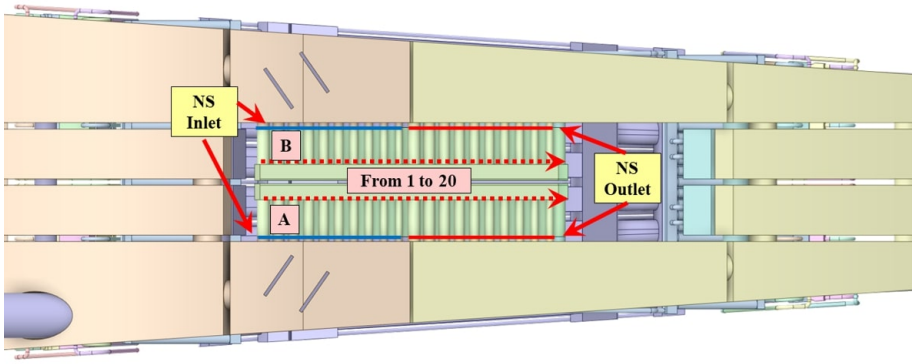

(b)

Figure 4.11: Upper (a) and lower (b) NS cooling channel nomenclature.

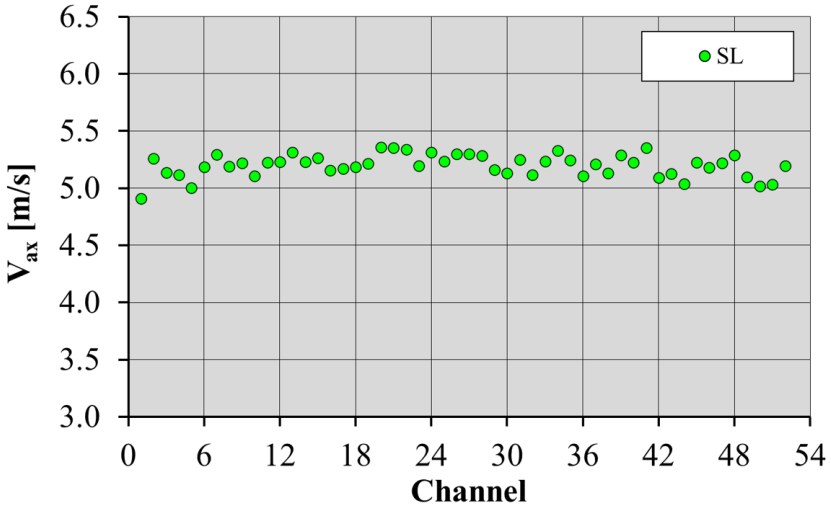

Figure 4.12: Coolant axial flow velocity distribution among SL FW channels.

Table 4.8: Coolant axial velocity distribution among SL FW channels main parameters.

	SL FW channels
V_{Max} **[m/s]**	5.358
V_{min} **[m/s]**	4.909
ϵ_V **[%]**	8.38
V_{ave} **[m/s]**	5.195
σ_V **[m/s]**	0.102
CV_V **[%]**	1.96

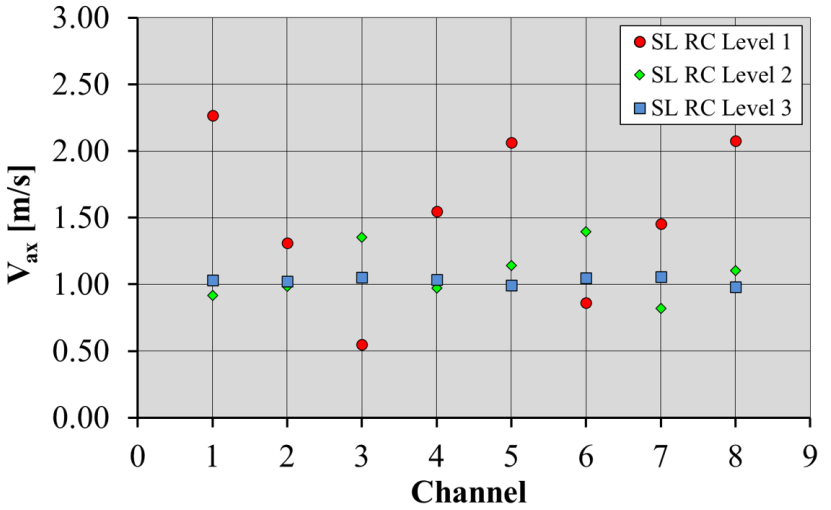

Figure 4.13: Coolant axial flow velocity distribution among SL RCs.

channels, and thus there is no requirement to obtain a smooth coolant distribution, as far as the temperature limits are met. It is however interesting to note that the coolant distribution becomes less spread at each passage inside the SL, due to the mixing effects occurring inside the manifolds separating each level of channels.

Concerning the RPs, a strongly uneven coolant distribution is observed both in

Table 4.9: Coolant axial velocity distribution among SL RCs main parameters.

	RC Level 1	**RC Level 2**	**RC Level 3**
V_{Max} **[m/s]**	2.265	1.394	1.059
V_{min} **[m/s]**	0.547	0.820	0.979
ϵ_V **[%]**	75.84	41.20	7.54
V_{ave} **[m/s]**	1.516	1.085	1.028
σ_V **[m/s]**	0.609	0.204	0.028
CV_V **[%]**	40.14	18.83	2.76

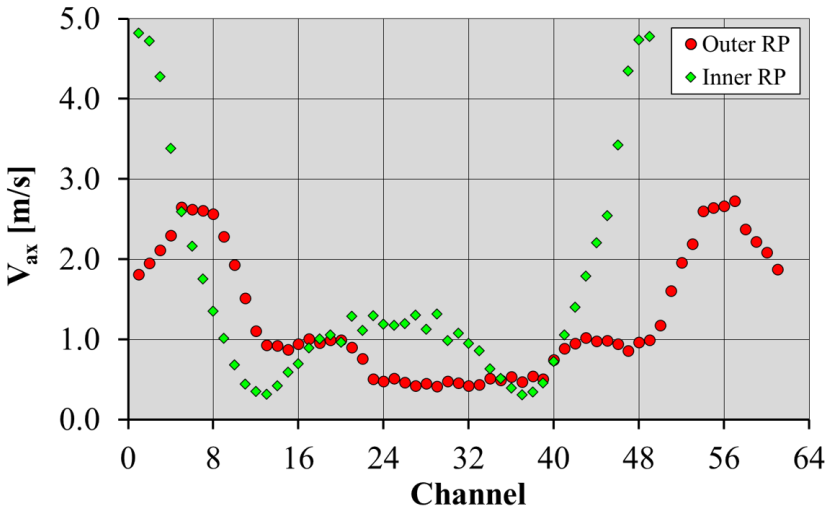

Figure 4.14: Coolant axial flow velocity distribution among RPs FW channels.

Table 4.10: Coolant axial velocity distribution among RPs FW channels main parameters.

	Outer RP	**Inner RP**
V_{Max} **[m/s]**	2.726	4.819
V_{min} **[m/s]**	0.418	0.308
ϵ_V **[%]**	84.66	93.62
V_{ave} **[m/s]**	1.284	1.592
σ_V **[m/s]**	0.782	1.344
CV_V **[%]**	60.94	84.37

Table 4.11: Coolant axial velocity distribution among RPs RCs main parameters.

	Outer RP	**Inner RP**
V_{Max} **[m/s]**	2.167	2.079
V_{min} **[m/s]**	0.012	0.015
ϵ_V **[%]**	99.43	99.30
V_{ave} **[m/s]**	0.644	0.808
σ_V **[m/s]**	0.616	0.706
CV_V **[%]**	95.80	87.43

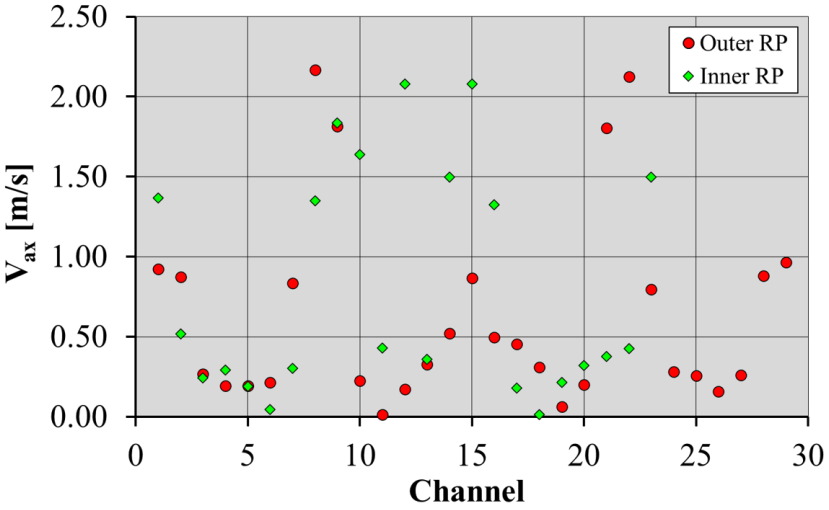

Figure 4.15: Coolant axial flow velocity distribution among RPs RCs.

FW channels and RCs. Despite these distributions are not optimal, the results of the thermal analysis reported in the next sections show that no bulk vaporisation phenomena or thermal hot spots in the structures occur. Consequently, the current design of the RPs cooling circuits can be accepted, at least as far as solely thermal aspects are concerned. The distribution of coolant axial velocity is observed to be quite uniform for the PFUs cooling channels, for which maximum deviations in the range of ±4% from the average values are observed. Moreover, it is interesting to underline that the average velocity inside IVT PFU cooling channels is remarkably higher than for the OVT one, being equal to ≈11.1 and ≈8.1 m/s, respectively. This difference can be explained considering that the same mass flow rate is routed inside 34 PFU cooling channels for IVT and 46 for OVT, with a consequent higher average velocity.

Additionally, it can be noted from figure 4.16 that the maximum axial velocity constraint in the PFU cooling channels is met, being the velocities lower than the limit value of 16 m/s. It should also be noted that the reported velocity has been appropriately scaled to account for the presence of STs, which are not modelled geometrically with the OVST approach.

Table 4.12: Coolant axial velocity distribution among PFU cooling channels main parameters.

	OVT	**IVT**
V_{Max} **[m/s]**	8.346	11.327
V_{min} **[m/s]**	7.792	10.751
ϵ_V **[%]**	6.64	5.08
V_{ave} **[m/s]**	8.103	11.109
σ_V **[m/s]**	0.117	0.123
CV_V **[%]**	1.45	1.11

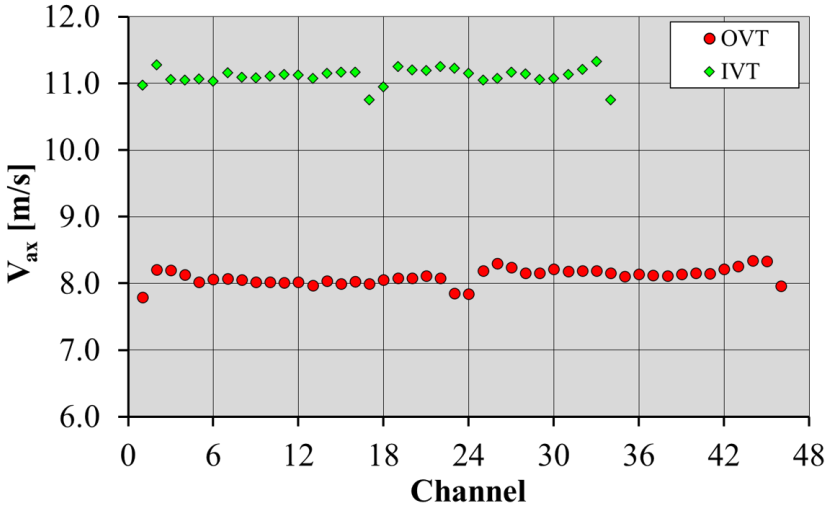

Figure 4.16: Coolant axial flow velocity distribution among PFU cooling channels.

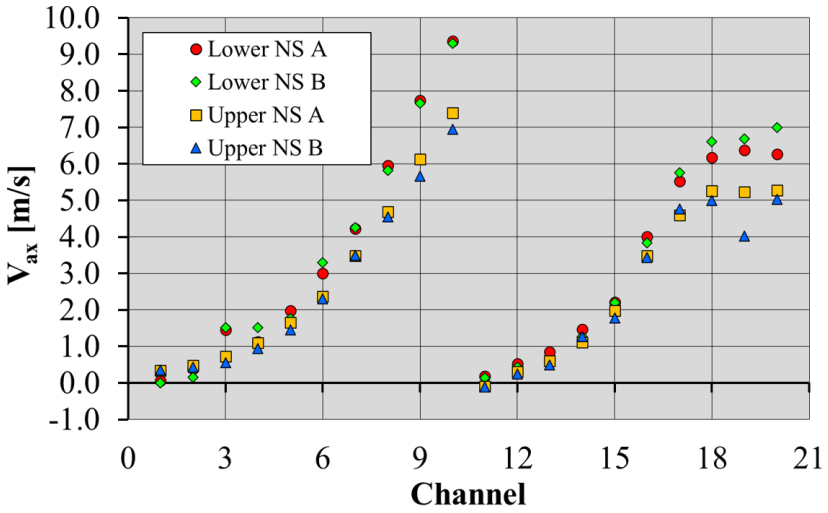

Figure 4.17: Coolant axial flow velocity distribution among NSs channels.

Table 4.13: Coolant axial velocity distribution among NS channels main parameters.

	Lower A	**Lower B**	**Upper A**	**Upper B**
V_{Max} **[m/s]**	9.361	9.304	7.394	6.945
V_{min} **[m/s]**	0.067	0.006	-0.095	-0.109
ϵ_V **[%]**	99.29	99.93	101.28	105.57
V_{ave} **[m/s]**	3.446	3.488	2.807	2.632
σ_V **[m/s]**	2.834	2.942	2.305	2.173
CV_V **[%]**	82.25	83.34	82.11	82.53

Finally, as far as the NSs cooling channels are concerned, the coolant distribution is strongly uneven, and flow reversal phenomena can be observed. However, as for the RPs, the results of the thermal analysis reported in the next sections show that no bulk vaporisation phenomena or thermal hot spots in the structures occur due to the low thermal loads to which these components are exposed. Therefore, no actions are foreseen to revise the design of these components.

Finally, the flow field inside the entire cassette cooling circuit is depicted figure 4.18, where it is possible to appreciate the regions of higher coolant velocity as well as the swirling motion inside the PFU cooling channels induced by the OVSTs.

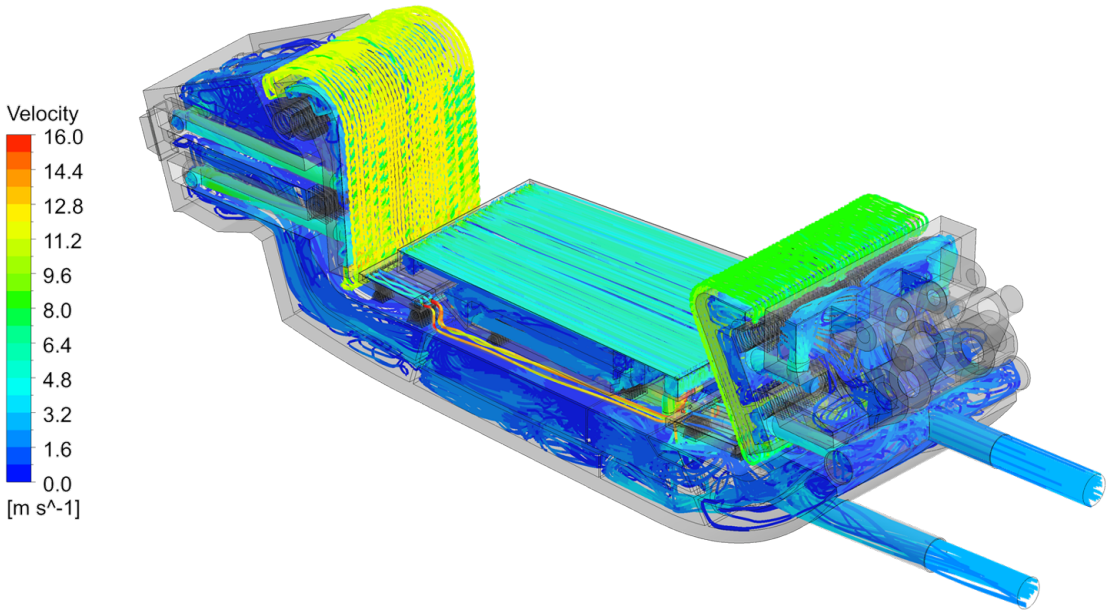

Figure 4.18: Divertor coolant velocity streamlines.

Fluid temperature and saturation margin distributions

The coolant temperature distribution is depicted in figure 4.19, while the coolant margin against saturation, defined according to equation (2.6), is shown in figure 4.20.

As it may be argued from figure 4.19, several hot spots occur in the fluid, due to the occurrence of local stagnation caused by some geometrical features of the cassette. Nevertheless, differently from the 2019 divertor design [26] characterized by localized boiling phenomena, no vaporization is predicted in the fluid domain, with always positive margins against saturation, due to the increased coolant operating pressure and the reduced inlet temperature.

It follows that the constraint on the minimum margin against saturation is respected, being the local minimum value obtained from the simulation ≈48°C, while the value at the outlet of the entire divertor cooling circuit is approximately 95°C.

Moreover, although not visible from the figures, no thermal hot spots are observed for the NSs, despite the presence of the highly uneven flow distribution shown in figure 4.17.

Additionally, attention was focused on the coolant bulk temperatures at the most relevant sections of the divertor cassette cooling circuit. In particular, coolant bulk

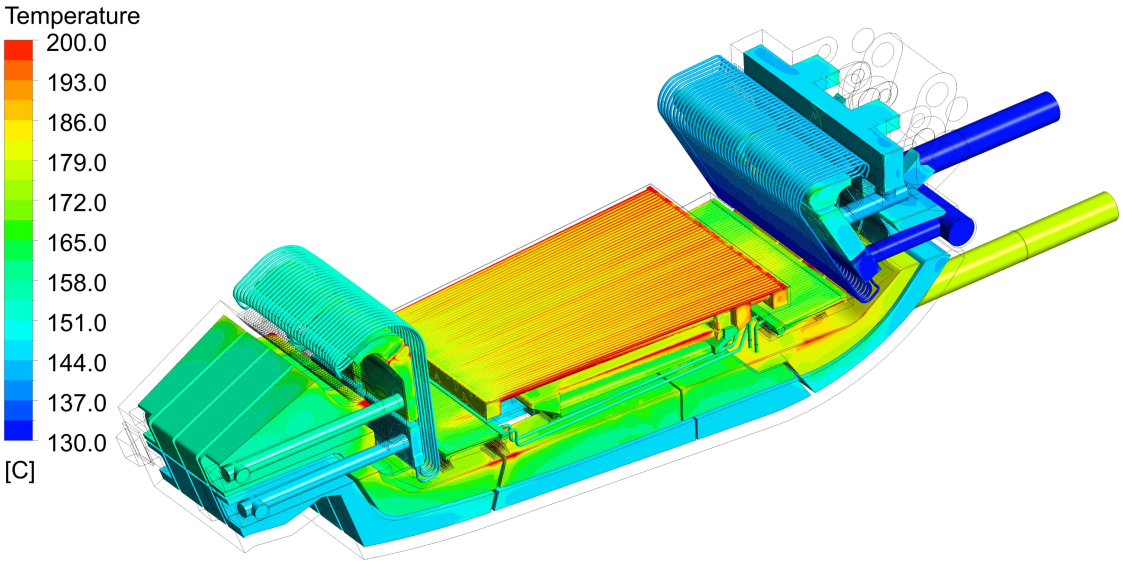

Figure 4.19: Divertor coolant temperature field.

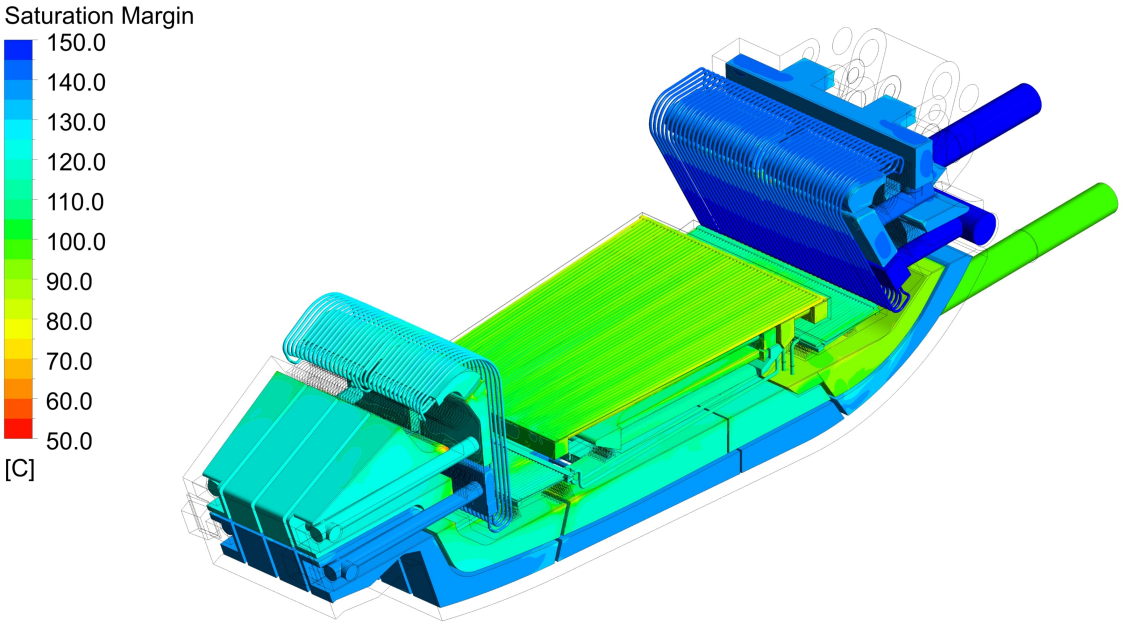

Figure 4.20: Divertor coolant margin against saturation field.

temperatures and margins against saturation calculated at the probing sections depicted in figure 4.21 are reported in table 4.14, showing high saturation margin values, higher than 90°C.

Table 4.14: Divertor cooling circuit bulk temperature and margin distributions.

Region	$\mathbf{T_{bulk}}$ [°C]	$\mathbf{\Delta T_{sat}}$ [°C]
Inlet	130.00	155.83
OVT Inlet	130.01	155.76
OVT Outlet	142.88	140.71
NS Low Inlet	144.14	139.20
NS Low Outlet	144.22	138.42
IVT Inlet	144.90	137.53
IVT Outlet	155.51	122.52
NS Up Inlet	157.94	119.87
Inner RP Inlet	156.65	120.75
NS Up Outlet	158.20	119.13
SL Inlet	158.71	118.39
SL Outlet	178.73	93.27
Inner RP Outlet	159.27	116.46
Outer RP Inlet	159.28	114.42
Outer RP Outlet	162.66	109.57
Outlet	176.48	94.96

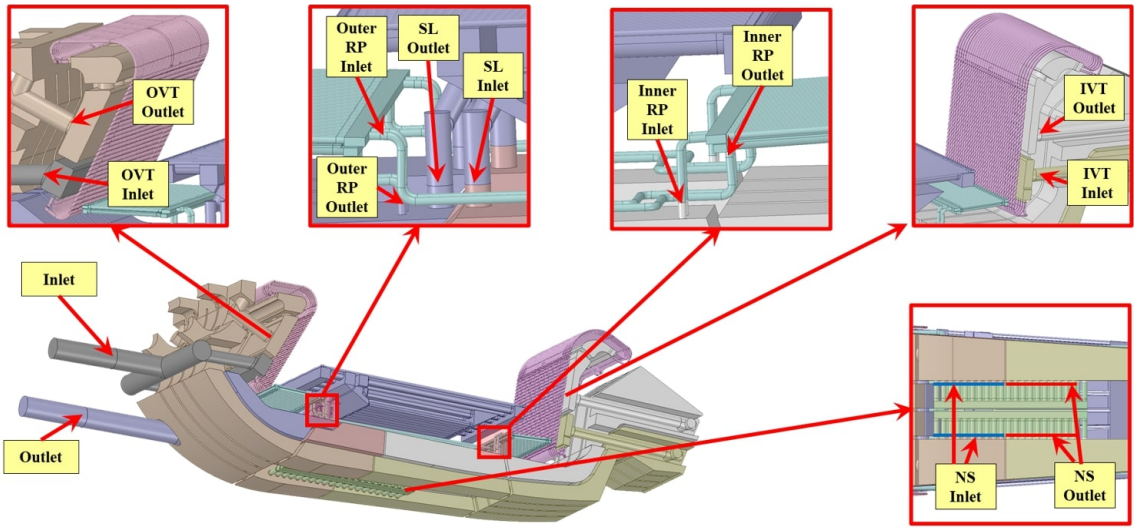

Figure 4.21: Divertor cassette cooling circuit probing sections.

CHF margins

The distributions of the margin against CHF onset within the SL FW, RPs FW and PFUs cooling channels were assessed adopting a different approach for the

different components in order to check whether its prescribed minimum value of 1.4 is guaranteed by the current cooling circuit design.

As far as the PFU cooling channels are concerned, the modified Tong-75 correlation already given in equation (2.8) is adopted, considering a maximum heat flux of 20 MW/m^2 as prescribed in [6].

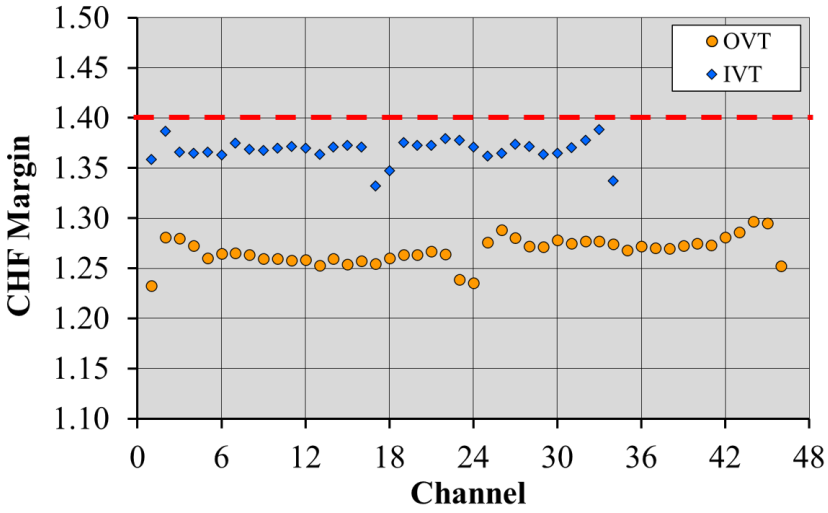

Figure 4.22: CHF margin distribution among PFU cooling channels.

Table 4.15: Coolant CHF margin distribution among PFU cooling channels main parameters.

	OVT	**IVT**
CHF_{Max} [-]	1.297	1.338
CHF_{min} [-]	1.233	1.332
ϵ_{CHF} [%]	4.94	4.05
CHF_{ave} [-]	1.268	1.368
σ_{CHF} [-]	0.014	0.011
CV_{CHF} [%]	1.07	0.83

The results obtained are depicted in figure 4.22 and summarized in table 4.15, and clearly show CHF margins too low to meet the threshold value of 1.4, indicated by the dotted line, being the minimum CHF margins equal to 1.33 and 1.23 respectively for the IVT and the OVT. These results are in line with those obtained with ADRANOS, respectively equal to 1.23 and 1.15. It follows that by adopting ADRANOS there is an underestimation of the CHF margins of approximately 6 to 8% compared to the complete simulations, a satisfactory result considering the huge difference in computational cost between parametric and complete 3D-CFD analyses.

When compared to the performances of the 2019 divertor [21], it can be argued that the lower values of CHF margins are mainly due to the significantly lower velocities in the PFU cooling channels, which are here equal to around 8 and 11

m/s for OVT and IVT respectively, compared to 14 and 13 m/s for the 2019 configuration. However, increasing these velocities is not a viable strategy, as it would cause an increase in pressure drop of the entire cooling circuit, overcoming the 14 bar maximum pressure drop constraint.

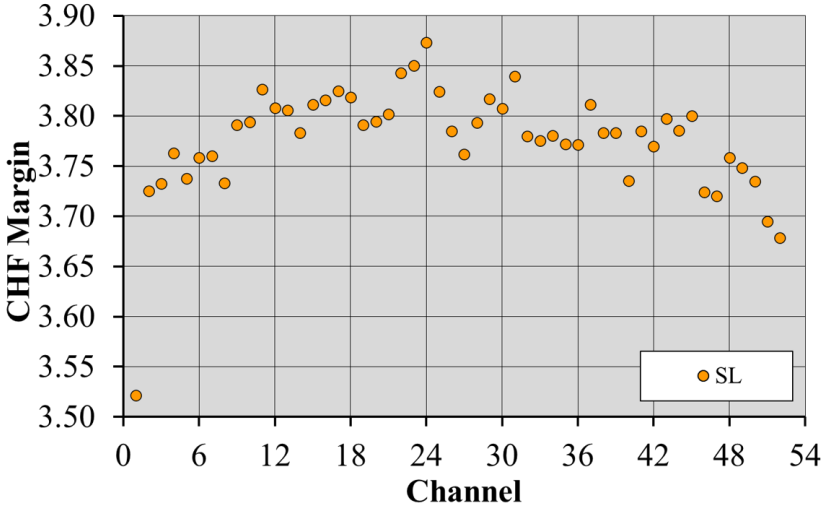

Figure 4.23: CHF margin distribution among SL FW channels.

Table 4.16: Coolant CHF margin distribution among SL FW channels main parameters.

	SL FW channels
CHF_{Max} [-]	3.873
CHF_{min} [-]	3.522
ϵ_{CHF} [%]	9.08
CHF_{ave} [-]	3.772
σ_{CHF} [-]	0.064
CV_{CHF} [%]	1.69

As for the CHF margin for SL and RPs FW channels, these were calculated starting from the CHF look-up tables of [99]. Design peak heat flux values of 1 MW/m^2 and 0.2 MW/m^2 were used according to the indications given in [6] respectively for the FW channels of FW and RPs, while conservative peaking factors f_p values draws from the CFD simulation were selected for SL and RPs. In particular, the peaking factors were estimated as the maximum local heat flux value at the FW cooling channels over the heat flux at the plasma-facing tungsten surface of the component.

The results relevant to the SL FW channels are depicted in figure 4.23 and summarized in table 4.16, calculated with a peaking factor of ≈2.9, while those of the RPs FW channels are shown in figure 4.24 and summarized in table 4.17, calculated with a peaking factor of ≈3.6.

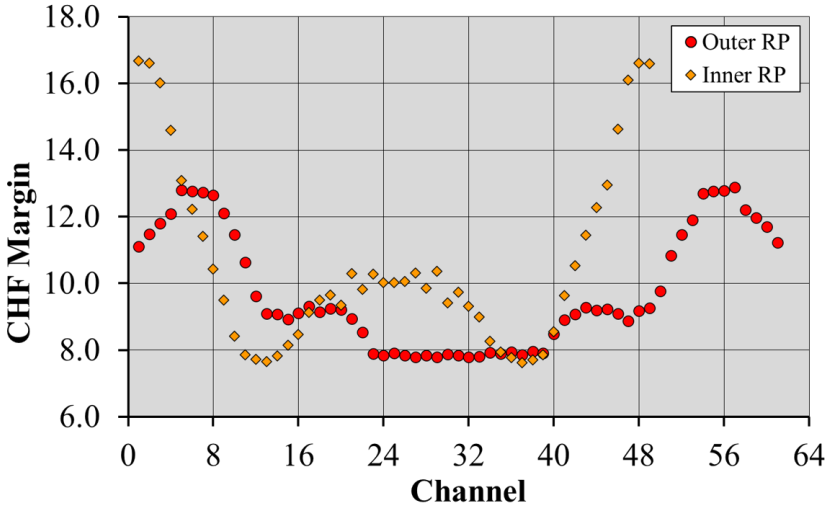

Figure 4.24: CHF margin distribution among RPs FW channels.

Table 4.17: Coolant CHF margin distribution among RPs FW channels main parameters.

	Outer RP	**Inner RP**
CHF_{Max} [-]	12.889	16.673
CHF_{min} [-]	7.787	7.629
ϵ_{CHF} [%]	39.58	54.24
CHF_{ave} [-]	9.809	10.596
σ_{CHF} [-]	1.792	2.773
CV_{CHF} [%]	18.27	26.17

It must be pointed out that such high f_p values are only observed at the first and last channels of the FW, which generally experiences higher heat fluxes due to the geometric features of these components, characterized by a toroidal distance between the extreme channels and the side walls of SL and RPs greater than the pitch between two adjacent channels. However, despite the CHF margins are calculated with very conservative values of f_p, they always remain well above the prescribed limit of 1.4 in every single channel.

Structure temperature distribution

Finally, the structure temperature field is reported in figure 4.25 with a focus on the range that extends from 130 °C (the coolant inlet temperature) to 550 °C. Additionally, the regions exceeding the 550°C limit are depicted in figure 4.26 to check that no zones inside the cassette reach excessive temperatures.

As can be seen from the figures, unduly high temperatures in the structure are observed in SL and IVT supports. Regarding the SL, the maximum temperature reaches a value of 566°C, whose position is circled in figure 4.27. As can be argued from these results, the SL cooling circuit layout can be possibly optimised by moving

the SL level 3 RCs towards the cassette by a few millimeters.

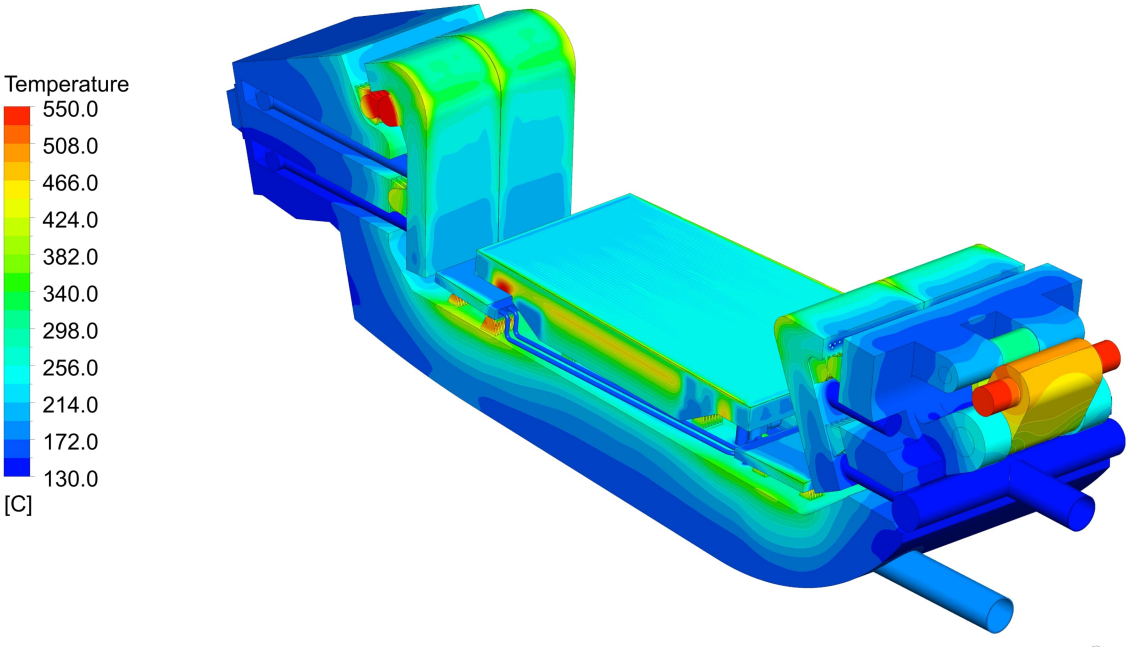

Figure 4.25: Divertor structure temperature field.

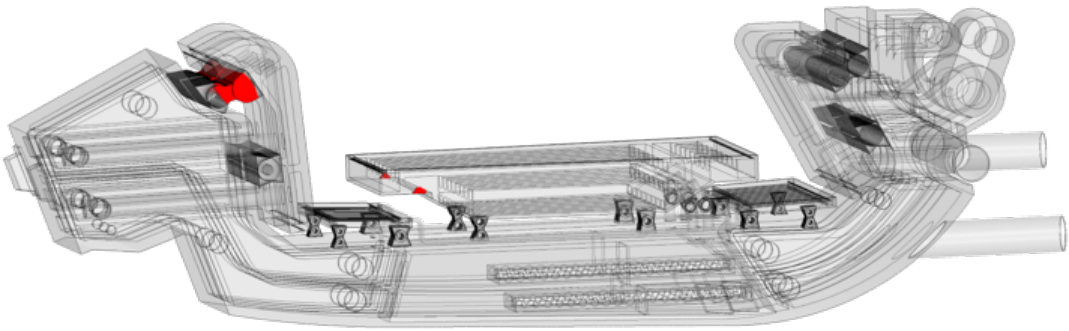

Figure 4.26: Divertor cassette structure critical regions exceeding the 550°C limit.

Regarding the IVT, a maximum of ≈680°C is reached, and a very large area of the upper supports is working at temperatures above 550°C, as visible in figure 4.28. It can be argued from the results that a deep revision of the design of the IVT and its supports is mandatory: in fact, it is probably not sufficient to just reduce the length of the upper supports aiming to decrease the distance to the heat sinks, but also to increase the thickness of the IVT TB, improving its neutron shielding performance.

The maximum temperatures reached in tungsten and in the wishbone are reported in table 4.18 for completeness. As can be argued from the results, the wishbone reaches quite high temperatures as it is not provided with a cooling circuit. The

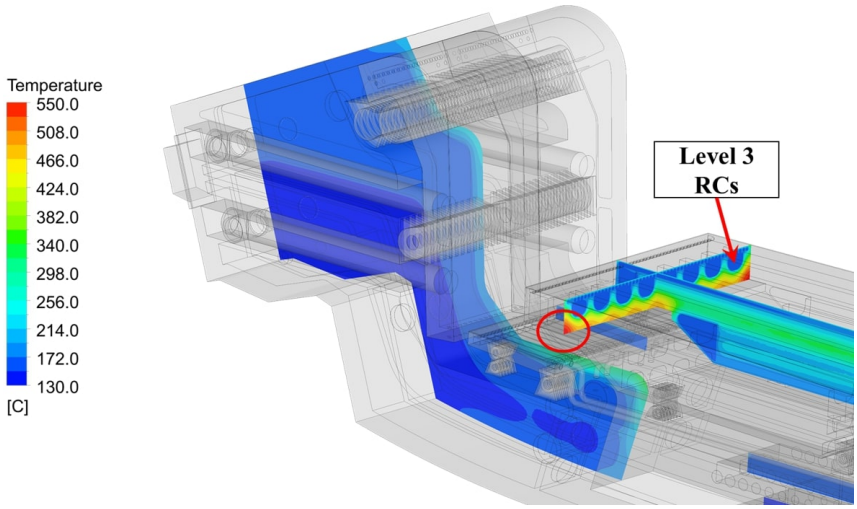

Figure 4.27: Detail of temperature distribution in SL and position of the thermal spot with respect to level 3 RCs

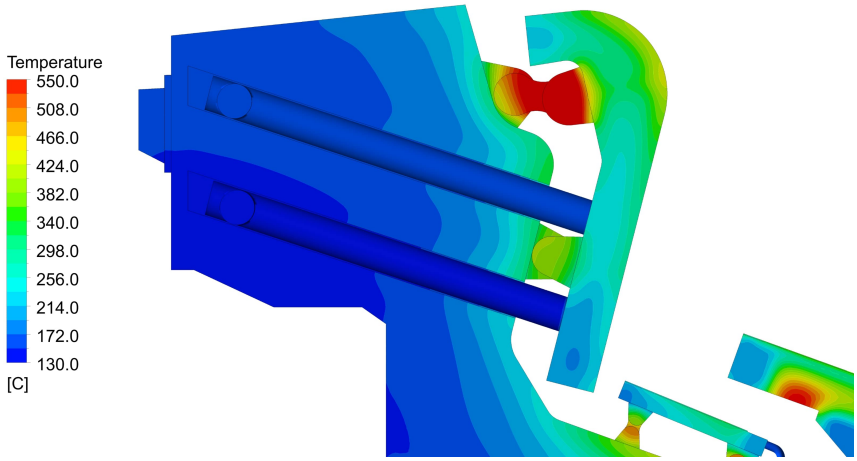

Figure 4.28: Detail of temperature distribution in IVT supports.

Table 4.18: Plasma-facing structures and wishbone maximum temperatures.

Component	**Maximum temperature [°C]**
SL tungsten	422.35
Outer RP tungsten	351.67
Inner RP tungsten	319.70
Wishbone	547.27

maximum calculated temperature is 547°C, but as can be seen from figure 4.25, this is strongly influenced by the boundary conditions used for the simulation. A correct estimation of the temperature distribution in this component would in fact require modelling not only the cassette, but also the outer fixation rail and the main components with which radiative heat exchange phenomena are established (VV and Blanket), with a consequent increase in the computational cost that would make it impossible to carry out the simulation. Regarding the SL and RPs tungsten plates, instead, the maximum temperatures are significantly lower than the limit

values reported in section 1.8.

4.3.2 Results - Nominal loads

Once verified the thermo-hydraulic performance of the divertor cassette under the steady-state normal operating conditions, a second steady-state 3D thermofluid-dynamic analysis was performed to evaluate if the system is able, considering the same mass flow rate adopted for the first analysis, to safely withstand the nominal loads expected for the SL and RPs, selected equal respectively to 1 and 0.2 MW/m^2. The analysis was thus carried out considering the same mesh and the same loads, assumptions and BCs summarized in table 4.5, with the only exception of the surface heat loads to which SL and RPs are exposed. The resulting power breakdown is reported in table 4.19, while the volumetric heat load breakdown is the same as the first scenario and can be drawn from table 4.2. As can be argued from the table, the surface loads are increased by ≈25% with respect to the first scenario, and the total loads (sum of surface and volumetric contribution) by ≈12%. If these heat loads had been considered for the calculation of the mass flow rate at a given coolant temperature increase, this would have been incorrectly raised by approximately 12%, resulting in an overestimation of the cooling capability of the divertor cooling circuit.

Table 4.19: Deposited power breakdown under nominal loads for each cassette.

Surface Heat Loads	
Component	**Power [MW]**
SL Surface	1.511
RPs Surface	0.123
VTs Surface	2.430
TOTAL	**4.064**

The results obtained by this second analysis are reported here only briefly, being similar to those of the first scenario. Concerning the overall pressure drop, it amounts to ≈13.74 bar, and an increase of 0.2% with respect to the first scenario is predicted. The mass flow rate split between the SL and the RPs branches is similarly only marginally affected, as well as the pumping power. Concerning the mass flow rate distribution among the different SL, RPs, PFU, and NSs cooling channels, it is not possible to clearly perform a comparison due to the numerical oscillations of the simulation, and therefore a comparison would be affected by not easily quantifiable noise.

Coolant bulk temperatures and margins against saturation at the most relevant sections of the divertor cooling circuit are reported in table 4.20. As it may be argued from the results, the outlet temperature is increased by approximately 5°C

with respect to the normal operating condition case, while the lowest margin against saturation is always located at the outlet section of the SL and it is reduced by ≈6°C, due to the increased heat load deposited into this component.

Table 4.20: Divertor cooling circuit bulk temperature and margin distributions under nominal loads.

Region	$\mathbf{T_{bulk}}$ [°C]	$\mathbf{\Delta T_{sat}}$ [°C]
Inlet	130.00	155.83
OVT Inlet	130.01	155.76
OVT Outlet	142.93	140.66
NS Low Inlet	144.11	139.26
NS Low Outlet	144.20	138.49
IVT Inlet	144.86	137.62
IVT Outlet	155.45	122.59
NS Up Inlet	157.86	119.95
Inner RP Inlet	156.41	120.98
NS Up Outlet	158.04	119.28
SL Inlet	158.82	118.28
SL Outlet	184.58	87.41
Inner RP Outlet	159.95	115.77
Outer RP Inlet	160.08	113.62
Outer RP Outlet	164.71	107.50
Outlet	181.17	90.25

As for the normal operating condition scenario, no bulk boiling issue is predicted by the simulation due to the quite high saturation temperature provided by the high coolant inlet pressure.

Concerning the CHF margins, the results relevant to the VTs are practically unchanged, being those components placed upstream of the regions where the increased surface loads are applied. The results pertaining to the SL FW channels are instead depicted in figure 4.29 and summarized in table 4.21, while those of the RPs FW channels are shown in figure 4.30 and summarized in table 4.22.

Table 4.21: Coolant CHF margin distribution among SL FW channels main parameters under nominal loads.

	SL FW channels
CHF_{Max} [-]	3.816
CHF_{min} [-]	3.404
ϵ_{CHF} [%]	10.80
CHF_{ave} [-]	3.695
σ_{CHF} [-]	0.075
CV_{CHF} [%]	2.02

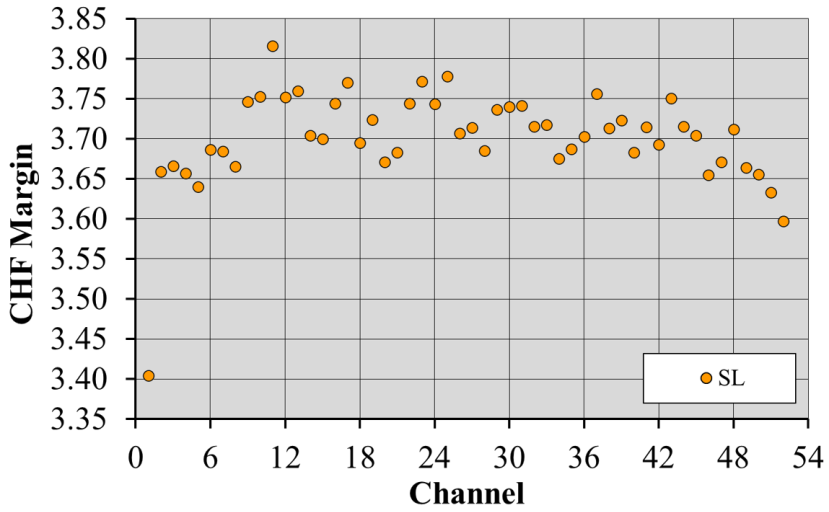

Figure 4.29: CHF margin distribution among SL FW channels under nominal loads.

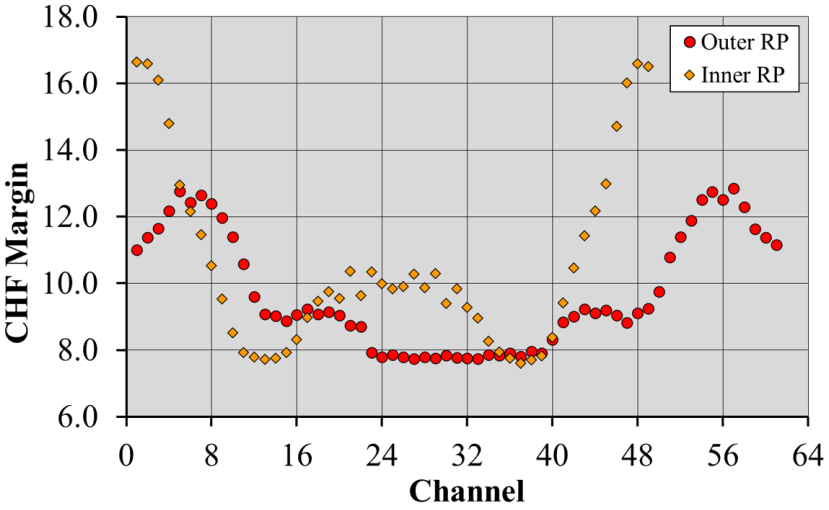

Figure 4.30: CHF margin distribution among RPs FW channels under nominal loads.

Table 4.22: Coolant CHF margin distribution among RPs FW channels main parameters under nominal loads.

	Outer RP	**Inner RP**
CHF_{Max} [-]	12.849	16.635
CHF_{min} [-]	7.739	7.602
ϵ_{CHF} [%]	39.77	54.30
CHF_{ave} [-]	9.737	10.576
σ_{CHF} [-]	1.760	2.780
CV_{CHF} [%]	18.08	26.29

As it may be argued from the results, the CHF margins are reduced if compared to the first scenario, but the magnitude of these reductions is limited, being affected uniquely by the higher coolant temperature inside the FW cooling channels due to the increased thermal loads. Finally, as far as the structure temperature is

concerned, its distribution is shown in figure 4.31, while the regions where the local temperature overcomes the 550°C limit are highlighted in figure 4.32.

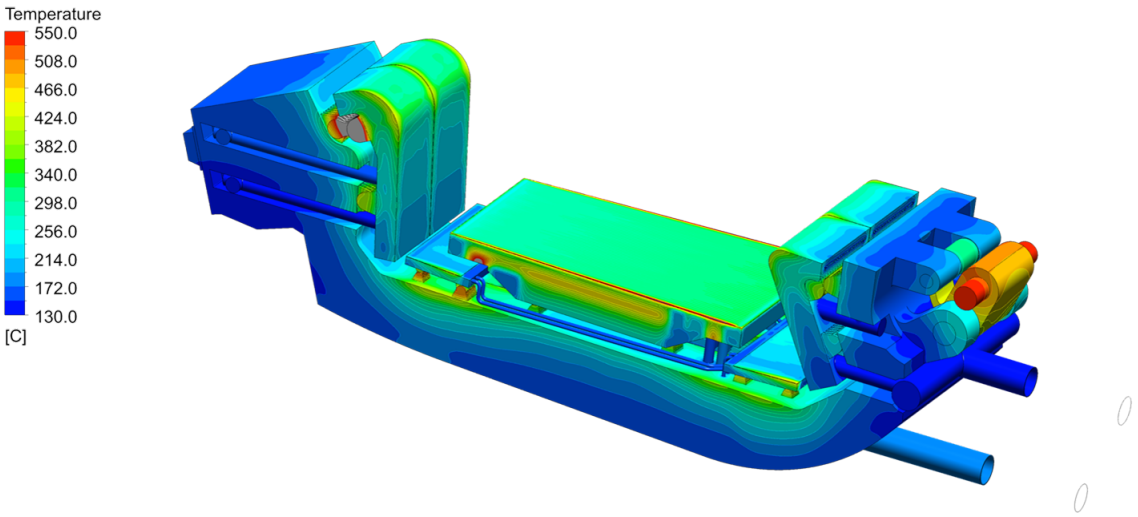

Figure 4.31: Divertor structure temperature field under nominal loads.

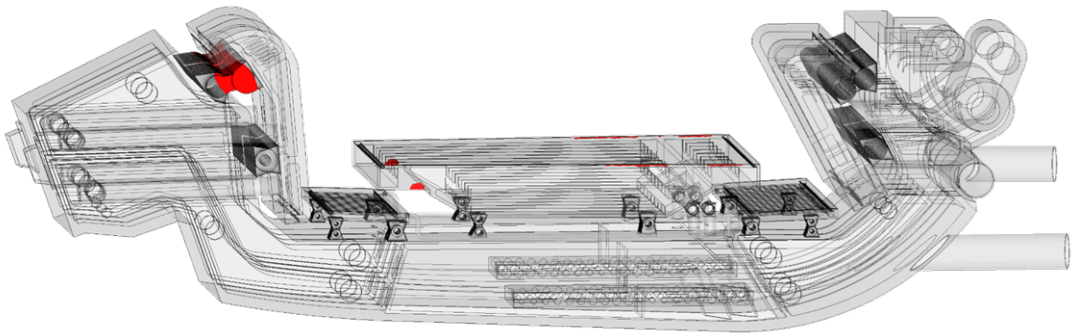

Figure 4.32: Divertor cassette structure critical regions exceeding the 550°C limit under nominal loads.

As it may be noted from the results, the same critical areas already found in nominal operating conditions are obviously present here, with an additional critical region in the upper outermost part of the SL structure, due to the increased surface heat load. At these locations occur the highest temperatures in the structure, reaching a maximum of 589°C.

Additionally, as for the case of the first heat load scenario, the maximum temperatures in tungsten and inside the wishbone are reported in table 4.23 for completeness.

Table 4.23: Plasma-facing structures and wishbone maximum temperatures.

Component	**Maximum temperature [°C]**
SL tungsten	602.80
Outer RP tungsten	444.78
Inner RP tungsten	387.16
Wishbone	547.30

In conclusion, the results obtained from the 3D-CFD simulations highlighted some criticalities of the single-circuit cooling option current design, namely the occurrence of thermal hot spots in SL and IVT supports (with Eurofer temperatures up to 680°C). Moreover, the analyses confirmed the results obtained with ADRANOS and thoroughly discussed in chapter 2. In particular, the occurrence of CHF margins remarkably smaller than 1.4 for every PFU cooling channel is observed, not meeting the design constraints.

Although it is easy to identify a set of design review actions for the divertor cooling circuit that would eliminate or mitigate the occurrence of the thermal hot spots in SL and IVT supports, it remains doubtful whether a solution can be found that can simultaneously ensure compliance with the CHF margin requirements in VTs and the total pressure drop of the cooling circuit without resorting to a reduction of the coolant inlet temperature and/or a further increase in operating pressure, unless different technological solutions for the PFCs and the structural materials are developed. An improvement of the CHF margins can indeed be achieved by increasing the coolant mass flow rate, but this rise would result in a significant growth in pressure drop. It follows that a profound revision of the cooling circuit itself would be necessary, made difficult by the need to keep unchanged the components that are most responsible for these losses, i.e. the PFUs and the SL cooling channels.

Conclusions

My research activity carried out during the XXXV cycle of the Ph.D. course in Energy and Information Technologies takes place within the framework of the activities promoted by the EUROfusion consortium, and was focused on the EU DEMO divertor thermal-hydraulic R&D.

The main purpose of this study was the thermofluid-dynamic assessment of the single-circuit cooling option divertor, aimed to identify its strengths and possible shortcomings. This novel divertor design has been proposed as an alternative solution to the baseline double-circuit concept, with the aim of simplifying the layout of the divertor PHTSs and easing maintenance operations.

In order to do that, the ADRANOS calculation tool was developed in MATLAB environment, with the aim of determining the thermofluid-dynamic operating map of this new divertor design solution, considering different coolant operating conditions and different cooling circuit layouts, and checking the compliance with several thermal and thermal-hydraulic constraints. ADRANOS was developed and optimized to perform an assessment of the mass flow rate, coolant temperature, and coolant pressure distribution among the different sub-components constituting the divertor cassette by adopting a lumped-parameters approach, and relies on a 2D-FEM module to evaluate the detailed temperature distribution inside the PFU structures, so to check the compliance with materials temperature limits.

The tool was validated against experimental results and exploited to carry out a broad parametric analysis campaign to determine the limits and acceptable operating ranges of several DEMO divertor cooling circuit layouts, both single and double circuit cooling options.

The outcomes of these analyses highlighted some crucial issues for the adoption of the single-circuit, being not possible to increase the coolant inlet temperature above certain values (that depend on the coolant inlet pressure) due to the constraints on PFCs CHF margins, unless a rather complex cooling circuit layout is adopted, foreseeing the VTs connected in parallel and a suitable CB bypass, which could potentially present some problems of erosion and flow instability, and which would require a remarkably higher pumping power. The low coolant operating temperature implies a reduced lifetime of the cassette, due to the combined effect of operating temperature and neutron-induced damage and He production, requiring more

frequent replacement. As a consequence, it can be expected a worsening in terms of plant availability, nuclear waste, overall plant electric efficiency, and definitively an increase in costs, drawbacks that significantly outweigh the advantages of employing this design solution.

Moreover, theoretical assessments allowed to determine maximum coolant inlet temperatures of approximately 185°C and 160°C with the VTs connected respectively in parallel and in series, supposing a reasonable coolant inlet pressure of 75 bar, not excessively higher than the current design pressure. These results are valid for any kind of divertor cooling circuit embedding the PFCs and thus applies to the single-circuit cooling option as well. More realistically, taking into account the several non-idealities of the divertor, the coolant inlet temperature should be kept lower than 150°C, thus resulting in a component lifetime that can be significantly lower than 1 FPY.

ADRANOS was moreover employed to assess suitable coolant operating conditions to be adopted for the PFC cooling circuit of a double-circuit cooling option divertor considering different slow transient heat load scenarios and allowing for some flexibility in the two most relevant constraints, i.e. the CHF margin and the maximum coolant axial velocity. The results of these analyses highlighted some aspects that should be considered in the future design of the divertor cooling circuit:

- a solution with targets in parallel was proved to be able to provide a better cooling potential if compared to the VTs connected in series;
- it could be necessary either a reduction of the coolant inlet temperature or an increase of the coolant pressure if stricter constraints on maximum coolant axial velocity are enforced, due to possible criticalities related to fretting and flow-accelerated corrosion;
- it is not possible to sustain heat fluxes significantly higher than 30 MW/m^2 for slow transient events because the tungsten melting cannot be avoided with the current monoblock technology, regardless of the choice of coolant operating conditions.

The ADRANOS code will be further developed in the next years, with the aim of extending its predictive capabilities, reducing computational time, and improving the graphical quality of the figures produced by the post-processing script. In particular, the possibility of solving parallels between more than two components will be implemented, while the adoption of meta-modelling techniques will be evaluated to significantly reduce the calculation time, mainly dictated by the 2D-FEM analyses.

Furthermore, it is currently under evaluation how to complement the code with thermo-structural assessments, to include other constraints to the divertor operating map, allowing for a more conservative evaluation of the acceptable operating

conditions. At the post-processing level, it is planned an improvement the clarity of the results, showing constraint curves only when they are physically relevant.

Additionally, complete 3D-CFD thermofluid-dynamic analyses of the entire divertor cassette were performed to confirm the outcomes obtained with ADRANOS and to highlight the possible occurrence of additional criticalities. Given the great complexity of the divertor, it was deemed necessary to preliminarily develop some modelling techniques to reduce the computational cost required to perform these CFD calculations.

The attention was focused on the ST-equipped PFU cooling channels, the most complex and detailed parts of the divertor, that would result difficult to integrate into the complete cassette CFD model, as they would require an excessive computational cost and an unduly high pre-processing effort. Therefore, several analysis campaigns were carried out to assess the flow field inside these components, estimating a suitable mesh size required to obtain fairly mesh-independent results, highlighting the considerable numerical errors that can be made if an inadequate mesh is used, and validating the results against several correlations available in literature. Additionally, complete PFU cooling channel analyses allowed to determine the occurrence of two peculiar fluid-dynamic phenomena that significantly affect pressure drop and heat transfer, i.e. a strong flow separation at the entrance of the ST-equipped section and a slow decay of the coolant swirling motion downstream the ST.

Then, the VST approach, a novel modelling technique based on the adoption of porous media, was developed, properly calibrated with dedicated optimization campaigns and validated in terms of pressure drop predictive capabilities. Three different VST models were developed and tested, showing the strengths and weaknesses of each one of them.

These models proved excellent pressure drop prediction capabilities, even when significant deviations from the coolant velocity condition adopted for calibration are considered, and are thus suitable for accurate and fast-running 3D-CFD isothermal analyses. However, the heat transfer coefficient is unacceptably underestimated, thus requiring the adoption of a workaround when thermal analyses have to be performed. The VST approach will be further developed in the future, to assess the possibility of improving the prediction capabilities of the heat transfer coefficient, possibly employing user-defined thermal wall functions.

Finally, the VST approach was employed to perform the complete 3D-CFD simulation of the single-circuit cooling option divertor cassette. First of all, an extensive mesh independence assessment of the divertor main components was performed, selecting the optimal mesh size to be adopted, thus guaranteeing a measurable mesh dependency of the results obtained in terms of pressure, temperature, and mass flow rate distribution. The calculations allowed obtaining

a detailed picture of the divertor cooling performance, confirming the criticalities already observed with ADRANOS, i.e. an unacceptably low CHF margin for both IVT and OVT. Additionally, the analyses highlighted additional issues that must be addressed in the future design revisions of the divertor cassette, i.e. the occurrence of severe thermal hot spots in the target supports and in the SL, exceeding the 550°C Eurofer temperature limit.

The overall research activity shows that the adoption of a single-circuit cooling option divertor for the EU DEMO may pose some severe criticalities, as it is not possible to meet the project requirements while guaranteeing a suitable divertor lifetime, at least considering the actual knowledge in terms of plasma heat load, the materials currently selected for the divertor and the technology of the PFCs, and the still incomplete knowledge of the properties of these materials exposed to high levels of neutron-induced damage at low operating temperatures.

Considering all these aspects and the results presented in this thesis, it is possible to provide some guidelines for the future development of the divertor cassette. In particular, it should be reconsidered the adoption of a double-circuit cooling option system, possibly with PFCs connected in parallel to improve the cooling circuit performance. As far as the PFC cooling circuit is concerned, low-temperature water with inlet pressures from 50 to 75 bar should be probably assumed, provided that thermo-structural or waste management criticalities are not envisaged due to the low temperature of the materials. Regarding the CB cooling circuit, instead, higher coolant operating temperatures and pressures should be investigated, as it is currently being done within the EUROfusion project, aiming to increase the cassette lifetime.

Acknowledgements

I would like to sincerely thank Prof. Pietro Alessandro Di Maio for encouraging me to embark on this Ph.D. journey, for mentoring and supporting me in this interesting research activity.

Special thanks go to Prof. Pierluigi Chiovaro, for his help in revising this thesis, for the friendship and for all the enlightening discussions (both on nuclear engineering and not) we have had over these years.

My gratitude goes to Dr.s Gianfranco Federici, Alessandro Spagnuolo and especially Ivo Moscato, for hosting me at the EUROfusion PMU, and having shared with me their outstanding expertise.

My thanks go to my friends and laboratory/misadventures fellows Gaetano and Eugenio, with whom I have shared life (and many coffees) in our lab over the past years. If you are wondering, no: I have not booked yet.

A special thank goes also to Francesca, who helped me in developing the ideas and results of chapters 3 and 4 and who kept me company over the last two months in Munich.

I wanted also to thank my fellow Ph.D. students and post-docs of our group, Ilenia, Giuseppe, Salvo, Alberto and Silvia, with whom I have always greatly enjoyed working.

I hope none of you will be offended, friends and colleagues: I should dedicate much more than these words to each one of you, but the acknowledgements are already becoming very long!

Finally, the warmest thanks are to my beloved girlfriend Eleonora, for supporting me, and always being there for me before, during and (hopefully) after my Ph.D.

Bibliography

[1] F. Romanelli, et al., A Roadmap to the Realisation of Fusion Energy, 2012, ISBN: 978-3-00-040720-8.

[2] T. Donné, W. Morris, European Research Roadmap to the Realisation of Fusion Energy, EUROfusion: Munich, Germany, 2018, ISBN: 978-3-00-061152-0.

[3] G. Federici, et al., Overview of the DEMO staged design approach in Europe, Nuclear Fusion 59 (2019) 066013. doi:10.1088/1741-4326/ab1178.

[4] Fusion on Earth, https://www.euro-fusion.org/fusion/fusion-on-earth/, accessed: 2022-12-06.

[5] A. Harms, K. Schoepf, D. Kingdon, Principles of Fusion Energy: An Introduction to Fusion Energy for Students of Science and Engineering, Principles of Fusion Energy: An Introduction to Fusion Energy for Students of Science and Engineering, World Scientific, 2000.

[6] J.H. You, et al., Divertor of the European DEMO: Engineering and technologies for power exhaust, Fusion Engineering and Design 175 (2022) 113010. doi:https://doi.org/10.1016/j.fusengdes.2022.113010.

[7] C. Bachmann, PDD - Plant Description Document, EUROfusion: Munich, Germany, 2020, EUROfusion IDM Ref.: 2KVWQZ v1.9.

[8] F. Maviglia, et al., Impact of plasma-wall interaction and exhaust on the EU-DEMO design, Nuclear Materials and Energy 26 (2021) 100897. doi:https://doi.org/10.1016/j.nme.2020.100897.

[9] R. Tivey, et al., ITER divertor, design issues and research and development, Fusion Engineering and Design 46 (2) (1999) 207–220. doi:https://doi.org/10.1016/S0920-3796(99)00047-2.

[10] A. Loarte, R. Neu, Power exhaust in tokamaks and scenario integration issues, Fusion Engineering and Design 122 (2017) 256–273. doi:https://doi.org/10.1016/j.fusengdes.2017.06.024.

[11] M. Turnyanskiy, et al., European roadmap to the realization of fusion energy: Mission for solution on heat-exhaust systems, Fusion Engineering and Design 96-97 (2015) 361–364. doi:https://doi.org/10.1016/j.fusengdes.2015.04.041.

[12] G. Federici, et al., European DEMO design strategy and consequences for materials, Nuclear Fusion 57 (9) (2017) 092002. doi:10.1088/1741-4326/57/9/092002.

[13] C. Gliss, Integrated design of the DEMO lower ports, EUROfusion: Munich, Germany, 2020, EUROfusion IDM Ref.: 2MSRLH v1.4.

[14] G. Mazzone, et al., Eurofusion-DEMO Divertor - Cassette Design and Integration, Fusion Engineering and Design 157 (2020) 111656. doi:10.1016/j.fusengdes.2020.111656.

[15] D. Marzullo, Report on DIV.JUS-2-CD1 Divertor System Detailed Design Description, EUROfusion: Munich, Germany, 2020, EUROfusion IDM Ref.: 2NSLJP v1.4.

[16] M. Merola, et al., Overview and status of ITER internal components, Fusion Engineering and Design 89 (7) (2014) 890–895. doi:10.1016/j.fusengdes.2014.01.055.

[17] M. Li, J.H. You, Structural impact of armor monoblock dimensions on the failure behavior of ITER-type divertor target components: Size matters, Fusion Engineering and Design 113 (2016) 162–170. doi:https://doi.org/10.1016/j.fusengdes.2016.10.014.

[18] V. Imbriani, et al., Insulated fixation system of plasma facing components to the divertor cassette in Eurofusion-DEMO, Fusion Engineering and Design 158 (2020) 111710. doi:https://doi.org/10.1016/j.fusengdes.2020.111710.

[19] D. Marzullo, et al., DIV-JUS-2-CD1 Divertor System Detailed Design Description, EUROfusion: Munich, Germany, 2020, EUROfusion IDM Ref.: 2NSLJP v1.4.

[20] D. Marzullo, et al., Progress in the pre-conceptual CAD engineering of European DEMO divertor cassette, Fusion Engineering and Design 146 (2019) 942–945. doi:https://doi.org/10.1016/j.fusengdes.2019.01.120.

[21] P.A. Di Maio, et al., Hydraulic assessment of an upgraded pipework arrangement for the DEMO divertor plasma facing components cooling circuit, Fusion Engineering and Design 168 (2021) 112368. doi:https://doi.org/10.1016/j.fusengdes.2021.112368.

[22] P.A. Di Maio, et al., Thermal-hydraulic behaviour of the DEMO divertor plasma facing components cooling circuit, Fusion Engineering and Design 124 (2017) 415–419. doi:10.1016/j.fusengdes.2017.02.025.

[23] P.A. Di Maio, et al., On the thermal-hydraulic optimization of DEMO divertor plasma facing components cooling circuit, Fusion Engineering and Design 136 (2018) 1438–1443. doi:10.1016/j.fusengdes.2018.05.032.

[24] P.A. Di Maio, et al., Hydraulic analysis of EU-DEMO divertor plasma facing components cooling circuit under nominal operating scenarios, Fusion Engineering and Design 146 (2019) 1764–1768. doi:10.1016/j.fusengdes.2019.03.030.

[25] P.A. Di Maio, et al., On the numerical assessment of the thermal-hydraulic operating map of the DEMO Divertor Plasma Facing Components cooling circuit, Fusion Engineering and Design 161 (2020). doi:10.1016/j.fusengdes.2020.111919.

[26] P.A. Di Maio, et al., Thermal-hydraulic study of the DEMO divertor cassette body cooling circuit equipped with a liner and two reflector plates, Fusion Engineering and Design 167 (2021) 112227. doi:https://doi.org/10.1016/j.fusengdes.2021.112227.

[27] S. Noce, et al., Neutronics analysis and activation calculation for tungsten used in the DEMO divertor targets: A comparative study between the effects of WCLL and HCPB blanket, different W compositions and chromium, Fusion Engineering and Design 169 (2021) 112428. doi:https://doi.org/10.1016/j.fusengdes.2021.112428.

[28] P.A. Di Maio, et al., Analysis of steady state thermal-hydraulic behaviour of the DEMO divertor cassette body cooling circuit, Fusion Engineering and Design 124 (2017) 437–441. doi:10.1016/j.fusengdes.2017.02.012.

[29] P.A. Di Maio, et al., Computational thermofluid-dynamic analysis of DEMO divertor cassette body cooling circuit, Fusion Engineering and Design 136 (2018) 1588–1592. doi:10.1016/j.fusengdes.2018.05.063.

[30] P.A. Di Maio, et al., Thermal-hydraulic optimisation of the DEMO divertor cassette body cooling circuit equipped with a liner, Fusion Engineering and Design 146 (2019) 220–223. doi:10.1016/j.fusengdes.2018.12.024.

[31] P.A. Di Maio, et al., On the thermal-hydraulic performances of the DEMO divertor cassette body cooling circuit equipped with a liner, Fusion Engineering and Design 156 (2020) 111613. doi:10.1016/j.fusengdes.2020.111613.

[32] G. Federici, J. Holden, C. Baylard, A. Beaumont, The EU DEMO staged design approach in the Pre-Concept Design Phase, Fusion Engineering and Design 173 (2021) 112959. doi:https://doi.org/10.1016/j.fusengdes.2021.112959.

[33] D. Marzullo, DIV-1-T007-D004 - CAD Design - 2020, EUROfusion: Munich, Germany, 2021, EUROfusion IDM Ref.: 2PB42X v1.0.

[34] D. Marzullo, V. Imbriani, F. Giovanna, DIV-DEMO.S.1-T001-D001_DEMO Divertor CAD model 2021, EUROfusion: Munich, Germany, 2021, EUROfusion IDM Ref.: 2PHRQZ v1.0.

[35] D. Stork, 1. WPDIV PCD Final Review Panel Report, EUROfusion: Munich, Germany, 2020, EUROfusion IDM Ref.: 2P32U3 v1.0.

[36] J.H. You, DIV-.JUS-2-CD1 Design & Manufacturing Feasibility Study for In-vessel Supports, EUROfusion: Munich, Germany, 2020, EUROfusion IDM Ref.: 2NVU8L v1.2.

[37] P.A. Di Maio, DIV-DEMO.S.1-T002-D001_Divertor Thermo-hydraulic assessment 2021, EUROfusion: Munich, Germany, 2022, EUROfusion IDM Ref.: 2PHWSW v1.0.

[38] L.V. Boccaccini, et al., Materials and design of the european demo blankets, Journal of Nuclear Materials 329-333 (2004) 148–155, proceedings of the 11th International Conference on Fusion Reactor Materials (ICFRM-11). doi:https://doi.org/10.1016/j.jnucmat.2004.04.125.

[39] G. Mazzone, et al., Choice of a low operating temperature for the DEMO EUROFER97 divertor cassette, Fusion Engineering and Design 124 (2017) 655–658. doi:https://doi.org/10.1016/j.fusengdes.2017.02.013.

[40] R. Villari, DIV-DEMO.S.1-T003-D001_Neutronics and shielding assessment report 2021, EUROfusion: Munich, Germany, 2022, EUROfusion IDM Ref.: 2PJ33J v1.0.

[41] R. Villari, D005-Neutronics_Villari, EUROfusion: Munich, Germany, 2021, EUROfusion IDM Ref.: 2PJ33J v1.0.

[42] E. Gaganidze, J. Aktaa, Assessment of neutron irradiation effects on RAFM steels, Fusion Engineering and Design 88 (3) (2013) 118–128. doi:https://doi.org/10.1016/j.fusengdes.2012.11.020.

[43] F. Domptail, et al., The design and optimisation of a monoblock divertor target for DEMO using thermal break interlayer, Fusion Engineering and Design 154 (2020) 111497. doi:https://doi.org/10.1016/j.fusengdes.2020.111497.

[44] M. Richou, et al., Recrystallization at high temperature of two tungsten materials complying with the ITER specifications, Journal of Nuclear Materials 542 (2020) 152418. doi:https://doi.org/10.1016/j.jnucmat.2020.152418.

[45] J.H. You, et al., High-heat-flux performance limit of tungsten monoblock targets: Impact on the armor materials and implications for power exhaust capacity, Nuclear Materials and Energy 33 (2022) 101307. doi:https://doi.org/10.1016/j.nme.2022.101307.

[46] A.R. Raffray, et al., Critical heat flux analysis and R&D for the design of the ITER divertor, Fusion Engineering and Design 45 (4) (1999) 377–407. doi:10.1016/S0920-3796(99)00053-8.

[47] The MathWorks, Inc., MATLAB Primer, 2021, Release: R2021b.

[48] FEATool Multiphysics v1.15, User's Guide, 2021.
URL https://www.featool.com

[49] ANSYS Inc., ANSYS CFX-Solver Theory Guide, ANSYS: Canonsburg, PA, USA, 2021, 2021, Release: 2021 R1.

[50] ANSYS Inc., Discovery SpaceClaim, ANSYS: Canonsburg, PA, USA, 2021, 2021, Release: 2021 R1.

[51] ANSYS Inc., ANSYS Meshing User's Guide, ANSYS: Canonsburg, PA, USA, 2021, 2021, Release: 2021 R1.

[52] International Association for the Properties of Water and Steam, Revised Release on the IAPWS Industrial Formulation 1997 for the Thermodynamic Properties of Water and Steam, 2007.

[53] F. Gillemot and et al., Material Property Handbook pilot project on EUROFER97 (MTA EK, KIT), EUROfusion: Munich, Germany, 2016, EUROfusion IDM Ref.: 2MRP77.

[54] ITER Material Properties Handbook, ITER Document No. G74 MA 16.

[55] P.A. Di Maio, et al., DIV-1-T007-D006 - Divertor Thermo-hydraulic assessment 2020, EUROfusion: Munich, Germany, 2021, EUROfusion IDM Ref.: 2P6AMZ v1.0.

[56] I. Moscato, Divertor PFC PHTS_layout and summary tables, EUROfusion: Munich, Germany, 2022, EUROfusion IDM Ref.: 2Q3PQG v1.0.

[57] A. Raffray, G. Federici, RACLETTE: a model for evaluating the thermal response of plasma facing components to slow high power plasma transients. Part I: Theory and description of model capabilities, Journal of Nuclear Materials 244 (2) (1997) 85–100. doi:https://doi.org/10.1016/S0022-3115(96)00680-0.

[58] T. D. Marshall, D. L. Youchison, L. C. Cadwallader, Modeling the Nukiyama Curve for Water-Cooled Fusion Divertor Channels, Fusion Technology 39 (2P2) (2001) 849–855. doi:10.13182/FST01-A11963345.

[59] Z. Jackson, J. Nicholas, P. Ireland, Development of a 1D thermofluid code for divertor target plate modeling, Fusion Engineering and Design 147 (2019) 111237. doi:https://doi.org/10.1016/j.fusengdes.2019.06.010.

[60] S. E.-D. El-Morshedy, Thermal-hydraulic modelling and analysis of ITER tungsten divertor monoblock, Nuclear Materials and Energy 28 (2021) 101035. doi:https://doi.org/10.1016/j.nme.2021.101035.

[61] M. Holmgren, X Steam, Thermodynamic properties of water and steam, MATLAB Central File Exchange. Retrieved March, 2022 (2022).

[62] J. Kiefer, Sequential minimax search for a maximum, Proceedings of the American Mathematical Society 4 (3) (1953) 502–506.

[63] P. J. Roache, Verification of Codes and Calculations, AIAA Journal 36 (5) (1998) 696–702. doi:10.2514/2.457.

[64] L. Eça, M. Hoekstra, A procedure for the estimation of the numerical uncertainty of CFD calculations based on grid refinement studies, Journal of Computational Physics 262 (2014) 104–130. doi:https://doi.org/10.1016/j.jcp.2014.01.006.

[65] E. Gaganidze, et al., DEMO-DEF-1-CD1 - Materials Properties Handbook - Tungsten, EUROfusion: Munich, Germany, 2020, EUROfusion IDM Ref.: 2P3SPL.

[66] E. Gaganidze, et al., DEMO-DEF-1-CD1 - Materials Properties Handbook - CuCrZr, EUROfusion: Munich, Germany, 2020, EUROfusion IDM Ref.: 2NV3Q6.

[67] Y. S. Touloukian, et al., Thermophysical Properties of Matter - The TPRC Data Series. Volume 1. Thermal Conductivity - Metallic Elements and Alloys, Tech. rep., Thermophysical and Electronic Properties Information Analysis Center Lafayette, IN (1970).

[68] T. Bergman, A. Lavine, F. Incropera, D. DeWitt, Fundamentals of Heat and Mass Transfer, 8th Edition, Wiley, 2017.

[69] W. Gambill, Heat transfer, burnout, and pressure drop for water in swirl flow through tubes with internal twisted tapes, Vol. 2911, Oak Ridge National Laboratory, 1960.

[70] S. N. Laboratories, U. S. D. of Energy. Office of Scientific, T. Information, FILM-30: A Heat Transfer Properties Code for Water Coolant, United States. Department of Energy, 2001.

[71] A. E. Bergles, W. M. Rohsenow, The Determination of Forced-Convection Surface-Boiling Heat Transfer, Journal of Heat Transfer 86 (3) (1964) 365–372. doi:10.1115/1.3688697.

[72] M. Araki, et al., Experiments on heat transfer of smooth and swirl tubes under one-sided heating conditions, International Journal of Heat and Mass Transfer 39 (14) (1996) 3045–3055. doi:https://doi.org/10.1016/0017-9310(95)00344-4.

[73] T. D. Marshall, J. M. McDonald, L. C. Cadwallader, D. Steiner, An Experimental Examination of the Loss-of-Flow Accident Phenomenon for Prototypical ITER Divertor Channels of Y = 0 and Y = 2, Fusion Technology 37 (1) (2000) 38–53. doi:10.13182/FST00-A120.

[74] T. D. Marshall, Experimental examination of the postcritical heat flux and loss-of-flow accident phenomena for prototypical ITER divertor channels, Rensselaer Polytechnic Institute, 1999.

[75] S. E.-D. El-Morshedy, A. Hassanein, Transient thermal hydraulic modeling and analysis of ITER divertor plate system, Fusion Engineering and Design 84 (12) (2009) 2158–2166. doi:https://doi.org/10.1016/j.fusengdes.2009.02.051.

[76] A. Tincani, et al., Hydraulic Characterization of the Full Scale Mock-Up of the DEMO Divertor Outer Vertical Target, Energies 14 (23) (2021). doi:10.3390/en14238086.

[77] F. Crescenzi, H. Greuner, S. Roccella, E. Visca, J. You, ITER-like divertor target for DEMO: Design study and fabrication test, Fusion Engineering and Design 124 (2017) 432–436. doi:https://doi.org/10.1016/j.fusengdes.2017.02.014.

[78] I. Moscato, Tokamak Thermal Power Flow, EUROfusion: Munich, Germany, 2022, EUROfusion IDM Ref.: 2Q3PUA v1.0.

[79] P.A. Di Maio, DIV-DEMO.S.1-T011-D001DEMO Divertor Thermo-hydraulic assessment 2022_ENEA, EUROfusion: Munich, Germany, 2022, EUROfusion IDM Ref.: 2Q47U2 v1.0.

[80] D. Marzullo, DIV-DEMO.S.1-T010-D001DEMO Divertor CAD model 2022_ENEA, EUROfusion: Munich, Germany, 2022, EUROfusion IDM Ref.: 2Q43XL v1.0.

[81] E. Vallone, BOP-2.1-T056-D003: HCPB DIV PFU PHTS DDD (Indirect Coupling Option), EUROfusion: Munich, Germany, 2020, EUROfusion IDM Ref.: 2MLKXY v1.5.

[82] G. Mazzone, et al, Structural verification and manufacturing procedures of the cooling system, for DEMO divertor target (OVT), Fusion Engineering and Design 146 (2019) 1610–1614. doi:https://doi.org/10.1016/j.fusengdes.2019.02.139.

[83] R. M. Manglik, A. E. Bergles, Swirl flow heat transfer and pressure drop with twisted-tape inserts, Vol. 36 of Advances in Heat Transfer, 2003, pp. 183–266. doi:https://doi.org/10.1016/S0065-2717(02)80007-7.

[84] A. V. Dedov, et al., Hydrodynamics and heat transfer in swirl flow under conditions of one-side heating. Part 1: Pressure drop and single-phase heat transfer, International Journal of Heat and Mass Transfer 53 (19) (2010) 4123–4131. doi:https://doi.org/10.1016/j.ijheatmasstransfer.2010.05.034.

[85] R. M. Manglik, A. E. Bergles, Heat Transfer and Pressure Drop Correlations for Twisted-Tape Inserts in Isothermal Tubes: Part II "Transition and Turbulent Flows, Journal of Heat Transfer 115 (4) (1993) 890–896. doi:10.1115/1.2911384.

[86] R. Lopina, A. Bergles, Heat Transfer and Pressure Drop in Tape-Generated Swirl Flow of Single-Phase Water, Journal of Heat Transfer 91 (3) (1969) 434–441. doi:10.1115/1.3580212.

[87] M. Ibragimov, E. Nomofilov, V. Subbotin, Heat Transfer and Hydraulic Resistance for Fluid Helical Motion in the Tube, Teploenergetika 7 (1961) 57–60.

[88] B. Donevski, J. Kulesza, Resistance coefficients for laminar and turbulent flow in swirling ducts, Archiwum Termodynamiki i Spalania 9 (3) (1978) 497–506.

[89] K. Watanabe, T. Taira, Y. Mori, Heat transfer augmentation in tubular flow by twisted tapes at high temperatures and optimum performance, Heat Transfer - Japanese Research 12 (1983) 1–31.

[90] P.A. Di Maio, et al., DIV-1-T001-D010 Thermo-hydraulic assessment report 2015, EUROfusion: Munich, Germany, 2016, EUROfusion IDM Ref.: 2MY45W v1.0.

[91] I.E. Idelchik, Handbook of Hydraulic Resistance, Jaico Publishing House, 2008.

[92] S. E. Haaland, Simple and Explicit Formulas for the Friction Factor in Turbulent Pipe Flow, Journal of Fluids Engineering 105 (1) (1983) 89–90. doi:10.1115/1.3240948.

[93] ANSYS Inc., ANSYS DesignXplorer User's Guide, ANSYS: Canonsburg, PA, USA, 2021, 2021, Release: 2021 R1.

[94] V. Gnielinski, New equations for heat and mass transfer in turbulent pipe and channel flow, International Chemical Engineering 16 (2) (1976) 359–368.

[95] E. Vallone, et al., Conference Paper. Thermal-hydraulic study of the Primary Heat Transfer System of EU-DEMO Divertor Plasma Facing Components, The 19 th International Topical Meeting on Nuclear Reactor Thermal Hydraulics (NURETH-19) Brussels, Belgium, March 6 - 11, 2022, ISBN 9789076971261, 2022.

[96] http://www.cresco.enea.it/english.

[97] T. Haertl, et al., Rationale for the selection of the operating temperature of the DEMO vacuum vessel, Fusion Engineering and Design 146 (2019) 1096–1099. doi:10.1016/j.fusengdes.2019.02.014.

[98] J. Mahaffy, et al., Best practice guidelines for the use of CFD in nuclear reactor safety applications, Tech. rep., Organisation for Economic Co-Operation and Development (2007).

[99] D.C. Groeneveld, et al., The 2006 CHF look-up table, Nuclear Engineering and Design 237 (15) (2007) 1909–1922. doi:https://doi.org/10.1016/j.nucengdes.2007.02.014.

Appendices

Appendix A

In this appendix, supplementary information is provided to complement the results of the ADRANOS analyses presented in chapter 2. The purpose of this appendix is to present some graphs illustrating how CHF margin, pressure drop, coolant axial velocity inside the PFU cooling channel, saturation margin, and maximum temperatures of the PFU strictures vary with respect to the coolant inlet pressure, temperature, and mass flow rate. Moreover, these quantities are compared to the applicable constraints, listed in table 2.4, and the trends are justified by referencing the relevant governing equations.

The results reported in the following figure A.1 to A.8 are calculated for the PFC cooling circuit of the double-circuit cooling option divertor (2019 design), but similar results are obtained for every divertor configuration investigated in this dissertation. The applicable limit values of table 2.4 are highlighted with a black dashed curve.

Figure A.1 depicts the CHF margin calculated for the OVT (constraint A of table 2.4), but qualitatively similar results are obtained for the IVT, with small differences due to the different number of PFU assemblies and due to the non-uniformities in coolant distribution between the two targets. As it may be argued from the figure, the CHF margins increase with the mass flow rate and the coolant inlet pressure and decrease with the temperature. These trends can be deduced by equations (2.8) to (2.11).

As far as the pressure drop is concerned (constraint C of table 2.4), the results obtained are depicted in figure A.2. The pressure drop is strongly influenced by the mass flow rate, as the iso-Δp curves are almost parallel to the iso-$\dot{m}$ lines, as can be easily deduced by equation (2.1). By increasing the coolant inlet temperature, the pressure drop of the cooling circuit is increased, due to the dependence of coolant density on the temperature, while the effects of pressure on the results are negligible.

Coolant maximum axial velocity inside the OVT PFU cooling channels curves are shown in figure A.3 (constraint D of table 2.4), while qualitatively similar results are obtained for the IVT PFU cooling channels (constraint E). The dependencies of this quantity on the coolant inlet pressure, inlet temperature and mass flow rate are the same as those of the pressure drop.

The saturation margin is depicted in figure A.4 (constraint F of table 2.4). As

it may be noted from the figures, there are no black dashed curves, as the results in the considered range of coolant conditions are always above the applicable limit values. The saturation margin always decreases with temperature and increases with pressure. The dependency on mass flow rate is not monotonic, as at low mass flow rate values an increase in $\dot{m}$ causes an increase of the saturation margin, due to the lower outlet temperatures (the total power deposited onto the component is the same). At higher mass flow rate values, instead, the pressure drop increases, and the effect of lower pressure on the saturation margin becomes more important than the reduction of the coolant temperature.

The following figure A.5 to A.8 represent the temperature distributions inside the PFU structures. To avoid any misinterpretation of the results, the regions in which the ADRANOS FEM module is not executed are filled in grey.

The temperature in the OVT CuCrZr under an incident heat flux of 10 MW/m^2 is depicted in figure A.5 (constraint G of table 2.4) and qualitatively similar results are obtained also for the IVT (constraint H). As can be observed from the figures, the temperature decreases with the mass flow rate, due to the increase in the heat transfer coefficient, while it increases with the coolant temperature. The effect of pressure on this quantity is negligible.

The temperature in the OVT CuCrZr under an incident heat flux of 20 MW/m^2 is depicted instead in figure A.6, and similar results are obtained also for the IVT (constraints I and J of table 2.4). The dependences of the results on the coolant inlet temperature and mass flow rate are the same as for the case of 10 MW/m^2 heat load scenario, while the effect of coolant inlet pressure is more evident. In particular, under 20 MW/m^2 heat load conditions, nucleate boiling heat transfer mechanisms are established, and the cooling channel wall temperature is locked to the saturation temperature at the given coolant pressure. With a higher coolant pressure, the saturation temperature increases and, as a consequence, the CuCrZr temperatures increase as well.

Finally, maximum temperature values in the OVT tungsten and copper under an incident heat flux of 20 MW/^{2} are depicted in figures A.7 and A.8 (constraints K and M of table table 2.4). Analogous results are obtained also for the IVT. The dependences of these temperatures on coolant inlet pressure, inlet temperature and mass flow rate are the same as those relevant to the CuCrZr cooling pipe under the same heat flux conditions, as the same physical reasoning detailed for the CuCrZr is valid for the other materials.

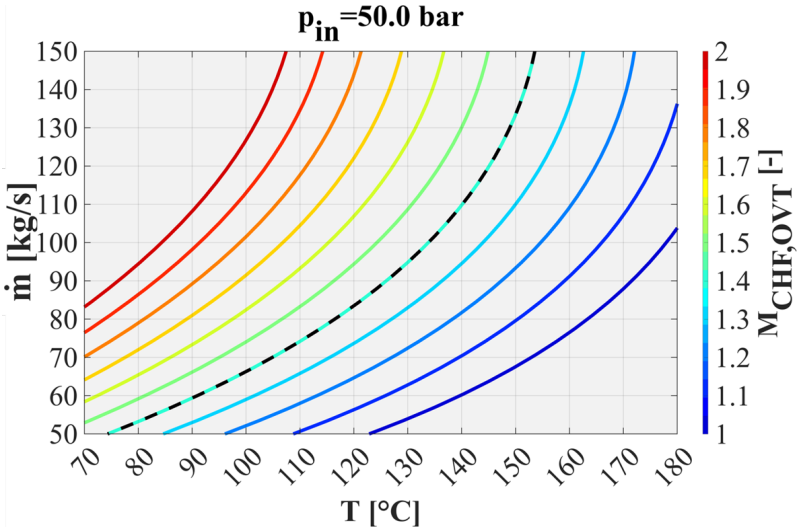

(a)

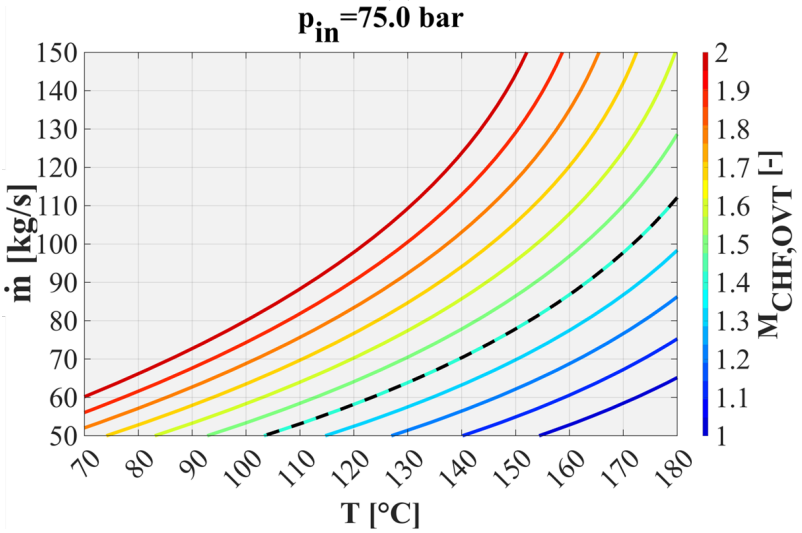

(b)

Figure A.1: CHF margin as a function of inlet coolant pressure and mass flow rate for the OVT calculated for a coolant inlet pressure of 50 (a) and 75 (b) bar.

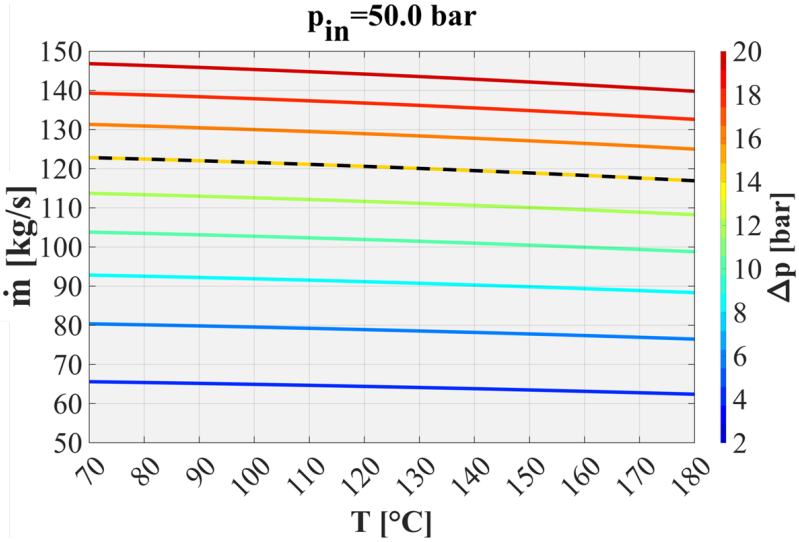

(a)

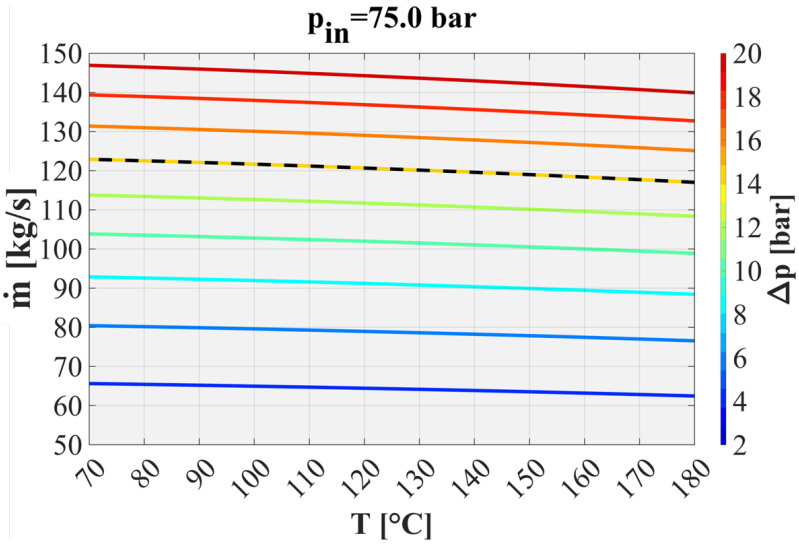

(b)

Figure A.2: Pressure drop as a function of inlet coolant pressure and mass flow rate calculated for a coolant inlet pressure of 50 (a) and 75 (b) bar.

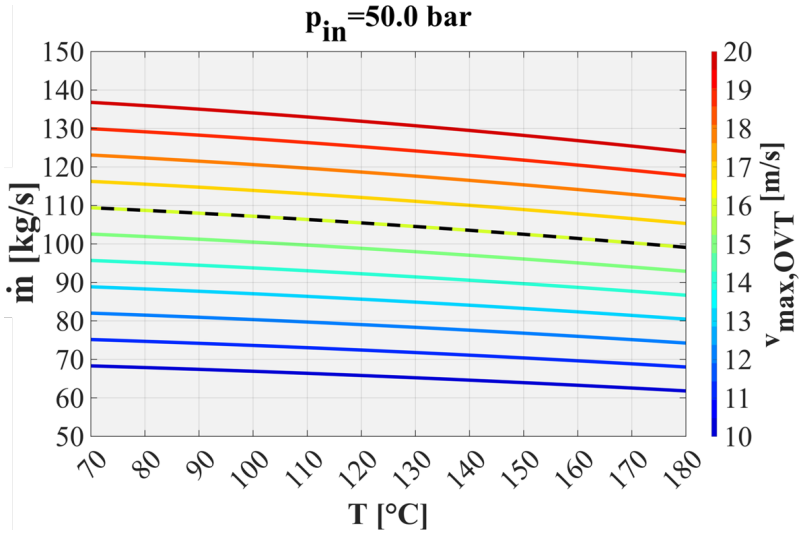

(a)

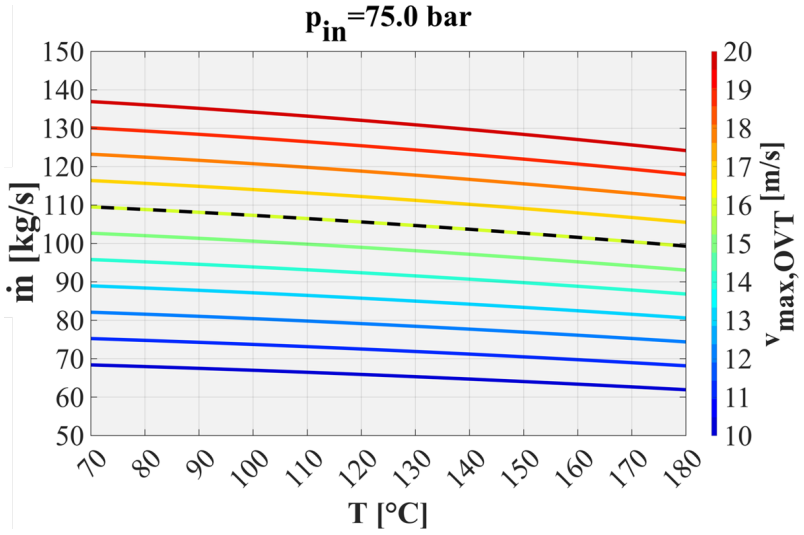

(b)

Figure A.3: Maximum coolant axial velocity as a function of inlet coolant pressure and mass flow rate for the OVT calculated for a coolant inlet pressure of 50 (a) and 75 (b) bar.

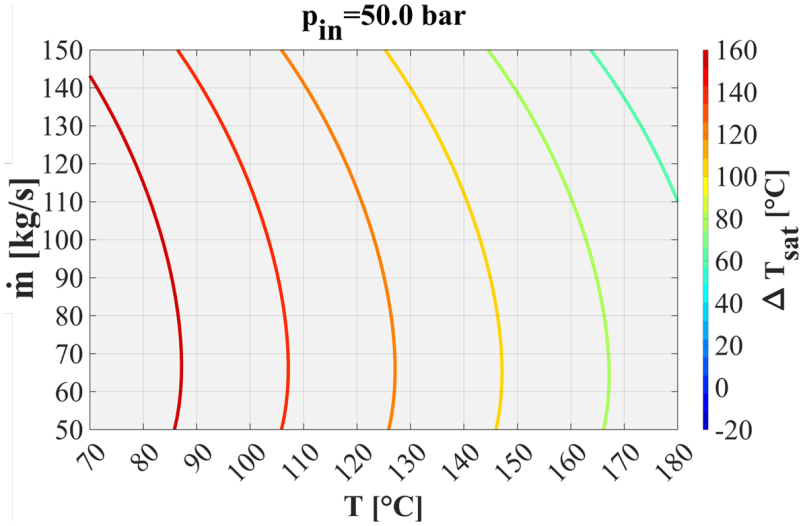

(a)

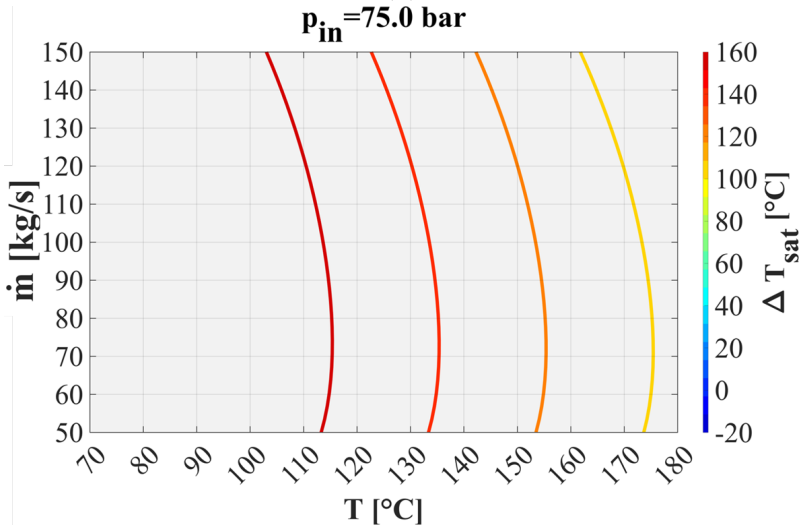

(b)

Figure A.4: Minimum saturation margin as a function of inlet coolant pressure and mass flow rate calculated for a coolant inlet pressure of 50 (a) and 75 (b) bar.

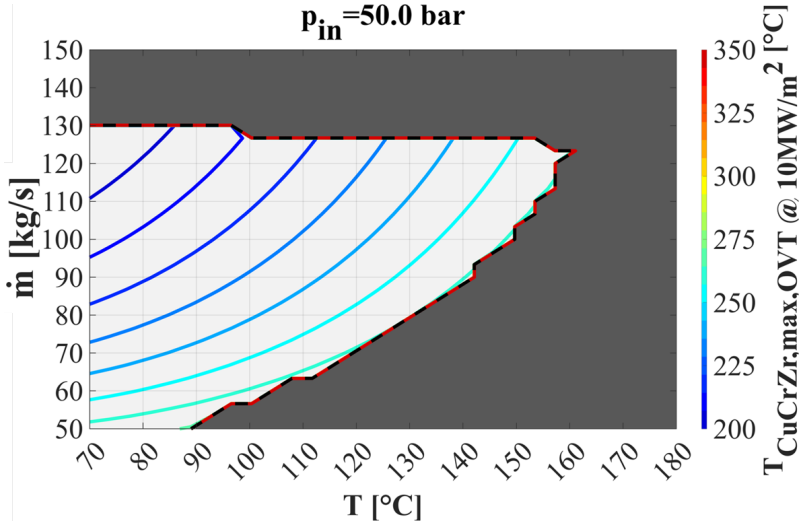

(a)

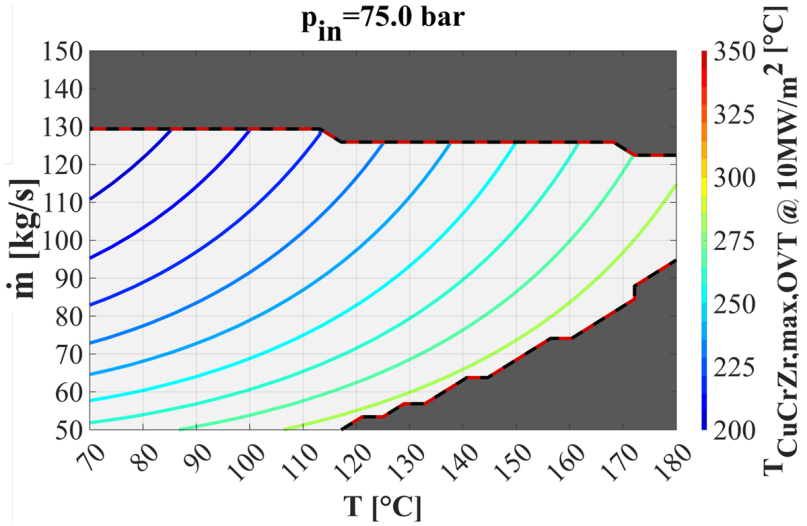

(b)

Figure A.5: CuCrZr maximum temperature under an incident heat flux of 10 MW/m^2 as a function of inlet coolant pressure and mass flow rate calculated for the OVT for a coolant inlet pressure of 50 (a) and 75 (b) bar.

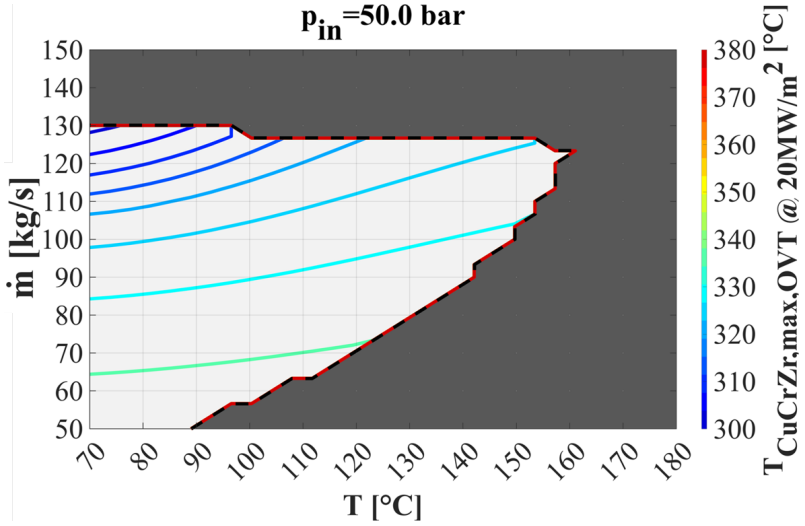

(a)

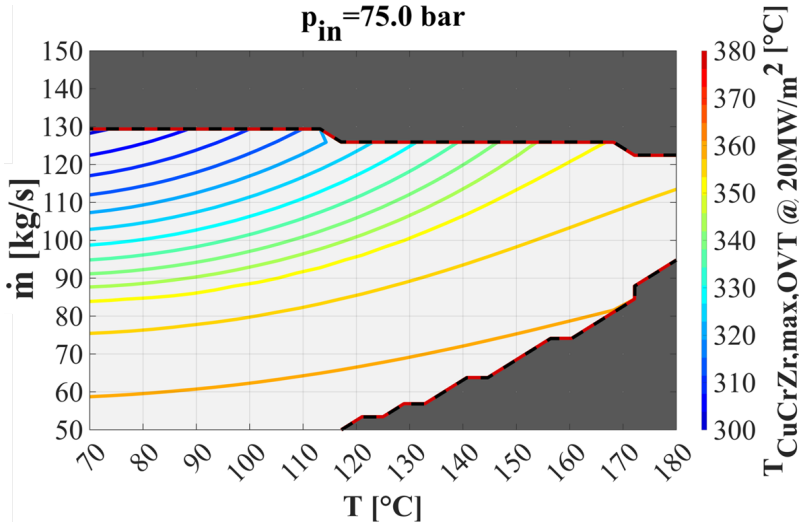

(b)

Figure A.6: CuCrZr maximum temperature under an incident heat flux of 20 MW/m^2 as a function of inlet coolant pressure and mass flow rate calculated for the OVT for a coolant inlet pressure of 50 (a) and 75 (b) bar.

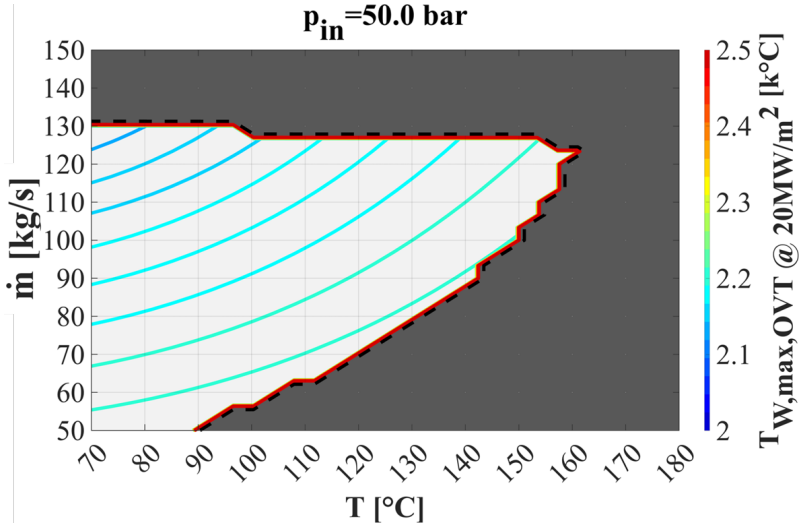

(a)

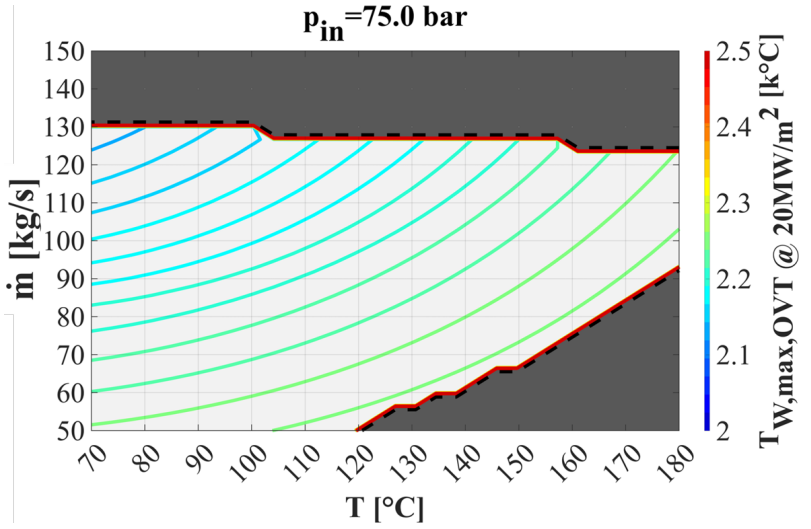

(b)

Figure A.7: Tungsten maximum temperature under an incident heat flux of 20 MW/m^2 as a function of inlet coolant pressure and mass flow rate calculated for the OVT for a coolant inlet pressure of 50 (a) and 75 (b) bar.

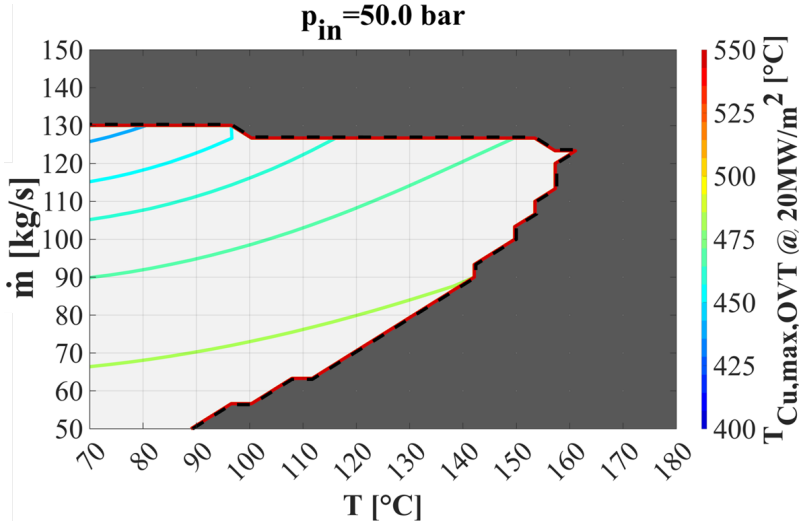

(a)

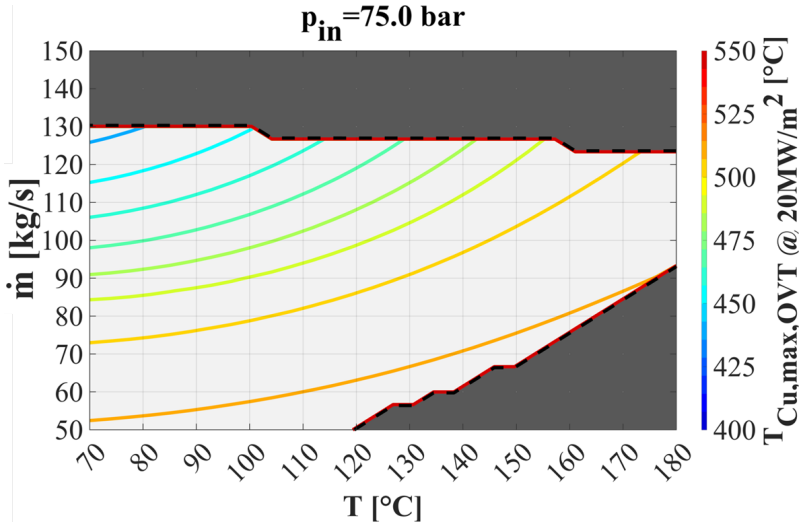

(b)

Figure A.8: Copper maximum temperature under an incident heat flux of 20 MW/m^2 as a function of inlet coolant pressure and mass flow rate calculated for the OVT for a coolant inlet pressure of 50 (a) and 75 (b) bar.